coatings

Biointerface Coatings for Biomaterials and Biomedical Applications

Edited by

Hsien-Yeh Chen and Peng-Yuan Wang

Printed Edition of the Special Issue Published in *Coatings*

www.mdpi.com/journal/coatings

MDPI

Biointerface Coatings for Biomaterials and Biomedical Applications

Biointerface Coatings for Biomaterials and Biomedical Applications

Editors

Hsien-Yeh Chen
Peng-Yuan Wang

MDPI • Basel • Beijing • Wuhan • Barcelona • Belgrade • Manchester • Tokyo • Cluj • Tianjin

Editors

Hsien-Yeh Chen	Peng-Yuan Wang
National Taiwan University	Chinese Academy of Sciences
Taiwan	China

Editorial Office
MDPI
St. Alban-Anlage 66
4052 Basel, Switzerland

This is a reprint of articles from the Special Issue published online in the open access journal *Coatings* (ISSN 2079-6412) (available at: https://www.mdpi.com/journal/coatings/special_issues/biointerface_coat_biomater_biomed_appl).

For citation purposes, cite each article independently as indicated on the article page online and as indicated below:

LastName, A.A.; LastName, B.B.; LastName, C.C. Article Title. *Journal Name* **Year**, *Volume Number*, Page Range.

ISBN 978-3-0365-2243-2 (Hbk)
ISBN 978-3-0365-2244-9 (PDF)

Contents

About the Editors

Hsien-Yeh Chen

Hsien-Yeh Chen's research focuses on vapor-based polymers for biomaterials and biomedical devices. These polymers have been successfully applied in bone and tooth implants, drug-eluting stents, intraocular lenses, micro- and nanocolloids, nanomedicine carriers, and bioelectronic devices. Polymer technology enables biomaterials to be produced with properties including antifouling and antibacterial activities, cell differentiation manipulations, superhydrophobic interfaces, and surface patterns. Prof. Chen was the receiver of the Ta-You Wu Memorial Award in 2017, the National Award for the Innovation in Biotechnology of Taiwan in 2016, and the Green Chemistry Application and Innovation Awards in 2021.

Peng-Yuan Wang

Peng-Yuan Wang received his Ph.D. from the Department of Chemical Engineering, National Taiwan University, in 2011. Dr Wang is currently the Principal Investigator at Oujiang Laboratory, Zhejiang, China. He was the Director of Shenzhen Key Laboratory, the Principal Investigator at the Shenzhen Institute of Advanced Technology (SIAT), Chinese Academy of Sciences (CAS), and the lecturer at Swinburne University. Dr Wang has been awarded several prestigious awards, including the Thousand Talent Fellowship in China; the Discovery Early Career Researcher Award (DECRA) and the Veski Victoria Fellowship in Australia. His research focuses on manipulating stem cell behavior using biophysical cues such as nanostructured patterns and cell compression, which provides new insights in mechanobiology, biomaterials, and regenerative medicine. Dr Wang has authored over 70 peer-reviewed SCI publications, 3 book chapters, and applied for/been issued over 10 patents worldwide. His works provide an essential framework for understanding biophysical effects on stem cells and the development of next-generation biomaterials and tools for regenerative medicine.

Preface to ”Biointerface Coatings for Biomaterials and Biomedical Applications”

In addition to meeting the minimal requirements for biocompatibility, advanced biomaterials have acquired functions allowing them to directly or indirectly influence specific biological environments. Modifications to biomaterials are elegantly achieved by establishing a biointerface layer to deliver the desired functions, but the definition and configuration required to balance such an interface between the exploited materials or devices and the encountered biological microenvironment pose challenges. The design of a successful biointerface usually depends on criteria such as controlled presentation of functional biomolecules on the surface, low nonspecific protein adsorption, responsive actions toward external stimuli, multifunctionality, compatibility with micro- to nanofabrication, surface morphology or microstructures, biodegradability, and physical or chemical gradients. Many promising approaches have been reported using existing surface modification technologies based on both physical and chemical methods for rendering fabricated coatings on biomaterials, from basic self-assembly of molecules to top-down construction of bulk materials. The development of technologies in this field is pursued by exploring complimentary and/or combinatorial strategies based on both existing and newly discovered methods, and these technologies are paving the way for advanced and effective functional biointerfaces for prospective biomaterials. This eBook provides insights into current obstacles in the development of biointerfaces for biomaterials and discuss current progress with examples of solutions to interface problems, and this work is suitable for audiences interested in biology and materials science who seek solutions to biointerface problems and challenges. The Editors are grateful for the contributing authors and their input regarding research and prospective insights for the eBook, the funding support (detailed in the Editorial) leading to the publication of the eBook, and finally the publication resources provided by MDPI Coatings.

• Surface coatings are useful for changing surface properties according to the requirements for numerous marine and biological applications. Surface coatings modified by vapor phase, plasma, dry-/wet-etching, and solutions also provide considerable advantages in forthcoming industrial technology.

• For this eBook, we invited experts from different fields and describe their latest technology in detail for material selection, deposition, characterization, and evaluation.

• In the editorial of the eBook, two Guest Editors summarize the latest technology and applications of surface coatings in biomedical engineering. They split the surface properties into three dominant factors, i.e., topography, chemistry, and stiffness, and discuss cell–material interactions at biointerfaces.

• In the review paper in this eBook, the surface coatings of orthopedic implants are discussed and summarized. The authors also highlight the currently available nanomaterial-based surface modification technologies available to augment the function and performance of these metallic bioimplants in a clinical setting.

• In the next two feature papers, bioceramic coatings fabricated by plasma spray for bone implants and microbicidal coatings for antimicrobial surfaces were investigated. The first paper shows that Sr–HT–G and HAp coatings both have good biocompatibility for bone marrow mesenchymal stem cells (BMSCs), whereas the second paper presents a new surface design for the production of durable microbicidal coatings. These two applications will be widely useful in clinics and beneficial in next-generation implants.

• In the next four research papers, the authors report different surface coating methods and characterizations, including chemical vapor sublimation and deposition (CVSD), micro-arc oxidation, magnetic poly(vinyl alcohol) (mPVA) gels, and matrix-assisted laser desorption/ionization-time of flight mass (MALDI-ToF mass) spectroscopy. These studies show the diversity of surface coatings and their applications.

• In the next two research papers, the authors focus on coatings for bone tissue engineering. The first paper suggests that the established NT-ICA-ASP/PLGA substrate is a promising candidate for functionalized coating materials in Ti implant surface modification. The second paper shows that PPy/PDA NW coating has better biocompatibility and bioactivity than pure PPy NWs, and PDA and has benefits for the adhesion, proliferation, and osteogenic differentiation of MC3T3-E1 cells cultured on the surface. In addition, PPy/PDA NWs can significantly promote the osteogenesis of MC3T3-E1 cells in combination with micro-galvanostatic electrical stimulation (ES).

• In the last two research papers, corrosion properties and anticorrosion coatings are studied and developed. The first paper reports that UMAO/PLGA/BR coatings have excellent biological activity, which can effectively solve the clinical problem of the rapid degradation of pure magnesium and easy infection. The second paper was inspired by mangrove leaves that have salt glands that can secrete excessive ions to control ion transport in and out. The authors fabricated bipolar, hydrophobic coatings by doping ion-selective resins and constructing surface structures, which restrict the transport of corrosive substances and electrochemical corrosion at the coating/metal interface. They showed that the bioinspired coatings effectively blocked and controlled the transport of both Na+ and Cl, and together with the hydrophobic surface, the coating system exhibited significantly improved anticorrosion properties, a more than three-fold decrease in corrosion current density compared with the control group (epoxy varnish).

• Surface coatings have a decisive impact on a material and are constantly evolving with new needs. It is expected that the above studies will be informative to the reader.

Hsien-Yeh Chen and Peng-Yuan Wang
Editors

coatings

Editorial

Special Issue: Biointerface Coatings for Biomaterials and Biomedical Applications

Hsien-Yeh Chen [1,*] and Peng-Yuan Wang [2,3,*]

[1] Department of Chemical Engineering, Molecular Imaging Center, National Taiwan University, Taipei 10617, Taiwan
[2] Shenzhen Key Laboratory of Biomimetic Materials and Cellular Immunomodulation, Shenzhen Institute of Advanced Technology, Chinese Academy of Sciences, Shenzhen 518055, China
[3] Department of Chemistry and Biotechnology, Swinburne University of Technology, Hawthorn, VIC 3122, Australia
* Correspondence: hsychen@ntu.edu.tw (H.-Y.C.); py.wang@siat.ac.cn (P.-Y.W.)

Citation: Chen, H.-Y.; Wang, P.-Y. Special Issue: Biointerface Coatings for Biomaterials and Biomedical Applications. *Coatings* **2021**, *11*, 423. https://doi.org/10.3390/coatings11040423

Received: 31 March 2021
Accepted: 2 April 2021
Published: 6 April 2021

The success of recent material science and applications in biotechnologies should be credited to developments of malleable surface properties, as well as the adaptation of conjugation reactions to the material surface [1–4]. An article additionally addressing the progress and challenges of biointerface modifications using integrated nanomaterial bioimplants for orthopedic applications was also thoroughly reviewed in the current Special Issue by Ahirwar et al [5]. A biointerface is the region of contact between a biomolecule, cell, biological tissue, or living organism considered living with another biomaterial or inorganic/organic material. The surface property of a material is highly important, even compared to the bulk property [6]. For example, a hydrogel is soft (e.g., 1–100 kPa) but could have a stiffer thin layer on the top surface (>100 kPa) that modulates cell adhesion at the biointerface. On the other hand, rigid materials can also be modified with a softer surface coating to enhance biocompatibility. Therefore, surface modification or coatings have immense potential and wide application in biomedical devices and implants [7]. The crucial biointerface properties of using biomaterials include the ability to control the presentation of biomolecules with precisely defined chemical topology, the ability to control and suppress undesirable background noise from nonspecific biomolecules (e.g., protein) adsorptions, smart response with respect to environmental stimuli, multiple functions that are simultaneously activated, and surface gradients with gradual and cascade guidance from physical and/or chemical cues. These properties may subsequently lead to successful biodevice/material performance and efficacy. In the article "*Proteomic Analysis of Biomaterial Surfaces after Contacting with Body Fluids by MALDI-TOF Mass Spectroscopy*", Hirohara et al. developed an analysis method to evaluate the composition of protein absorbed on solid surfaces while preventing the effects of pipetting artifacts. The method includes denaturation, reduction, alkylation, digestion, and spotting of the matrix followed by matrix-assisted laser desorption/ionization-time of flight mass (MALDI-TOF mass) spectroscopy. The authors also developed an algorithm to evaluate the adsorbed proteins by collating the experimental and theoretical peak positions of fragmented peptides. Their results showed the mechanism of how the cell and tissues are affected after biomaterial contact [8].

Furthermore, biomolecular engineering technologies have enabled the successful use of these polymer materials. The use of physical approaches or chemical means to install biological functions onto polymer materials is of interest within this area of research. From a physical point of view, the ability to control biomolecules at the solid/liquid interface requires adequate knowledge and understanding of surface interactions, transport phenomena of interacting molecules, interactions with external stimuli, and surface functional groups. From a chemical point of view, conjugation reactions seek a fast reaction time, mild reaction conditions, and, more importantly, specificity to achieve successful conjugation in the vast array of functionalities present in biological microenvironments [9].

Recently demonstrated and promising concepts have focused on the creation of multiple surface functionalities on material surfaces [10–15]. The approaches consider the physical and chemical surface properties while delivering cascading and/or simultaneous activities to respond to sophisticated bioenvironments. Moreover, the need to precisely incorporate biomolecules at specific locations on a micro/nanoscale, i.e., in confined micro/nanodomains and to induce topographically derived responses toward biological environments, has also become essential. These concepts have fueled modern schemes for the design of prospective polymer materials for biological applications as well as more advanced developments in biointerface science. In the article "*Facile Route of Fabricating Long-Term Microbicidal Silver Nanoparticle Clusters against Shiga Toxin-Producing Escherichia coli O157:H7 and Candida auris*", Gangadoo et al. reported a facile coating technique using silver nanoparticles (Ag NPs) to fabricate a surface with long-term microbiocidal activity. The Ag NP coating was fabricated on copper surfaces via an ion-exchange and reduction reaction followed by a silanization step, resulting in high-aspect-ratio Ag NP clusters. Their results demonstrated the durability and high efficiency of microbiocidal activity against both Shiga toxin-producing *E. coli* and *C. auris* cells [16]. In the article "*One-Step Preparation of Nickel Nanoparticle-Based Magnetic Poly (Vinyl Alcohol) Gels*", Li et al. established a one-step synthetic method of magnetic poly (vinyl alcohol) (mPVA) gels. Using this method, multiresponsive gels were obtained by incorporating Ni nanoparticles (NPs) into a stimuli-responsive polymer. Ni-NP PVA gels are anticipated to be applied for controlled drug delivery systems, especially anticancer applications. This novel and facile method can be utilized for magnetic gels for biotechnology [17]. In the article "*Mangrove Inspired Anti-Corrosion Coatings*", Cui et al. discovered that well-controlled transport of corrosive substances is the critical key to anti-corrosion performance. The authors demonstrated a bipolar hydrophobic coating that can effectively block and control the transport of both Na + and Cl-, exhibiting significantly improved anti-corrosion properties and a more than three orders of magnitude decrease in corrosion current density. These bioinspired coatings may lead to outstanding and long-term anti-corrosion performance [18].

Surface topography, including nanostructure and roughness, is one of the critical parameters of materials at biointerfaces. Advanced technologies, including electron beam lithography, laser ablation, and electrochemical etching, have been developed to generate surface nanotopographies [19,20]. In the article "*Vapor-Stripping and Encapsulating to Construct Particles with Time-Controlled Asymmetry and Anisotropy*", Wu et al. demonstrated the fabrication method of particles with asymmetric and anisotropic structures by utilizing a time-controlled vapor stripping and encapsulating process. The results showed that the innovative process, chemical vapor sublimation and deposition (CVSD), enabled sensitive soybean agglutinin (SBA) protein tubes to be encapsulated in poly-p-xylylene particles. The SBA protein tubes retained their original morphology and could be used to construct particles with asymmetric and anisotropic structures. In addition, the size of the particles could be predicted and controlled. The CVSD process is a promising strategy for fabricating particles [21]. Nevertheless, these methods are material-dependent. For example, silicon has been commonly used in lithography and etching methods. Nanostructures have been used to control cell adhesion and differentiation. The outcomes depend on the size, geometry, arrangement, density, and, not surprisingly, cell type. In general, nanostructures are biocompatible, cell adhesive, low bacterial adhesive, low inflammatory, and biofunctional. For example, nanostructures on a bone implant should induce a mild inflammatory effect and good bone cell affinity and bone integration. In the article "*Icariin/Aspirin Composite Coating on TiO_2 Nanotubes Surface Induce Immunomodulatory Effect of Macrophage and Improve Osteoblast Activity*", Ma et al. used an aspirin (ASP)/poly (lactic–co–glycolic acid) (PLGA) coating on icariin (ICA)-loaded TiO_2 nanotubes (NT-ICA-ASP/PLGA). Compared to those cultured on the Ti surface, macrophages on the NT-ICA-ASP/PLGA substrate displayed decreased M1 proinflammatory and enhanced M2 pro-regenerative gene and protein expression, which implied an activated immunomodulatory effect. Moreover, when cultured with conditioned medium from macrophages, osteoblasts on the NT-ICA-ASP/PLGA substrate showed improved cell proliferation, adhesion and osteogenic gene and protein expression compared with those on the Ti surface. These results suggested that the NT-ICA-ASP/PLGA substrate is a promising candidate for functionalized coating material in Ti implant surface modification [22]. In the article "*The Bioactive Polypyrrole/Polydopamine Nanowire Coating with Enhanced Osteogenic Differentiation Ability with Electrical Stimulation*", He et al. used a two-step method to construct a functional conductive coating of polypyrrole/polydopamine (PPy/PDA) nanocomposites for bone regeneration. The PPy/PDA NW coating exhibited better biocompatibility and bioactivity than pure PPy NWs and PDA and was beneficial for the adhesion, proliferation, and osteogenic differentiation of MC3T3-E1 cells cultured on the surface. In addition, PPy/PDA NWs significantly promoted the osteogenesis of MC3T3-E1 cells in combination with micro galvanostatic electrical stimulation (ES) [23].

Surface chemistry, including material chemistry, biomolecule grafting, and chemical coatings, is another critical parameter of materials at biointerfaces [24–26]. Surface chemistry represents functional groups, electrostatic properties, and wettability on the material surface. These properties are crucial in interactions with proteins, cells, and tissues. For example, the carboxy group can stimulate osteogenic differentiation of mesenchymal stem cells (MSCs). Uniform coatings such as spin coating provide a thin layer of polymer (~submicrons) on materials. The adhesive force between the thin layer and substrate is essential for the long-term application of the materials. Nonuniform coatings can be achieved using dewetting methods, which in turn generate nano or micrometer-scale features. In the article "*Corrosion Behavior and Biological Activity of Microarc Oxidation Coatings with Berberine on a Pure Magnesium Surface*", Mu et al. reported a coating named ultrasonic microarc oxidation/polylactic acid and glycolic acid copolymer/berberine (UMAO/PLGA/BR) on a pure magnesium substrate for bone materials. Different amounts of berberine (BR) can seal the corrosion channel to different extents. These coatings have a self-corrosion current density (Icorr) at least one order of magnitude lower than that of the UMAO coatings. When the BR content was 3.0 g/L, the self-corrosion current density of the UMAO/PLGA/BR coatings was the lowest (3.14×10^{-8} A/cm^2), and the corrosion resistance was improved. UMAO/PLGA/BR coatings have excellent biological activity, which can effectively solve the clinical problem of rapid degradation of pure magnesium and easy infection [27]. In the report "*Chemical and Biological Roles of Zinc in a Porous Titanium Dioxide Layer Formed by Micro-Arc Oxidation*" by Shimabukuro et al., zinc incorporated by microarc oxidation (MAO) in porous titanium dioxide was investigated under physiological saline conditions. The time transient state from zinc to zinc oxide led to early stage release in 7 days and antibacterial ability after 28 days of incubation. Additionally, there was no interruption of osteogenic cell proliferation and calcification in zinc specimens. In conclusion, time-transient zinc not only gives antibacterial properties but also shows great compatibility with osteogenic cells and has great potential in chemical and biological fields [28].

Surface stiffness in the material top surface (~submicrons) is crucial in controlling cell adhesion, the cytoskeleton, and cell differentiation [29]. In vivo, the stiffness of the extracellular matrix (ECM) ranges from a few kPa (e.g., brain) to GPa (e.g., bone). Thus, it makes sense that surfaces with different stiffnesses could mimic the native ECM and guide cells to become a specific cell type. The top surface of materials is easily oxidized, altering the stiffness of the surface. Because the top surface has a more dominant effect on cell behavior than the bulk material, technology with higher resolution is needed to analyze the mechanical properties of the top layer. In the article "*Mechanical Properties of Strontium–Hardystonite–Gahnite Coating Formed by Atmospheric Plasma Spray*", Pham et al. measured the mechanical properties and tested the cell viability of a bioceramic coating, strontium–hardystonite–gahnite (Sr–HT–G, Sr–$Ca_2ZnSi_2O_7$–$ZnAl_2O_4$), to evaluate the potential use of this novel bioceramic for bone regeneration applications contrasted to the properties of the well-known commercial standard coating of hydroxyapatite (HAp: $Ca_{10}(PO_4)_6(OH)_2$). The Sr–HT–G coating exhibited a more uniform distribution of hardness and elastic moduli across its cross-section compared to HAp. The Sr–HT–G coating also revealed higher microhardness, nanohardness and elastic moduli than those shown for the HAp coating. The nanoscratch tests for the Sr–HT–G coating presented a low volume of material removal without high plastic deformation. Furthermore, the Sr–HT–G coating had a lower wear volume than the HAp. The Sr–HT–G coating had a slightly higher cell attachment density and spreading area of bone marrow mesenchymal stem cells (BMSCs) than the HAp coating [30].

Finally, biointerfaces often contain a combination of surface topography, chemistry, and stiffness. These three properties are sometimes difficult to distinguish. For example, the generation of surface nanotopography could change the surface wettability, and polymer coating could alter the surface nanotopography. Recently, a new family of two-dimensional (2D) materials called colloidal self-assembled patterns (cSAPs), composed of different particles, has been developed [31,32]. The formed particle patterns can be hexagonal, close-packed, or randomly distributed. The topography of cSAPs can be tuned by controlling particle-particle interactions. It is easy to decorate biosignals on cSAPs using pre- or postmodification of particles. cSAPs can be used as substrates, coatings, and free-standing membranes, depending on the application. cSAPs can be the next-generation material at biointerfaces. As more stringent specifications are required for designing the surface properties of prospective materials and the development of new devices is pursued with complicated geometries and minimized sizes, the surface properties of such materials/devices now also require a more defined and flexible presentation of the chemical functionalities (e.g., multifunctional or gradient distribution) and the precise confinement of these chemical conducts in relevant locations of interest [33]. The emerging applications of the existing technologies and/or new technologies from two dimensions into more sophisticated three-dimensional regions [34] are challenging the field of biointerfaces science, and further research developments are expected on this path.

Author Contributions: Conceptualization, H.-Y.C. and P.-Y.W.; writing—original draft preparation, H.-Y.C. and P.-Y.W.; writing—review and editing, H.-Y.C. and P.-Y.W.; supervision, H.-Y.C. and P.-Y.W.; funding acquisition, H.-Y.C. and P.-Y.W. All authors have read and agreed to the published version of the manuscript.

Funding: This research was funded by the Ministry of Science and Technology of Taiwan (MOST 108-2221-E-002-169-MY3; 108-2218-E-007-045; 109-2314-B-002-041-MY3; 109-2634-F-002-042). Funding support also came from the Ministry of Science and Technology of China (2019YFE0113000); the National Natural and Science Foundation of China (31870988); the Chinese Academy of Sciences (172644KYSB20200002, 172644KYSB20200048, CAS-ITRI201902); the Science, Technology, and Innovation Commission of Shenzhen Municipality (20180921173048123); the Shenzhen Key Laboratory of Biomimetic Materials and Cellular Immunomodulation (ZDSYS20190902093409851).

Conflicts of Interest: The authors declare no conflict of interest. The funders had no role in the design of the study; in the collection, analyses, or interpretation of data; in the writing of the manuscript; or in the decision to publish the results.

References

1. Sun, T.; Qing, G.; Su, B.; Jiang, L. Functional biointerface materials inspired from nature. *Chem. Soc. Rev.* **2011**, *40*, 2909–2921. [CrossRef] [PubMed]
2. Liu, X.; Wang, S. Three-dimensional nano-biointerface as a new platform for guiding cell fate. *Chem. Soc. Rev.* **2014**, *43*, 2385–2401. [CrossRef]
3. Iwasaki, Y.; Ishihara, K. Cell membrane-inspired phospholipid polymers for developing medical devices with excellent biointerfaces. *Sci. Technol. Adv. Mater.* **2012**, *13*, 064101. [CrossRef] [PubMed]
4. Jiang, Y.; Tian, B. Inorganic semiconductor biointerfaces. *Nat. Rev. Mater.* **2018**, *3*, 473–490. [CrossRef] [PubMed]
5. Ahirwar, H.; Zhou, Y.; Mahapatra, C.; Ramakrishna, S.; Kumar, P.; Nanda, H.S. Materials for Orthopedic Bioimplants: Modulating Degradation and Surface Modification Using Integrated Nanomaterials. *Coatings* **2020**, *10*, 264. [CrossRef]
6. Dalby, M.J.; García, A.J.; Salmeron-Sanchez, M. Receptor control in mesenchymal stem cell engineering. *Nat. Rev. Mater.* **2018**, *3*, 17091. [CrossRef]
7. Shi, Y.; Liu, K.; Zhang, Z.; Tao, X.; Chen, H.-Y.; Kingshott, P.; Wang, P.-Y. Decoration of Material Surfaces with Complex Physicochemical Signals for Biointerface Applications. *ACS Biomater. Sci. Eng.* **2020**, *6*, 1836–1851. [CrossRef]

8. Hirohara, M.; Maekawa, T.; Mondarte, E.A.; Nyu, T.; Mizushita, Y.; Hayashi, T. Proteomic Analysis of Biomaterial Surfaces after Contacting with Body Fluids by MALDI-ToF Mass Spectroscopy. *Coatings* **2020**, *10*, 12. [CrossRef]
9. Sletten, E.M.; Bertozzi, C.R. Bioorthogonal Chemistry: Fishing for Selectivity in a Sea of Functionality. *Angew. Chem. Int. Ed.* **2009**, *48*, 6974–6998. [CrossRef]
10. Wu, C.-Y.; Chang, C.-W.; Yuan, R.-H.; Chiang, Y.-C.; Chen, J.-T.; Kang, D.-Y.; Chen, H.-Y. Multifunctional nanoparticles with controllable dimensions and tripled orthogonal reactivity. *Nanoscale* **2017**, *9*, 14787–14791. [CrossRef]
11. Tsai, M.-Y.; Chen, Y.-C.; Lin, T.-J.; Hsu, Y.-C.; Lin, C.-Y.; Yuan, R.-H.; Yu, J.; Teng, M.-S.; Hirtz, M.; Chen, M.H.-C.; et al. Vapor-Based Multicomponent Coatings for Antifouling and Biofunctional Synergic Modifications. *Adv. Funct. Mater.* **2014**, *24*, 2281–2287. [CrossRef]
12. Chen, H.-Y.; Lin, T.-J.; Tsai, M.-Y.; Su, C.-T.; Yuan, R.-H.; Hsieh, C.-C.; Yang, Y.-J.; Hsu, C.-C.; Hsiao, H.-M.; Hsu, Y.-C. Vapor-based tri-functional coatings. *Chem. Commun.* **2013**, *49*, 4531–4533. [CrossRef] [PubMed]
13. Guan, Z.-Y.; Wu, C.-Y.; Wu, J.-T.; Tai, C.-H.; Yu, J.; Chen, H.-Y. Multifunctional and Continuous Gradients of Biointerfaces Based on Dual Reverse Click Reactions. *ACS Appl. Mater. Interfaces* **2016**, *8*, 13812–13818. [CrossRef] [PubMed]
14. Mertgen, A.-S.; Trossmann, V.T.; Guex, A.G.; Maniura-Weber, K.; Scheibel, T.; Rottmar, M. Multifunctional Biomaterials: Combining Material Modification Strategies for Engineering of Cell-Contacting Surfaces. *ACS Appl. Mater. Interfaces* **2020**, *12*, 21342–21367. [CrossRef]
15. Kim, S.; Jung, U.T.; Kim, S.-K.; Lee, J.-H.; Choi, H.S.; Kim, C.-S.; Jeong, M.Y. Nanostructured Multifunctional Surface with Antireflective and Antimicrobial Characteristics. *ACS Appl. Mater. Interfaces* **2015**, *7*, 326–331. [CrossRef]
16. Gangadoo, S.; Elbourne, A.; Medvedev, A.E.; Cozzolino, D.; Truong, Y.B.; Crawford, R.J.; Wang, P.-Y.; Truong, V.K.; Chapman, J. Facile Route of Fabricating Long-Term Microbicidal Silver Nanoparticle Clusters against Shiga Toxin-Producing Escherichia coli O157:H7 and Candida auris. *Coatings* **2020**, *10*, 28. [CrossRef]
17. Li, J.; Lee, K.-P.; Gopalan, A.I. One-Step Preparation of Nickel Nanoparticle-Based Magnetic Poly(Vinyl Alcohol) Gels. *Coatings* **2019**, *9*, 744. [CrossRef]
18. Cui, M.; Wang, P.-Y.; Wang, Z.; Wang, B. Mangrove Inspired Anti-Corrosion Coatings. *Coatings* **2019**, *9*, 725. [CrossRef]
19. Wang, P.-Y.; Clements, L.R.; Thissen, H.; Jane, A.; Tsai, W.-B.; Voelcker, N.H. Screening Mesenchymal Stem Cell Attachment and Differentiation on Porous Silicon Gradients. *Adv. Funct. Mater.* **2012**, *22*, 3414–3423. [CrossRef]
20. Tsai, Y.-T.; Wu, C.-Y.; Guan, Z.-Y.; Sun, H.-Y.; Cheng, N.-C.; Yeh, S.-Y.; Chen, H.-Y. Topologically Controlled Cell Differentiation Based on Vapor-Deposited Polymer Coatings. *Langmuir* **2017**, *33*, 8943–8949. [CrossRef]
21. Wu, T.-Y.; Gao, C.; Huang, M.-C.; Zhang, Z.; Wang, P.-Y.; Chen, H.-Y.; Chen, G.; Chen, H.-Y. Vapor-Stripping and Encapsulating to Construct Particles with Time-Controlled Asymmetry and Anisotropy. *Coatings* **2020**, *10*, 1248. [CrossRef]
22. Ma, A.; You, Y.; Chen, B.; Wang, W.; Liu, J.; Qi, H.; Liang, Y.; Li, Y.; Li, C. Icariin/Aspirin Composite Coating on TiO2 Nanotubes Surface Induce Immunomodulatory Effect of Macrophage and Improve Osteoblast Activity. *Coatings* **2020**, *10*, 427. [CrossRef]
23. He, Y.; Dai, L.; Zhang, X.; Sun, Y.; Shi, W.; Ge, D. The Bioactive Polypyrrole/Polydopamine Nanowire Coating with Enhanced Osteogenic Differentiation Ability with Electrical Stimulation. *Coatings* **2020**, *10*, 1189. [CrossRef]
24. Wang, P.-Y.; Clements, L.R.; Thissen, H.; Tsai, W.-B.; Voelcker, N.H. Screening rat mesenchymal stem cell attachment and differentiation on surface chemistries using plasma polymer gradients. *Acta Biomater.* **2015**, *11*, 58–67. [CrossRef] [PubMed]
25. Guan, Z.-Y.; Wu, C.-Y.; Chen, H.-Y. Stepwise and Programmable Cell Differentiation Pathways of Controlled Functional Biointerfaces. *ACS Biomater. Sci. Eng.* **2017**, *3*, 1815–1821. [CrossRef]
26. Sun, T.-P.; Tai, C.-H.; Wu, J.-T.; Wu, C.-Y.; Liang, W.-C.; Chen, H.-Y. Multifaceted and route-controlled "click" reactions based on vapor-deposited coatings. *Biomater. Sci.* **2016**, *4*, 265–271. [CrossRef]
27. Mu, L.; Ma, Z.; Wang, J.; Yuan, S.; Li, M. Corrosion Behavior and Biological Activity of Micro Arc Oxidation Coatings with Berberine on a Pure Magnesium Surface. *Coatings* **2020**, *10*, 837. [CrossRef]
28. Shimabukuro, M.; Tsutsumi, Y.; Nozaki, K.; Chen, P.; Yamada, R.; Ashida, M.; Doi, H.; Nagai, A.; Hanawa, T. Chemical and Biological Roles of Zinc in a Porous Titanium Dioxide Layer Formed by Micro-Arc Oxidation. *Coatings* **2019**, *9*, 705. [CrossRef]
29. Wang, P.-Y.; Tsai, W.-B.; Voelcker, N.H. Screening of rat mesenchymal stem cell behaviour on polydimethylsiloxane stiffness gradients. *Acta Biomater.* **2012**, *8*, 519–530. [CrossRef]
30. Pham, D.Q.; Berndt, C.C.; Sadeghpour, A.; Zreiqat, H.; Wang, P.-Y.; Ang, A.S.M. Mechanical Properties of Strontium–Hardystonite–Gahnite Coating Formed by Atmospheric Plasma Spray. *Coatings* **2019**, *9*, 759. [CrossRef]
31. Diba, F.S.; Boden, A.; Thissen, H.; Bhave, M.; Kingshott, P.; Wang, P.-Y. Binary colloidal crystals (BCCs): Interactions, fabrication, and applications. *Adv. Colloid Interface Sci.* **2018**, *261*, 102–127. [CrossRef] [PubMed]
32. Wang, P.-Y.; Thissen, H.; Kingshott, P. Stimulation of Early Osteochondral Differentiation of Human Mesenchymal Stem Cells Using Binary Colloidal Crystals (BCCs). *ACS Appl. Mater. Interfaces* **2016**, *8*, 4477–4488. [CrossRef]
33. Chiu, Y.-R.; Hsu, Y.-T.; Wu, C.-Y.; Lin, T.-H.; Yang, Y.-Z.; Chen, H.-Y. Fabrication of Asymmetrical and Gradient Hierarchy Structures of Poly-p-xylylenes on Multiscale Regimes Based on a Vapor-Phase Sublimation and Deposition Process. *Chem. Mater.* **2020**, *32*, 1120–1130. [CrossRef]
34. Lee, C.-Y.; Hu, S.-M.; Xiao, J.-Q.; Chang, Y.-M.; Kusanagi, T.; Wu, T.-Y.; Chiu, Y.-R.; Yang, Y.-C.; Huang, C.-W.; Chen, H.-Y. Vapor Sublimation and Deposition to Fabricate a Porous Methyl Propiolate-Functionalized Poly-p-xylylene Material for Copper-Free Click Chemistry. *Polymers* **2021**, *13*, 786. [CrossRef]

coatings

MDPI

Review

Materials for Orthopedic Bioimplants: Modulating Degradation and Surface Modification Using Integrated Nanomaterials

Harbhajan Ahirwar [1], Yubin Zhou [2,3,*], Chinmaya Mahapatra [4], Seeram Ramakrishna [5], Prasoon Kumar [6,*] and Himansu Sekhar Nanda [1,*]

[1] Biomedical Engineering and Technology (BET) Laboratory, Discipline of Mechanical Engineering, Indian Institute of Information Technology Design and Manufacturing (IIITDM), Jabalpur-482005, MP, India; 1723601@iiitdmj.ac.in
[2] School of Pharmacy, Guangdong Medical University, Dongguan 523808, China
[3] Marine Medical Research Institute of Guangdong Zhanjiang, Guangdong Zhanjiang Marine Biomedical Research Institute, Zhanjiang 524023, China
[4] Institute of Biomaterial Science and Berlin-Brandenburg Center for Regenerative Therapies, Helmholtz-Zentrum Geesthacht, 14513 Teltow, Germany; cmbbsr@gmail.com
[5] Centre for Nanofibers and Nanotechnology, Department of Mechanical Engineering, National University of Singapore, Engineering Drive 3, Singapore 117587, Singapore; seeram@nus.edu.sg
[6] Department of Medical Devices, National Institute of Pharmaceutical Education and Research–Ahmadabad, Near Air force Station, Palaj, Gandhinagar-382355, Gujarat, India
* Correspondence: zybresearch@126.com (Y.Z.); prasoon.kumar@niperahm.ac.in (P.K.); himansu@iiitdmj.ac.in (H.S.N.); Tel.: +86-0769-2289-6561 (Y.Z.); +91-810-5648-520 (P.K.); +91-761-2794-429 (H.S.N.)

Received: 24 January 2020; Accepted: 10 March 2020; Published: 12 March 2020

Abstract: Significant research and development in the field of biomedical implants has evoked the scope to treat a broad range of orthopedic ailments that include fracture fixation, total bone replacement, joint arthrodesis, dental screws, and others. Importantly, the success of a bioimplant depends not only upon its bulk properties, but also on its surface properties that influence its interaction with the host tissue. Various approaches of surface modification such as coating of nanomaterial have been employed to enhance antibacterial activities of a bioimplant. The modified surface facilitates directed modulation of the host cellular behavior and grafting of cell-binding peptides, extracellular matrix (ECM) proteins, and growth factors to further improve host acceptance of a bioimplant. These strategies showed promising results in orthopedics, e.g., improved bone repair and regeneration. However, the choice of materials, especially considering their degradation behavior and surface properties, plays a key role in long-term reliability and performance of bioimplants. Metallic biomaterials have evolved largely in terms of their bulk and surface properties including nano-structuring with nanomaterials to meet the requirements of new generation orthopedic bioimplants. In this review, we have discussed metals and metal alloys commonly used for manufacturing different orthopedic bioimplants and the biotic as well as abiotic factors affecting the failure and degradation of those bioimplants. The review also highlights the currently available nanomaterial-based surface modification technologies to augment the function and performance of these metallic bioimplants in a clinical setting.

Keywords: bioimplants; orthopedic; metallic biomaterials; degradation; surface modification; coatings; nanomaterials

1. Introduction

Orthopedic bioimplants play a significant role in improving the quality of human life [1]. In this regard, bone–implant interface greatly influences bone healing through an osseointegration process [2].

The appropriate surface properties of orthopedic bioimplants include modulation of the differentiation of mesenchymal stem cells to express osteogenic phenotype [3,4]. Besides, surface modification of these bioimplants can also facilitate the biodegradation process [5,6], improve the mechanical properties commensurate with the native bone and improve integration with host tissue nearby. Furthermore, surface modification can provide antibacterial properties to avoid any post-surgery infections [7]. The above requirements of surface modifications can be adapted by metallic materials that have inherent bulk properties to be used in orthopedic applications.

Metallic bioimplants are manufactured by innovative manufacturing technologies to meet the ever-increasing demand for orthopedic applications [1]. Among the various bioimplants that have been developed for orthopedic, bioimplants used to assist bone fracture are currently in demand [8,9]. Amid the reported metallic biomaterials, materials such as stainless steel (SS 316L), titanium alloy (Ti-6Al-4V) and cobalt-chromium (Co-Cr) alloy have been investigated a lot owing to their suitable bulk properties [10]. Other non-metallic materials that have been explored in bone fracture fixation that include alumina (Al_2O_3), nylon 6/6, polymethyl methacrylate (PMMA), etc. [8,9,11,12]. Efforts have also been directed towards the modification of bulk properties of metallic biomaterials to render them with mechanical properties commensurate with that of a native bone, which could reduce stress shielding at an interface of tissue and bioimplant [12,13]. The excellent biocompatibility, hemocompatibility and high fatigue strength have positioned the metallic biomaterials as most suitable materials for orthopedic applications [14]. However, these bioimplants are prone to problems of wear and corrosion in a blood/tissue milieu [15,16]. The leachates of corrosion and infection labile nature of metallic surface may trigger immunological reactions [17,18], leading to the need for heavy intake of immunosuppressant or other treatments causing deleterious effects on the patient's health [19]. The major limitations of metallic biomaterials are their non-integration with host tissue owing to the above-mentioned inappropriate surface properties, vulnerability to post-surgery microbial infections, and other related risks that may demand a revision surgery and removal of bioimplants [8,12,20].

Although efforts have been directed to overcome the challenges associated with bulk and surface properties of these metallic bioimplants, nanomaterials have of late emerged as an alternative to alter the surface properties for their better integration with host tissue, reducing the immunogenicity, providing an infection-free surface and enabling the drug loading [21–26].

Surfaces of the orthopedic bioimplants serve as the site of interaction for surrounding living tissue. Hence, it is imperative to enhance the biological performance of these bioimplants using bioactive nanomaterials [27–32]. Surface engineering using nanomaterials and other suitable coating technologies aims to design and develop the bioimplants with improved osseointegration for orthopedic applications [28,33,34]. The commercialized surface treatment strategies for several of the orthopedic metallic bioimplants have already been developed; those include grit-blasting followed by washing with non-etching acid and distilled water, spark anodization in the presence of calcium phosphate, sandblasted and acid-etched (SLA) treatment for the generation of macro/micro scale topography, laser-lok technology to generate structured grooves and channels, chemical treatment for the creation of nanoscale topography, molecular impregnation of calcium phosphate on a surface, plasma treatment, and acid etching [35–42]. Some of the common commercial generated surfaces include tiunite surface on titanium implants (Nobel Biocare Implant System) [43], SLA surfaces on Roxolid™—an alloy of titanium and zirconium (Straumann Implant System) [44], Microchannelled surfaces through laser-lok technology (Bio-horizons Implant System) [45], micro textured surface created by grit-blasting on titanium (Zimmer Implant System) [46], NanoTite™ surfaces on bone implants (3i Dental Implants) [47], and others. Surface modification processes such as grit blasting are achieved by bombardment of bioimplant surfaces by means of silica, hydroxyapatite, alumina, or TiO_2 nanomaterials, and thereafter the surface is treated with a non-etching acid and distilled water to clean the un-bonded nanomaterials [37,39,42]. Acid-etching treatments are generally performed using strong acids such as hydrofluoric, nitric, or sulphuric acid to create micro/nanoscale roughness on the surface of the bioimplants [35,37,38]. Several other techniques such as deposition techniques including dip coating, laser technology that creates hydrophilic and chemically active surface that promote osseoconductivity, surface patterning by micro/nanochannels/groves for cellular infiltration, thermal spraying, biomimetic deposition of calcium phosphate and hydroxyapatite for better bone integration, and sol-gel deposition have also been developed to alter the surface of the metallic bioimplants [40,48]. These techniques have already been clinically accepted and have been used as a surface treatment solution for several orthopedic bioimplants.

The current review incorporates the description of the metals and metal-alloys that are commonly used in manufacturing of different orthopedic bioimplants. The review critically discusses the biotic as well as abiotic factors responsible for the degradation and failure of metallic/metallic-alloy bioimplants. It also highlights the currently available advanced nanomaterial-based surface modification technologies to enhance the function and performance of these metallic bioimplants. To further stimulate the exchange of ideas among the experts in the field, the opinion from some of our experts is also included to make this review more interesting and appealing for future readers, expecting more practical and mature orthopedic bioimplants to be explored to improve human health.

2. Materials for Orthopedic Bioimplants

Appropriate selection of materials to support fracture and healing is critical for the long-term success of orthopedic bioimplants. The choice of a bioimplant is primarily driven by the intended application, amenability to manufacturing, and the potential market size. Among the different types of biomaterials, metallic biomaterials including metals and metal alloys are widely used for manufacturing of orthopedic bioimplants because of their biocompatibility, low cost, rich in resources, and appropriate mechanical properties such as high tensile strength that provides strength to the fractured bones [1]. Some of the key metals and metal alloys used for orthopedic bioimplant manufacturing are discussed. Table 1 summarizes the different biomedical metals, their properties and the manufactured bioimplants from these metals and their applications.

Table 1. Biomedical metals, properties, manufactured bioimplants, and their applications.

Biomedical Metals	Properties	Applications	Ref.
Ti and its alloys	Biocompatible, high fatigue strength, flexible, low Young's modulus, expensive, low wear and corrosion resistance, good tensile strength, reduced Stress shielding, good osteointegration	total knee replacement (TKR), total hip replacement (THR), bone screws and plates for bone fracture fixation, screws/plates for maxillofacial application in the cranio-facial and mandibular areas.	[7,49–61]
SS 316L	Biocompatible, low fatigue strength, high Young's modulus, cheaper, high tensile strength, Stress shielding	Bone plates, medullary nails, screws, pins, sutures and steel threads used in fixation of fractures.	[10,12,13,49,62,63]
Co-Cr alloy	Biocompatible, high tensile strength, high Young's modulus, stress shielding	Orthopedic prostheses for the knee, shoulder, ankle and hip as well as fracture fixation devices	[10,13,49,64,65]
Magnesium (Mg) and its alloys	Biocompatible, good osteointegration, lower Young's modulus, high strength, biodegradable, no stress shielding	Used as a mesh cage for segmental defect in long bone, 3-D scaffold design (tissue engineering) for bone regeneration	[20,66–72]

2.1. Titanium (Ti) and Ti-Alloys

Titanium (Ti) and its alloys have the characteristics of low density, high mechanical strength and excellent biocompatibility [73]. Ti in combination with other metals forms biocompatible Ti-alloys, which are widely used in bioimplant manufacturing. One of the most commonly used Ti-alloy is Ti-6Al-4V. It occupies approximately 45% of the total industrial production of Ti-based bioimplants [74]. The Young's modulus of Ti alloys is in the range of 55–110 GPa, which is higher than that of a native bone [52]. Therefore, the stress shielding effect remains an issue that can only be reduced, but currently impossible to avoid [74]. Ti and its alloys are non-toxic and inert at in vivo environment due to their corrosion resistant properties [73]. However, some studies have reported that aluminum and vanadium ions released from Ti-6Al-4V alloys can potentially damage vital organs [75]. Vanadium ions are cytotoxic and known to cause poor osteointegration, while aluminum ions are known to cause neurological disorders [76,77]. These concerns have led to the development of Al/V-free $\alpha + \beta$ type Ti alloys with improved mechanical, tribological, and biological properties. These Ti-alloys have almost similar characteristics as that of Ti-6Al-4V. However, elastic modulus is still much higher than that of cortical bones (30 GPa). Thus, the generated stress shielding effect may further loosen the implanted bioimplants [53]. Other new generation β-type Ti-alloy includes Ti35Nb2Ta3Zr, Ti-Nb-Ta-O, Ti-Nb-Ta-Zr, Ti-35Zr-5Fe-6Mn, and Ti-33Zr-7Fe-4Cr, which have shown their respective advantages for manufacturing of orthopedic bioimplants [51,54,57–61]. β type Ti-alloys are known to consist of β-stabilizing elements such as Nb, Mn, Sn, Ta, and Zr. These elements are considered as safe for human health and hence the alloys are considered as biocompatible in nature.

To overcome the challenges of infection and support better osseointegration, the surface of Ti-alloys were modified through nanotexturing by the surface mechanical attrition treatment (SMAT) process [50,56,78]. Other methods such as coating technologies using micro-arc oxidation (MAO) have also been used to enhance the surface characteristics, biocompatibility, and osseointegration of the bioimplants manufactured from Ti-alloys, especially of β type. For example, TiO_2 doped calcium-phosphate coating (Ca-P) and calcium-phosphate-strontium coating (Ca-P-Sr) were used to improve the surface properties of Ti35Nb2Ta3Zr to enhance the in vitro and in vivo performance of the bioimplant [79].

Titanium or their alloys are used to develop the tibial tray that accommodates tibial polyethylene component in prosthesis for total knee replacement (TKR), femoral stem of endoprosthesis for total hip replacement (THR), and bone screws and plates to fix fractures and plates/screws for maxillofacial applications in the cranio-facial and mandibular areas [55,80,81].

2.2. Stainless Steel (SS)

Stainless Steel (SS) is one of the most widely used metallic biomaterials in orthopedics because of their ease of manufacturing, low cost, and wide resource availability. SS contains a minimum of 10.5% chromium and varying amounts of other elements such as iron, carbon, etc. [82]. As a result of chromium addition, the surface of SS develops a thin and relatively passive metal oxide layer that protects the surface against corrosion. In addition, at least 0.03% carbon in stainless steel (SS 316L) increases its mechanical strength and maximizes the corrosion resistance properties and improves the overall tribological performance of the bioimplants [82]. The SS 316L is inexpensive, reliable, and widely used in orthopedic bioimplant manufacturing [12]. It has a lower carbon content than SS 316 (a stainless-steel grade having 0.08% carbon) and offers excellent toughness to the overall bioimplant. SS 316L exhibits relatively good biocompatibility compared to SS316 [49,82]. It has much higher elastic modulus (about 200 GPa) than that of a typical human femur cortical bone (10–30 GPa) [11]. This may result in high stress-shielding at bioimplant–tissue interface leading to the failure of the implanted bioimplant [13,82]. In addition, SS bioimplants also succumb to fatigue damage due to their low fatigue strength [62]. SS-based bioimplants either need revision surgery or to be used as a permanent bioimplant after bioactive coating or surface modification using bioactive nanomaterials. The modification of SS with bioactive hydroxyapatite (HA) improves the osseointegration and bio-integration properties of an orthopedic bioimplant [63,83,84]. Typical applications include bone plates, medullary nails, screws, pins, sutures, and steel threads used in fixation of fractures [14,85–90].

2.3. Cobalt (Co) Alloy

Co alloys are wear, corrosion, and heat-resistant metallic materials used in bioimplant manufacturing [64]. In vitro and in vivo tests confirmed that these alloys as biocompatible and appropriate materials for manufacturing of surgical bioimplants such as orthopedic prostheses for the knee, shoulder, and hip as well as fracture fixation devices. Typical Co-based alloy (Co-Cr-Mo alloy) in conjunction with an ultra-high molecular weight polyethylene (UHMWPE) is used in prosthetic knees and ankles [91]. The major alloying elements include Co, Cr, Mo, and Ni. Although these are essential trace elements in a human body, they have been well proven to be toxic when leached out in a body due to corrosion of cobalt alloys. The excessive presence of these trace elements (Co, Cr, and Mo) has been reported to damage organs such as the kidney, liver, lungs, and also blood cells [92]. The elastic modulus and ultimate tensile strength of the Co-alloys are 200–230 GPa and 430–1028 MPa, respectively, which is approximately 10 times higher than that of a human bone [49]. Hence, the bioimplants manufactured from these materials may result in stress-shielding effect at a bioimplant–tissue interface [13]. The surface modification of Co-Cr-Mo alloy implants could be achieved by low temperature plasma treatment, where surface get alloyed with nitrogen and carbon through S-phase transformation [65]. This process improves the hardness, corrosion, and wear resistant properties of Co-Cr-Mo alloys.

2.4. Biodegradable Metals

Biodegradable metal-based orthopedic bioimplants eliminates the complications associated with the long-term presence of bioimplants in human body. Once these materials degrade, the degradation products can be metabolized to fulfill the elemental requirements of the metabolic pathways [20,66]. Among the different metals, magnesium (Mg) shows a great promise as a biocompatible and biodegradable material [66,69]. The attractive characteristics of Mg are its high strength, elastic modulus, and a close resemblance to the modulus of a human bone. The properties such as high mechanical strength can reduce the amount of bioimplant material needed for an applied load and hence to manufacture the bioimplant. The reduced elastic modulus of the bioimplant can prevent the modulus mismatch between a bone and Mg-based bioimplant, leading to the reduction in the stress shielding at bone–bioimplant interfaces [66]. The mechanical properties of the Mg alloys can be enhanced by alloying with aluminum and other alloying elements [68]. Current investigations are centered on identifying the new Mg-alloys with no or low cytotoxicity. Various biomedical Mg-alloys such as Mg-Y-Nd [93] and Mg-Ca [94] have been studied for the development of biodegradable Mg-alloy-based orthopedic bioimplants. Alloying metals have to be carefully selected to avoid metal-related toxicity and corrosion [20]. The major limitation of Mg and Mg-alloys is their low corrosion resistance. Low corrosion resistance results in rapid release of the degradation products due to fast in vivo degradation. These necessitate the surface modification of these materials too [71]. Mg-alloys are also being explored for tissue engineering (3-D scaffold design) for bone tissue regeneration [67,68,70,95].

3. Degradation of Orthopedic Bioimplants

Degradation is one of the major considerations in bioimplant design, processing, and application. Biodegradable implants are expected to degrade progressively over a period of time to assist in the healing process and compensate for the clinical need. Bioimplants are designed either to degrade or remain inside a body rather than their removal after their function is served. Degradation of the bioimplants is desirable in several cases such as absorbable sutures, drug delivery system, and tissue engineering [3,96,97].

3.1. Metallic Bioimplant Degradation: Role of Biological Factors

Metallic materials used for the manufacturing of orthopedic bioimplants are high strength and corrosion-resistant metals and metal alloys. The prospective applications of these materials are to provide long-term mechanical support to the biological structures, while remaining inert and interacting minimally with the neighboring biological tissues [98]. However, these metallic materials undergo degradation following a time-dependent kinetics after being in contact with biological moieties for a long period of time (Figure 1a). Biological components are also chemically active, generating various ionic species during their metabolism. These chemical moieties are known to interact with the surface of metal/metal alloy-based bioimplants [99]. After initial phases of adsorption and surface oxidation, the proteins slowly interact with the implant surface in a size-dependent manner, with smaller proteins interacting being the initiator. Johnson et al. reported the degradation effects of fetal bovine serum

(FBS) on a Mg-alloy bioimplant [100]. The investigation demonstrated an oxidized Mg-Yttrium (MgY) was much more resistant to degradation in FBS compared to a native Mg-Y. The response of host body chemistry to the implant such as inflammation-dependent release of reactive oxygen species (ROS) creating an oxidative environment determines the degradation pattern of metal and metal-alloy [101].

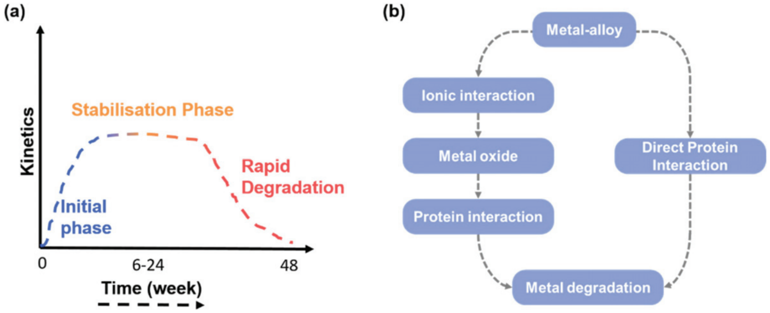

Figure 1. (**a**) Graphic illustration of the degradation kinetics of a typical metal bioimplant and (**b**) cyclic representation of metallic bioimplant degradation pathway [99]. Adapted with permission from [99]; 2018 Springer.

3.2. Time Dependent Degradation Effects

The degradation process starts immediately after the bioimplants are implanted inside the body. The overall degradation is a time dependent process, as illustrated in Figure 1a. The degradation pattern of a metallic bioimplant (for example, Mg-alloy-based bioimplant) undergoes an initial linear degradation that includes the oxide layer formation followed by a metal-protein-based degradation mechanism. The process is further followed by an encapsulation of a bioimplant by a fibrous tissue causing a complete isolation of a bioimplant from the surrounding tissue site. In the final step, the chronic inflammation starts clearing up the metallic implant materials via secretion of alkaline enzymes and ROS [102]. The transition from an early phase of metal-alloy chemistry to late stage of macrophages engulfing results in the erosion of metal particles, elevating the inflammation, and rapid degradation of the bulk material. Long-term studies on metallic degradation (6–24 weeks) have shown a time dependent decrease in the metal ion release in the tissue compared to the incremental degradation observed in nature. This type of degradation was also found to pass through a stabilization phase during a period of 6 to 24 weeks as shown in Figure 1a. Furthermore, it is also evident that some proteins can bypass the normal route of metal-alloy interaction and directly bind to the metal surface without the formation of an oxide layer as shown in Figure 1b. In addition, initiation of localized corrosion at the load-bearing site contributes towards the metal erosion to a greater extent than the other parts [99].

3.3. Degradation Mechanism

Metal and metal alloy-based bioimplants are prone to corrosion in a tissue and blood milieu. The corrosion process is a hallmark of a degradation process. It usually starts with the redox reactions and hydrolysis at the interface involving electron or proton exchanges (Figure 2a). These reactions yield hydroxides that precipitate over the metal surface. These precipitates are known to cause foreign body reactions, further resulting in a severe inflammation and long-term fibrous tissue development. Metals such as silver (Ag) and gold (Au) are more resistant to the corrosion as compared to iron (Fe) or aluminum (Al). These precious metals are sometimes used as a coating to modulate the corrosion rate of the bulk metals used in manufacturing of the load bearing bioimplants for an orthopedic application. Iron or related materials usually precipitate as metal-protein complexes in the subsequent steps (Figure 2b). Steinemann et al. have reported that the produced metal–protein complexes are insoluble in a body fluid and determine the stability of the hydrolyzed products [103]. In addition, metal oxidation depends on the physical properties of a metal such as crystalline or amorphous nature of a metal [104]. It has been observed that the rate of degradation is lower for the amorphous metal oxides compared to the crystalline oxides [104]. The slow degradation of any amorphous oxides is due to the higher capacity of amorphous metal oxides to form organic complexes compared to crystalline metal oxides in an aqueous medium dominated by hydroxyl ions. The observed effect could also be due to weaker metal-oxide bonding with each other owing to larger inter-atomic distances in amorphous metal oxides. This weaker bonding could be easily leveraged by the macromolecules such as proteins, giving rise to the complexes (metal–proteins) that protects the underlying metal layer [105]. In this contest, metals such as Ti form the most stable oxide layer. The metal alloy-based orthopedic bioimplants manufactured from titanium–aluminum–vanadium (TiAlV) have further shown promising resistance to corrosion and metal ion release in the presence of proteins compared to the bioimplants made from metal-alloys such as SS 316L [73]. In addition, the physical imperfections and long-term wear and tear are also responsible for the corrosion of metal implants. Santos et al. have reported the initiation of degradation in metallic screws and plates at the site of wear/tear that have undergone specific corrosion at the load bearing areas [106]. In the implants such as screws and plates that bear regular load, there is a greater tendency to accumulate maximum precipitate at the grain boundaries of these metal/metal alloys implants (Figure 2c). Deposition of a larger precipitate at the grain boundary in combination with the regular abrasive motion on the surfaces deems them much susceptible to corrosion [106,107]. Furthermore, physical imperfections have also been known to contribute towards the localized corrosion, precipitation, and aggregation of a large quantity of metal–protein complexes at the specific site, thereby weakening the load-bearing structures. The physical imperfection also leads to fretting corrosion that is a combined form of local imperfections and micro motion, observed specifically in screw plate models of orthopedic bioimplants (Figure 2d).

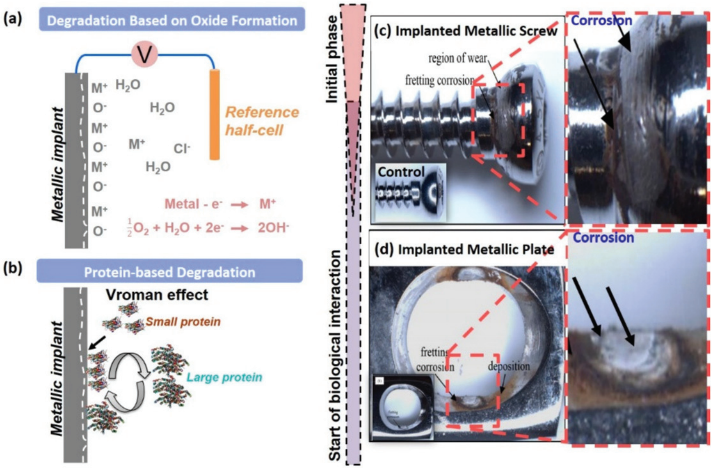

Figure 2. Mechanism of metallic bioimplant degradation (**a**,**b**) [15,16] and fretting corrosion tests on orthopedic plates and screws made of ASTM F138 stainless steel (**c**,**d**) [106]. Adapted with permission from [15]; 2008 John Wiley & Sons; Adapted with permission from [16]; 2003 Springer.

Following ionic interactions, proteins are known to get adsorbed relatively quickly within seconds to hours, even on a metal's surface with similar charges. The differences in the kinetics of adsorption of the different proteins leading to an intense competition for binding to the oxide layer on the metallic surface. Moreover, this oxide layer formation is itself influenced by the surface properties like roughness, surface energy, and others [108]. The formation of these metal oxide–protein complexes accelerates the degradation process. Several other factors in an in vivo environment such as ionic strength of the local environment, pH, and physical stress on the oxide layer further govern the degradation kinetics [108]. For example, albumin with high concentration in synovial fluid strongly binds to the metal surfaces. The presence of any defect further enhances these phenomena generating metal–protein complexes, which in turn reduce the rate of erosion of a metal surface [109].

3.4. Metal Self-Induced Biological Responses

Metal–protein conjugates can act as signaling molecules for the secondary inflammation that is more intense than the primary inflammation [102]. The debris of the materials can sensitize the immune system depending upon the size of debris (nano or macro size), which induces increased cellular responses causing rapid degradation [110]. In in vivo environment, bioimplants subjected to mechanical stresses are more vulnerable to degradation. Hence, metal-alloy bioimplants that are mostly used in the high stress and load bearing conditions need to be evaluated for their long-term fatigue and friction-based degradation [111]. Oxidative stress in the tissue due to an increased ROS generation, Fenton chemistry-based corrosion in combination with fatigue-based degradation, significantly promotes the degradation rate [112].

4. Surface Modification Effects

Surface modification is usually carried out to minimize bacterial adhesion, inhibit biofilm formation, and provide effective bacterial extermination to protect the implanted biomaterials [7,28,113,114]. Furthermore, their role is to provide stealth properties to a bioimplant for any immunogenic reactions, better integration with the surrounding tissue, and enable appropriate cellular responses. For example, Ag nanoparticle coating over the Ti surface has been carried out to construct an improved bioactive and biocompatible surface (Figure 3a–c) [115]. Ti-based bioimplant and tissue integration could be promoted by surface decorated with Ag nanoparticles, through the promotion of H_2S production. The production of H_2S upregulates the expression of sulphur containing proteins such as albumin that is highly beneficial for the enhanced metal–protein interactions. Further the tissue could well interact with the Ti-Ag complex, resulting in an enhanced bone regeneration as shown in the Figure 3b. Controlled degradation behavior of Ti-Ag complex could cause the local release of Ag^+ ions, resulting in an enhanced tissue integration, anti-bacterial effect, osteoconductivity, and long-term low toxicity (Figure 3c). These effects could demonstrate multiple therapeutic effects of Ag-nanoparticle coating on a bioimplant surface. Similarly, different strategies are employed to prevent infection on a metallic bioimplant surface using antibiotics, antimicrobial peptides, inorganic antibacterial metal elements, and antibacterial polymers [116]. Certain surface modifications could also cause changes in the mechanical and biological properties of the bioimplant material. The physical/bulk modification is performed to obtain an optimum shape and size of a biomaterial with an appropriate mechanical behavior, while chemical modification is carried out to render bioactivity to the surface of a material. These alterations to materials empower them with improved cell adhesion, attachment, and eventually proliferation [115,117]. The tissue interacts predominantly with these materials at an interface where nanomaterials decorate the surface of a bioimplant. As shown in the Figure 3d, Ag-nanoparticle could act as a focal point of tissue adhesion and bone growth through interaction with calcium that regulates the biological responses. Nanomaterials are the advanced materials that could be effectively utilized to improve the surface and bulk properties of orthopedic bioimplants. A class of nanomaterials in response to electric/magnetic fields or polarization exhibit anti-bacterial properties without affecting the surface chemistry of bioimplants [118]. Nanotechnologies could improve the antibacterial response of the prosthetic bioimplants, which include compositional modification, surface chemistry alteration, as well as the application of properly tuned external stimuli [7,118]. Various desirable surface properties such as protein adsorption, osteoblast attachment, osteoblast differentiation, antibacterial activity, biocompatibility with living tissues is achieved through nanomaterials. Further, corrosion resistance of the bone–bioimplant interface has been achieved by modifying the surface of the bioimplants through nano-structuring and functional nanocoating. A number of antibacterial agents, such as Ag, Au, zinc oxide (ZnO), zirconium nitrate ($Zr(NO_3)_4$), zirconium oxide (ZrO_2), titanium oxide (TiO_2), have been incorporated in a hydroxyapatite (HA) matrix to develop HA-based antibacterial coatings for orthopedic metallic bioimplants, which allows no bacterial growth on the bioimplant substrate and improves bio-integration properties [25,119–123].

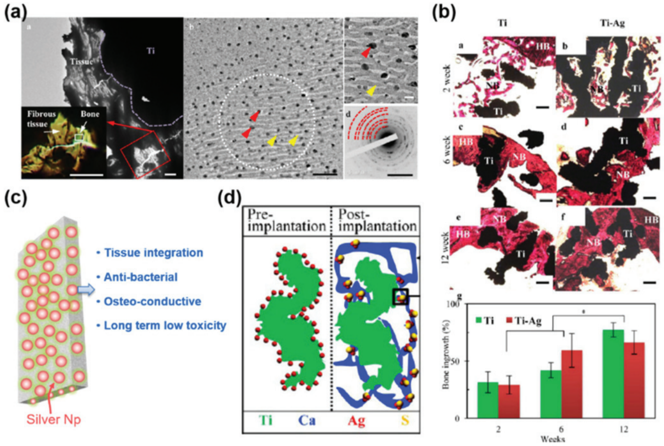

Figure 3. (**a**) Ti-based bioimplant–tissue integration promoted by Ag nanoparticles; (**b**) H&E staining at 2, 6, and 12 weeks of implantation showing enhanced bone growth around the bioimplant. (**c**) Controlled release of Ag-nanoparticle (Ag NPs) from Ti surface causing enhanced tissue integration, anti-bacterial effect, osteoconductivity, and long-term low toxicity; (**d**) Schematic showing AgNPs acting as focal point of tissue adhesion and bone growth through interaction with calcium that regulates the biological responses [115]. Adapted with permission from [115]; 2017 American Chemical Society.

5. Improving the Surface Properties of Bioimplants Using Integrated Nanomaterials

A proper design of a bioimplant material is aimed to provide durability, functional stability, and an appropriate biological response. Durability and functionality depend on the bulk properties of the material, whereas biological response depends on the surface chemistry, surface topography, and surface energy of a biomaterial. Surface modifications of bioimplants play a vital role in matching the complexities of the biological system and improving the performance of the bioimplant materials [25]. In this context, nanomaterials could be effectively utilized to improve the surface properties of several orthopedic bioimplants [26,124].

5.1. Surface Coating Using Ag-Based Nanocomposites

Silver (Ag) possesses an inherent antibacterial property and low toxicity to human cells, rendering it as an appropriate antibacterial agent for biomedical applications [125]. Ag can be used in the form of ions and compounds to destroy the bacterial cells [26,121,125]. Ciobanu et al. introduced a method for synthesizing Ag-doped nanocrystalline hydroxyapatite (HA) [126] in which Ag doped nanocrystals of HA was synthesized at 100 °C in deionized water. The Ag-doped nano-HA materials demonstrated an excellent cell adhesion and cell proliferation resulting in the synthesis of bone-related proteins and deposition of calcium. These hybrid nanomaterials could be used as a promising candidate for the coating and the surface modification of orthopedic bioimplants. There are two major mechanisms primarily responsible for the antibacterial response of Ag in several nanomaterials [127]. Primarily, it forms Ag^+ ions during its oxidation, which is highly reactive with bacterial cells. These ions in the form of nanoparticles can bind to DNA, RNA, and proteins in bacterial cells to further inhibit the growth of bacteria [128]. Ag^+ ions are also responsible for bringing the structural changes in the bacteria and promote cell distortion. The antibacterial activity of Ag-based nanocomposite could also be attributed to the formation of ROS, which includes free radicals such as super oxides, hydroxyl radicals, etc. These super oxides and hydroxyl-free radicals are responsible for the antibacterial response from these surface modified orthopedic metallic bioimplants [121]. In order to induce antibacterial properties to Ti bioimplants, Yang et al. utilized friction stir processing (FSP) to embed silver nanoparticles (AgNPs) in a Ti-6Al-4V (TC4) substrate. Here, silver nanoparticles placed in the preformed grooves on the surface of TC4 when subjected to FSP, they get homogenously distributed in the surface of TC4 matrix. The distribution profile of AgNPs is dependent on the depth of the preformed grooves [129,130]. On examination, it was observed that silver-rich NPs with a size ranging from 10 to 20 nm were diffused into the substrate. Thus, both FSP and the addition of silver increase the corrosion resistance and reduce the infection rate. The antibacterial effect is independent of Ag^+ ion release and is likely due to the number of embedded silver NPs on the surface. TC4/Ag metal matrix nanocomposite is a potential nanocomposite that embeds AgNPs on a biomaterial surface for creating balance between the antibacterial effect and biocompatibility. The modified surface possesses an antibacterial properties [129,130].

5.2. Surface Coating Using Nano-TiO_2 and TiO_2-Based Metal Nanocomposites

Titanium oxide (TiO_2) nanomaterials have an excellent biocompatibility and chemical stability for which these nanomaterials have been used as coating over the metallic bioimplants [131]. In presence of light, TiO_2 oxidizes to produce free radicals (e.g., hydrogen peroxide, superoxide and hydroxyl free radicals). These free radicals have already demonstrated to elicit antibacterial responses [132]. TiO_2 coating on metallic bioimplants could be activated using direct organic coating like spray coating of polymers where doped antibacterial metal ions (Ag^+) are released as an "antibiotic" providing antibacterial property to a bioimplant surface. In this process, Ti-based bioimplant surface is doped with Ag^+ through hydrothermal treatment on polyethylene glycol (PEO), which significantly modulates the surface chemistry of the metallic bioimplant. The remodeled surface undergoes a patterned and slow degradation releasing Ag^+ ions in a controlled manner, leading to increase in the expression of ROS that is detrimental to the bacterial cell wall integrity (Figure 4a) [121]. The other method could be the unique redox photochemical induced mechanism that promotes enhanced bone–bioimplant integration [123]. The inorganic coating onto the bioimplant serves as a site for the redox photochemical reaction. The photochemical reaction results in the development of an electrolytic process by release of ions from the bulk material surface upon exposure to ultraviolet rays. The redox photochemical-based deposition of TiO_2 demonstrated highly active surface-induced antimicrobial activity by its capacity to generate cations (Figure 4b). The later mechanism also creates an excellent corrosion resistance TiO_2 layer over the bioimplant surface that protects an orthopedic bioimplant from bacterial attack as well as corrosion. TC4 surface modification is being explored by FSP to create a nanocomposite of TiO_2 and TC4. It is a method where an intense, localized plastic deformation is produced on the surface of a TC4. This results in the formation of nanocrystalline and amorphous TiO_2 on the surface of TC4. The presence of nanocrystalline and amorphous TiO_2 improved the surface properties like surface microhardness, biocompatibility, and resistance to corrosion [133]. The FSP also resulted in the uniform incorporation of TiO_2 particles to the surface of TC4 matrix. Due to the grain refinement and phase transformation, the surface microhardness and corrosion resistance properties of modified TC4 was improved. In vitro studies demonstrated an enhanced cell adhesion and proliferation capability of the TC4 substrate and modulated the biocompatibility of TC4 substrate [133,134].

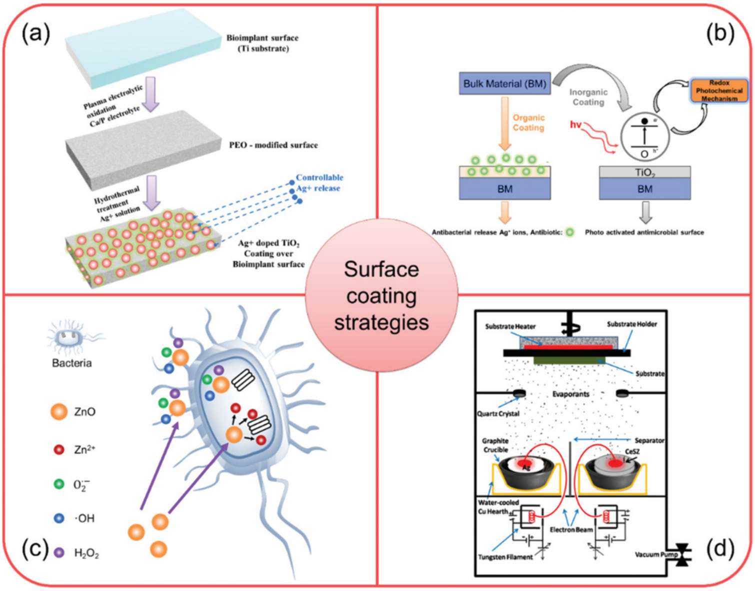

Figure 4. (**a**) Schematic demonstrating stepwise fabrication of antibacterial responsive coating of Ag^+ doped TiO_2 [121]; (**b**) Schematic showing the deposition and antibacterial action of TiO_2 coated bioimplant via redox photochemical method [123]; (**c**) Schematic illustration of antibacterial response of ZnO-based nanomaterial coating [118]; (**d**) Schematic showing ion beam assisted coating of antibacterial Ag-CeSZ-based nanomaterial coating [120]. Adapted with permission from [118]; 2018 ACS Publications; Adapted with permission from [120]; 2019 Elsevier; Adapted with permission from [123]; 2011 SAGE Publications.

5.3. Surface Coating Using ZnO-Based Nanocomposite

The surface modification using HA-ZnO nanocomposite can reduce ions leaching from a metal alloy and prevents the bacteria colonization over a bioimplant surface (Figure 4c) [118]. The experimental investigation suggested that the number of bacterial colonies could be reduced to 13% from 50.45% when ZnO content was increased from 1.5% to 30% (wt) in a HA-ZnO nanocomposite. The antimicrobial responses of ZnO-based composites are due to the formation of ROS and release of Zn^{2+} ions as shown in Figure 4c [119]. ROS are toxic to gram-negative bacteria, while Zn^{2+} ions are responsible for killing of gram-positive bacteria. ROS reacts with lipid layer of the cell wall (gram-negative bacteria) leading to the distortion of the bacterial cell wall. Such distortion destroys the cell wall and eventually leads to bacterial cell death. Zn^{2+} ions diffuse inside the cell (Gram-positive bacteria) and disrupt the amino acid metabolism and enzymes, resulting in a cell death [119].

5.4. Surface Coating Using Ag-CeSZ Nanocomposite

The surface modification using silver-ceria stabilized zirconia (Ag-CeSZ)-based nanomaterials have well proven to offer better mechanical properties and fracture toughness to the bioimplant compared to a conventional yttrium stabilized zirconia [120]. Three source electron beam physical vapor deposition (EBPVD) is used for the deposition of these coatings over several orthopedic bioimplants (Figure 4d). Silver block (99.99% purity) and CeSZ sintered pellets are taken in two separate graphite crucibles and kept separately in a water-cooled copper hearth. The electron beam is then generated and controlled with an accelerating voltage of 8 kV. The filament current is varied between 30 and 60 mA using a 30 kV TT controller. In a case of Ag-CeSZ nanocomposite coating, both Ag and CeSZ are evaporated separately using two E-beam guns. The substrates are kept at the temperature of 673 K and the thickness of the coating can be controlled in a range of 2 μm. Ti bioimplants when coated with Ag-CeSZ nanocomposite coatings show improved mechanical and biological properties. The mechanical properties of Ag-CeSZ nanocomposite coatings are due to its crystalline nature. The coating also demonstrates excellent cell adhesion, antibacterial activity and resistance to sodium fluoride (2%), showing its promising multifunctional importance in orthopedic coating technologies [135].

5.5. Surface Coating Using Ti/SiC Metal Matrix Nanocomposite

The metal matrix composites offer increased stiffness, strength, and wear resistance over monolithic matrix materials. Nanocomposites based on silicon carbide (SiC) have exhibited enhanced mechanical properties. Recent reports on SiC have indicated that its biocompatibility is comparable to that of HA, with respect to the long-term osteogenic properties [136]. The crystalline SiC surface promotes adhesion, proliferation, and differentiation of the primary cultured osteoblast cells. Interestingly, SiC also improves the wear resistance and hardness of the bioimplant on which it is coated. During FSP, the metallic surface undergoes a plastic deformation, leading to an effective grain refinement. This ultrafine-grained metal substrate produced by the application of plastic deformation provides superior cell substrate attachment and biocompatibility. The surface nanocomposites produced by FSP exhibit excellent bonding with the underlying metallic substrate. Zhu et al. have fabricated a novel Ti/SiC metal matrix nanocomposite (MMNC) using FSP and investigated its microstructure and mechanical properties. Additionally, the proliferation and osteogenic differentiation properties of rat bone marrow stromal cells (BMSCs) on the sample surface were investigated and it was demonstrated that the modified surfaces supported the cell attachment and osseointegration [137].

6. Conclusions and Future Recommendation

Manufacturing of bioimplants often involves the integration of processes of material selection, design, and fabrication of bioimplants, and surface modifications through micro/nano texturing or nanomaterial coating. Engineering native metals by converting them into alloys amalgamate best properties of different metals in a single formulation. This provides the flexibility in tailoring the bulk properties of metals as per the orthopedic requirements. However, the surface properties of bioimplants based on alloys/metals require appropriate modification to elicit favorable biological responses. The surface modification of bioimplants through nanocomposites materials have the potential to enhance the host response in the long-run. These nanomaterials play a key role in minimizing the bacterial adhesion to further inhibit biofilm formation to protect the implanted biomaterials from microbial attack. They also play a vital role in eliciting appropriate cellular responses like cell migration through contact guidance on patterned deposition of nanomaterials, cellular differentiation, and gene expression through modulation of stiffness/hydrophobicity of the surfaces, initiation of degree of immunogenicity, delayed surface erosion, and degradation and composition of microenvironment at or in the vicinity of the bioimplant site. Advanced nanomaterials can also serve as a reservoir of drugs to be delivered at the bioimplant site. Thus, coated nanomaterials have the potential to alter the surfaces of various metallic materials for their adoption in orthopedic applications. However, care must be taken during the preparation and deposition of the nanomaterials on the surface of bioimplants like control over the size distribution of the nanomaterials, bonding of the nanomaterials with the bioimplant surface, thickness of the deposited nanomaterial, and eventually, the scalability of the process being used during nanomaterial deposition. In summary, it is imperative to say that the modulation of the degradation process and surface modification using emerging nanomaterials is going to generate a plethora of bioimplants for orthopedic applications in the near future. Therefore, the application of nanotechnology would be critical for the future success of orthopedic bioimplants.

Author Contributions: H.A., Y.Z., and C.M. wrote the paper. H.S.N. and P.K. formulated the work plan and designed the manuscript layout. H.S.N., P.K., and Y.Z. edited the entire manuscript and added significant

discussions. S.R. provided critical comments on which H.S.N., P.K., and Y.Z. have worked and revised further. All authors have read and agreed to the published version of the manuscript.

Funding: The authors would like to acknowledge the funding support from the Faculty Initiation Grant to Biomedical Engineering and Technology (BET) Laboratory, Indian Institute of Information Technology Design and Manufacturing (IIITDM) Jabalpur and Guangdong Medical University Scientific Research Foundation (4SG19003Ga).

Acknowledgments: The authors would like to thank Mamta Anand (Assistant Professor in Humanities and Management, IIITDM Jabalpur) for assisting us in English language editing of the revised manuscript.

Conflicts of Interest: The authors declare no conflicts of interest.

References

1. Kang, C.-W.; Fang, F.-Z. State of the art of bioimplants manufacturing: Part I. *Adv. Manuf.* **2018**, *6*, 20–40. [CrossRef]
2. Albrektsson, T.; Wennerberg, A. On osseointegration in relation to implant surfaces. *Clin. Implant Dent. Relat. Res.* **2019**, *21*, 4–7. [CrossRef] [PubMed]
3. Nanda, H.S.; Nakamoto, T.; Chen, S.; Cai, R.; Kawazoe, N.; Chen, G. Collagen microgel-assisted dexamethasone release from PLLA-collagen hybrid scaffolds of controlled pore structure for osteogenic differentiation of mesenchymal stem cells. *J. Biomater. Sci. Polym. Ed.* **2014**, *25*, 1374–1386. [CrossRef] [PubMed]
4. Mahapatra, C.; Kim, J.-J.; Lee, J.-H.; Jin, G.-Z.; Knowles, J.C.; Kim, H.-W. Differential chondro- and osteo-stimulation in three-dimensional porous scaffolds with different topological surfaces provides a design strategy for biphasic osteochondral engineering. *J. Tissue Eng.* **2019**, 10. [CrossRef] [PubMed]
5. Asri, R.I.M.; Harun, W.S.W.; Samykano, M.; Lah, N.A.C.; Ghani, S.A.C.; Tarlochan, F.; Raza, M.R. Corrosion and surface modification on biocompatible metals: A review. *Mater. Sci. Eng. C* **2017**, *77*, 1261–1274. [CrossRef] [PubMed]
6. Uddin, M.S.; Hall, C.; Murphy, P. Surface treatments for controlling corrosion rate of biodegradable Mg and Mg-based alloy implants. *Sci. Technol. Adv. Mater.* **2015**, *16*, 053501. [CrossRef] [PubMed]
7. Gallo, J.; Holinka, M.; Moucha, C.S. Antibacterial surface treatment for orthopaedic implants. *Int. J. Mol. Sci.* **2014**, *15*, 13849–13880. [CrossRef]
8. Ambrose, C.G.; Clanton, T.O. Bioabsorbable implants: Review of clinical experience in orthopedic surgery. *Ann. Biomed. Eng.* **2004**, *32*, 171–177. [CrossRef]
9. Carpintero, P.; Caeiro, J.R.; Carpintero, R.; Morales, A.; Silva, S.; Mesa, M. Complications of hip fractures: A review. *World J. Orthop.* **2014**, *5*, 402–411. [CrossRef]
10. Wilson, J.M.; Jones, N.; Jin, L.; Shin, Y.C. Laser deposited coatings of Co-Cr-Mo onto Ti-6Al-4V and SS316L substrates for biomedical applications. *J. Biomed. Mater. Res. Part B Appl. Biomater.* **2013**, *101*, 1124–1132. [CrossRef]
11. Dhanopia, A.; Bhargava, M. Finite Element Analysis of Human Fractured Femur Bone Implantation with PMMA Thermoplastic Prosthetic Plate. *Procedia Eng.* **2017**, *173*, 1658–1665. [CrossRef]
12. Abdul Khadar, S.D. Mechanical Strength Evaluation Analysis of Stainless Steel and Titanium Locking Plate for Femur Bone Fracture. *Eng. Sci. Technol. Int. J.* **2012**, *3*, 381–388.
13. Ridzwan, M.I.Z.; Shuib, S.; Hassan, A.Y.; Shokri, A.A.; Ibrahim, M.N.M. Problem of Stress Shielding and Improvement to the Hip Implant Designs: A Review. *J. Med. Sci.* **2007**, *7*, 460–467. [CrossRef]
14. Niinomi, M.; Nakai, M.; Hieda, J. Development of new metallic alloys for biomedical applications. *Acta Biomater.* **2012**, *8*, 3888–3903. [CrossRef]
15. Balamurugan, A.; Rajeswari, S.; Balossier, G.; Rebelo, A.H.S.; Ferreira, J.M.F. Corrosion aspects of metallic implants—An overview. *Mater. Corros.* **2008**, *59*, 855–869. [CrossRef]
16. Kamachimudali, U.; Sridhar, T.M.; Raj, B. Corrosion of bio implants. *Sadhana* **2003**, *28*, 601–637. [CrossRef]
17. Wooley, P.H.; Nasser, S.; Fitzgerald, R.H., Jr. The immune response to implant materials in humans. *Clin. Orthop. Relat. Res.* **1996**, 63–70. [CrossRef]
18. Kargozar, S.; Ramakrishna, S.; Mozafari, M. Chemistry of Biomaterials: Future Prospects. *Curr. Opin. Biomed. Eng.* **2019**, *10*, 181–190. [CrossRef]

19. Min, D.I.; Monaco, A.P. Complications Associated with Immunosuppressive Therapy and Their Management. *Pharmacother. J. Hum. Pharmacol. Drug Ther.* **1991**, *11*, 119S–125S. [CrossRef]
20. Prakasam, M.; Locs, J.; Salma-Ancane, K.; Loca, D.; Largeteau, A.; Berzina-Cimdina, L. Biodegradable Materials and Metallic Implants-A Review. *J. Funct. Biomater.* **2017**, *8*, 44. [CrossRef]
21. Tran, P.A.; Sarin, L.; Hurt, R.H.; Webster, T.J. Opportunities for nanotechnology-enabled bioactive bone implants. *J. Mater. Chem.* **2009**, *19*, 2653–2659. [CrossRef]
22. Sekhar Nanda, H.; Chandra Mishra, N. "Amphotericin B" Loaded Natural Biodegradable Nanofibers as a Potential Drug Delivery System against Leishmaniasis. *Curr. Nanosci.* **2011**, *7*, 943–949. [CrossRef]
23. Wen, C. *Surface Coating and Modification of Metallic Biomaterials*; Woodhead Publishing: Sawston/Cambridge, UK, 2015; pp. 1–431.
24. Nethi, S.K.; Nanda, H.S.; Steele, T.W.; Patra, C.R. Functionalized nanoceria exhibit improved angiogenic properties. *J. Mater. Chem. B* **2017**, *5*, 9371–9383. [CrossRef]
25. Mahajan, A.; Sidhu, S.S. Surface modification of metallic biomaterials for enhanced functionality: A review. *Mater. Technol.* **2018**, *33*, 93–105. [CrossRef]
26. Kumar, S.; Nehra, M.; Kedia, D.; Dilbaghi, N.; Tankeshwar, K.; Kim, K.-H. Nanotechnology-based biomaterials for orthopaedic applications: Recent advances and future prospects. *Mater. Sci. Eng. C* **2020**, *106*, 110154. [CrossRef] [PubMed]
27. Sun, L.; Berndt, C.C.; Gross, K.A.; Kucuk, A. Material fundamentals and clinical performance of plasma-sprayed hydroxyapatite coatings: A review. *J. Biomed. Mater. Res.* **2001**, *58*, 570–592. [CrossRef] [PubMed]
28. Christenson, E.M.; Anseth, K.S.; van den Beucken, J.J.; Chan, C.K.; Ercan, B.; Jansen, J.A.; Laurencin, C.T.; Li, W.J.; Murugan, R.; Nair, L.S. Nanobiomaterial applications in orthopedics. *J. Orthop. Res.* **2007**, *25*, 11–22. [CrossRef]
29. Moura, C.C.G.; Souza, M.A.; Dechichi, P.; Zanetta-Barbosa, D.; Teixeira, C.C.; Coelho, P.G. The effect of a nanothickness coating on rough titanium substrate in the osteogenic properties of human bone cells. *J. Biomed. Mater. Res. Part A* **2010**, *94A*, 103–111. [CrossRef]
30. Ramakrishna, S.; Ramalingam, M.; Kumar, T.S.; Soboyejo, W.O. *Biomaterials: A Nano Approach*; CRC Press: Boca Raton, FL, USA, 2016.
31. Kiran, A.; Kumar, T.; Sanghavi, R.; Doble, M.; Ramakrishna, S. Antibacterial and bioactive surface modifications of titanium implants by PCL/TiO2 nanocomposite coatings. *Nanomaterials* **2018**, *8*, 860. [CrossRef]
32. Kiran, A.S.K.; Kumar, T.S.; Perumal, G.; Sanghavi, R.; Doble, M.; Ramakrishna, S. Dual nanofibrous bioactive coating and antimicrobial surface treatment for infection resistant titanium implants. *Prog. Org. Coat.* **2018**, *121*, 112–119. [CrossRef]
33. Jayaraman, P.; Gandhimathi, C.; Venugopal, J.R.; Becker, D.L.; Ramakrishna, S.; Srinivasan, D.K. Controlled release of drugs in electrosprayed nanoparticles for bone tissue engineering. *Adv. Drug Deliv. Rev.* **2015**, *94*, 77–95. [CrossRef] [PubMed]
34. Kiran, A.S.K.; Kizhakeyil, A.; Ramalingam, R.; Verma, N.K.; Lakshminarayanan, R.; Kumar, T.S.; Doble, M.; Ramakrishna, S. Drug loaded electrospun polymer/ceramic composite nanofibrous coatings on titanium for implant related infections. *Ceram. Int.* **2019**, *45*, 18710–18720. [CrossRef]
35. Daugaard, H.; Elmengaard, B.; Bechtold, J.E.; Soballe, K. Bone growth enhancement in vivo on press-fit titanium alloy implants with acid etched microtexture. *J. Biomed. Mater. Res. Part A* **2008**, *87*, 434–440. [CrossRef] [PubMed]
36. Dohan Ehrenfest, D.M.; Coelho, P.G.; Kang, B.-S.; Sul, Y.-T.; Albrektsson, T. Classification of osseointegrated implant surfaces: Materials, chemistry and topography. *Trends Biotechnol.* **2010**, *28*, 198–206. [CrossRef] [PubMed]
37. Prodanov, L.; Lamers, E.; Wolke, J.; Huiberts, R.; Jansen, J.A.; Walboomers, X.F. In vivo comparison between laser-treated and grit blasted/acid etched titanium. *Clin. Oral Implant. Res.* **2014**, *25*, 234–239. [CrossRef]
38. Herrero-Climent, M.; Lázaro, P.; Vicente Rios, J.; Lluch, S.; Marqués, M.; Guillem-Martí, J.; Gil, F.J. Influence of acid-etching after grit-blasted on osseointegration of titanium dental implants: In vitro and in vivo studies. *J. Mater. Sci. Mater. Med.* **2013**, *24*, 2047–2055. [CrossRef] [PubMed]

39. Lieblich, M.; Barriuso, S.; Ibáñez, J.; Ruiz-de-Lara, L.; Díaz, M.; Ocaña, J.; Alberdi, A.; González-Carrasco, J.L. On the fatigue behavior of medical Ti6Al4V roughened by grit blasting and abrasiveless waterjet peening. *J. Mech. Behav. Biomed. Mater.* **2016**, *63*, 390–398. [CrossRef]
40. Jayaprakash, K. Surface coating of implants—A review. *Int. J. Dent. Clin.* **2012**, *4*, 32–35.
41. Bosco, R.; Van Den Beucken, J.; Leeuwenburgh, S.; Jansen, J. Surface engineering for bone implants: A trend from passive to active surfaces. *Coatings* **2012**, *2*, 95–119. [CrossRef]
42. Kim, Y.-W. Surface Modification of Ti Dental Implants by Grit-Blasting and Micro-Arc Oxidation. *Mater. Manuf. Process.* **2010**, *25*, 307–310. [CrossRef]
43. Coelho, P.G.; Granjeiro, J.M.; Romanos, G.E.; Suzuki, M.; Silva, N.R.; Cardaropoli, G.; Thompson, V.P.; Lemons, J.E. Basic research methods and current trends of dental implant surfaces. *J. Biomed. Mater. Res. Part B: Appl. Biomater.* **2009**, *88*, 579–596. [CrossRef] [PubMed]
44. Chiapasco, M.; Casentini, P.; Zaniboni, M.; Corsi, E.; Anello, T. Titanium-zirconium alloy narrow-diameter implants (Straumann Roxolid((R))) for the rehabilitation of horizontally deficient edentulous ridges: Prospective study on 18 consecutive patients. *Clin. Oral Implant. Res.* **2012**, *23*, 1136–1141. [CrossRef] [PubMed]
45. Pecora, G.E.; Ceccarelli, R.; Bonelli, M.; Alexander, H.; Ricci, J.L. Clinical evaluation of laser microtexturing for soft tissue and bone attachment to dental implants. *Implant Dent.* **2009**, *18*, 57–66. [CrossRef] [PubMed]
46. Mazor, Z.; Cohen, D.K. Preliminary 3-dimensional surface texture measurement and early loading results with a microtextured implant surface. *Int. J. Oral Maxillofac. Implant.* **2003**, *18*, 729–738.
47. Liu, R.; Lei, T.; Dusevich, V.; Yao, X.; Liu, Y.; Walker, M.P.; Wang, Y.; Ye, L. Surface characteristics and cell adhesion: A comparative study of four commercial dental implants. *J. Prosthodont.* **2013**, *22*, 641–651. [CrossRef] [PubMed]
48. Yang, Y.; Kim, K.-H.; Ong, J.L. A review on calcium phosphate coatings produced using a sputtering process—An alternative to plasma spraying. *Biomaterials* **2005**, *26*, 327–337. [CrossRef]
49. Lemons, J.E.; Niemann, K.M.; Weiss, A.B. Biocompatibility studies on surgical-grade titanium-, cobalt-, and iron-base alloys. *J. Biomed. Mater. Res.* **1976**, *10*, 549–553. [CrossRef]
50. Liu, X.; Chu, P.K.; Ding, C. Surface modification of titanium, titanium alloys, and related materials for biomedical applications. *Mater. Sci. Eng. R Rep.* **2004**, *47*, 49–121. [CrossRef]
51. Wang, L.; Lu, W.; Qin, J.; Zhang, F.; Zhang, D. Microstructure and mechanical properties of cold-rolled TiNbTaZr biomedical β titanium alloy. *Mater. Sci. Eng. A* **2008**, *490*, 421–426. [CrossRef]
52. Geetha, M.; Singh, A.K.; Asokamani, R.; Gogia, A.K. Ti based biomaterials, the ultimate choice for orthopaedic implants—A review. *Prog. Mater. Sci.* **2009**, *54*, 397–425. [CrossRef]
53. Wei, Q.; Wang, L.; Fu, Y.; Qin, J.; Lu, W.; Zhang, D. Influence of oxygen content on microstructure and mechanical properties of Ti–Nb–Ta–Zr alloy. *Mater. Des.* **2011**, *32*, 2934–2939. [CrossRef]
54. Guo, Y.; Chen, D.; Cheng, M.; Lu, W.; Wang, L.; Zhang, X. The bone tissue compatibility of a new Ti35Nb2Ta3Zr alloy with a low Young's modulus. *Int. J. Mol. Med.* **2013**, *31*, 689–697. [CrossRef] [PubMed]
55. Li, Y.; Yang, C.; Zhao, H.; Qu, S.; Li, X.; Li, Y. New Developments of Ti-Based Alloys for Biomedical Applications. *Materials* **2014**, *7*, 1709–1800. [CrossRef] [PubMed]
56. Azadmanjiri, J.; Berndt, C.C.; Kapoor, A.; Wen, C. Development of Surface Nano-Crystallization in Alloys by Surface Mechanical Attrition Treatment (SMAT). *Crit. Rev. Solid State Mater. Sci.* **2015**, *40*, 164–181. [CrossRef]
57. Wang, L.; Qu, J.; Chen, L.; Meng, Q.; Zhang, L.-C.; Qin, J.; Zhang, D.; Lu, W. Investigation of deformation mechanisms in β-type Ti-35Nb-2Ta-3Zr alloy via FSP leading to surface strengthening. *Metall. Mater. Trans. A* **2015**, *46*, 4813–4818. [CrossRef]
58. Wang, L.; Xie, L.; Lv, Y.; Zhang, L.-C.; Chen, L.; Meng, Q.; Qu, J.; Zhang, D.; Lu, W. Microstructure evolution and superelastic behavior in Ti-35Nb-2Ta-3Zr alloy processed by friction stir processing. *Acta Mater.* **2017**, *131*, 499–510. [CrossRef]
59. Rabadia, C.; Liu, Y.J.; Wang, L.; Sun, H.; Zhang, L. Laves phase precipitation in Ti-Zr-Fe-Cr alloys with high strength and large plasticity. *Mater. Des.* **2018**, *154*, 228–238. [CrossRef]
60. Acharya, S.; Panicker, A.G.; Laxmi, D.V.; Suwas, S.; Chatterjee, K. Study of the influence of Zr on the mechanical properties and functional response of Ti-Nb-Ta-Zr-O alloy for orthopedic applications. *Mater. Des.* **2019**, *164*, 107555. [CrossRef]
61. Rabadia, C.D.; Liu, Y.; Chen, L.-Y.; Jawed, S.F.; Wang, L.; Sun, H.; Zhang, L. Deformation and strength characteristics of Laves phases in titanium alloys. *Mater. Des.* **2019**, *179*, 107891. [CrossRef]

62. Weldon, L.M.; McHugh, P.E.; Carroll, W.; Costello, E.; O'Bradaigh, C. The influence of passivation and electropolishing on the performance of medical grade stainless steels in static and fatigue loading. *J. Mater. Sci. Mater. Med.* **2005**, *16*, 107–117. [CrossRef]
63. Assadian, M.; Jafari, H.; Ghaffarishahri, S.; Idris, M.; Gholampour, B. Corrosion resistance of EPD nanohydroxyapatite coated 316L stainless steel. *Surf. Eng.* **2014**, *30*, 806–813. [CrossRef]
64. Marti, A. Cobalt-base alloys used in bone surgery. *Injury* **2000**, *31*, D18–D21. [CrossRef]
65. Liu, R.; Li, X.; Hu, X.; Dong, H. Surface modification of a medical grade Co-Cr-Mo alloy by low-temperature plasma surface alloying with nitrogen and carbon. *Surf. Coat. Technol.* **2013**, *232*, 906–911. [CrossRef]
66. Brar, H.; Platt, M.; Sarntinoranont, M.; Martin, P.; Manuel, M. Magnesium as a biodegradable and bioabsorbable material for medical Implants. *JOM J. Miner. Met. Mater. Soc.* **2009**, *61*, 31–34. [CrossRef]
67. Nguyen, T.L.; Staiger, M.P.; Dias, G.J.; Woodfield, T.B. A novel manufacturing route for fabrication of topologically-ordered porous magnesium scaffolds. *Adv. Eng. Mater.* **2011**, *13*, 872–881. [CrossRef]
68. Li, N.; Zheng, Y. Novel Magnesium Alloys Developed for Biomedical Application: A Review. *J. Mater. Sci. Technol.* **2013**, *29*, 489–502. [CrossRef]
69. Manivasagam, G.; Suwas, S. Biodegradable Mg and Mg based alloys for biomedical implants. *Mater. Sci. Technol.* **2014**, *30*, 515–520. [CrossRef]
70. Yazdimamaghani, M.; Razavi, M.; Vashaee, D.; Moharamzadeh, K.; Boccaccini, A.R.; Tayebi, L. Porous magnesium-based scaffolds for tissue engineering. *Mater. Sci. Eng. C* **2017**, *71*, 1253–1266. [CrossRef]
71. Li, L.-Y.; Cui, L.-Y.; Zeng, R.-C.; Li, S.-Q.; Chen, X.-B.; Zheng, Y.; Kannan, M.B. Advances in functionalized polymer coatings on biodegradable magnesium alloys—A review. *Acta Biomater.* **2018**, *79*, 23–36. [CrossRef]
72. Li, C.; Guo, C.; Fitzpatrick, V.; Ibrahim, A.; Zwierstra, M.J.; Hanna, P.; Lechtig, A.; Nazarian, A.; Lin, S.J.; Kaplan, D.L. Design of biodegradable, implantable devices towards clinical translation. *Nat. Rev. Mater.* **2020**, *5*, 61–81. [CrossRef]
73. Veiga, C.; Davim, J.P.; Loureiro, A.J.R. Properties and applications of titanium alloys: A brief review. *Rev. Adv. Mater. Sci.* **2012**, *32*, 133–148.
74. Marsh, A.C.; Chamorro, N.P.; Chatzistavrou, X. 15—Long-term performance and failure of orthopedic devices. In *Bone Repair Biomaterials*, 2nd ed.; Pawelec, K.M., Planell, J.A., Eds.; Woodhead Publishing: Sawston/Cambridge, UK, 2019; pp. 379–410.
75. Khadija, G.; Saleem, A.; Akhtar, Z.; Naqvi, Z.; Gull, M.; Masood, M.; Mukhtar, S.; Batool, M.; Saleem, N.; Rasheed, T. Short term exposure to titanium, aluminum and vanadium (Ti 6Al 4V) alloy powder drastically affects behavior and antioxidant metabolites in vital organs of male albino mice. *Toxicol. Rep.* **2018**, *5*, 765–770. [CrossRef] [PubMed]
76. Thompson, G.; Puleo, D. Ti-6Al-4V ion solution inhibition of osteogenic cell phenotype as a function of differentiation timecourse in vitro. *Biomaterials* **1996**, *17*, 1949–1954. [CrossRef]
77. Choubey, A.; Balasubramaniam, R.; Basu, B. Effect of replacement of V by Nb and Fe on the electrochemical and corrosion behavior of Ti–6Al–4V in simulated physiological environment. *J. Alloys Compd.* **2004**, *381*, 288–294. [CrossRef]
78. Zhang, L.-C.; Chen, L.-Y.; Wang, L. Surface Modification of Titanium and Titanium Alloys: Technologies, Developments and Future Interests. *Adv. Eng. Mater.* **2020**, *22*, 1901258.
79. Liu, W.; Cheng, M.; Wahafu, T.; Zhao, Y.; Qin, H.; Wang, J.; Zhang, X.; Wang, L. The in vitro and in vivo performance of a strontium-containing coating on the low-modulus Ti35Nb2Ta3Zr alloy formed by micro-arc oxidation. *J. Mater. Sci. Mater. Med.* **2015**, *26*, 203. [CrossRef]
80. Zembic, A.; Sailer, I.; Jung, R.E.; Hämmerle, C.H.F. Randomized-controlled clinical trial of customized zirconia and titanium implant abutments for single-tooth implants in canine and posterior regions: 3-year results. *Clin. Oral Implant. Res.* **2009**, *20*, 802–808. [CrossRef]
81. Khorasani, A.M.; Goldberg, M.; Doeven, E.H.; Littlefair, G. Titanium in biomedical applications—properties and fabrication: A review. *J. Biomater. Tissue Eng.* **2015**, *5*, 593–619. [CrossRef]
82. Syrett, B.C.; Davis, E.E. In vivo evaluation of a high-strength, high-ductility stainless steel for use in surgical implants. *J. Biomed. Mater. Res.* **1979**, *13*, 543–556. [CrossRef]
83. Sutha, S.; Karunakaran, G.; Rajendran, V. Enhancement of antimicrobial and long-term biostability of the zinc-incorporated hydroxyapatite coated 316L stainless steel implant for biomedical application. *Ceram. Int.* **2013**, *39*, 5205–5212. [CrossRef]

84. Bekmurzayeva, A.; Duncanson, W.J.; Azevedo, H.S.; Kanayeva, D. Surface modification of stainless steel for biomedical applications: Revisiting a century-old material. *Mater. Sci. Eng. C* **2018**, *93*, 1073–1089. [CrossRef] [PubMed]
85. Kapila, S.; Sachdeva, R. Mechanical properties and clinical applications of orthodontic wires. *Am. J. Orthod. Dentofac. Orthop.* **1989**, *96*, 100–109. [CrossRef]
86. Gurappa, I. Development of appropriate thickness ceramic coatings on 316 L stainless steel for biomedical applications. *Surf. Coat. Technol.* **2002**, *161*, 70–78. [CrossRef]
87. Niinomi, M. Recent metallic materials for biomedical applications. *Metall. Mater. Trans. A* **2002**, *33*, 477. [CrossRef]
88. Yoshioka, T.; Tsuru, K.; Hayakawa, S.; Osaka, A. Preparation of alginic acid layers on stainless-steel substrates for biomedical applications. *Biomaterials* **2003**, *24*, 2889–2894. [CrossRef]
89. Hayes, J.; Richards, R. The use of titanium and stainless steel in fracture fixation. *Expert Rev. Med. Devices* **2010**, *7*, 843–853. [CrossRef]
90. Hosseinalipour, S.; Ershad-Langroudi, A.; Hayati, A.N.; Nabizade-Haghighi, A. Characterization of sol–gel coated 316L stainless steel for biomedical applications. *Prog. Org. Coat.* **2010**, *67*, 371–374. [CrossRef]
91. Katti, K.S. Biomaterials in total joint replacement. *Colloids Surf. B Biointerfaces* **2004**, *39*, 133–142. [CrossRef]
92. Goldhaber, S.B. Trace element risk assessment: Essentiality vs. toxicity. *Regul. Toxicol. Pharmacol.* **2003**, *38*, 232–242. [CrossRef]
93. Nie, J.F.; Muddle, B.C. Characterisation of strengthening precipitate phases in a Mg–Y–Nd alloy. *Acta Mater.* **2000**, *48*, 1691–1703. [CrossRef]
94. Li, Z.; Gu, X.; Lou, S.; Zheng, Y. The development of binary Mg–Ca alloys for use as biodegradable materials within bone. *Biomaterials* **2008**, *29*, 1329–1344. [CrossRef] [PubMed]
95. Brunello, G.; Sivolella, S.; Meneghello, R.; Ferroni, L.; Gardin, C.; Piattelli, A.; Zavan, B.; Bressan, E. Powder-based 3D printing for bone tissue engineering. *Biotechnol. Adv.* **2016**, *34*, 740–753. [CrossRef] [PubMed]
96. Nanda, H.S.; Chen, S.; Zhang, Q.; Kawazoe, N.; Chen, G. Collagen scaffolds with controlled insulin release and controlled pore structure for cartilage tissue engineering. *Biomed. Res. Int.* **2014**. [CrossRef] [PubMed]
97. Nanda, H.S.; Kawazoe, N.; Zhang, Q.; Chen, S.; Chen, G. Preparation of collagen porous scaffolds with controlled and sustained release of bioactive insulin. *J. Bioact. Compat. Polym.* **2014**, *29*, 95–109. [CrossRef]
98. Prasad, K.; Bazaka, O.; Chua, M.; Rochford, M.; Fedrick, L.; Spoor, J.; Symes, R.; Tieppo, M.; Collins, C.; Cao, A.; et al. Metallic Biomaterials: Current Challenges and Opportunities. *Materials* **2017**, *10*, 884. [CrossRef] [PubMed]
99. Hedberg, Y.S. Role of proteins in the degradation of relatively inert alloys in the human body. *NPJ Mater. Degrad.* **2018**, *2*, 26. [CrossRef]
100. Johnson, I.; Jiang, W.; Liu, H. The Effects of Serum Proteins on Magnesium Alloy Degradation in Vitro. *Sci. Rep.* **2017**, *7*, 14335. [CrossRef]
101. Amerstorfer, F.; Fischerauer, S.F.; Fischer, L.; Eichler, J.; Draxler, J.; Zitek, A.; Meischel, M.; Martinelli, E.; Kraus, T.; Hann, S.; et al. Long-term in vivo degradation behavior and near-implant distribution of resorbed elements for magnesium alloys WZ21 and ZX50. *Acta Biomater.* **2016**, *42*, 440–450. [CrossRef]
102. Leung, C.-H.; Lin, S.; Zhong, H.-J.; Ma, D.-L. Metal complexes as potential modulators of inflammatory and autoimmune responses. *Chem. Sci.* **2015**, *6*, 871–884. [CrossRef]
103. Tengvall, P.; Lundström, I. Physico-chemical considerations of titanium as a biomaterial. *Clin. Mater.* **1992**, *9*, 115–134. [CrossRef]
104. Li, Q.; Zhou, Q.; Shi, L.; Chen, Q.; Wang, J. Recent advances in oxidation and degradation mechanisms of ultrathin 2D materials under ambient conditions and their passivation strategies. *J. Mater. Chem. A* **2019**, *7*, 4291–4312. [CrossRef]
105. Bennett, T.D.; Cheetham, A.K. Amorphous Metal–Organic Frameworks. *Acc. Chem. Res.* **2014**, *47*, 1555–1562. [CrossRef] [PubMed]
106. Santos, C.; Barbosa, C.; Monteiro, M.; Abud, I.; Caminha, I.; Roesler, C. Fretting corrosion tests on orthopedic plates and screws made of ASTM F138 stainless steel. *Rev. Bras. Eng. Biomed.* **2015**, *31*, 169–175. [CrossRef]
107. Eliaz, N.; Baldev, R. *Biomaterials and Corrosion*; Narosa Publishing House: New Delhi, India, 2008; pp. 356–397.
108. Jimbo, R.; Ivarsson, M.; Koskela, A.; Sul, Y.-T.; Johansson, C.B. Protein adsorption to surface chemistry and crystal structure modification of titanium surfaces. *J. Oral Maxillofac. Res.* **2010**, *1*, e3. [CrossRef]

109. Lehtovirta, L.; Reito, A.; Parkkinen, J.; Peräniemi, S.; Vepsäläinen, J.; Eskelinen, A. Association between periprosthetic tissue metal content, whole blood and synovial fluid metal ion levels and histopathological findings in patients with failed metal-on-metal hip replacement. *PLoS ONE* **2018**, *13*, e0197614. [CrossRef]
110. Goodman, S.B. Wear particles, periprosthetic osteolysis and the immune system. *Biomaterials* **2007**, *28*, 5044–5048. [CrossRef]
111. Erdmann, N.; Angrisani, N.; Reifenrath, J.; Lucas, A.; Thorey, F.; Bormann, D.; Meyer-Lindenberg, A. Biomechanical testing and degradation analysis of MgCa0.8 alloy screws: A comparative in vivo study in rabbits. *Acta Biomater.* **2011**, *7*, 1421–1428. [CrossRef]
112. Liu, Y.; Chen, B. In vivo corrosion of CoCrMo alloy and biological responses: A review. *Mater. Technol.* **2018**, *33*, 127–134. [CrossRef]
113. Nanda, H.S. Surface modification of promising cerium oxide nanoparticles for nanomedicine applications. *RSC Adv.* **2016**, *6*, 111889–111894. [CrossRef]
114. Nanda, H.S. Preparation and Biocompatible Surface Modification of Redox Altered Cerium Oxide Nanoparticle Promising for Nanobiology and Medicine. *Bioengineering* **2016**, *3*, 28. [CrossRef]
115. Geng, H.; Poologasundarampillai, G.; Todd, N.; Devlin-Mullin, A.; Moore, K.L.; Golrokhi, Z.; Gilchrist, J.B.; Jones, E.; Potter, R.J.; Sutcliffe, C.; et al. Biotransformation of Silver Released from Nanoparticle Coated Titanium Implants Revealed in Regenerating Bone. *ACS Appl. Mater. Interfaces* **2017**, *9*, 21169–21180. [CrossRef] [PubMed]
116. Qing, Y.; Cheng, L.; Li, R.; Liu, G.; Zhang, Y.; Tang, X.; Wang, J.; Liu, H.; Qin, Y. Potential antibacterial mechanism of silver nanoparticles and the optimization of orthopedic implants by advanced modification technologies. *Int. J. Nanomed.* **2018**, *13*, 3311–3327. [CrossRef] [PubMed]
117. Xie, C.-M.; Lu, X.; Wang, K.-F.; Meng, F.-Z.; Jiang, O.; Zhang, H.-P.; Zhi, W.; Fang, L.-M. Silver Nanoparticles and Growth Factors Incorporated Hydroxyapatite Coatings on Metallic Implant Surfaces for Enhancement of Osteoinductivity and Antibacterial Properties. *ACS Appl. Mater. Interfaces* **2014**, *6*, 8580–8589. [CrossRef] [PubMed]
118. Singh, A.; Dubey, A.K. Various Biomaterials and Techniques for Improving Antibacterial Response. *ACS Appl. Biol. Mater.* **2018**, *1*, 3–20. [CrossRef]
119. Applerot, G.; Lipovsky, A.; Dror, R.; Perkas, N.; Nitzan, Y.; Lubart, R.; Gedanken, A. Enhanced Antibacterial Activity of Nanocrystalline ZnO Due to Increased ROS-Mediated Cell Injury. *Adv. Funct. Mater.* **2009**, *19*, 842–852. [CrossRef]
120. Alagarsamy, K.; Vishwakarma, V.; Saravanan, G.; Kamalan kirubaharan, A.M. Silver-ceria stabilized zirconia composite coatings on titanium for potential implant applications. *Surf. Coat. Technol.* **2019**, *368*, 224–231.
121. Wang, J.; Li, J.; Guo, G.; Wang, Q.; Tang, J.; Zhao, Y.; Qin, H.; Wahafu, T.; Shen, H.; Liu, X.; et al. Silver-nanoparticles-modified biomaterial surface resistant to staphylococcus: New insight into the antimicrobial action of silver. *Sci. Rep.* **2016**, *6*, 32699. [CrossRef]
122. Ciobanu, C.S.; Iconaru, S.L.; Chifiriuc, M.C.; Costescu, A.; Le Coustumer, P.; Predoi, D. Synthesis and antimicrobial activity of silver-doped hydroxyapatite nanoparticles. *Biomed. Res. Int.* **2013**, *2013*, 916218. [CrossRef]
123. Visai, L.; De Nardo, L.; Punta, C.; Melone, L.; Cigada, A.; Imbriani, M.; Arciola, C.R. Titanium oxide antibacterial surfaces in biomedical devices. *Int. J. Artif. Organs* **2011**, *34*, 929–946. [CrossRef]
124. Kargupta, R.; Bok, S.; Darr, C.M.; Crist, B.D.; Gangopadhyay, K.; Gangopadhyay, S.; Sengupta, S. Coatings and surface modifications imparting antimicrobial activity to orthopedic implants. *Wires Nanomed. Nanobiotechnology* **2014**, *6*, 475–495. [CrossRef]
125. Burdușel, A.-C.; Gherasim, O.; Grumezescu, A.M.; Mogoantă, L.; Ficai, A.; Andronescu, E. Biomedical Applications of Silver Nanoparticles: An Up-to-Date Overview. *Nanomaterials* **2018**, *8*, 681. [CrossRef]
126. Ciobanu, C.S.; Massuyeau, F.; Constantin, L.V.; Predoi, D. Structural and physical properties of antibacterial Ag-doped nano-hydroxyapatite synthesized at 100 °C. *Nanoscale Res. Lett.* **2011**, *6*, 1–8. [CrossRef] [PubMed]
127. Slavin, Y.N.; Asnis, J.; Häfeli, U.O.; Bach, H. Metal nanoparticles: Understanding the mechanisms behind antibacterial activity. *J. Nanobiotechnology* **2017**, *15*, 65. [CrossRef] [PubMed]
128. Pratsinis, A.; Hervella, P.; Leroux, J.-C.; Pratsinis, S.E.; Sotiriou, G.A. Toxicity of Silver Nanoparticles in Macrophages. *Small* **2013**, *9*, 2576–2584. [CrossRef] [PubMed]

129. Yang, Z.; Gu, H.; Sha, G.; Lu, W.; Yu, W.; Zhang, W.; Fu, Y.; Wang, K.; Wang, L. TC4/Ag metal matrix nanocomposites modified by friction stir processing: Surface characterization, antibacterial property, and cytotoxicity in vitro. *ACS Appl. Mater. Interfaces* **2018**, *10*, 41155–41166. [CrossRef] [PubMed]
130. Ding, Z.; Fan, Q.; Wang, L. A Review on Friction Stir Processing of Titanium Alloy: Characterization, Method, Microstructure, Properties. *Metall. Mater. Trans. B* **2019**, *50*, 2134–2162. [CrossRef]
131. Wu, S.; Weng, Z.; Liu, X.; Yeung, K.W.K.; Chu, P.K. Functionalized TiO2 Based Nanomaterials for Biomedical Applications. *Adv. Funct. Mater.* **2014**, *24*, 5464–5481. [CrossRef]
132. Zhao, L.; Chu, P.K.; Zhang, Y.; Wu, Z. Antibacterial coatings on titanium implants. *J. Biomed. Mater. Res. Part B Appl. Biomater.* **2009**, *91*, 470–480. [CrossRef]
133. Zhang, C.; Ding, Z.; Xie, L.; Zhang, L.-C.; Wu, L.; Fu, Y.; Wang, L.; Lu, W. Electrochemical and in vitro behavior of the nanosized composites of Ti-6Al-4V and TiO2 fabricated by friction stir process. *Appl. Surf. Sci.* **2017**, *423*, 331–339. [CrossRef]
134. Ding, Z.; Zhang, C.; Xie, L.; Zhang, L.-C.; Wang, L.; Lu, W. Effects of friction stir processing on the phase transformation and microstructure of TiO 2-compounded Ti-6Al-4V alloy. *Metall. Mater. Trans. A* **2016**, *47*, 5675–5679. [CrossRef]
135. Kaliaraj, G.S.; Vishwakarma, V.; Kirubaharan, K.; Dharini, T.; Ramachandran, D.; Muthaiah, B. Corrosion and biocompatibility behaviour of zirconia coating by EBPVD for biomedical applications. *Surf. Coat. Technol.* **2018**, *334*, 336–343. [CrossRef]
136. Jingyu, W.; Lin, W.; Yong, G.; Jinsong, Z.; Cuicui, Z. Experimental study on the osseointegration of foam TiC/Ti composites. *Biomed. Mater.* **2013**, *8*, 045001. [CrossRef] [PubMed]
137. Zhu, C.; Lv, Y.; Qian, C.; Qian, H.; Jiao, T.; Wang, L.; Zhang, F. Proliferation and osteogenic differentiation of rat BMSCs on a novel Ti/SiC metal matrix nanocomposite modified by friction stir processing. *Sci. Rep.* **2016**, *6*, 38875. [CrossRef] [PubMed]

coatings

Article

Mechanical Properties of Strontium–Hardystonite–Gahnite Coating Formed by Atmospheric Plasma Spray

Duy Quang Pham [1], Christopher C. Berndt [1], Ameneh Sadeghpour [2], Hala Zreiqat [3], Peng-Yuan Wang [4,5] and Andrew S. M. Ang [1,*]

[1] Department of Mechanical and Production Design Engineering, Surface Engineering for Advanced Materials (SEAM), Swinburne University of Technology, Hawthorn, VIC 3122, Australia; dqpham@swin.edu.au (D.Q.P.); cberndt@swin.edu.au (C.C.B.)
[2] Department of Innovation, Quality Assurance and Regulatory Affairs, Allegra Orthopaedics Limited, Sydney, NSW 2066, Australia; Ameneh.Sadeghpour@allegraorthopaedics.com
[3] School of Aerospace, Mechanical and Mechatronic Engineering, Innovative Bioengineering, The University of Sydney, Sydney, NSW 2006, Australia; hala.zreiqat@sydney.edu.au
[4] Center for Human Tissues and Organs Degeneration, Institute of Biomedicine and Biotechnology, Shenzhen Institutes of Advanced Technology, Chinese Academy of Sciences, Shenzhen 518055, China; pengyuanwang@swin.edu.au
[5] Department of Chemistry and Biotechnology, Swinburne University of Technology, Victoria 3122, Australia
* Correspondence: aang@swin.edu.au; Tel.: +61-3-9214-4964

Received: 1 October 2019; Accepted: 12 November 2019; Published: 15 November 2019

Abstract: In this work, we measured the mechanical properties and tested the cell viability of a bioceramic coating, strontium–hardystonite–gahnite (Sr–HT–G, Sr–$Ca_2ZnSi_2O_7$–$ZnAl_2O_4$), to evaluate potential use of this novel bioceramic for bone regeneration applications. The evaluation of Sr–HT–G coatings deposited via atmospheric plasma spray (APS) onto Ti–6Al–4V substrates have been contrasted to the properties of the well-known commercial standard coating of hydroxyapatite (HAp: $Ca_{10}(PO_4)_6(OH)_2$). The Sr–HT–G coating exhibited uniform distribution of hardness and elastic moduli across its cross-section; whereas the HAp coating presented large statistical variations of these distributions. The Sr–HT–G coating also revealed higher results of microhardness, nanohardness and elastic moduli than those shown for the HAp coating. The nanoscratch tests for the Sr–HT–G coating presented a low volume of material removal without high plastic deformation, while the HAp coating revealed ploughing behaviour with a large pileup of materials and plastic deformation along the scratch direction. Furthermore, nanoscanning wear tests indicated that Sr–HT–G had a lower wear volume than the HAp coating. The Sr–HT–G coating had slightly higher cell attachment density and spreading area compared to the HAp coating indicating that both coatings have good biocompatibility for bone marrow mesenchymal stem cells (BMSCs).

Keywords: Sr–HT–Gahnite; hydroxyapatite; atmospheric plasma spray; nanoindentation; mechanical properties

---

1. Introduction

Substitutional materials for bone have been active research areas since the 1970s and ceramics account for the majority of these replacements [1]. These bioceramics include three groups: (i) bioinert, (ii) bioactive, and (iii) biodegradable or bioresorbable ceramics [2]. In brief, bioinert ceramics have no or very little interaction with surrounding tissues when they are placed into the host body. However, bioactive ceramics can form chemical bonds with surrounding bones and these biodegradable ceramics are gradually replaced by endogenous tissues after implantation into the host body [2].

Calcium phosphate ceramics are commonly used for bioactive applications of bone tissue repair and augmentation because of their similar chemical composition to minerals in bone [3].

Hydroxyapatite (HAp:$Ca_{10}(PO_4)_6(OH)_2$) is the most widely accepted biocompatible and bioactive calcium phosphate ceramic with respect to tissues [4]. In bulk form, HAp presents excellent physio-chemical properties as a bioceramic; however, these attributes are deteriorated by an intrinsic brittleness, low impact resistance and low tensile strength limit when implanted for load-bearing applications [5]. One method to improve the mechanical properties while maintaining the bio-adaptive properties is by forming a HAp coating onto a metallic biomaterial [6] in applications where the bioceramic is under compressive loads. Implants that are based on a HAp coated metal can provide excellent bioactivity and biocompatibility to the host bone, while retaining the good strength and ductile properties of the metallic substrate [4].

Although a HAp coating on a metallic substrate has demonstrate good clinical and commercial outcomes [7], the demand for improving the mechanical properties of a HAp coating is still imperative. For example, the high-velocity suspension flame spray method has been used to coat a nano-structured HAp/Ti composite onto 316L stainless steel (SS) substrates [8], and the suspension plasma spray (SPS) method has been employed to produce a nano-diamond reinforced hydroxyapatite composite coating onto a titanium substrate [9]. The advantages of these two methods using suspension-based feedstock are the ability to deposit materials in submicron sizes or create new composite materials for thermal spray coating [10]. However, the feedstock feeder system and torch re-configurations are required in order to adapt to the suspension feedstock, which is considered costly and complicated. Using flame spray as a coating method has been the preferred method in the last decades because it is a low cost system, portable and easy to use, but a high porous coating with oxidation and low jet temperature with low particle velocity are the major concerns of the flame spray [11]. In contrast, atmospheric plasma spray (APS) is the most commonly used coating method for orthopedic implants and has been approved by Food and Drug Administration [12]. The APS technology allows high jet temperature and velocity so it can be used to create a denser coating with the same material [11].

Introducing substitute bioceramics that may enhance mechanical properties and biocompatibility is an alternative approach addressed in this research. It is known that silicon is a trace element in the human body that occurs naturally; e.g., 100 ppm in bone and 200–600 ppm in cartilage and other connective tissues [13]. Silicon performs as a biological linkage to form the structure of connective tissues and engages in the process of biomineralization to promote bone growth [14]. The development of Si-containing biomaterials is an active area of research such as developing bioglasses and Si-doped bioceramics [15]. Calcium silicate (Ca–Si) based ceramics, in particular $CaSiO_3$ and Ca_2SiO_4 are currently used in orthopaedic implants since they are bioactive materials that induce a bond with bone to form an apatite layer and promote the bone growth [16–18]. However, the main concerns of these bioceramics are low chemical stability with a high ionic dissolution and high degradation rates; This instability affects the mechanical strength and osseointegration at high pH levels [19], i.e., pH = 8.34 after soaking $CaSiO_3$ 25 days in a simulated body fluid (SBF) solution [20]. One method to control the dissolution is by incorporating metal ions into Ca-Si based bioceramics, which often uses zinc or/and strontium metals [19]. Zinc supports bone formation, increases bone protein and alkaline phosphatase activity in osteoblasts differentiation and mineralization, and enhances cell proliferation osteoconductivity [21]. Strontium is associated with bone through two main mechanisms which are (i) incorporation of Sr into bone crystal lattice–surface exchanging and (ii) ionic exchange with bone–ionic substitution [19].

Therefore, strontium doped hardystonite (Sr–$Ca_2ZnSi_2O_7$), named Sr–HT, is a Ca-Si based ceramic that incorporates zinc and strontium, and which shows improvements in cellular activity and chemical stability compared with $CaSiO_3$ [19]. Sr–HT in the form of a scaffold (pore interconnectivity: 99%, pore size: 300 to 500 µm, and porosity: 78%) has shown exceptional bioactivity as a scaffold to repair large-sized bone defects. It presented a high compressive strength of 2.16 ± 0.52 MPa, which is a favorable property for load-bearing applications. By mixing ~80 wt % Sr–HT with ~20 wt % gahnite

($ZnAl_2O_4$) [22], the Sr–HT–G ceramic had high fracture toughness and compressive strength properties that were superior to those of cortical bone [22]. A Sr–HT–G scaffold (pore interconnectivity: 100%, pore size: 500 µm, and porosity: 85%) presented higher compressive strength of 4.1 ± 0.3 MPa than solely Sr–HT [22]. Sr–HT–G scaffolds are able to repair the large bone defects, which are outstanding against the β-tricalcium phosphate/hydroxyapatite (TCP/HA) scaffolds [22]. The Sr–HT–G scaffolds can promote the attachment of adipose derived stem cells and the alkaline phosphatase activity of these cells when contrasting with β-TCP/HA scaffolds [23]. These scaffolds also enhance the migration, proliferation and differentiation of human umbilical vein endothelial cells without adverse effect on viability cells [23]. The 3D-printed Sr–HT–G scaffolds in the study of Li et al. have shown a significant effect in repairing bone defects in sheep tibia for 3 and 12 months, where the bone formation significantly bridged the defects [24].

In this study, the atmospheric plasma spray (APS) technique was employed to deposit Sr–HT–G powders onto Ti–6Al–4V substrates in order to evaluate the possibility of using this coating for applications of orthopedic implants. Commercial hydroxyapatite powders were used to produce control samples. The study compares the mechanical and chemical properties of the Sr–HT–G to HAp coating and includes: (i) surface characteristics of the coatings, (ii) chemical analysis and phases of coatings, (iii) Vickers microhardness, (iv) distribution of hardness and elastic moduli via nanoindentation, (v) nanoscratch and nanowear behavior, and (vi) stem cell culture study.

2. Materials and Methods

2.1. Powder Preparation

The Sr–HT–G powders were prepared by Allegra Orthopaedics Limited (Sydney NSW, Australia) following the method that is described in the study of Roohani-Esfahani et al. [22]. Briefly, Hardystonite ($Ca_2ZnSi_2O_7$) powders were prepared through the sol–gel method from tetraethyl orthosilicate (“TEOS” of formula ($(C_2H_5O)_4Si$), zinc nitrate hexahydrate ($Zn(NO_3)_2{\cdot}6H_2O$) and calcium nitrate tetrahydrate ($Ca(NO_3)_2{\cdot}4H_2O$). Then, strontium ions (from $Sr(NO_3)_2$, 5 wt %) were added to substitute calcium ions to form Sr–HT. Finally, alumina (Al_2O_3) powder (15 wt %) was added into the Sr–HT system. Initially, the Sr–HT–G powder was of submicrometer size and was not suitable for APS due to poor powder flow characteristics. The flow behavior was improved by initially mixing the Sr–HT–G powder with 5 wt % polyvinyl alcohol (PVA, Sigma Aldrich, St. Louis, MO, USA). This mixture was consolidated into bulk form by heating in an oven at 70 °C for 24 h. The consolidated mass was then ground in a mortar and pestle before sieving to 45–106 µm. The HAp powder, from Medicoat SAS (Etupes, France), exhibited particle sizes of 45 to 125 µm.

2.2. Plasma Coating Set Up and Operation

A Metco 9MB plasma torch with a 7 mm-Metco GH nozzle (Sulzer Metco, Westbury, NY, USA) was used to deposit Sr–HT–G and HAp powders onto Ti–6Al–4V substrates. The coatings were deposited at room temperature, using a six-axis robot (YR-SK16-J00; Motoman Robotics, Miamisburg, OH, USA) to control the torch position with the velocity of between 100 to 150 mm/s. The same coating parameters were applied for both Sr–HT–G and HAp powders (Table 1).

Table 1. Setup parameters for plasma coating of Sr–HT–G and HAp powders.

Parameters	Value
Power (kW)	21
Primary gas flow, Ar (slpm)	30
Secondary gas flow, H_2 (slpm)	5
Powder carrier gas flow, Ar (slpm)	9
Number of torch passes	5
Stand-off distance (mm)	90

2.3. Coating Characterisations

Phase compositions of powders and coatings are analysed by the Bruker D8 Advance XRD system (Bruker Corp., Billerica, MA, USA) with Cu Kα radiation. The XRD system operates at 40 kV and 30 mA to scan over the range of 20°–70° with a step size of 0.08° and 2 s of dwell time. The XRD results were indexed using Diffracplus EVA software (EVA V5, Bruker Corp., Billerica, MA, USA) and then compared with database PDF2018-PDF-2-Release 2018 RDB from the International Center for Diffraction Data (ICDD, Newtown Square, PA, USA). The crystallinity level is calculated based on the intensity of peaks, which is described in Equation (1), where A_c and A_a are total intensity of peaks and total intensity of amorphous phase [25].

$$\text{Crystallinity} = A_c/(A_c + A_a) \times 100\% \tag{1}$$

where A_c and A_a are total intensity of peaks and total intensity of amorphous phase.

Chemical analysis of coatings was conducted using an X-ray photoelectron spectrometer (XPS) with a Kratos Axis Nova system (Kratos Analytical, Manchester, UK) and Raman microspectroscopy with an In-Via Raman Microscope system (Renishaw®, Gloucestershire, UK). The XPS system has the X-ray source of Al Kα with hν = 1486.69 eV that operates at 150 W. XPS data were analysed by CasaXPS software (Version 2.3.15, CASA Software Ltd., Cheshire, UK) after a Shirley background subtraction with the correction of binding energy for carbon at 285 eV. The XPS characterisation was done on the as-sprayed samples, which is how it would be used in actual orthopedic applications. Raman microspectroscopy used 785 nm laser wavelength with 10% of the 150 W laser power and 10 s for exposure time. High-resolution electron micrographs were obtained using a field emission SEM (SUPR 40 VP, Carl Zeiss, Oberkochen, Germany) at 5 kV. In all cases, the coating surfaces were cleaned by ethanol and then dried by compress air. After that, the samples were place in a vacuum environment till it underwent characterisation.

Coatings were cut and prepared following ASTM E1290-03 "Standard Guide for Metallographic Preparation of Thermal Sprayed Coatings" [26] to get cross sections of coatings for analysis. A Vickers microhardness tester (Micromet 2103 Microhardness tester, BUEHLER, Lake Bluff, IL, USA) was setup to perform the microhardness test on cross sections of coatings at the load of 300 gf and dwell time of 15 s. Forty readings was recorded on each sample and the Weibull distribution analysis was performed to analyse coating properties and reliability. Surface roughness, R_a, was measured using a portable surface roughness tester SJ-210 (Mitutoyo, Kawasaki, Japan) with a 2 µm stylus diameter together with a 3D optical profiler system (Bruker Corporation, Billerica, MA, USA).

A nanoindenter (Hysitron TI Premier, Bruker, Eden Prairie, MN, USA) with a Berkovich diamond tip was used to perform the nanohardness and elastic moduli. A cono-spherical 1 µm diameter diamond tip was used in the nanoindentation system to performe nanoscratch and nanowear tests. The resolutions of the nanoindentation system are 1.0 nN and 0.006 nm for the applied load and tip displacement, respectively. The distributions of hardness and elastic moduli of coatings were investigated using accelerated property mapping (XPM) with the support of the scanning probe microscopy (SPM) method. The nanoindentation test were performed following the testing procedure, which was described in the previous study of Pham et al. [27]. Briefly, the tests were done on areas of 30 × 30 μm^2 with 400 indents in each area (1.5 µm gap between indents). Fifteen areas was selected along the cross section of each coating, and the applied loads were from 500 to 3000 µN. Elastic moduli and hardness were determined by measuring penetration depths after indenting at the applied load using the Oliver–Pharr method [28].

Nanoscratch tests were performed at the loads from 1000 to 2000 µN with the scratch length of 10 µm. Nanowear test was conducted by applying a load of 200 µN onto the area of 10 × 10 μm^2 and scanned over the section three times for each selected areas at the scanned frequency of 0.8 Hz. The wear volumes were calculated by measuring the different heights between the before and after of the scanned areas, and multiplying the height difference with the scanning size. The results from nanoscratch and nanowear tests were analysed by TriboView software (Version 10.0.0.2, Hysitron TI Premier, Bruker, Eden Prairie, MN, USA).

2.4. Stem Cell Culture

Human bone marrow mesenchymal stem cells (BMSCs) were purchased from Cyagen Biosciences (HUXMF-0101, Suzhou Inc., Suzhou, China) at passage 2 and maintained in a complete growth media (HUXMF-90011, Cyagen Bioscience). The complete growth media of BMSC was composed of 440 mL basal medium, 50 mL fetal bovine serum, 5 mL glutamine, 5 mL penicillin-streptomycin. It was used as purchased without the addition of extra growth factors. The growth media is only used for BMSC maintenance. For the biocompatibility test, cells were seeded at a density 5000 cells/cm^2 and fixed after 24 h. Phalloidin-Rhodamine B (cat# P1961, Sigma, Tokyo, Japan) and DAPI (cat# D1306, Sigma) were employed for F-actin filament and cell nucleus staining, respectively. Immunostained samples were washed thoroughly and examined under an inverted fluorescence microscope (IX73 Olympus, Tokyo, Japan) at 20 magnification. Cell density (cells/mm^2) and cell spreading area (μm^2) on three different substrates including as-received Ti, HAp coating, and Sr–HT–G coating, which were quantitatively analysed based on the obtained images. The cell number and cell spreading area were analysed from the DAPI stained and F-actin stained cells via NIH ImageJ software (Version 1.52). DAPI stained images were processed via threshold color and the number of nuclei was automatically determined via the plugin of cell counter in Image J software (Version 1.52); Similarly, F-actin stained images were processed via threshold color and the occupied area was automatically measured via Image J software (Version 1.52).

3. Results and Discussions

3.1. Feedstock Morphology

Morphologies of Sr–HT–G (after of mixing with PVA, consolidating, grinding and sieving) and HAp powders are indicated in Figure 1a,b, respectively. Sr–HT–G powders were manually ground and sieved so the powders are described as angular and blocky, while HAp powders are spherical-like shape. The morphology of Sr–HT–G powders provide higher ratio of surface area to volume than that of HAp powders, which can lead to a better degree of heating in plasma plumes [29]. HAp may present better flow transportation characteristics than Sr–HT–G because spherical powders are preferable morphology in plasma spray. These HAp particles can easily enter into the center of the plasma plume to be well deposited, while Sr–HT–G powders may not be injected ideally into the plasma flame due to irregular sizes [11,29].

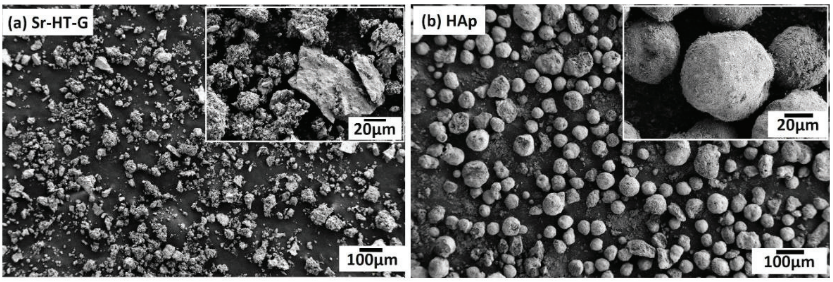

Figure 1. Feedstock morphology of strontium–hardystonite–gahnite (Sr–HT–G) (**a**) and hydroxyapatite (HAp) (**b**).

3.2. Coating Surface Analysis

3.2.1. Phase Compositions

Figure 2 presents the XRD results of powders and coatings for Sr–HT–G and HAp. Sr–HT–Ga powders consist of two distinct phases in Figure 2a, which are Sr–HT (PDF 01-072-1603) and gahnite (PDF 01-070-8181). The gahnite phase in starting powders is formed by the reaction between zinc in Sr–HT and alumina during the sintering process at high temperatures to produce powders [22]. Similar to the staring powders, the coating of Sr–HT–G also presents two phases, which are Sr–HT and gahnite. The peaks of Sr–HT–G coating are significantly less sharp and are broaden after the plasma coating, which indicate the reduction in the level of crystallinity. However, there is no new peaks formed in the Sr–HT–G coating, but they are slightly shifted in the peaks of the coating comparing with its powders. The reason for the peak shifts could be the internal or residual stress after coating, which causes the change in lattice parameters. On the other hand, HAp powders present high purity with phase of HAp, but its coating presented the phase of $Ca_{10}(PO_4)_6(OH)_2$ (PDF 00-064-0738) and a new phase of tricalcium phosphate-TCP ($Ca_3(PO_4)_2$) (PDF 01-072-7587) in Figure 2b. This new phase TCP was formed by the reaction of HAp in the high temperature region of plasma plume [30].

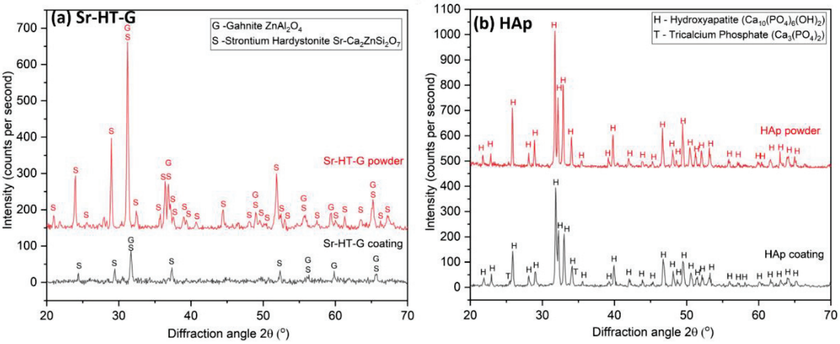

Figure 2. XRD results of Sr–HT–G powder and coating (**a**) and HAp powder and coating (**b**).

Both coatings illustrate lower intensity levels or lower crystallinity compared with their starting powders. Significant lower intensity of the peaks in a coating comparing to its starting powder can be seen in the result of Sr–HT–G, of which the level of crystallinity from Equation (1) are 74.6% and 32.7% for powders and the coating, respectively. On the other hand, levels of crystallinity in HAp powders and coating are not significantly different, which are 84.8% and 75.5% for powders and the coating, respectively. The lower crystallinity in the coating is a feature of the plasma process, which feedstock are exposed and heated by a 10,000 °C plasma flame, then rapidly cooled at about 10^6 degrees per second, where the feedstock do not have enough time to recrystallize [29]. It can be seen that the Sr–HT–G coating presents lower levels of crystallinity than that in the HAp coating. Sr–HT–G is a Ca-Si ceramic with the sorosilicate (Si_2O_7) group that has a more intricate crystalline structure, so the process of recrystallize will be more complex than that of HAp [31]. In contrast, HAp powders with larger particle sizes are well deposited with a larger quantity in the coating because they are fed into the center of the plasma flame. As the result, a greater amount of bulk crystalline can be found in the coating, which leads to a higher percentage of crystallinity [32].

3.2.2. XPS on Coating Surfaces

Figure 3a presents the XPS analysis result of Sr–HT–G coating with the presence of Sr, Ca, Zn, Si, O, Al on the coating surface. Two peaks of Zn in the spectrum are Zn 2*p* and Zn 2*p*1/2 at 1022.9 and 1045.9 eV, respectively. Furthermore, the presenting of the peaks Al 2*p* at 74.0 eV and Al 2*s* at

119.0 eV together with the peak O 1*s* at 531.5 eV indicates the formation of $ZnAl_2O_4$ on the coating surface [33,34]. In a high-resolution scan presented in Figure 3c, Si presented the peak of Si 2*p* at 102 eV, which refers to the presence of a silicate group [35]. This silicate group is Si_2O_7, which is in the structure of Sr–HT. Formation of Sr–HT and gahnite phases are further supported by results from the analysis in XRD. The Sr–HT and gahnite composite ceramic has shown an improvement in biocompatibility and bioactivity, which has been evaluated by its capability in osteoconduction and osteoinduction [36]. Thus, a plasma coating with the present of Sr–HT and gahnite phases will potentially produce good biocompatibility and bioactivity.

Chemical elements on the surface of HAp coating under XPS analysis are shown in Figure 3b. The surface of HAp coating consists of Ca, P, and O as the main elements in its starting powders. The peak of P 2*p* is 132.8 eV, while the peak of O 1*s* is 530.8 eV. This result indicates the present of the PO_4^{3-} group [35], which is in the structure of hydroxyapatite $Ca_{10}(PO_4)_6(OH)_2$. Calcium has four peaks, which are Ca 2*s*, Ca 2*p*, Ca 3*s*, and Ca 3*p*. The Ca 2*s* presents a peak at 438.6 eV, while the Ca 2*p* consists of a doublet with values of 346.9 and 350.4 eV for Ca 2*p*3/2 and Ca 2*p*1/2, respectively. The peaks of Ca 3*i* and Ca 3*p* are 44.0 and 25.3 eV that are illustrated in Figure 3d. The results of calcium peaks indicate the formation of $Ca_3(PO_4)_2$ [37]. These HAp phases have been shown to support the in vitro and in vivo formation of bone.

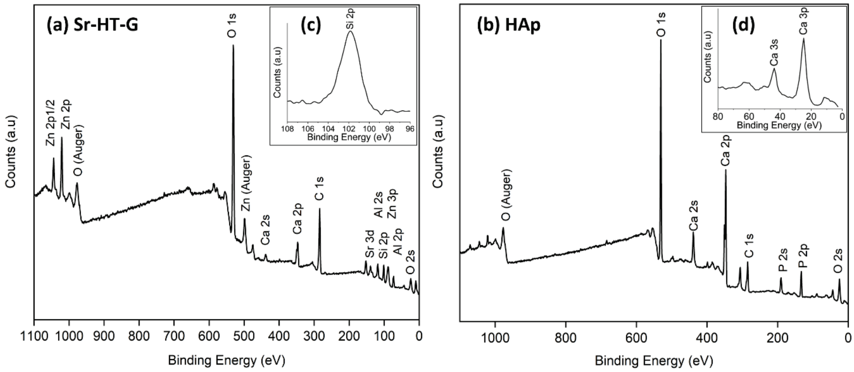

Figure 3. XPS analysis of Sr–HT–G coating (**a**) and HAp coating (**b**). The peaks of Si 2*p* (**c**), Ca 3*i* and Ca 3*p* (**d**).

3.2.3. Morphologies of Coating Surfaces

Surfaces of the Sr–HT–G and the HAp coatings are shown in Figure 4a,b, respectively, where both coatings show well-melted splats. However, the Sr–HT–G coating shows more uniform surface morphology with spherical-like splat shapes, while HAp coating presents irregular splats with a big splash at the rims. Furthermore, some fragmentations can be found within splats of the HAp coating, whilst the Sr–HT–G coating shows more consistent structure on the surface with more uniform splats. Under the melting and re-solidify processes in APS, well-melted splats or partially melted particles will spread onto the substrate and form layers of splats [38]. Molten particles of Sr–HT–G show higher spreading ability than the HAp, which could be closely related to its viscosity characteristics and eventually reveals more regular Sr–HT–G splats [39].

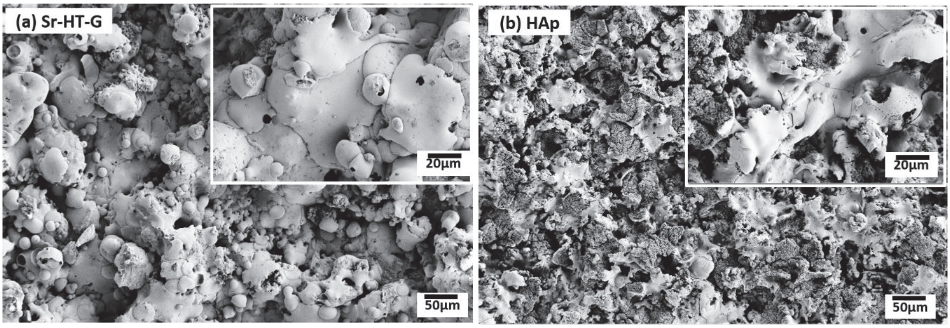

Figure 4. SEM of coating surfaces of Sr–HT–G (**a**) and HAp (**b**).

3.3. Coating Cross Section Analysis

3.3.1. Coating Microstructures

Figure 5 indicates the microstructure of the Sr–HT–G and the HAp coatings at cross sections. Both coatings present features of thermal spray coating including cracks, pores, and unmelted particles [38]. Different phases can be found in the HAp coating as the result of different contrasts, which are shown in bright gray and dark gray. The amorphous phase is easily removed during the polishing process, which causes the height to be lower than the crystalline areas. As the result, the amorphous phase appears to be darker. This observation has been re-confirmed with Raman spectroscopy. Similar results have been presented in the works of Gross et al. [30,40]. However, there is not much difference in contrast of phases in the Sr–HT–G coating as its microstructure presents a similar contrast to the source of ignition during the SEM process. It can be seen that the Sr–HT–G coating has less cracks in microstructure, while the HAp coating presents more cracks. Moreover, due to the reaction of alumina with zinc in Sr–HT, a more uniform structure is formed [36], where the Sr–HT–G coating has a denser structure and a more consistent microstructure compared with the HAp coating. Less pores in the structure of the Sr–HT–G coating could come from the larger distribution of powder sizes, where different sizes of Sr–HT–G splats are likely to fill up the pores in the microstructure during the process of deposition [11]. In addition, the interface of coating-substrate in the Sr–HT–G coating is quite consistent with crack-free features, while the HAp coating shows minor cracks at the coating-substrate interface.

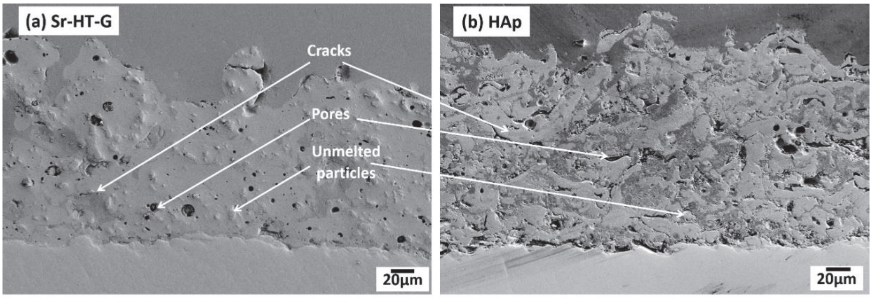

Figure 5. Microstructure of Sr-HT-G (**a**) and HAp (**b**) on coating cross section.

3.3.2. Vickers Microhardness

The results of Vickers microhardness are shown in Figure 6, where the hardness of the Sr–HT–G and the HAp coatings are 330.4 ± 54.4 HV300 and 120.2 ± 24.3 HV300, respectively. Vickers microhardness in the coating of Sr–HT–G is significantly high due to the addition of Zn into the Ca-Si structure [19,21], which is almost triple the hardness of the HAp coating. In addition, the formation of a glass phase between Sr–HT grains and the existence of a strong restraint surrounding the Sr–HT grains from the glass-ceramic phase of gahnite also leads to the improvement in mechanical properties of the Sr–HT–G coating [36]. The coefficient of variant (CoV = standard deviation divided by the mean) of the Sr–HT–G is coating slightly lower than that of the HAp coating, which are 16% and 20%, respectively. The coating of Sr–HT–G has lower CoV values in microhardness because the Sr–HT–G coating possesses a more uniform microstructure compared to those in the HAp coating. The Weibull analysis of microhardness of the Sr–HT–G and HAp coatings are presented in Figure 6, where both coatings present good regression fits with R^2 values of 0.97 and 0.96, respectively [41]. The Weibull moduli m, which presents the scattering behavior of results within the distribution [41], show that both the Sr–HT–G and HAp coatings have low values of Weibull modulus but they are the typical values in thermal spray. The Sr–HT–G coating has a slightly higher value of Weibull moduli than the HAp coating, which indicates less variation in the microhardness results in the Sr–HT–G coating.

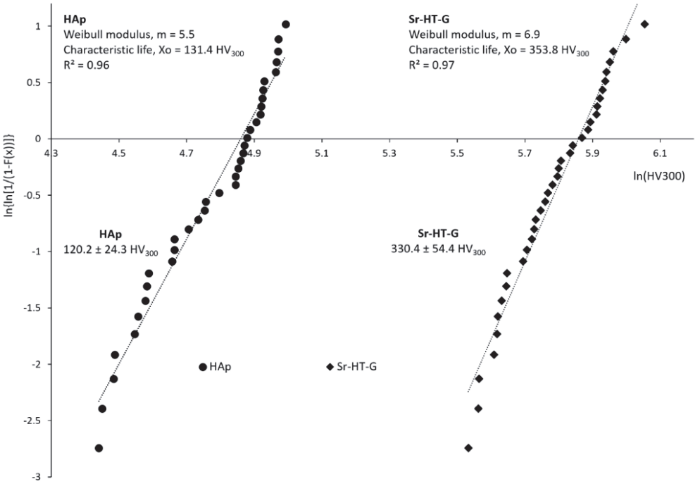

Figure 6. Weibull regression analysis of the Vickers hardness test of HAp and Sr–HT–G coatings.

3.3.3. Nanohardness and Elastic Moduli

The cross section of the Sr–HT–G coating shows a uniform structure in the coating, shown in Figure 7a. Figure 7b,d presents corresponding the SPM and SEM images of the same area after performing the nanoindentation. The indentation mapping results of the Sr–HT–G coating are presented by the distributions of elastic moduli and hardness in Figure 7c,e, respectively. The variant in the distributions of nanohardness and elastic moduli depends on the features of the selected area such as element compositions, phase structure, cracks, and pores. Generally, lower hardness and lower elastic moduli can be found in pore and crack areas [42]. Uniform distributions of nanohardness and elastic modulus can be achieved in the Sr–HT–G coating, which indicate the consistent of mechanical properties across the coating. This uniformity could be achieved by the presence of the gahnite phase in the coating that could enhance the mechanical properties across the coating [36].

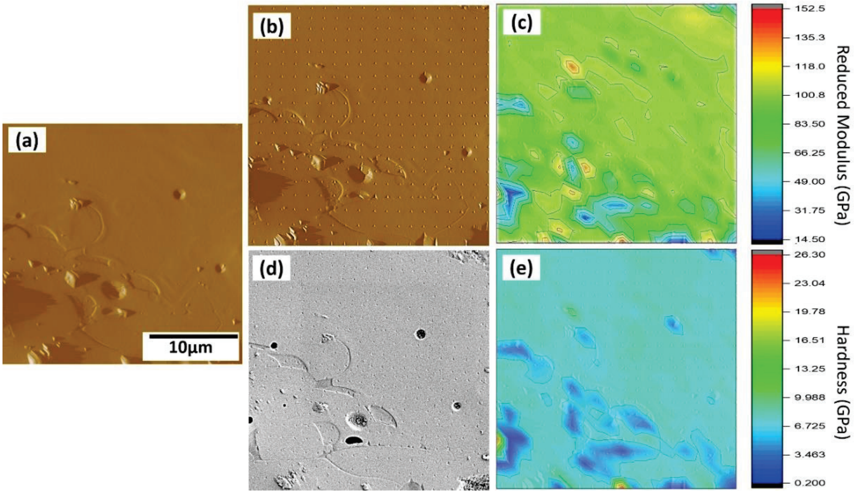

Figure 7. Results of the nanoindentation test of the Sr–HT–G coating. (**a**) The SPM image of surface before applying the indents; (**b**) and (**d**) the SPM and SEM image of surface after applying the indents; (**c**) and (**e**) property map of reduced modulus and hardness of the coating.

The distributions of nanohardness and elastic moduli in a selected area from the HAp coating are found in Figure 8. Similar to the testing procedure of the Sr–HT–G coating, Figure 8a presents a selected area that was pre-scanned to capture the features before performing the nanoindentation. After performing the nanoindentation, the surface was captured again via SPM and SEM techniques, which are shown in Figure 8b,d, respectively. The difference in contrast of the SEM image present different phases that have formed, which are named as “A” and “B” regions. The results of elastic moduli and nanohardness of the HAp coating are shown in Figure 8c,e in the form of distribution maps, respectively. The marks of indents in the HAp coating at the “A” area present deeper and larger sizes than those in the “B” area. Raman microspectroscopy was used to analyze the functional groups of the highlighted Region A and B of the HAp coating. It can be seen that both regions have same functional groups as the result of similar positions of Raman peaks in Figure 9. However, sharper peaks with higher intensity can be found in Region B, which indicates the formation of crystalline HAp while Region A presents the formation of an amorphous phase [43]. Similar to the study of J. Wen et al. [44], Region B yielded better mechanical properties, which it showed higher results of nanohardness and elastic moduli than Region A.

This indicates there is less uniformity of coating phases in the HAp coating when comparing with the Sr–HT–G coating. As the result, both nanohardness and elastic moduli showed high variants in distribution of values across the HAp coating. The average values of elastic moduli and nanohardness of the Sr–HT–G coating were 93.0 ± 16.6 and 7.2 ± 2.1 GPa, respectively. On the other hand, lower results of both elastic modulus and nanohardness can be found in the HAp coating, which the average values were 77.6 ± 41.5 and 4.4 ± 3.2 GPa, respectively. The average results of both nanohardness and elastic moduli in the Sr–HT–G coating showed significantly better results than that of the HAp coating, which were in accordance with the results in the Vickers microhardness tests. Furthermore, the Sr–HT–G coating presented lower values of CoV in both hardness and elastic moduli with 17.8% and 29.2%, respectively, while these values of hardness and elastic moduli in the HAp coating were higher at 53.4% and 72.7% due to the lack of uniform phases.

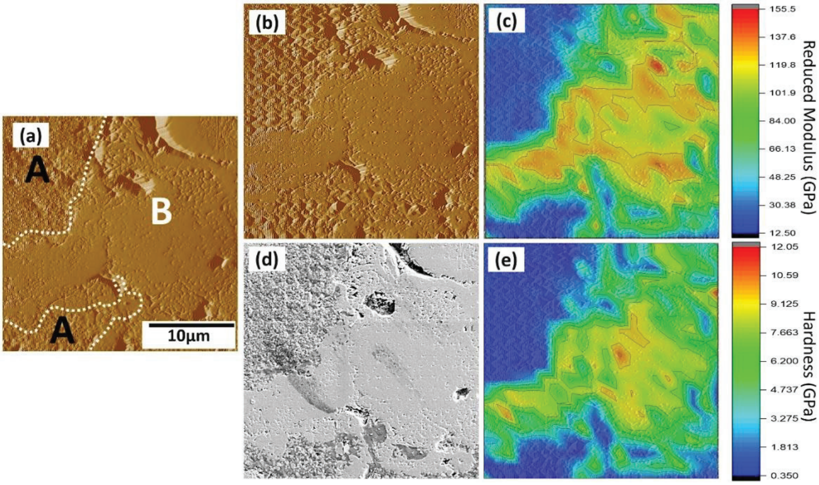

Figure 8. Results of the nanoindentation test of the HAp coating. (**a**) The SPM image of surface before applying the indents; (**b**) and (**d**) the SPM and SEM image of surface after applying the indents; (**c**) and (**e**) property map of reduced modulus and hardness of the coating.

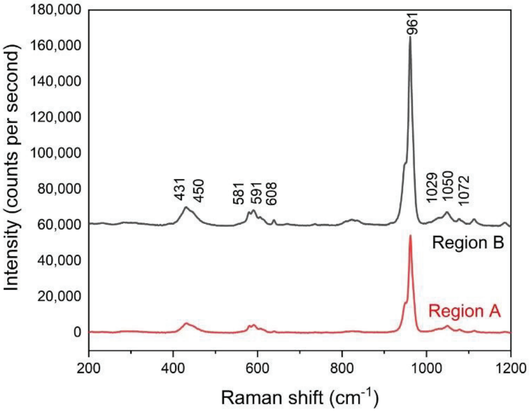

Figure 9. Raman microspectroscopy of the regions in the HAp coating.

3.3.4. Nanoscratch and Nanoscanning Wear Performance

Results of nanoscratch tests under the load of 1000 µN are presented in Figure 10, where Figure 10a,d shows the surfaces of the selected areas after the scratching of Sr–HT–G and HAp coatings, respectively. It can be seen that the Sr–HT–G coating depicts tearing behavior only with shallow depths of penetration, while deeper and more plastic flow across the edge of the scratch direction can be found in the HAp coating. The 3D maps in Figure 10b,e render more details of the behavior of these coatings under scratch tests. The HAp coating experienced more plastic deformation with large pileup of materials that represents ploughing behavior under the scratch test.

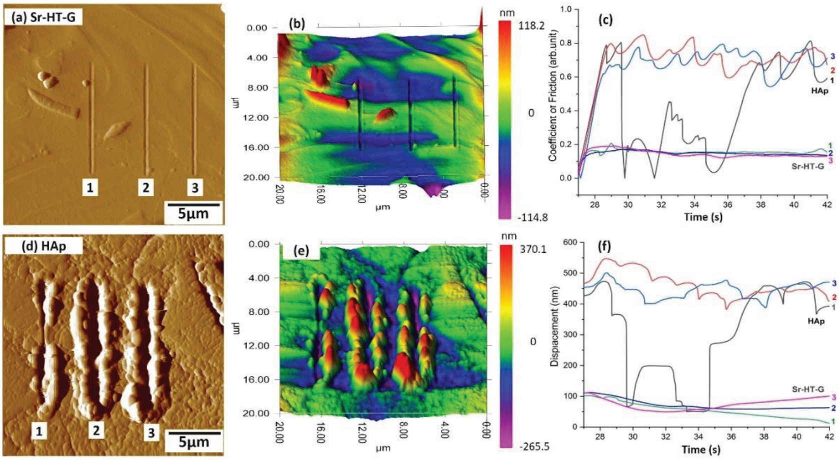

Figure 10. Nanoscratch test results of the Sr–HT–G coating (**a**,**b**); and the HAp coating (**d**,**e**); friction coefficient (**c**); and normal displacement (**f**).

Figure 10c,f reveals the coefficient of friction (CoF) and depth of the scratch (displacement) of the Sr–HT–G and the HAp coatings, respectively, which show the details of Scratch 1, 2, and 3 from the Figure 10a,c. In the nanoscratch test, the actual applied load started from the 27th second to the 42nd second, while other times for loading and unloading periods are not considered. From the results of the nanoscratch tests, CoFs and displacements of the Sr–HT–G coating show high consistency with low values of CoFs and low penetration depths in all the scratches. On the other hand, CoF values and displacements in the HAp coating fluctuate continuously, i.e., values of CoF and displacement significantly decreased from 29.5 to 35 s in the scratches due to higher scratch resistance in this region of the HAp coating. This result could have originated from the significant difference in mechanical properties of different phases in the HAp coating, which has a similar trend with the distribution of hardness and elastic moduli.

The average depths of scratch are 60.9 ± 9.7 nm (CoV = 16%) and 245.0 ± 150.4 nm (CoV = 61%) for the Sr–HT–G and the HAp coatings, respectively. Lower scratch depth with less removal of materials in the Sr–HT–G coating indicate that the Sr–HT–G coating is more resistant to scratches. Furthermore, the average CoF of the Sr–HT–G coating is 0.14 ± 0.02 (CoV = 14%), which is much lower than the average CoF in the HAp coating, 0.69 ± 0.14 (CoV = 20%). Similar to the analysis in the nanoindentation, the lower result of CoV in the scratch test shows the coating microstructure of the Sr–HT–G coating presents more uniform features than the HAp coating. This results in the Sr–HT–G coating shows better scratch resistance than the HAp coating.

The wear behavior of the Sr–HT–G and the HAp coating under the applied load of 1000 μN are presented in Figure 11, in which the pre-wear test, and post-wear test images were evaluated. The black square areas indicate the regions that were selected to perform nanowear tests. The surface before performing wear tests are presented in Figure 11a,d,g; while Figure 11b,e,h and Figure 11c,f,i illustrate the surface after the wear test of SPM images and their 3D views, respectively. Similar to the result from nanoindentation and nanoscratch tests, the Sr–HT–G coating presents uniform distribution with consistent results of wear volume in Figure 11b,c. On the other hand, the HAp coating reveals more variance of wear behavior due to a significant difference in the region of "A" and "B" as amorphous and crystalline regions, respectively, in Figure 11e,h. It can be seen that amorphous areas present less wear resistance than crystalline areas, showing similar trends in nanoindentation and nanoscratch tests. The wear volume for Sr–HT–G and HAp coatings are 0.11 ± 0.03 and 5.52 ± 2.90 μm^3, respectively. This enhanced mechanical properties of the Sr–HT–G coating was achieved by doping zinc into a Ca-Si ceramic together with the formation of gahnite in the structure [19,36]. This result indicates that the Sr–HT–G coating possesses superior wear resistance than the HAp coating.

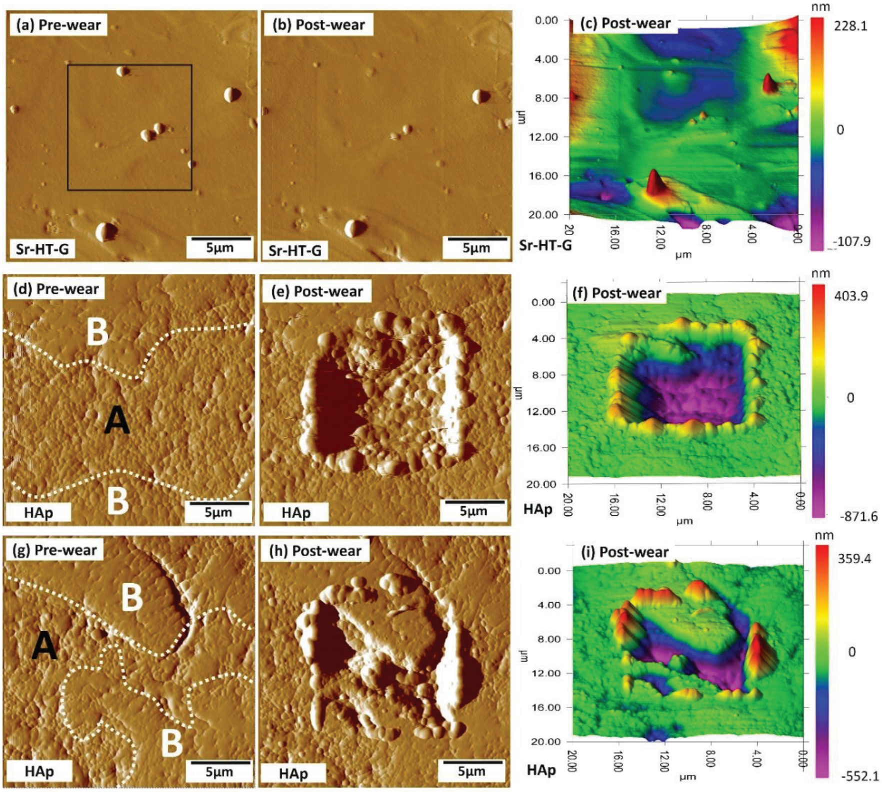

Figure 11. Nanowear test results of the Sr–HT–G coating (**a**–**c**) and the HAp coating (**d**–**i**).

3.4. Results of Stem Cell Culture

After cell culture for 24 h, BMSC adhered on all the substrates indicating a good biocompatibility, which can be seen in Figure 12a. Cell density on Ti substrates was relatively higher than samples of the Sr–HT–G coating and the HAp coating in Figure 12b. In addition, BMSCs have a relatively larger cell spread on Ti substrates than that of the Sr–HT–G and HAp coatings, which can be seen in Figure 12c. This strong cell attachment on the Ti substrate is related to the differences in surface roughness profiles; both coatings had similar and higher surface roughness than the Ti. The surface roughness (R_a) of the Sr–HT–G coating and the HAp coating were 13.7 ± 0.76 and 10.2 ± 0.7 µm, respectively; while the roughness of the as-receive Ti was about 0.1 µm. Nonetheless, the results indicate both coatings have good biocompatibility for BMSCs, in which the Sr–HT–G coating presented slightly higher cell density and spreading area of cell attachment compared to the HAp coating.

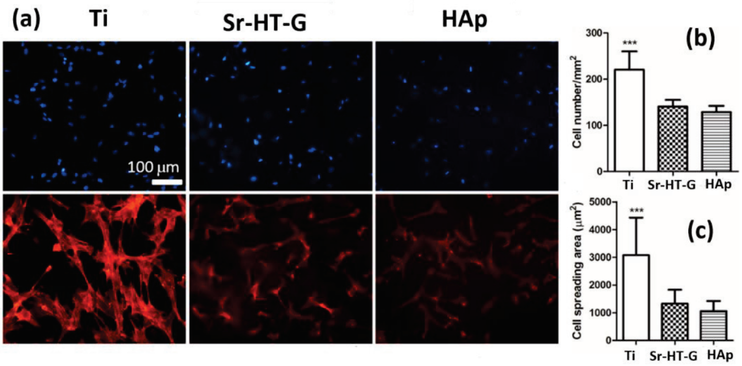

Figure 12. Biocompatibility tests of different substrates using bone marrow stem cells. (**a**) BMSC morphology on Ti, Sr–HT–G, and HAp surfaces. Cell nucleus (blue) and F-actin (red) were stained. (**b**) Cell density and (**c**) spreading area on various substrates. ** $p < 0.01$ and *** $p < 0.001$ compared to Sr–HT–G and HAp surfaces.

4. Conclusions

The deposition of Sr–HT–G powders onto Ti–6Al–4V as a novel coating via an atmospheric plasma spray technique has demonstrated significant improvement in mechanical properties compared with the current commercial relevant hydroxyapatite coating. The Sr–HT–G coating showed more uniform microstructures with consistent distributions of hardness, elastic moduli, compared to the HAp coating. The as sprayed Sr–HT–G coating presented phases of Sr-HT and gahnite without formation of new phases. Vickers microhardness of the Sr–HT–G coating was significantly higher than results from the HAp coating; 330.4 ± 54.4 and 120.2 ± 24.3 HV300, respectively. Nanoindentation tests revealed consistent distributions of nanohardness and elastic moduli in the Sr–HT–G coating with the average values of 93.0 ± 16.6 and 7.2 ± 2.1 GPa for hardness and elastic moduli, respectively. On the contrary, the HAp coating showed lower and high variation in the distribution of hardness and elastic moduli, especially between the distinct areas of crystalline and amorphous phases. The nanohardness and elastic moduli of the HAp coating were 77.6 ± 41.5 and 4.4 ± 3.2 GPa, respectively. The Sr–HT–G coating also showed better resistance to scratch and wear compared to the HAp coating under the same tests. In addition, the Sr–HT–G coating presented slightly higher density and spreading area of cell attachment in contrast to the HAp coating, indicating that the Sr–HT–G coatings possess good biocompatibility with good attachment of bone marrow mesenchymal stem cells. This study indicates that atmospheric plasma sprayed Sr–HT–G can be a viable approach for orthopaedic implants.

Author Contributions: Conceptualization, A.S., H.Z., C.C.B. and A.S.M.A.; methodology, D.Q.P., A.S.M.A. and C.C.B.; software, D.Q.P. and Y.-P.W.; validation, C.C.B., A.S.M.A. and H.Z.; formal analysis, D.Q.P.; investigation, D.Q.P.; resources, A.S., D.Q.P. and A.S.M.A.; data curation, D.Q.P., A.S.M.A.; writing—original draft preparation, D.Q.P., P.-Y.W.; writing—review and editing, D.Q.P., A.S.M.A., C.C.B. and P.-Y.W.; visualization, D.Q.P., A.S.M.A.; supervision, A.S.M.A., C.C.B., H.Z.; project administration, A.S.M.A., C.C.B.; funding acquisition, A.S., H.Z. and C.C.B.

Funding: This research is funded by the Centre for Innovative BioEngineering under the Industrial Transformation Training Centre (ITTC) scheme via the Australian Research Council (ARC) Award IC170100022. PYW thanks the support from the National Key Research and Development Program of China (2018YFC1105201), the National Natural Science Foundation of China, and the International cooperative research project of Shenzhen collaborative innovation program (20180921173048123).

Acknowledgments: The authors also would like to thank Deming Zhu for his assistance in operating the XPS and Andrew Moore for expert assistance in the preparation of samples. We deeply appreciate Ping Du from SIAT who performed the biocompatibility test.

Conflicts of Interest: The authors declare no conflict of interest.

References

1. Wu, C.; Chang, J. A review of bioactive silicate ceramics. *Biomed. Mater.* **2013**, *8*, 032001. [CrossRef] [PubMed]
2. Park, J.B.; Bronzino, J.D. *Biomaterials: Principles and Applications*; CRC Press: Boca Raton, FL, USA, 2002. [CrossRef]
3. Dorozhkin, S.V.; Epple, M. Biological and medical significance of calcium phosphates. *Angew. Chem. Int. Ed.* **2002**, *41*, 3130–3146. [CrossRef]
4. Sun, L.; Berndt, C.C.; Gross, K.A.; Kucuk, A. Material fundamentals and clinical performance of plasma-sprayed hydroxyapatite coatings: A review. *J. Biomed. Mater. Res.* **2001**, *58*, 570–592. [CrossRef] [PubMed]
5. Hench, L.L. Biomaterials: A forecast for the future. *Biomaterials* **1998**, *19*, 1419–1423. [CrossRef]
6. Berndt, C.; Haddad, G.; Farmer, A.; Gross, K.A. Thermal spraying for bioceramic applications. *Mater. Forum.* **1990**, *14*, 161–173.
7. Dorozhkin, S.V. Bioceramics of calcium orthophosphates. *Biomaterials* **2010**, *31*, 1465–1485. [CrossRef]
8. Yao, H.-L.; Zou, Y.-L.; Bai, X.-B.; Wang, H.-T.; Ji, G.-C.; Chen, Q.-Y. Microstructures, mechanical properties and electrochemical behaviors of nano-structured HA/Ti composite coatings deposited by high-velocity suspension flame spray (HVSFS). *Ceram. Int.* **2018**, *44*, 13024–13030. [CrossRef]
9. Chen, X.; Zhang, B.; Gong, Y.; Zhou, P.; Li, H. Mechanical properties of nanodiamond-reinforced hydroxyapatite composite coatings deposited by suspension plasma spraying. *Appl. Surf. Sci.* **2018**, *439*, 60–65. [CrossRef]
10. Rauch, J.; Bolelli, G.; Killinger, A.; Gadow, R.; Cannillo, V.; Lusvarghi, L. Advances in high velocity suspension flame spraying (HVSFS). *Surf. Coat. Technol.* **2009**, *203*, 2131–2138. [CrossRef]
11. Tucker, R.C., Jr. *ASM Handbook, Volume 05A—Thermal Spray Technology*; ASM International: Materials Park, OH, USA, 2013. [CrossRef]
12. Sun, L. Thermal spray coatings on orthopedic devices: When and how the FDA reviews your coatings. *J. Therm. Spray Technol.* **2018**, *27*, 1280–1290. [CrossRef]
13. Schwarz, K. A bound form of silicon in glycosaminoglycans and polyuronides. *Proc. Natl. Acad. Sci. USA* **1973**, *70*, 1608–1612. [CrossRef] [PubMed]
14. Carlisle, E.M. Silicon: A possible factor in bone calcification. *Science* **1970**, *167*, 279. [CrossRef] [PubMed]
15. Hench, L.L. Bioceramics: From concept to clinic. *J. Am. Ceram. Soc.* **1991**, *74*, 1487–1510. [CrossRef]
16. Abe, Y.; Kokubo, T.; Yamamuro, T. Apatite coating on ceramics, metals and polymers utilizing a biological process. *J. Mater. Sci. Mater. Med.* **1990**, *1*, 233–238. [CrossRef]
17. Liu, X.; Tao, S.; Ding, C. Bioactivity of plasma sprayed dicalcium silicate coatings. *Biomaterials* **2002**, *23*, 963–968. [CrossRef]
18. Ni, S.; Chang, J.; Chou, L.; Zhai, W. Comparison of osteoblast-like cell responses to calcium silicate and tricalcium phosphate ceramics in vitro. *J. Biomed. Mater. Res. Part B Appl. Biomater.* **2007**, *80*, 174–183. [CrossRef]
19. Zreiqat, H.; Ramaswamy, Y.; Wu, C.; Paschalidis, A.; Lu, Z.; James, B.; Birke, O.; McDonald, M.; Little, D.; Dunstan, C.R. The incorporation of strontium and zinc into a calcium–silicon ceramic for bone tissue engineering. *Biomaterials* **2010**, *31*, 3175–3184. [CrossRef]
20. Iimori, Y.; Kameshima, Y.; Okada, K.; Hayashi, S. Comparative study of apatite formation on $CaSiO_3$ ceramics in simulated body fluids with different carbonate concentrations. *J. Mater. Sci. Mater. Med.* **2005**, *16*, 73–79. [CrossRef]
21. Wu, C.; Chang, J.; Zhai, W. A novel hardystonite bioceramic: Preparation and characteristics. *Ceram. Int.* **2005**, *31*, 27–31. [CrossRef]
22. Roohani-Esfahani, S.I.; Dunstan, C.R.; Li, J.J.; Lu, Z.; Davies, B.; Pearce, S.; Field, J.; Williams, R.; Zreiqat, H. Unique microstructural design of ceramic scaffolds for bone regeneration under load. *Acta Biomater.* **2013**, *9*, 7014–7024. [CrossRef]
23. Wang, G.; Roohani-Esfahani, S.-I.; Zhang, W.; Lv, K.; Yang, G.; Ding, X.; Zou, D.; Cui, D.; Zreiqat, H.; Jiang, X. Effects of Sr-HT-Gahnite on osteogenesis and angiogenesis by adipose derived stem cells for critical-sized calvarial defect repair. *Sci. Rep.* **2017**, *7*, 41135. [CrossRef] [PubMed]

24. Li, J.J.; Dunstan, C.R.; Entezari, A.; Li, Q.; Steck, R.; Saifzadeh, S.; Sadeghpour, A.; Field, J.R.; Akey, A.; Vielreicher, M.; et al. A novel bone substitute with high bioactivity, strength, and porosity for repairing large and load-bearing bone defects. *Adv. Healthc. Mater.* **2019**, *8*, e1801298. [CrossRef] [PubMed]
25. Sun, L.; Berndt, C.C.; Grey, C.P. Phase, structural and microstructural investigations of plasma sprayed hydroxyapatite coatings. *Mater. Sci. Eng. A* **2003**, *360*, 70–84. [CrossRef]
26. ASTM-E1920-03. *Standard Guide for Metallographic Preparation of Thermal Sprayed Coatings*; ASTM International: West Conshohocken, PA, USA, 2014.
27. Pham, D.Q.; Berndt, C.C.; Gbureck, U.; Zreiqat, H.; Truong, V.K.; Ang, A.S.M. Mechanical and chemical properties of Baghdadite coatings manufactured by atmospheric plasma spraying. *Surf. Coat. Technol.* **2019**, *378*, 124945. [CrossRef]
28. Oliver, W.C.; Pharr, G.M. An improved technique for determining hardness and elastic modulus using load and displacement sensing indentation experiments. *J. Mater. Res.* **1992**, *7*, 1564–1583. [CrossRef]
29. Berndt, C.C.; Hasan, F.; Tietz, U.; Schmitz, K.P. A review of hydroxyapatite coatings manufactured by thermal spray. In *Advances in Calcium Phosphate Biomaterials*; Ben-Nissan, B., Ed.; Springer: Berlin/Heidelberg, Germany, 2014; pp. 267–329. [CrossRef]
30. Gross, K.A.; Berndt, C.C.; Herman, H. Amorphous phase formation in plasma-sprayed hydroxyapatite coatings. *J. Biomed. Mater. Res.* **1998**, *39*, 407–414. [CrossRef]
31. Najafinezhad, A.; Abdellahi, M.; Ghayour, H.; Soheily, A.; Chami, A.; Khandan, A. A comparative study on the synthesis mechanism, bioactivity and mechanical properties of three silicate bioceramics. *Mater. Sci. Eng. C* **2017**, *72*, 259–267. [CrossRef]
32. Levingstone, T.J.; Ardhaoui, M.; Benyounis, K.; Looney, L.; Stokes, J.T. Plasma sprayed hydroxyapatite coatings: Understanding process relationships using design of experiment analysis. *Surf. Coat. Technol.* **2015**, *283*, 29–36. [CrossRef]
33. Strohmeier, B.R. Zinc Aluminate ($ZnAl_2O_4$) by XPS. *Surf. Sci. Spectra* **1994**, *3*, 128–134. [CrossRef]
34. Strohmeier, B.R.; Hercules, D.M. Surface spectroscopic characterization of the interaction between zinc ions and γ-alumina. *J. Catal.* **1984**, *86*, 266–279. [CrossRef]
35. Moulder, J.F.; Stickle, W.F.; Sobol, P.E. *Handbook of X-ray Photoelectron Spectroscopy: A Reference Book of Standard Spectra for Identification and Interpretation of XPS Data*; Physical Electronics, Inc.: Eden Prairie, MN, USA, 1995.
36. Zreiqat, H.; Roohani-Esfahani, S.-I.; Dunstan, C.; Li, J.J. Biocompatible Material and Uses Thereof. U.S. Patent No. US 9,220,806 B2, 29 December 2015.
37. Demri, B.; Muster, D. XPS study of some calcium compounds. *J. Mater. Process. Technol.* **1995**, *55*, 311–314. [CrossRef]
38. Ang, A.S.M.; Berndt, C.C. A review of testing methods for thermal spray coatings. *Int. Mater. Rev.* **2014**, *59*, 179–223. [CrossRef]
39. Madejski, J. Solidification of droplets on a cold surface. *Int. J. Heat Mass Transf.* **1976**, *19*, 1009–1013. [CrossRef]
40. Gross, K.A.; Saber-Samandari, S.; Heemann, K.S. Evaluation of commercial implants with nanoindentation defines future development needs for hydroxyapatite coatings. *J. Biomed. Mater. Res. Part B Appl. Biomater.* **2010**, *93*, 1–8. [CrossRef]
41. Lin, C.K.; Berndt, C.C. Statistical analysis of microhardness variations in thermal spray coatings. *J. Mater. Sci.* **1995**, *30*, 111–117. [CrossRef]
42. Deram, V.; Minichiello, C.; Vannier, R.N.; Le Maguer, A.; Pawlowski, L.; Murano, D. Microstructural characterizations of plasma sprayed hydroxyapatite coatings. *Surf. Coat. Technol.* **2003**, *166*, 153–159. [CrossRef]
43. De Grauw, C.; de Bruijn, J.; Otto, C.; Greve, J. Investigation of bone and calcium phosphate coatings and crystallinity determination using Raman microspectroscopy. *Cells Mater.* **1996**, *6*, 6.
44. Wen, J.; Leng, Y.; Chen, J.; Zhang, C. Chemical gradient in plasma-sprayed HA coatings. *Biomaterials* **2000**, *21*, 1339–1343. [CrossRef]

coatings

MDPI

Article

Facile Route of Fabricating Long-Term Microbicidal Silver Nanoparticle Clusters against Shiga Toxin-Producing *Escherichia coli* O157:H7 and *Candida auris*

Sheeana Gangadoo [1], Aaron Elbourne [1], Alexander E. Medvedev [2], Daniel Cozzolino [1], Yen B. Truong [3], Russell J. Crawford [1], Peng-Yuan Wang [4], Vi Khanh Truong [1,5,*] and James Chapman [1,*]

[1] Nanobiotechnology Lab, School of Science, RMIT University, Melbourne VIC 3001, Australia; sheeana.gangadoo@rmit.edu.au (S.G.); aaron.elbourne@rmit.edu.au (A.E.); daniel.cozzolino@rmit.edu.au (D.C.); russell.crawford@rmit.edu.au (R.J.C.)
[2] RMIT Centre for Additive Manufacturing, School of Engineering, RMIT University, Melbourne VIC 3001, Australia; alexander.medvedev@rmit.edu.au
[3] CSIRO Manufacturing, Bayview Avenue, Clayton, VIC 3169, Australia; Yen.Truong@csiro.au
[4] Institute of Biomedicine and Biotechnology, Shenzhen Institute of Advanced Technology, Shenzhen 518055, China; py.wang@siat.ac.cn
[5] Department of Chemical and Biomolecular Engineering North Carolina State University, Raleigh, NC 27695, USA
* Correspondence: vi.khanh.truong@rmit.edu.au (V.K.T.); james.chapman@rmit.edu.au (J.C.)

Received: 4 November 2019; Accepted: 17 December 2019; Published: 1 January 2020

Abstract: Microbial contamination remains a significant issue for many industrial, commercial, and medical applications. For instance, microbial surface contamination is detrimental to numerous aspects of food production, infection transfer, and even marine applications. As such, intense scientific interest has focused on improving the antimicrobial properties of surface coatings via both chemical and physical routes. However, there is a lack of synthetic coatings that possess long-term microbiocidal performance. In this study, silver nanoparticle cluster coatings were developed on copper surfaces via an ion-exchange and reduction reaction, followed by a silanization step. The durability of the microbiocidal activity for these develped surfaces was tested against pathogenic bacterial and fungal species, specifically *Escherichia coli* O157:H7 and *Candida auris*, over periods of 1- and 7-days. It was observed that more than 90% of *E. coli* and *C. auris* were found to be non-viable following the extended exposure times. This facile material fabrication presents as a new surface design for the production of durable microbicidal coatings which can be applied to numerous applications.

Keywords: copper nanoparticles; silver nanoparticles; nanostructure; nanocluster; antifungal; antibacterial; escherichia coli; candida auris

1. Introduction

The surface colonization of bacteria and fungi on abiotic substrates is commonly referred to as a biofilm formation and significantly contributes to healthcare and industrial concerns [1,2]. This issue is further impacted by the current rise in antibiotic resistance amongst microbial species, which has caused a significant increase in persistent infections and related deaths [3]. Recent economic projections have estimated that bacterial infections could be responsible for approximately 10 million deaths per annum by 2050 if new antimicrobial surface therapies are not developed [4,5].

In particular, *Escherichia coli (E. coli)* and *Candida auris (C. auris)* are common pathogenic microbes responsible for recent outbreaks [6,7]. Shiga toxin-producing *E. coli* (STEC) O157 has emerged as

Coatings **2020**, *10*, 28; doi:10.3390/coatings10010028

a public health threat following its initial identification as a pathogen in 1982, which was initiated when an outbreak of illness was associated with the consumption of undercooked ground beef [8]. A 2018 outbreak of the *E. coli* strain O157:H7 was reported across 36 states, infecting 210 people [6]. *C. auris* is another emerging pathogen currently responsible for invasive disease in healthcare facilities around the world [7,9] and the fungal infection carries an astonishingly high mortality rate of 60% among infected patients, representing a significant healthcare issue [7,9]. This high mortality rate has occurred due to the simultaneous emergence of multidrug-resistant *C. auris* isolates across three separate continents [9], raising pressing concerns regarding the identification and detection of invasive candidiasis isolates [10].

Silver nanoparticles (Ag NPs) are highly effective microbiocidal agents against both bacteria and fungi [11]. Ag NPs have been used in forms including solutions, thin-film coatings, or embedding in polymers [12–14]. While there have been some reported cases in which bacteria and fungi were found to be resistant against Ag NPs [15,16], recent reviews have shown alternative ways in eradicating bacterial cells via mechanical rupturing with nanostructure modifications [13,17–19]. There is a lack of significant research within the ability of these nanostructures to rupture fungal cells, in particular with the combination of Ag NPs and nanostructures not implemented as treatment strategies towards both bacterial and fungal cell surfaces.

In this work, a facile route was used to fabricate Ag NPs coatings on copper (Cu) surfaces, in which Ag NPs would assemble into high-aspect-ratio clusters. These surfaces were assessed for their long-term microbiocidal activity against both Shiga toxin-producing *E. coli* and *C. auris* cells. The fabricated surfaces present a new direction in the design of durable microbicidal surface coatings.

2. Materials and Methods

2.1. Fabrication of Hydrophobized Ag NP Coatings on Cu Surfaces

Cu surfaces were cut into 2 × 2 cm^2 squares, pre-cleaned, and washed with HCl (Merck Pty Ltd, VIC, Australia) and MilliQ water (Synergy®UV Millipak Express 20, Merck Pty Ltd, VIC, Australia). The surfaces were then submerged with 0.1 M $AgNO_3$ for 5 min, where Ag NPs formed on the Cu surface via a series of reduction–oxidation reactions. Surfaces were again washed carefully with MilliQ water, then with 100% ethanol (Merck Pty Ltd, VIC, Australia), and with MilliQ water as a last wash, and were blown dry with compressed nitrogen. This study adopted the fabrication method used in the previous work [20]. The Cu surfaces were further submerged with 0.1 M dichloromethyl silane (Sigma–Aldrich, Castle. Hill, NSW, Australia) in dichloromethane (Sigma–Aldrich Pty Ltd, NSW, Australia) for 15 min and were then washed with ethanol and MilliQ water to remove all chemical residues. In this study, pristine 'copper surfaces' are noted as 'Cu surfaces' and 'silver nanoparticles embedding on copper surfaces' were noted as 'Ag NPs-Cu surfaces'.ImageJ version 1.8.0 (https://imagej.nih.gov/ij/) was implemented to analyze SEM images. Color Threshold and Analyze Particles Plugins were used to determine the dimensions of non-spherical Ag NPs. A total of 90 data points per system were used over three SEM micrographs to determine the distribution of NP clusters.

2.2. Bacterial Strains, Growth Conditions, and Sample Preparation

The antimicrobial efficacy of the surfaces was investigated using the strains *E. coli* O157:H7 and *C. auris,* which were obtained from the American Type Culture Collection and SA Pathology Lab, respectively, and were chosen as representatives of two major emerging pathogen outbreaks. The *E. coli* bacterial cultures were grown on Luria–Bertani (LB) agar (BD Difco, VIC, Australia) and fungal *C. auris* cultures were grown on Potato Dextrose Agar (PDA) (Sigma-Aldrich Pty Ltd, NSW, Australia) overnight at 37 °C. Bacterial and fungal cells were collected at the logarithmic stage of growth. To determine similar numbers of cells, despite variations in cell densities following collection, the density of the bacterial and fungal suspensions was adjusted to OD 600 = 0.1 at the logarithmic stage of cell growth. To quantify cell numbers in the adjusted bacterial suspensions before attachment experiments, a hemocytometer was used as suggested previously [21]. Pristine Cu and Ag NPs-Cu surfaces were cut into squares of 0.5 × 0.5 cm^2. The surfaces were pre-sterilized with 70% ethanol, dried within a sterilized laminar flow cabinet for 24 h and placed in a sterilized 24-well plates (Thermo Fischer Scientific Australia Pty Ltd, VIC, Australia). Bacterial and fungal suspensions were prepared as above with $OD_{600} = 0.1$ and 1 ml of each suspension was added into 24-well plates containing the sterilized surfaces. The plates were incubated at 25 °C in dark conditions, to avoid any effects of light on cell viability. The samples were incubated in static conditions for 1 and 7 days without any disturbance from media addition or exchange. This procedure was adopted to avoid any effects of fresh media and shaking on antimicrobial assays. Two technical replicates were done.

2.3. Confocal Laser Scanning Microscopy (CLSM)

The surfaces were washed with 10 mM PBS (pH = 7.4) prior to the CLSM imaging conducted using ZEISS LSM 880 Airyscan upright microscope (Zeiss, Oberkochen, BW, Germany). To assess their viability, adhered cells were stained using a LIVE/DEAD® BacLight™ Viability Kit (including SYTO® 9 and propidium iodide) (Molecular Probes™, Invitrogen, Grand Island, NY, USA). In this kit, SYTO® 9 binds to nucleic acids in both intact and damaged cells, while propidium iodide (PI) predominantly enters cells with a damaged membrane considered non-viable. The bacterial and fungal cells on surfaces were stained according to the manufacturer's protocol [22]. The proportions of live and dead cells on pristine Cu and Ag NPs-Cu surfaces were then evaluated using a ZEISS LSM 880 Airyscan upright microscope (Zeiss, Oberkochen, BW, Germany). To determine the percentage of non-viable cells, CellC Cell Counting Software (https://sites.google.com/site/cellcsoftware/) was used as previously instructed [19]. An analysis was done over 5 representative micrographs over 2 technical replicates. A student *t*-test (Microsoft Excel) was conducted to compare the antimicrobial performance of these samples.

2.4. SEM Characterization

Prior to the SEM imaging, bacterial and fungal cells on Cu and Ag NPs-Cu surfaces were fixed using 3% glutaraldehyde and were dehydrated using a series of ethanol concentrations (30%, 50%, 70%, 80%, 90%, 100%). The samples were removed and dried under the laminar flow of a Biosafety Cabinet Class II for 2–4 h. Fixed cells were coated with a thin film of gold prior to imaging. SEM images were taken using a field-emission scanning electron microscope (FE-SEM) (FEI Verios, FEI company, OR, United States) at 5 kV, where imaging of the systems uses methods that have been previously described [23].

2.5. Focussed Ion Beam-Scanning Electron Microscopy (FIB-SEM) Characterization

Surfaces were affixed and dehydrated using the identical dehydration steps described above. A cross-sectional analysis was carried out to show the interaction of *E. coli* and *C. auris* with the Ag NP cluster substrates was performed using a FEI Scios Dualbeam FIB-SEM. The cells were first coated with platinum (Pt) using an ion gun at 16 kV/0.15 nA to prevent further damage, followed by a sequential ion slicing at 16 kV/0.15 nA. The imaging was carried out using a standard secondary electron (ETD) and upper in-lens column (T2) detectors at 2 kV/0.1 nA.

3. Results

3.1. Fabrication and Characterisation of Hydrophobized Ag NP-Coated Cu Surfaces

Ag NP clusters were fabricated directly onto Cu surfaces via a single-step electrochemical synthesis. A further surface silanization step was added to create a hydrophobic Ag NP cluster on the Cu surfaces. The fabricated Ag NPs-Cu surfaces were then characterized using SEM and energy dispersive X-ray (EDX) spectroscopy. In Figure 1A,B, the SEM micrographs show that the Ag NPs exhibit sizes that are consistently less than 100 nm in diameter. These Ag NPs were found to form clusters, with wide sizes ranging from 70 nm to 1200 nm and an average size of ~350 nm per cluster. The aspect-ratio of the clusters was estimated using the ratio of length (nm) to width (nm). This measurement revealed that the clusters possess an aspect-ratio (length/width) ranging from 1 to 14. With the addition of silane to the clusters, the surfaces exhibit water contact angles of ~120°, meaning that the surfaces are hydrophobic in nature. Silane coatings are well-known corrosion-inhibitors [24] and therefore provide a strong potential in preventing the corrosion of Ag–Cu surfaces. In Figure 1C, chemical mapping using Energy Dispersive X-ray Analysis (EDX) revealed that the Ag NPs are formed via replacing Cu(0) using a series of electroless galvanic reactions (see Equations (1) and (2)) [25,26]:

$$\text{Red: } -2\text{Ag}^{+} + 2\text{e}^{-} \rightarrow 2\text{Ag}^{0} \tag{1}$$

$$\text{Ox: Cu} \rightarrow \text{Cu}^{2+} + 2\text{e}^{-} \tag{2}$$

Galvanic replacement reactions are commonly known to produce Ag NPs via this route [27,28]. Importantly, low level of oxidation was detected on the Ag NPs-Cu surfaces. Therefore we provide a simple method to fabricate Ag NP clusters which have demonstrated several advantages: simplicity, facility, and a low fabrication cost. This galvanic replacement reaction method can be used on an industrial scale, which highlights the utility of this synthetic route [29].

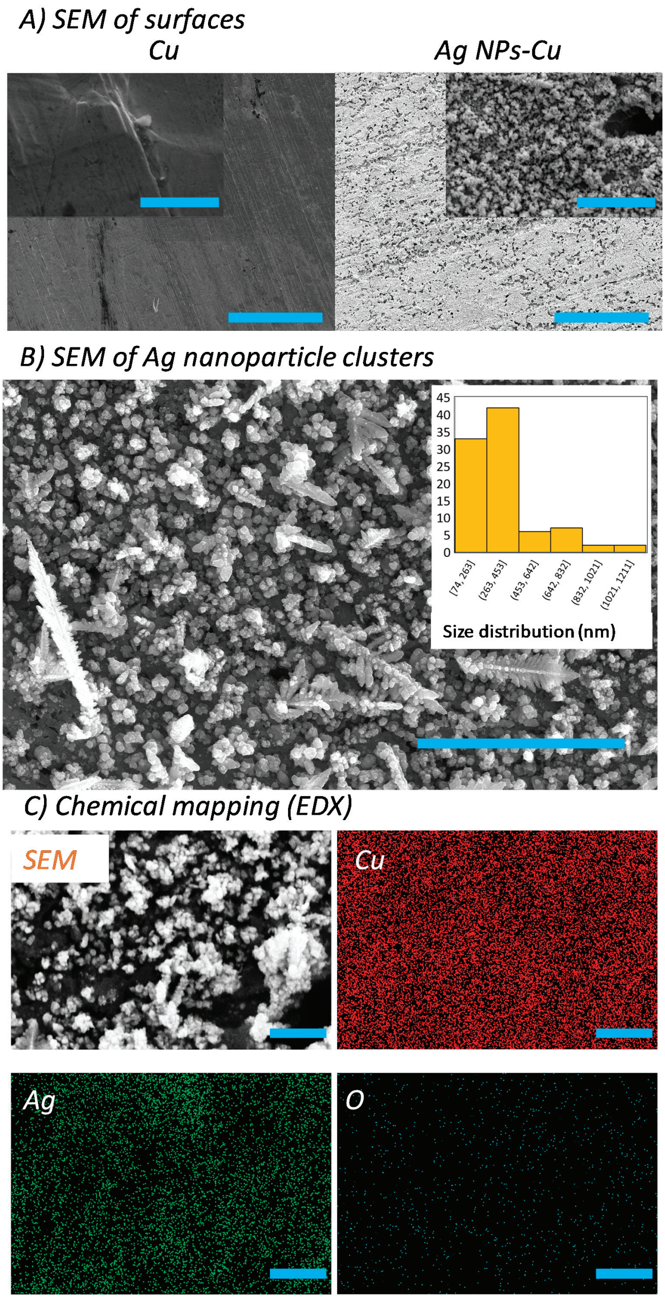

Figure 1. Surface characterization of pristine Cu and Ag nanoparticle coatings (Ag NPs-Cu). (**A**) SEM images showing the surface topography of pristine Cu (left) and Ag NPs-Cu (right) surfaces (Scale bar 20 µm, inset 3 µm). (**B**) High resolution SEM image showing Ag NPs cluster domains (scale bar 4 µm). The inset shows the cluster size distribution. (**C**) EDX spectroscopy showing the distribution of Cu, Ag, and O elements across the Ag NPs-Cu surfaces (scale bar 1 µm).

3.2. Microbicidal Performance of Ag NPs-Cu Surfaces over 1- and 7-day Incubations

Two representative species of major global disease outbreaks in recent years, Shiga toxin-producing *E. coli* O157:H7 and *C. auris*, were selected to study the relative material and surface interactions, with the use of glass surfaces employed as control substrates (Figures S1 and S2). The data in this study reveal the native cell morphology and viability of the respective bacterial and fungal pathogens incubated on both pristine and Ag NPs-Cu surfaces for periods of 1 and 7 days. To assess their viability, LIVE/DEAD Fluorescent Kits (Molecular Probes$^{\mathrm{TM}}$, Invitrogen, Grand Island, NY, USA) were used to stain the viable and non-viable cells [22]. SYTO® 9 dye enter the viable cells and propidium iodide would enter the non-viable cells with compromised cell membranes. Control glass surfaces demonstrated over 90% cell viability for both *E. coli* and *C. auris* over a 7-day incubation (Figure S2) while pristine Cu surfaces showed slight killing activity against the cells as shown in Figure 1, despite the inherent antimicrobial activity native of Cu surfaces. *E. coli* specifically formed a well-established biofilm on the pristine Cu surfaces. In comparison, Ag NPs-Cu surfaces inhibited the growth of *E. coli* and *C. auris* (Figure 2), with 75% and 98% of non-viability observed respectively, after a 1-day incubation only. Greater results were obtained after a 7-day incubation on the Ag NPs-Cu surfaces with more than 90% and ~100% non-viability observed for *E. coli* and *C. auris* respectively. Further investigation of the interactions between bacteria/fungi and Ag NP clusters was carried out using FIB-SEM and clear deformations of *E. coli* and *C. auris* were examined and shown by tearing of the cell membrane and presence of multiple hole features in the cell morphology, as shown in Figure 3A,B. Past studies have reported similar examinations [18,30].

The antimicrobial behavior of Ag NPs is known to occur via several mechanisms: (1) physical damage by direct contact [31], (2) the release of silver ions [32,33], and (3) reactive oxygen species production [34,35]. The breadth of information concerning the antibacterial mechanism of Ag NPs is beyond the scope of this article; however, the interested reader is directed towards several important reviews in the field [11,34]. In previous work, Ag NPs have been reported as effective antimicrobial agents against both bacteria (*E. coli* and *Staphylococcus aureus*) and fungi (e.g., *Candida albicans*) [11,12,16,36], but past investigations have failed in showing the long-term effect of silver coatings against both bacteria and fungi over a 7-day incubation, as shown in this study. Furthermore, this study is the first showing the effects of antifungal coating towards *C. auris*. There are a number of studies demonstrating that high-aspect-ratio nanostructures can be used to capture bacteria and disrupt bacterial membranes [18,37–40]. Surface nanostructures have been considered to be "promising methods" to stop bacterial adhesion and proliferation; still, there are a number of questions that should be answered before being applied in the actual environments [41]. However, the synergy between both surface nanostructure and chemistry should be considered to be the good candidate in the development of antimicrobial approaches.

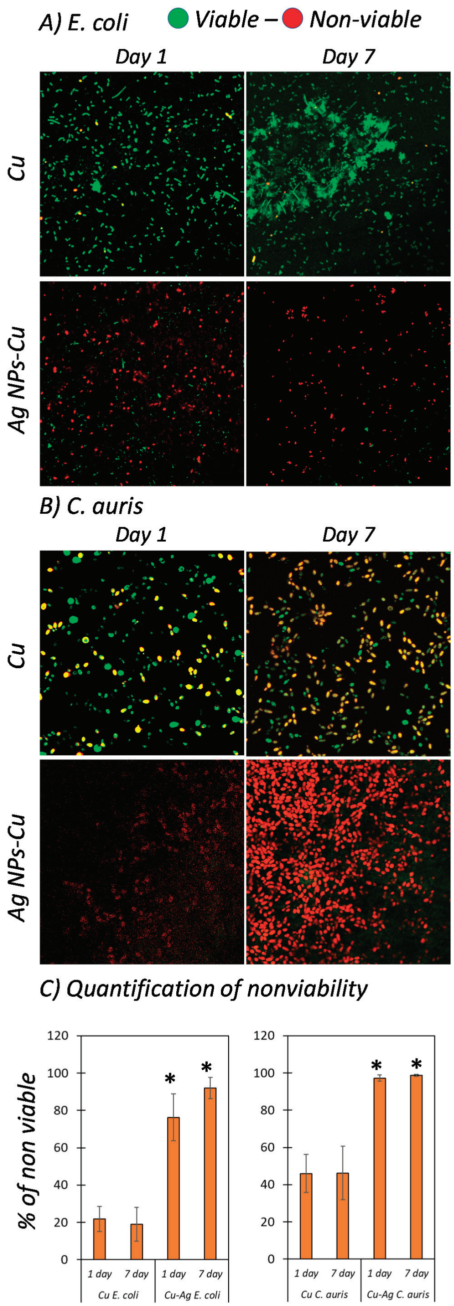

Figure 2. Assessment of Shiga-toxin-producing *E. coli* O157:H7 and *C. auris* on copper and Ag NPs-Cu surfaces over 1- and 7-day incubations. CSLM micrographs showing the viability of (**A**) *E. coli* and (**B**) *C. auris* on pristine Cu and Ag NPs-Cu surfaces (green indicating viable cells; and red indicating non-viable cells). CLSM images are 150 µm × 150 µm. (**C**) Quantification of cell viability on Cu and Ag NPs-Cu (* indicating $p < 0.05$ comparing with Cu surfaces on day 1 and 7, respectively, $n = 10$).

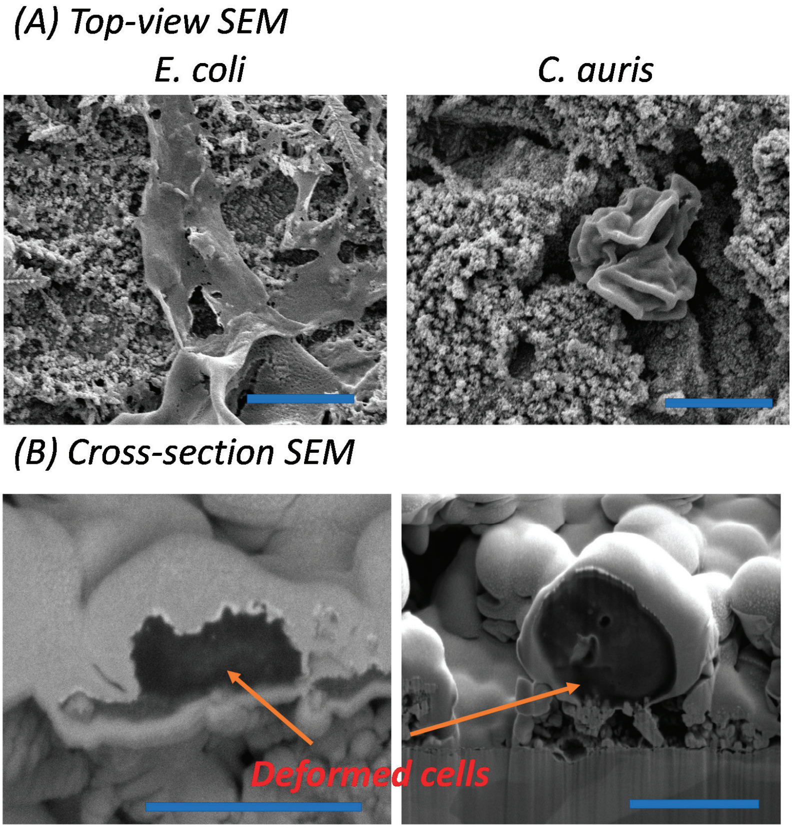

Figure 3. Morphology of *E. coli* and *C. auris* on control and Ag NPs-Cu surfaces (Scale bar 5 µm). (**A**) Top-view SEM micrographs showing the cell deformation under the Ag NP clusters (scale bar 5 µm). (**B**) SEM cross-sections using FIB-SEM reveal the interfacial interaction between cell surfaces and nanostructures (left scale bar 1 µm; right scale bar 4 µm).

4. Conclusions

Both *E. coli* and *C. auris* have been reported to be the main cause of recent outbreaks of disease. These two microbes were chosen to investigate the antimicrobial activity of durable Ag NP cluster coated Cu surfaces. Microbiocidal composite Ag NP cluster–Cu coatings were fabricated via an ion-exchange reduction reaction. The durability of microbicidal efficacy of the surfaces was established against pathogenic fungal and bacterial species, specifically *E. coli* O157:H7 and *C. auris*, over exposure periods of 1 and 7 days. It was observed that more than ~90% of *E. coli* and ~100% *C. auris* were non-viable, after only 7 days of surface immersion. The surfaces reported in this study provide a facile fabrication route and a new design parameter to produce durable microbicidal coatings for numerous applications.

Supplementary Materials: The following are available online at http://www.mdpi.com/2079-6412/10/1/28/s1, Figure S1: Scanning electron micrographs of *E. coli* and *C. auris* on glass surfaces (scale bar 2 µm). The morphology of *E. coli* and *C. auris* were found to be intact and no damage on glass substrates, Figure S2: Confocal scanning laser microscopic images of *E. coli* and *C. auris* on glass surfaces (scale bar 10 µm). Most of the cells were found to be viable on glass substrates.

Author Contributions: For research articles with several authors, a short paragraph specifying their individual contributions must be provided. The following statements should be used "conceptualization, V.K.T. and J.C.;

methodology, S.G., A.E., A.E.M., D.C., Y.B.T., R.J.C., P.W., V.K.T., J.C.; formal analysis, S.G., A.E.M., V.K.T., J.C.; writing—original draft preparation, S.G., A.E., V.K.T., J.C.; writing—review and editing, S.G., A.E., A.E.M., D.C., Y.B.T., R.J.C., P.W., V.K.T., J.C.; supervision, V.K.T., J.C. All authors have read and agreed to the published version of the manuscript.

Funding: The work is supported by the School of Science, RMIT University.

Acknowledgments: The authors thank both the Microscopy and Microanalysis Facility (RMMF) and the MicroNano Research Facility (MNRF) at RMIT University for the use of their facilities.

Conflicts of Interest: The authors declare no conflict of interest.

References

1. Lewis, K. Riddle of biofilm resistance. *Antimicrob. Agents Chemother.* **2001**, *45*, 999–1007. [CrossRef] [PubMed]
2. Flemming, H.-C.; Wingender, J. The biofilm matrix. *Nat. Rev. Microbiol.* **2010**, *8*, 623–633. [CrossRef] [PubMed]
3. Rodvold, K.A.; McConeghy, K.W. Methicillin-resistant *staphylococcus aureus* therapy: Past, present, and future. *Clin. Infect. Dis.* **2014**, *58*, S20–S27. [CrossRef] [PubMed]
4. Humphreys, G.; Fleck, F. United Nations Meeting on Antimicrobial Resistance. *World Health Organ. Bull. World Health Organ.* **2016**, *94*, 638.
5. O'Neill, J. *Tackling Drug-Resistant Infections Globally: Final Report and Recommendations*; HM Government: London, UK; Welcome Trust: London, UK, 2016.
6. CDC. *Multistate Outbreak of e. Coli o157:H7 Infections Linked to Chopped Romaine Lettuce*; US Centers for Disease Control and Prevention (CDC): Atlanta, GA, USA, 2018.
7. Nett, J.E. *Candida auris*: An emerging pathogen "incognito"? *PLoS Pathog.* **2019**, *15*, e1007638. [CrossRef] [PubMed]
8. Riley, L.W.; Remis, R.S.; Helgerson, S.D.; McGee, H.B.; Wells, J.G.; Davis, B.R.; Hebert, R.J.; Olcott, E.S.; Johnson, L.M.; Hargrett, N.T. Hemorrhagic colitis associated with a rare *Escherichia coli* serotype. *N. Engl. J. Med.* **1983**, *308*, 681–685. [CrossRef] [PubMed]
9. Lockhart, S.R.; Etienne, K.A.; Vallabhaneni, S.; Farooqi, J.; Chowdhary, A.; Govender, N.P.; Colombo, A.L.; Calvo, B.; Cuomo, C.A.; Desjardins, C.A. Simultaneous emergence of multidrug-resistant *candida auris* on 3 continents confirmed by whole-genome sequencing and epidemiological analyses. *J. Clin. Infect. Dis.* **2016**, *64*, 134–140. [CrossRef]
10. Lockhart, S.R.; Jackson, B.R.; Vallabhaneni, S.; Ostrosky-Zeichner, L.; Pappas, P.G.; Chiller, T. Thinking beyond the common *candida* species: Need for species-level identification of *candida* due to the emergence of multidrug-resistant *candida auris*. *J. Clin. Microbiol.* **2017**, *55*, 3324–3327. [CrossRef]
11. Prabhu, S.; Poulose, E.K. Silver nanoparticles: Mechanism of antimicrobial action, synthesis, medical applications, and toxicity effects. *Int. Nano Lett.* **2012**, *2*, 32. [CrossRef]
12. Petica, A.; Gavriliu, S.; Lungu, M.; Buruntea, N.; Panzaru, C. Colloidal silver solutions with antimicrobial properties. *Mater. Sci. Eng. B* **2008**, *152*, 22–27. [CrossRef]
13. Elbourne, A.; Truong, V.K.; Cheeseman, S.; Rajapaksha, P.; Gangadoo, S.; Chapman, J.; Crawford, R.J. The use of nanomaterials for the mitigation of pathogenic biofilm formation. In *Methods in Microbiology*; Academic Press: Cambridge, MA, USA, 2019.
14. Qing, Y.; Cheng, L.; Li, R.; Liu, G.; Zhang, Y.; Tang, X.; Wang, J.; Liu, H.; Qin, Y. Potential antibacterial mechanism of silver nanoparticles and the optimization of orthopedic implants by advanced modification technologies. *Int. J. Nanomed.* **2018**, *13*, 3311–3327. [CrossRef] [PubMed]
15. Panáček, A.; Kvítek, L.; Smékalová, M.; Večeřová, R.; Kolář, M.; Röderová, M.; Dyčka, F.; Šebela, M.; Prucek, R.; Tomanec, O.; et al. Bacterial resistance to silver nanoparticles and how to overcome it. *Nat. Nanotechnol.* **2018**, *13*, 65–71. [CrossRef] [PubMed]
16. Graves, J.L.; Tajkarimi, M.; Cunningham, Q.; Campbell, A.; Nonga, H.; Harrison, S.H.; Barrick, J.E. Rapid evolution of silver nanoparticle resistance in *escherichia coli*. *Front. Genet.* **2015**, *6*, 42. [CrossRef] [PubMed]
17. Lin, N.; Berton, P.; Moraes, C.; Rogers, R.D.; Tufenkji, N. Nanodarts, nanoblades, and nanospikes: Mechano-bactericidal nanostructures and where to find them. *Adv. Colloid Interface Sci.* **2018**, *252*, 55–68. [CrossRef] [PubMed]

18. Elbourne, A.; Chapman, J.; Gelmi, A.; Cozzolino, D.; Crawford, R.J.; Khanh Truong, V. Bacterial-nanostructure interactions: The role of cell elasticity and adhesion forces. *J. Colloid Interface Sci.* **2019**, *546*, 192–210. [CrossRef] [PubMed]
19. Rajapaksha, P.; Cheeseman, S.; Hombsch, S.; Murdoch, B.J.; Gangadoo, S.; Blanch, E.W.; Truong, Y.B.; Cozzolino, D.; McConville, C.F.; Crawford, R.J.; et al. Antibacterial properties of graphene oxide-copper oxide nanoparticle nanocomposites. *ACS Appl. Biol. Mater.* **2019**, *2*, 5687–5696. [CrossRef]
20. Chapman, J.; Regan, F. Nanofunctionalized superhydrophobic antifouling coatings for environmental sensor applications—Advancing deployment with answers from nature. *Adv. Eng. Mater.* **2012**, *14*, B175–B184. [CrossRef]
21. Liu, S. Chapter 11—How cells grow. In *Bioprocess Engineering*, 2nd ed.; Liu, S., Ed.; Elsevier: Amsterdam, The Netherlands, 2017; pp. 629–697.
22. Berney, M.; Hammes, F.; Bosshard, F.; Weilenmann, H.-U.; Egli, T. Assessment and interpretation of bacterial viability by using the live/dead baclight kit in combination with flow cytometry. *Appl. Environ. Microbiol.* **2007**, *73*, 3283. [CrossRef]
23. Truong, V.K.; Lapovok, R.; Estrin, Y.S.; Rundell, S.; Wang, J.Y.; Fluke, C.J.; Crawford, R.J.; Ivanova, E.P. The influence of nano-scale surface roughness on bacterial adhesion to ultrafine-grained titanium. *Biomaterials* **2010**, *31*, 3674–3683. [CrossRef]
24. Child, T.F.; van Ooij, W.J. Application of silane technology to prevent corrosion of metals and improve paint adhesion. *Trans. IMF* **1999**, *77*, 64–70. [CrossRef]
25. He, X.; He, R.; Lan, Q.; Duan, F.; Xiao, J.; Song, M.; Zhang, M.; Chen, Y.; Li, Y. A facile fabrication of silver-coated copper nanowires by galvanic replacement. *J. Nanomater.* **2016**, *2016*, 8. [CrossRef]
26. Chen, X.; Ku, S.; Weibel, J.A.; Ximenes, E.; Liu, X.; Ladisch, M.; Garimella, S.V. Enhanced antimicrobial efficacy of bimetallic porous cuo microspheres decorated with ag nanoparticles. *ACS Appl. Mater. Interfaces* **2017**, *9*, 39165–39173. [CrossRef] [PubMed]
27. Brevnov, D.A.; Olson, T.S.; López, G.P.; Atanassov, P. Electroless deposition of silver by galvanic displacement on aluminum alloyed with copper. *J. Phys. Chem. B* **2004**, *108*, 17531–17536. [CrossRef]
28. Chee, S.W.; Tan, S.F.; Baraissov, Z.; Bosman, M.; Mirsaidov, U. Direct observation of the nanoscale kirkendall effect during galvanic replacement reactions. *Nat. Commun.* **2017**, *8*, 1224. [CrossRef]
29. da Silva, A.G.M.; Rodrigues, T.S.; Haigh, S.J.; Camargo, P.H.C. Galvanic replacement reaction: Recent developments for engineering metal nanostructures towards catalytic applications. *Chem. Commun.* **2017**, *53*, 7135–7148. [CrossRef]
30. Rajapaksha, P.; Elbourne, A.; Gangadoo, S.; Brown, R.; Cozzolino, D.; Chapman, J. A review of methods for the detection of pathogenic microorganisms. *Analyst* **2019**, *144*, 396–411. [CrossRef]
31. Chatterjee, T.; Chatterjee, B.K.; Majumdar, D.; Chakrabarti, P. Antibacterial effect of silver nanoparticles and the modeling of bacterial growth kinetics using a modified gompertz model. *Biochim. Et Biophys. Acta (BBA) Gen. Subj.* **2015**, *1850*, 299–306. [CrossRef]
32. Morones, J.R.; Elechiguerra, J.L.; Camacho, A.; Holt, K.; Kouri, J.B.; Ramírez, J.T.; Yacaman, M.J. The bactericidal effect of silver nanoparticles. *Nanotechnology* **2005**, *16*, 2346–2353. [CrossRef]
33. Xiu, Z.-M.; Zhang, Q.-B.; Puppala, H.L.; Colvin, V.L.; Alvarez, P.J.J. Negligible particle-specific antibacterial activity of silver nanoparticles. *Nano Lett.* **2012**, *12*, 4271–4275. [CrossRef]
34. Durán, N.; Durán, M.; de Jesus, M.B.; Seabra, A.B.; Fávaro, W.J.; Nakazato, G. Silver nanoparticles: A new view on mechanistic aspects on antimicrobial activity. *Nanomed. Nanotechnol. Biol. Med.* **2016**, *12*, 789–799. [CrossRef]
35. Zhang, W.; Li, Y.; Niu, J.; Chen, Y. Photogeneration of reactive oxygen species on uncoated silver, gold, nickel, and silicon nanoparticles and their antibacterial effects. *Langmuir* **2013**, *29*, 4647–4651. [CrossRef] [PubMed]
36. Lara, H.H.; Romero-Urbina, D.G.; Pierce, C.; Lopez-Ribot, J.L.; Arellano-Jiménez, M.J.; Jose-Yacaman, M. Effect of silver nanoparticles on *candida albicans* biofilms: An ultrastructural study. *J. Nanobiotechnol.* **2015**, *13*, 91. [CrossRef] [PubMed]
37. Masigol, M.; Fattahi, N.; Barua, N.; Lokitz, B.S.; Retterer, S.T.; Platt, T.G.; Hansen, R.R. Identification of critical surface parameters driving lectin-mediated capture of bacteria from solution. *Biomacromolecules* **2019**, *20*, 2852–2863. [CrossRef] [PubMed]

38. Shahali, H.; Hasan, J.; Mathews, A.; Wang, H.; Yan, C.; Tesfamichael, T.; Yarlagadda, P.K.D.V. Multi-biofunctional properties of three species of cicada wings and biomimetic fabrication of nanopatterned titanium pillars. *J. Mater. Chem. B* **2019**, *7*, 1300–1310. [CrossRef]
39. Elbourne, A.; Crawford, R.J.; Ivanova, E.P. Nano-structured antimicrobial surfaces: From nature to synthetic analogues. *J. Colloid Interface Sci.* **2017**, *508*, 603–616. [CrossRef] [PubMed]
40. Elbourne, A.; Dupont, M.F.; Collett, S.; Truong, V.K.; Xu, X.; Vrancken, N.; Baulin, V.; Ivanova, E.P.; Crawford, R.J. Imaging the air-water interface: Characterising biomimetic and natural hydrophobic surfaces using in situ atomic force microscopy. *J. Colloid Interface Sci.* **2019**, *536*, 363–371. [CrossRef]
41. Luan, Y.; Liu, S.; Pihl, M.; van der Mei, H.C.; Liu, J.; Hizal, F.; Choi, C.-H.; Chen, H.; Ren, Y.; Busscher, H.J. Bacterial interactions with nanostructured surfaces. *Curr. Opin. Colloid Interface Sci.* **2018**, *38*, 170–189. [CrossRef]

coatings

Article

Vapor-Stripping and Encapsulating to Construct Particles with Time-Controlled Asymmetry and Anisotropy

Ting-Ying Wu [1,†], Chendi Gao [2,†], Man-Chen Huang [3], Zhi Zhang [2], Peng-Yuan Wang [4], Hsun-Yi Chen [3,*], Guosong Chen [2,*] and Hsien-Yeh Chen [1,5,6,*]

[1] Department of Chemical Engineering, National Taiwan University, Taipei 10617, Taiwan; tilee824@gmail.com
[2] The State Key Laboratory of Molecular Engineering of Polymers, Department of Macromolecular Science, Fudan University, Shanghai 200433, China; 17110440002@fudan.edu.cn (C.G.); 18110440016@fudan.edu.cn (Z.Z.)
[3] Department of Biomechatronics Engineering, National Taiwan University, Taipei 10617, Taiwan; jenny22930794@gmail.com
[4] Center for Human Tissues and Organs Degeneration, Institute of Biomedicine and Biotechnology, Shenzhen Institutes of Advanced Technology, Chinese Academy of Sciences, Shenzhen 518055, China; py.wang@siat.ac.cn
[5] Molecular Imaging Center, National Taiwan University, Taipei 10617, Taiwan
[6] Advanced Research Center for Green Materials Science and Technology, National Taiwan University, Taipei 10617, Taiwan
* Correspondence: hsunyichen@ntu.edu.tw (H.-Y.C.); guosong@fudan.edu.cn (G.C.); hsychen@ntu.edu.tw (H.-Y.C.); Tel.: +886-233-669-476 (H.-Y.C.)
† Ting-Ying Wu and Chendi Gao contributed equally to this work.

Received: 13 November 2020; Accepted: 14 December 2020; Published: 18 December 2020

Abstract: An innovative chemical vapor sublimation and deposition (CVSD) process was shown to produce nanoscale anisotropic hybrid materials. Taking advantage of controlled thermodynamic properties and the mass transfer of molecules, this process allowed for water vapor sublimation from an iced template/substrate and stagewise vapor deposition of poly-*p*-xylylene onto the sublimating ice substrate. In this study, the use of sensitive soybean agglutinin (SBA) protein tubes was demonstrated as an example to prepare the anisotropic hybrid material based on the CVSD process. The rationale of a timing parameter, Δt, was controlled to program the sublimation of the SBA-ice templates and the deposition of poly-*p*-xylylene during the CVSD process. As a result of this control, a stripping stage occurred, during which SBA tubes were exposed on the particle surface, and a subsequent encapsulation stage enabled the transformation of the ice templates into a nanometer-sized anisotropic hybrid material of poly-*p*-xylylene as the matrix with encapsulated SBA tubes. The timing parameter Δt and the controlled stripping and encapsulating stages during CVSD represent a straightforward and intriguing mechanism stemming from physical chemistry fundamentals for the fabrication of hybrid materials from sensitive molecules and with predetermined sizes and asymmetrical shapes. A simulation analysis showed consistency with the experimental results and controllability of the timing mechanism with predictable particle sizes.

Keywords: vapor sublimation; vapor deposition; nanoparticle; anisotropic material; timed control

---

1. Introduction

Anisotropic micro- and nano-objects enable dissimilar and multiple properties in physical, chemical, and biological aspects, thereby offering unrivaled synergistic multifunctional properties compared to the simple functions usually found in conventional isotropic materials. These advanced anisotropic materials have been shown to be useful in a wide range of applications as energy materials, optical materials, and biomaterials [1–3]. Many review articles have outlined recent progress in the fabrication processes and the promising applications of these anisotropy materials [4–9].

Exciting combinations used to access anisotropy across the building blocks of distinct materials have generated complexity with regard to a new dimension of combined physical (geometrical) properties and chemical (material) functionalities. Although successfully predicted [2], there are challenges regarding different thermodynamic complexities, such as intermolecular interactions between diverse molecules in composited systems [10,11], unfavorable and phase-separated boundaries, compromised functionality due to structural disorders, and limited experimental methods for the fabrication of sophisticated and sensitive anisotropic materials. Currently, existing methods for producing these materials include colloidal assembly [12], the application of postmachinal force to reshape structures [13,14], the application of regional modifications to create directional patches [15,16], and electrified jetting with combined jetting solutions (cojetting) [17,18]. Specific limitations, however, include restricted sizes and low yields, problematic intermolecular interactions, e.g., chemical reactions or physical bindings, causing various forms of aggregations, and uncontrollable diffusion or phase separation, resulting in undesired cross-boundary issues in each component composed of sensitive structures, which are subjected to irreversible deconstruction and denaturation during the fabrication process. These problems still limit the construction of anisotropic materials composed of sensitive structures and delicate functionalities, and novel approaches to produce these anisotropic materials easily with high yields are still in great demand. Chemical vapor sublimation and deposition (CVSD) is a unique and versatile technique to construct porous materials with sizes ranging from centimeters to nanometers [19,20]. This technique has been successfully employed for vapor-depositing a poly-*p*-xylylene polymer system on an iced template substrate. Compared to the stationary substrates used in conventional vapor deposition, the CVSD deposition occurred on a dynamic sublimation substrate, where shrinkage in the volume and perimeter of the sublimating substrate caused a mobile surface in the direction of shrinkage. The resulting poly-*p*-xylylene deposition on this mobile substrate enabled not only the planar coverage of poly-*p*-xylylene on the substrate surface, but also allowed for deposition into the third depth dimension due to the mobile substrate, resulting in a three-dimensional bulk material of poly-*p*-xylylene. Whereas past studies have exploited a refined CVSD approach to form nanometer-sized objects [19,21], we found that CVSD on a mixed solution of a solid template containing nonvolatile components can result in the construction of an anisotropic material final product (Figure 1). Two stages were proposed to fabricate the anisotropic object by CVSD and were controlled by a programmable time (Δt) parameter to regulate the sublimation and deposition in the stripping stage and the encapsulation stage during the CVSD process, i.e., an iced template was subjected to sublimation to evaporate water molecules, and the same template was subjected to vapor-deposited poly-*p*-xylylene to transform the template into a poly-*p*-xylylene matrix for encapsulation of the SBA protein tubes. CVSD offers the same advantages as the conventional chemical vapor deposition process, i.e., no solvent, dry process, and conformal deposition with respect to the substrate topology and geometry [22–24]. Additionally, it provides (1) controlled unsteady-state mass transport by using a sublimation substrate, avoiding problematic intermolecular and phase separation issues, (2) a time-dependent control parameter to independently regulate the mass transport of each component in the sublimation phase and the deposition phase during CVSD, enabling the construction of the final anisotropic object with tunable bulk size and/or geometric shape, and (3) the predetermined distribution of the solute phases (one or multiple), eliminating stresses from interphase and intermolecular interactions due to changes in concentrations and rehydration, which frequently occur in conventional solution-based systems [25,26] and freeze-dried products [27,28], enabling the preservation of the delicate function and structure of sensitive molecules.

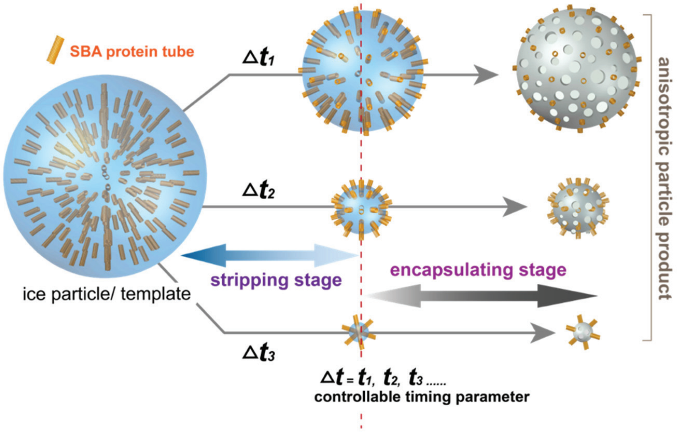

Figure 1. Illustration of the CVSD fabrication process to construct anisotropic nanomaterials. A time-dependent (Δ*t*) control parameter was used to control both the stripping stage and encapsulating stage during CVSD to tune the final hybrid products with a determined size and dimensional configuration.

2. Materials and Methods

2.1. Preparation Process of SBA Protein Tubes

First, 4-(2-Hydroxyethyl)-1-piperazineethanesulfonic acid (HEPES) buffer was prepared by dissolving 0.952 g HEPES and 0.468 g NaCl into 200 mL pure water ([HEPES] = 20 mM and [NaCl] = 40 mM). The pH of the buffer was adjusted by adding 1 mM NaOH solution until a value of 7.2 was achieved. The SBA protein, $CaCl_2$, $MnCl_2$ and the ligands were dissolved in buffer separately and kept at 4 °C for one day. All solutions were filtered through a 0.22 µm membrane before use. The SBA tube sample was generated by simply mixing these solutions and adjusting the final concentration of the sample to [SBA] = 0.1 mM, [ligand] = 0.1 mM, $[CaCl_2]$ = 5 mM, $[MnCl_2]$ = 5 mM), [HEPES] = 20 mM and [NaCl] = 40 mM. The formation of these SBA protein assemblies was induced by dual-supramolecular interactions: carbohydrate−protein interactions occurred first between the protein and N-acetyl-α-D-galactosamine on the ligand, followed by rhodamine dimerization between two ligands. The protein tubes were formed in 48 h, and their length gradually increased with increasing time. These protein tubes remained stable for more than one year at 4 °C in a mild neutral pH = 7.2 buffer solution.

2.2. Fabrication Process

The synthesized SBA protein tube solution with a concentration of 0.1 mmol/L was used to prepare the ice-particle templates. Droplets of the solution were formed by spraying the solution onto a hydrophobic poly(tetrafluoroethylene) (PTEF) substrate. A solidification procedure using a liquid nitrogen bath was performed to transform the solution droplets into iced particles. These ice particles served as templates for the subsequent CVSD process. The ice particles were placed in a homemade vapor deposition chamber [23,24] for the sublimation and deposition processes. The processing conditions were a pressure of 150 mTorr and at a deposition temperature of 4 °C. For the vapor deposition of poly-*p*-xylylene, polymerization from a precursor dichloro-[2,2]-paracyclophane (Galxyl C, Galentis, Marcon, Italy) was performed by vaporizing the precursor at approximately 120 °C, followed by a higher temperature of 650 °C to pyrolyze the vapor precursor into quinodimethane radicals. The deposition and polymerization finally occurred in a cooled sample holder at 4 °C. Argon carrier gas at a flow rate of 15 sccm was used during the process to deliver the vapor precursors and the radicals. A deposition rate of 0.5 Å/s was monitored by in situ quartz crystal microbalance (QCM) equipment (STM-100/MF, Sycon Instruments, East Syracuse, New York, NY, USA) mounted on the deposition chamber.

2.3. Characterizations

The vapor compositions during the CVSD fabrication process were characterized by real-time mass spectrometry with a residual gas analyzer (RGA, HAL RC 511, Hiden Analytical, Warrington, UK). The operation conditions were a pressure of 10^{-7} mbar, an electron ionization energy of 70 eV and an ionization emission current of 20 μA. The mass detection range was from 0 amu to 400 amu. SEM images were recorded with a Nova$^{\text{TM}}$ NanoSEM (FEI, Hillsboro, OR, USA) at a primary voltage of 10 eV and emission current of 204 μA with an Everhart-Thornley detector (ETD). Negative TEM images were obtained by staining the samples with 1 wt% uranyl acetate for 10 s. The TEM experiments were then performed with an H-7650 TEM (Hitachi, Tokyo, Japan) at 25 kV, and the images were captured by a Veleta TEM camera (Olympus, Tokyo, Japan). Cryo-TEM samples were obtained using Vitrobot (Thermo Fisher, Waltham, MA, USA) then transferred to Fischione 2550 Cryo transfer holder (Fischione, Export, PA, USA) and images were captured under 200 kV by a Tecnai TF20 TEM (FEI, Hillsboro, OR, USA). AFM experiments were acquired by a nanoscope IIIa (Veeco, Edina, MN, USA) in tapping mode using silicon nitride tips (Bruker, Billerica, MA, USA) with a tip radius of 12 nm and a spring constant of 0.04 N/m. FT-IR spectra of the fabricated particle samples were recorded by a Spectrum 100 spectrometer (PerkinElmer, Waltham, MA, USA) equipped with an advanced grazing angle specular reflectance accessory (AGA, PIKE Technologies, Fitchburg, WI, USA) equipped with a liquid nitrogen-cooled MCT detector. The recorded spectra ranged from 600 to 4500 cm^{-1} with 16 scan times at 4 cm^{-1} resolution. An IX71 fluorescence microscope (Olympus, Center Valley, PA, USA) equipped with a Lumen200 200 W fluorescence lamp (Prior, Cambridge, UK) was used to detect the ligand within the SBA proteins, and a VK-9500 3D profile microscope (Keyence, Osaka, Japan) was also used to analyze the morphology and height of the fabricated particle samples.

2.4. Simulations

A simulation of the sublimation of an ice particle was performed and constructed with COMSOL Multiphysics, and two-dimensional (2D) and three-dimensional (3D) finite element analysis were applied. The deformed geometry method was employed to trace the sublimation interface. The model framework was constructed based on the assumption of homogeneous and isotropic composition of the ice particle with a symmetric and spherical geometry. The velocity of the deformed interface was derived based on mass and heat balance and was given by:

$$N\Delta H_{sub} = V_S \rho_{ice} \Delta H_{sub} = Q_S \tag{1}$$

where N is the mass flux of water vapor, ΔH_{sub} is the latent heat of sublimation of ice, which is determined by the Clapeyron equation [29] since we assumed that the frozen ice phase is in equilibrium with the water vapor at the ice-air interface, V_S is the interface velocity, ρ_{ice} is the density of ice, and Q_S is the heat flux at the interface. The interface velocity was determined by the Stefan condition [30] and arbitrary Lagrangian–Eulerian (ALE) formulation [31]. The saturation vapor pressure at the boundary was obtained from the real-time mass detector, which is measured to be 5×10^{-8} torr. The general and reasonable diffusion coefficient assumed a constant dependence on temperature [32]. The bulk and interface temperatures were room temperature (20 °C) and at a phase change temperature of water at 150 mTorr, respectively.

3. Results and Discussion

Delicate soybean agglutinin (SBA) protein assemblies were fabricated by the ligand strategy following previously reported procedures, and were used for the generation of the proposed anisotropic object due to their unique structure, which is symmetric and tubular in three dimensions. Briefly, SBA assemblies were constructed utilizing the specific sugar-binding capability of its four monomers in the presence of Mn^{2+} and Ca^{2+} [33]. Through the assistance of a developed ligand composed of N-acetyl-α-D-galactosamine, ethylene oxide spacer and rhodamine B, a self-assembled SBA tetramer structure with a helical tube with a diameter of approximately 20 nm and a length of 100–2000 nm was generated. The synthesized SBA was characterized with dynamic light scattering (DLS) and Cryo-TEM (cryogenic transmission electron microscopy), and the results showed an SBA tube approximately 250 nm in size and 26 nm in diameter (Figure 2a,b). Suspension solutions of the synthesized SBA protein tubes with a defined composition were then prepared to form droplets on hydrophobic surfaces [21] and transformed into solidified protein solution particles by a temperature solidification process, e.g., liquid nitrogen or dry ice bath, resulting in a sublimation template for the CVSD process used in this study. The thermodynamic conditions (approximately 0.2 mbar and 20 °C) of the CVSD operation favored the transformation of the solid-phase water component (ice) of the solidified protein solution into water vapor, similar to the generation of CO_2 vapor from dry ice in ambient conditions [34] or to the freeze-drying process to evaporate the water (or solvent) phase from a solution mixture used in many purification and processing operations [35,36]. Under the CVSD conditions, water molecules were evaporated by sublimation from the solid iced particles, whereas the nonsublimating protein molecules retained their controlled distribution on the substrate and were seamlessly encapsulated into the deposited polymer structure [20,21].

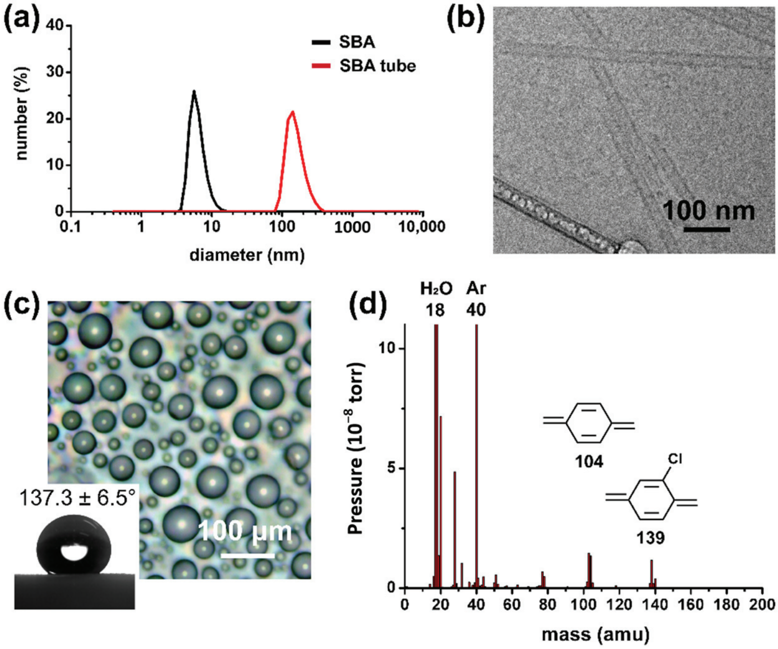

Figure 2. (**a**) DLS and (**b**) Cryo-TEM data showed that the fabricated SBA tubes were approximately 234.3 ± 26.3 nm in length and 26 nm in diameter. (**c**) Droplets of protein solution were formed on a hydrophobic surface. A measured water contact angle value of 137.3 ± 6.5 degrees was shown in the inset. (**d**) Mass spectrometric analysis of vapor composition during the CVSD process. Characteristic peaks at approximately 18 amu (water molecule), 104 amu (quinodimethane), and 139 amu (chloro-quinodimethane) were detected.

The construction of the proposed anisotropic objects was therefore established by CVSD with a controllable two-stage process: (i) stripping stage, (ii) encapsulating stage, where the time-dependent parameter, Δt, was used to control the sublimation degree of the sublimated ice template, and the elapsed time was propositional to the sublimated volume of shrinkage. More specifically, in the stripping stage, the protein molecules were used as a nonsublimation-solute system in the ice particles with the sublimating water molecules (solvent system). The sublimation of water molecules resulted in a smaller volume and receding interface perimeters of the ice particles, where the protein molecules were located towards the outer particle surfaces, while in the encapsulating stage, the vapor deposition of poly-*p*-xylylene occurred stagewise (after the same programmed time), and the remaining volume (mass) of the sublimating ice particles was transformed into porous structures of poly-*p*-xylylene, which was used a matrix for the encapsulation of the protein molecules without affecting their configuration and structure. Compared to the stripping stage, during which mass transport flux only occurred in one (outward) direction through sublimation, the encapsulating stage additionally involved the mass flux of deposited poly-*p*-xylylene into the system onto the sublimating template/substrate, which led to a transformation through the replacement of vaporized water molecules with the deposited poly-*p*-xylylene molecules. The stagewise stripping and encapsulating processes finally resulted in the proposed anisotropic nanoparticle product, which was composed of poly-*p*-xylylene as the matrix and distributed SBA proteins within the poly-*p*-xylylene structure. In the experiments, symmetrical sphere ice particles of the described protein solution were prepared by forming droplets on hydrophobic surfaces (water contact angle approximately 137.3 ± 6.5 degrees, Figure 2c) followed by a solidification process using a liquid nitrogen bath. The ice particles served as sublimation templates, and the operation time (Δt_1, Δt_2, Δt_3, …) was controlled and resulted in emerging and eventually exposed nonvolatile components of the protein solutes by the time-dependent shrinkage of the ice perimeter due to sublimation in the two-stage process of the fabrication process. The controllable Δt parameter regulated the timing of the sequences (i) and (ii) during the fabrication process and determined the aspect ratio and shape of the finalized (hybrid-) nanoparticle products. A real-time mass spectroscopic gas analyzer was used to monitor the vapor composition (Figure 2d), and the correspondent species including water vapor (18 amu), carrier gas of argon (40 amu), derivatives of quinodimethanes (104 amu and 139 amu) were detected in the studied vapor system of the CVSD fabrication process. A more systematic analysis of the changes in mass was further performed to verify the controllability of time during the stripping and encapsulating stages in the CVSD process. As revealed in Figure 3, the detection of an increased level of water vapor (18 amu) indicated the occurrence of sublimation in the stripping stage, and similarly, a vaporized chloro-quinodimethane precursor (139 amu) was detected to indicate the initiation of deposition in the encapsulation stage. The timing parameter, with values of $\Delta t_1 = 60$ s, $\Delta t_2 = 120$ s, and $\Delta t_3 = 185$ s, was shown to control and program both the stripping stage and the encapsulating stage, resulting in changes in the vapor compositions at the selected and designated times. From a chemical point of view, characterizations for the resultant hybrid particles products were also performed by using FT-IR analysis. As shown in Figure 4, the recorded spectra showed the characteristic –C–Cl and –C–H bands from poly-*p*-xylylene, similar to other reported poly-*p*-xylylene systems. For the hybrid product comprised both SBA and poly-*p*-xylylene, despite possible overlapped peaks of –C=O and –C–O with the –C–Cl peaks, additional –N–H and –O–H bands from solely SBA were detected and confirmed the successful fabrication of the hybrid materials of poly-*p*-xylylene/SBA.

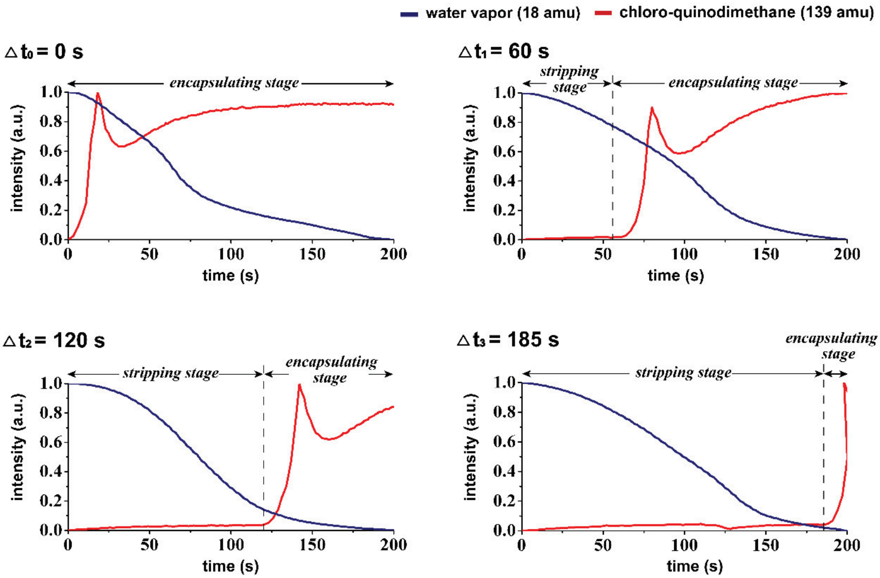

Figure 3. Real-time mass spectrometry analysis of the vapor compositions during the CVSD process showed controllable timing of Δt_1, Δt_2, Δt_3, with corresponding regulations of vapor compositions in the stripping stage and the encapsulating stage.

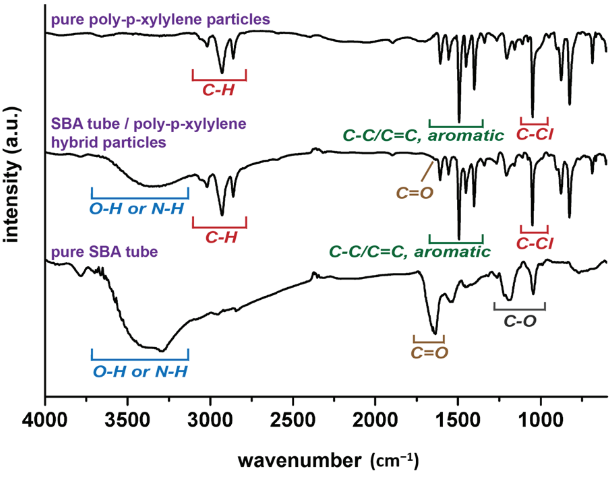

Figure 4. FT-IR spectra showed the chemical composition of the fabricated anisotropic composite particles with poly-*p*-xylylene as the matrix and the encapsulated SBA proteins. Spectra were also recorded for pure poly-*p*-xylylene and pure SBA for comparison.

A simulation analysis was then performed to understand the timing mechanism during the CVSD and to rationalize the controllability of the geometrical properties vs. the Δt parameters. Taking advantage of the similarity of a freeze-drying process with the ice-template sublimation process of the current system during the proposed stripping stage, a reported mathematical freeze-drying model was used in the simulations [37]. Our model framework was designed according to the proposed dimensional scale of an ice particle system, and the simulated dimensional and temporal information was collected. Briefly, a spherical ice particle was initiated and coupled through heat and mass transfer mechanisms in its sublimation process, and the moving sublimation boundary was treated as a sharp interface. The interfacial temperature was obtained by the saturation vapor pressure, while the interface velocity was determined by the normal heat flux difference at the interface. The processing pressure of the CVSD process was used as the pressure of the external environment of the ice sphere. Although the SBA tubes were described as nonsublimating solutes within the ice template, they were sparsely distributed and nonreactive during the CVSD process. Therefore, the SBA proteins should have a limited effect on the sublimation process in the simulation. The simulation results were consistent with the experimental results, for example, a Δt = 60 s reduced the size of an ice particle from the initial 50 μm to 32 μm, 160 s resulted in a size decrease to 5 μm, 177 s to 500 nm, and 178 s to 250 nm, as shown in Figure 5a. After the stripping stage, with the determined dimension configurations according to the set Δt, the subsequent encapsulating stage initiated the transformation by inducing mass transfer of poly-*p*-xylylene through vapor deposition (in contrast to retrograding mass transfer by sublimation) onto the sublimating ice particle. The final asymmetrical nanoparticles were obtained by replacement of the remaining ice/water molecules with the aforementioned polymerized poly-*p*-xylylene molecules. As revealed in Figure 5b, combinations of characterization techniques, including optical microscopy, scanning electron microscopy (SEM), transmission electron microscopy (TEM), and AFM, showed that the encapsulation and poly-*p*-xylylene deposition occurred by retrograding the outer surface of the ice particles, thereby exposing the protein to the particle surface, and a time-dependent configuration of the size and the exposed protein-assembly dimensions was found, which was consistent with the simulation results. Particles with 38.3 ± 8.6 μm size were fabricated when Δt = 60 s, 6.3 ± 1.6 μm when Δt = 160 s, 608.3 ± 56.8 nm when Δt = 177 s, and 294.3 ± 38.6 nm when Δt = 178 s; a first-order linear correlation of Δt vs. length ($\sqrt[3]{\Delta V}$) was found, which supported the simulation data and the reported results [19]. The fabricated anisotropic particle structure was preserved without compromising the delicate SBA tube structure, and a tube diameter of approximately 40 nm were found to be consistent with the prepared SBA tube dimension in the solution phase. The approximately 14 nm-increased diameter thickness (from 26 nm of a bare SBA tube to 40 nm) was found to be comparable to the deposited thickness of poly-*p*-xylylene and was due to the deposition on the nonsublimating SBA tube, analogous to conventional poly-*p*-xylylene depositions on a solid substrate [22,38]. To compare the results, the time-dependent particle sizes based on the simulation trajectory and the fabricated particles are plotted in Figure 6, and a recorded simulation video showing a sublimating ice particle template with respect to the elapsed time is included in the supporting information.

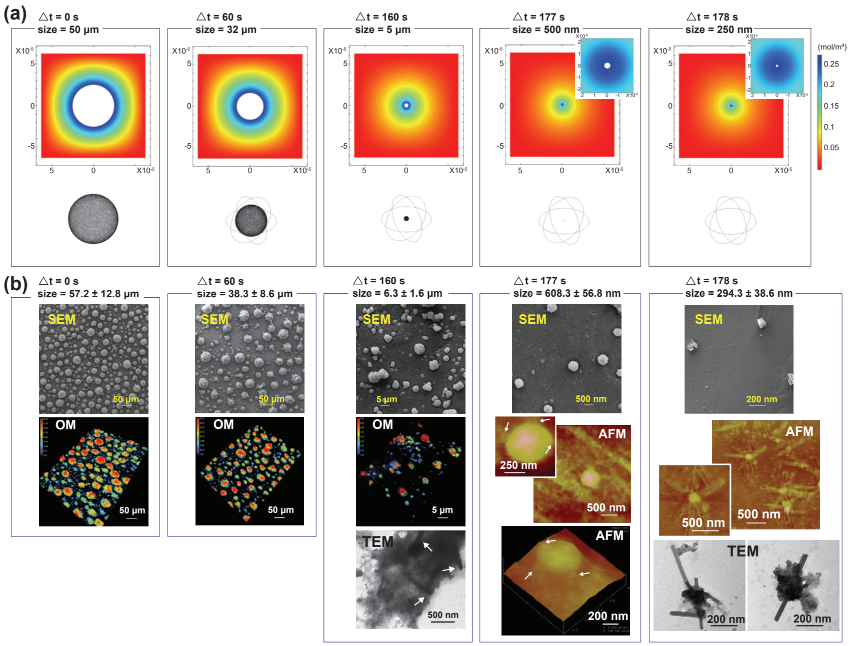

Figure 5. (**a**) Simulation results showed that Δt = 60 s reduced an initial 50 μm ice particle to 32 μm, Δt = 160 s to 5 μm, Δt = 177 s to 500 nm, and a Δt = 178 s to 250 nm. (**b**) Combinations of characterizations by optical microscopy (OM), SEM, TEM, and AFM of the fabricated anisotropic nanoparticles. Controlled sizes and geometries are shown with respect to the specified Δt.

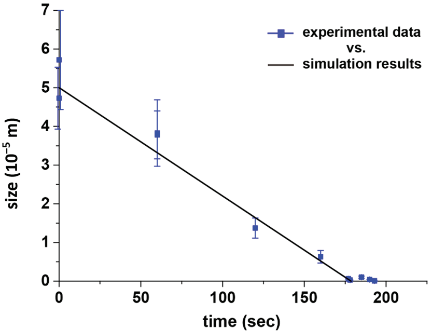

Figure 6. Controlled particle size based on the programmed time-parameter during the two-stage CVSD fabrication process. The simulation and experimental results were mutually consistent. The data points were expressed as the mean value and the standard deviation based on three independent experiments.

4. Conclusions

In summary, controlling material anisotropy and asymmetry is a fascinating technique adopted from nature which offers superior and diverse properties derived from both the chemical and physical compartments of the materials. The current study demonstrated the challenge of inducing a sensitive, self-assembled SBA protein into a vapor-deposited poly-*p*-xylylene structure that was fabricated via a two-staged stripping and encapsulating process. The reported process employed a vapor-phase construction process using water and ice as templates, and the controllable timing parameter with controlled thermodynamic conditions and mass transport, particularly in the vapor phases of sublimation and deposition, offering flexible control over the particle sizes and aspect ratios in the nanometer range. The sizes of the fabricated anisotropic materials were shown to range from approximately 57 μm to 294 nm, and the simulation results were able to accurately predict the size of fabrication (from 50 μm to 250 nm). With the ability to extend this straightforward CVSD process to other nonsensitive materials (functional materials), we foresee the development of prospective anisotropic and asymmetric materials with unlimited functional products and applications in materials sciences.

Author Contributions: Conceptualization, H.-Y.C. (Hsien-Yeh Chen), H.-Y.C. (Hsun-Yi Chen), P.-Y.W., and G.C.; methodology, H.-Y.C. (Hsien-Yeh Chen) and T.-Y.W.; software, T.-Y.W. and M.-C.H.; validation, T.-Y.W., H.-Y.C. (Hsien-Yeh Chen), and P.-Y.W.; formal analysis, T.-Y.W. and C.G.; investigation, T.-Y.W. and C.G.; resources, T.-Y.W., C.G., P.-Y.W., and Z.Z.; data curation, T.-Y.W.; writing—original draft preparation, T.-Y.W., C.G., H.-Y.C. (Hsien-Yeh Chen), H.-Y.C. (Hsun-Yi Chen), and G.C.; writing—review and editing, T.-Y.W. and H.-Y.C. (Hsien-Yeh Chen); visualization, T.-Y.W. and H.-Y.C. (Hsien-Yeh Chen); supervision, H.-Y.C. (Hsien-Yeh Chen), H.-Y.C. (Hsun-Yi Chen), and G.C.; project administration, H.-Y.C. (Hsien-Yeh Chen), H.-Y.C. (Hsun-Yi Chen), and G.C.; funding acquisition, H.-Y.C. (Hsien-Yeh Chen), H.-Y.C. (Hsun-Yi Chen), and G.C. All authors have read and agreed to the published version of the manuscript.

Funding: This research was funded by the Ministry of Science and Technology of Taiwan, grant number MOST 108-2221-E-002-169-MY3, MOST 108-2218-E-007-045, and MOST 109-2314-B-002-041-MY3. This work was further supported by the “Advanced Research Center for Green Materials Science and Technology” from The Featured Area Research Center Program within the framework of the Higher Education Sprout Project by the Ministry of Education (107 L9006) and the Ministry of Science and Technology in Taiwan (MOST 109-2634-F-002-042). The work was also funded by the NSFC of China, Grant number 51721002, 21861132012, 91956127, and 21975047.

Conflicts of Interest: The authors declare no conflict of interest. The funders had no role in the design of the study; in the collection, analyses, or interpretation of data; in the writing of the manuscript, or in the decision to publish the results.

References

1. Perro, A.; Reculusa, S.; Ravaine, S.; Bourgeat-Lami, E.; Duguet, E. Design and synthesis of Janus micro- and nanoparticles. *J. Mater. Chem.* **2005**, *15*, 3745–3760. [CrossRef]
2. Glotzer, S.C.; Solomon, M.J. Anisotropy of building blocks and their assembly into complex structures. *Nat. Mater.* **2007**, *6*, 557–562. [CrossRef] [PubMed]
3. Mitragotri, S.; Lahann, J. Physical approaches to biomaterial design. *Nat. Mater.* **2009**, *8*, 15–23. [CrossRef] [PubMed]
4. Lee, K.J.; Yoon, J.; Lahann, J. Recent advances with anisotropic particles. *Curr. Opin. Colloid Interface Sci.* **2011**, *16*, 195–202. [CrossRef]
5. Lattuada, M.; Hatton, T.A. Synthesis, properties and applications of Janus nanoparticles. *Nano Today* **2011**, *6*, 286–308. [CrossRef]
6. Wurm, F.; Kilbinger, A.F.M. Polymeric Janus Particles. *Angew. Chem. Int. Ed.* **2009**, *48*, 8412–8421. [CrossRef]
7. Walther, A.; Müller, A.H.E. Janus particles. *Soft Matter* **2008**, *4*, 663–668. [CrossRef]
8. Pawar, A.B.; Kretzschmar, I. Fabrication, Assembly, and application of patchy particles. *Macromol. Rapid Commun.* **2010**, *31*, 150–168. [CrossRef]
9. Li, W.; Palis, H.; Mérindol, R.; Majimel, J.; Ravaine, S.; Duguet, E. Colloidal molecules and patchy particles: Complementary concepts, synthesis and self-assembly. *Chem. Soc. Rev.* **2020**, *49*, 1955–1976. [CrossRef]
10. Hu, X.; Cebe, P.; Weiss, A.S.; Omenetto, F.; Kaplan, D.L. Protein-based composite materials. *Mater. Today* **2012**, *15*, 208–215. [CrossRef]
11. Välimäki, S.; Mikkilä, J.; Liljeström, V.; Rosilo, H.; Ora, A.; Kostiainen, M.A. Hierarchically ordered supramolecular protein-polymer composites with thermoresponsive properties. *Int. J. Mol. Sci.* **2015**, *16*, 10201–10213. [CrossRef] [PubMed]
12. Evers, C.H.J.; Luiken, J.A.; Bolhuis, P.G.; Kegel, W.K. Self-assembly of microcapsules via colloidal bond hybridization and anisotropy. *Nature* **2016**, *534*, 364–368. [CrossRef] [PubMed]
13. Champion, J.A.; Katare, Y.K.; Mitragotri, S. Making polymeric micro- and nanoparticles of complex shapes. *Proc. Natl. Acad. Sci. USA* **2007**, *104*, 11901–11904. [CrossRef] [PubMed]

14. Rolland, J.P.; Maynor, B.W.; Euliss, L.E.; Exner, A.E.; Denison, G.M.; DeSimone, J.M. Direct fabrication and harvesting of monodisperse, shape-specific nanobiomaterials. *J. Am. Chem. Soc.* **2005**, *127*, 10096–10100. [CrossRef] [PubMed]
15. Chen, H.-Y.; Rouillard, J.-M.; Gulari, E.; Lahann, J. Colloids with high-definition surface structures. *Proc. Natl. Acad. Sci. USA* **2007**, *104*, 11173–11178. [CrossRef] [PubMed]
16. Zhang, Z.; Glotzer, S.C. Self-assembly of patchy particles. *Nano Lett.* **2004**, *4*, 1407–1413. [CrossRef] [PubMed]
17. Badrossamay, M.R.; Balachandran, K.; Capulli, A.K.; Golecki, H.M.; Agarwal, A.; Goss, J.A.; Kim, H.; Shin, K.; Parker, K.K. Engineering hybrid polymer-protein super-aligned nanofibers via rotary jet spinning. *Biomaterials* **2014**, *35*, 3188–3197. [CrossRef] [PubMed]
18. Lahann, J. Recent progress in nano-biotechnology: Compartmentalized micro- and nanoparticles via electrohydrodynamic co-jetting. *Small* **2011**, *7*, 1149–1156. [CrossRef]
19. Tung, H.-Y.; Guan, Z.-Y.; Liu, T.-Y.; Chen, H.-Y. Vapor sublimation and deposition to build porous particles and composites. *Nat. Commun.* **2018**, *9*, 2564. [CrossRef]
20. Tung, H.-Y.; Sun, T.-P.; Sun, H.-Y.; Guan, Z.-Y.; Hu, S.-K.; Chao, L.; Chen, H.-Y. Construction and control of 3D porous structure based on vapor deposition on sublimation solids. *Appl. Mater. Today* **2017**, *7*, 77–81. [CrossRef]
21. Chiu, Y.-R.; Hsu, Y.-T.; Wu, C.-Y.; Lin, T.-H.; Yang, Y.-Z.; Chen, H.-Y. Fabrication of asymmetrical and gradient hierarchy structures of poly-*p*-xylylenes on multiscale regimes based on a vapor-phase sublimation and deposition process. *Chem. Mater.* **2020**, *32*, 1120–1130. [CrossRef]
22. Chen, H.-Y. Micro- and nano-surface structures based on vapor-deposited polymers. *Beilstein J. Nanotechnol.* **2017**, *8*, 1366–1374. [CrossRef]
23. Chen, H.-Y.; Lin, T.-J.; Tsai, M.-Y.; Su, C.-T.; Yuan, R.-H.; Hsieh, C.-C.; Yang, Y.-J.; Hsu, C.-C.; Hsiao, H.-M.; Hsu, Y.-C. Vapor-based tri-functional coatings. *Chem. Commun.* **2013**, *49*, 4531–4533. [CrossRef] [PubMed]
24. Tsai, M.-Y.; Chen, Y.-C.; Lin, T.-J.; Hsu, Y.-C.; Lin, C.-Y.; Yuan, R.-H.; Yu, J.; Teng, M.-S.; Hirtz, M.; Chen, M.H.-C.; et al. Vapor-based multicomponent coatings for antifouling and biofunctional synergic modifications. *Adv. Funct. Mater.* **2014**, *24*, 2281–2287. [CrossRef]
25. Mezzenga, R.; Jung, J.-M.; Adamcik, J. Effects of charge double layer and colloidal aggregation on the isotropic−nematic transition of protein fibers in water. *Langmuir* **2010**, *26*, 10401–10405. [CrossRef] [PubMed]
26. Kern, N.; Frenkel, D. Fluid-fluid coexistence in colloidal systems with short-ranged strongly directional attraction. *J. Chem. Phys.* **2003**, *118*, 9882–9889. [CrossRef]
27. Deng, Y.; Luo, Y.; Wang, Y.; Yue, J.; Liu, Z.; Zhong, Y.; Zhao, Y.; Yang, H. Drying-induced protein and microstructure damages of squid fillets affected moisture distribution and rehydration ability during rehydration. *J. Food Eng.* **2014**, *123*, 23–31. [CrossRef]
28. Anchordoquy, T.J.; Izutsu, K.-I.; Randolph, T.W.; Carpenter, J.F. Maintenance of quaternary structure in the frozen state stabilizes lactate dehydrogenase during freeze-drying. *Arch. Biochem. Biophys.* **2001**, *390*, 35–41. [CrossRef]
29. Murphy, D.M.; Koop, T. Review of the vapour pressures of ice and supercooled water for atmospheric applications. *Q. J. R. Meteorol. Soc.* **2005**, *131*, 1539–1565. [CrossRef]
30. Alexiades, V.; Solomon, A.D. *Mathematical Modeling of Melting and Freezing Processes*; Hemisphere Publishing Corporation: Boca Raton, FL, USA, 1993.
31. Jambon-Puillet, E.; Shahidzadeh, N.; Bonn, D. Singular sublimation of ice and snow crystals. *Nat. Commun.* **2018**, *9*, 6. [CrossRef]
32. Monteith, J.L.; Unsworth, M.H. *Principles of Environmental Physics*; Academic Press: Cambridge, MA, USA, 2013; pp. 25–35.
33. Yang, G.; Zhang, X.; Kochovski, Z.; Zhang, Y.F.; Dai, B.; Sakai, F.J.; Jiang, L.; Lu, Y.; Ballauff, M.; Li, X.M.; et al. Precise and reversible protein-microtubule-like structure with helicity driven by dual supramolecular interactions. *J. Am. Chem. Soc.* **2016**, *138*, 1932–1937. [CrossRef] [PubMed]
34. Zhang, X.-R.; Yamaguchi, H. An experimental study on heat transfer of CO_2 solid-gas two phase flow with dry ice sublimation. *Int. J. Therm. Sci.* **2011**, *50*, 2228–2234. [CrossRef]
35. Madihally, S.V.; Matthew, H.W.T. Porous chitosan scaffolds for tissue engineering. *Biomaterials* **1999**, *20*, 1133–1142. [CrossRef]
36. Deville, S. Freeze-casting of porous ceramics: A review of current achievements and issues. *Adv. Eng. Mater.* **2008**, *10*, 155–169. [CrossRef]

37. Lopez-Quiroga, E.; Antelo, L.T.; Alonso, A.A. Time-scale modeling and optimal control of freeze-drying. *J. Food Eng.* **2012**, *111*, 655–666. [CrossRef]
38. Chen, H.-Y.; Lahann, J. Designable biointerfaces using vapor-based reactive polymers. *Langmuir* **2010**, *27*, 34–48. [CrossRef]

coatings

MDPI

Article

One-Step Preparation of Nickel Nanoparticle-Based Magnetic Poly(Vinyl Alcohol) Gels

Jun Li [1,*], Kwang-Pill Lee [2,3] and Anantha Iyengar Gopalan [3]

[1] School of Pharmaceutical Sciences, Capital Medical University, Beijing 100069, China
[2] Department of Chemistry Graduate School, Kyungpook National University, Daegu 41566, Korea; kplee@knu.ac.kr
[3] Department of Chemistry, Kyungpook National University, Daegu 41566, Korea; agopalan@knu.ac.kr
* Correspondence: lijun88@ccmu.edu.cn

Received: 3 September 2019; Accepted: 29 October 2019; Published: 9 November 2019

Abstract: Magnetic nanoparticles (MNPs) are of great interest due to their unique properties, especially in biomedical applications. MNPs can be incorporated into other matrixes to prepare new functional nanomaterials. In this work, we described a facile, one-step strategy for the synthesis of magnetic poly(vinyl alcohol) (mPVA) gels. In the synthesis, nickel nanoparticles and cross-linked mPVA gels were simultaneously formed. Ni nanoparticles (NPs) were also incorporated into a stimuli-responsive polymer to result in multiresponsive gels. The size of and distribution of the Ni particles within the mPVA gels were controlled by experimental conditions. The mPVA gels were characterized by field emission scanning electron microscope, X-ray diffraction, magnetic measurements, and thermogravimetric analysis. The new mPVA gels are expected to have applications in drug delivery and biotechnology.

Keywords: one-step preparation; nickel nanoparticles; magnetic poly(vinyl alcohol) gels

---

1. Introduction

In biological and pharmaceutical fields, polymers have been highly advanced by developing the synthesis methods, controlling the manufacturing steps, and designing the properties. Among such materials, hydrogels have been widely applied to meet versatile requirements [1]. Since PVA hydrogel was first formed by gamma rays in 1958, PVA hydrogels have been largely produced. Hydrogels were used in the biomedical and biotechnological fields in the 1990s. With high water content, elasticity, and biocompatibility, PVA hydrogels are widely used as biomaterials. However, there are limitations for PVA hydrogels: the characteristics of low permeability, stability, and fixation. In order to overcome the limitations, the properties of PVA hydrogels are enhanced by blending with other materials, such as other polymers, metals, and clays. Polyvinyl alcohols (PVA) are synthetic polymers widely used in industrial, medical, and food fields since the early 1930s [2]. PVA is relatively harmless when administered orally, because PVA does not accumulate in the body.

Magnetic metal nanoparticles have gained research interest in biomedicine for their chemical, electrical, and magnetic properties [3]. The crystalline structure, particle size, and magnetic properties of the magnetic metal nanoparticles can control and improve the polymers for applications in medical fields such as treatment of hyperthermia and drug delivery. The chemical composition and fabrication processes have great effects on the sizes and shapes of the particles. To achieve different properties, the synthesis routes are co-precipitation, sol-gel, ball-milling, gamma irradiation, laser irradiation, the photoinduced method, e1tc. The mediated polymers improve the quality of the particles for drug delivery. The idea of drug delivery was proposed by Paul Ehrlich [4]. To reduce the systemic distribution and the required drug dosage, magnetic carriers are used. In 1976, Zimmermann and Pilwat proposed magnetic erythrocytes for the drug delivery. Since then, researchers began to use magnetic microparticles and nanoparticles (NPs) to target specific sites within the body. Some magnetic carriers are magnetic cores encapsulated in a biocompatible polymeric coating with drug loading capability. The magnetic cores are NPs of metal or metallic oxide moieties with sizes between 1 and 100 nm.

Magnetic gels aconsist of magnetic particles embedded within polymers [5]. The term is commonly applied to magnetic nanoparticles being immersed in a hydrogel. They are stimuli-responsive in an external magnetic field, but biological matter is tolerant to magnetic fields. They are promising candidates for controlled drug release due to the interplay between magnetic and elastic properties. The magnetogels combine the advantages of hydrogels and magnetic nanoparticles [6]. Hydrogels are similar to the cellular matrix with their high portion of water. Magnetic nanoparticles made of any transition metal (Fe, Ni, Co, Cr, or Mn) and its oxides allow for the control to a specific location under a magnetic field. The nanosystems improve target specificity, therapeutic effectiveness, magnetic resonance imageology, and hyperthermia for cancer therapy.

The magnetic drug carrier particles have been applied for over 40 years under an external magnetic field [7]. The magnetic nanoparticles can be removed to reduce risk of particle aggregation after therapy is completed. The nanoparticles can be synthesized in the presence of polyvinyl alcohol (PVA) or another substance to make them appropriate for in vivo applications. The polymers make the NPs stable [8,9]. One of the challenges is to improve the localization of cross-linker release to minimize in vivo toxicity. Controlling the density of cross-links in the gel matrix can tune the porous structure and the swelling properties of the hydrogels in the aqueous environment. Manufacturing processes still need to be developed for better-controlled hydrogels in terms of size, shape, distribution, and mechanics [10].

Ni-based nanomaterials can be used as magnetically-responsive therapeutic platforms for anticancer drugs [11]. Many different synthetic routes for magnetic nanoparticle synthesis have been reported [12] Some of them are one-step, while others are multi-step procedures. They all have advantages and disadvantages. But none of them provides a universal solution for all types of magnetic nanoparticles. Employing simpler and easier synthetic routes for the magnetic nanoparticles with desired characteristics remains highly challenging.

Doxorubicin (DOX) is a kind of cytotoxic anticancer drug. It is widely used in clinical therapy [13] To reduce the limitation of cardiotoxicity and improve the biocompatibility and efficiency, drug delivery systems are being developed [14]. The superparamagnetic nanodevice is designed to deliver DOX under a magnetic field, with good stability [15]. The main aim of this work is to design a new formation strategy of the magnetic polymer for the anti-cancer drug delivery system. An easy, one-step synthetic method for nickel nanoparticles based on poly(vinyl alcohol) gel is described. Nickel chloride was reduced by sodium borohydride in aqueous PVA solution. The Ni PVA gels were characterized by various techniques. The loading and release process was studied.

2. Experimental

2.1. Materials

PVA was purchased from Aldrich (Saint Louis, MO, USA) with a hydrolysis degree of 98%–99% and a molecular average weight of 85,000–124,000 g/mol. Nickel(II) chloride hexahydrated was from Junsei Chemical Co. (Tokyo, Japan). Sodium borohydride was from Kanto Chemical Co. (Tokyo, Japan). Doxorubicin hydrochloride (DOX) was obtained from Korea United Pharm. Inc. (Chungnam, Korea).

2.2. Synthesis of Ni-NP PVA Gel

Ni-NP PVA gel was prepared by reducing nickel chloride in PVA solution with sodium borohydride as the reducing agent. The aqueous solution of 10 wt.% PVA was first prepared by dissolving PVA in deionized water at 80 °C for 3 h. An aqueous solution of nickel chloride was then added to the PVA solution in a beaker. $NaBH_4$ solution was added drop wise, using a separation funnel, to the nickel chloride solution, while the temperature was maintained between 80 °C with continuous stirring. The reaction mixture was allowed to stir for about 1 h at 80 °C, by which time black-colored solution was obtained, and at the same time a large amount of gas bubbles of H_2 were generated. The water in this solution was evaporated at 70 °C. After evaporation of most solvent, the hot residue was poured into a Petri dish. The black mixture was dried overnight at room temperature. After that, the residue was dried in an oven at 70 °C, and thus a gel was generated. The resulting gel was washed with distilled water, and further dried in an oven at 70 °C for 24 h. The resulting product was but to small pieces for various tests with scissors.

2.3. Characterization

The morphology and elemental composition of the structure, and microstructural characterization of the samples, were characterized using field-emission scanning electron microscopy (FE-SEM) (S-4200, Hitachi, Tokyo, Japan), operated at 3–10 kV electron potential difference and equipped with a semiconductor detector that allowed for the detection of energy dispersive X-rays (EDX). X-ray diffraction analysis (XRD) patterns on samples were measured on a model D8-Advanced AXS diffractometer (Bruker, Billerica, MA, USA) using Cu Kα radiation. Samples were supported on glass slides. Measurements were taken using a glancing angle of incidence detector at an angle of 2°, for 2θ values over 10°–80° in steps of 0.02°. Magnetic properties of the samples were measured by using a super-conducting quantum interface device (SQUID) magnetometer (MPMS-X 1, Quantum Design, San Diego, CA, USA) under an applied magnetic field, at room temperature. Thermogravimetric analysis (TGA) of the sample was performed on a TGA 7/DX Thermal Analyzer (Perkin-Elmer, Waltham, MA, USA) with a scan rate of 10 °C/min by pursuing N_2 gas as a carrier at a flow rate of 100 mL/min. The differential scanning calorimetric (DSC) experiment was carried out using a DSC2010 Differential Scanning Calorimeter (TA Instruments, New Castle, DE, USA) over a temperature range 20 to 1200 °C at a scan rate of 10 °C/min.

2.4. Swelling Studies

For the swelling kinetics' measurement, the gel (about 0.5 mm thick) was cut to 1 cm × 0.5 cm. The gel was then immersed in distilled water. The rate of gel expansion was determined by measuring the change in gel length at various time intervals. The dimensional change was estimated from the length ratio of the swollen hydrogel sample after 24 h (at the equilibrium) compared to its original length. The change in dimensions of the swollen samples (L_s) was calculated according to equation:

$$L_\mathrm{s}(\%) = \frac{L_\mathrm{t} - L_0}{L_0} \times 100\% \tag{1}$$

where L_0 is the original gel length, and L_t is the equilibrium gel length at a given time.

The water uptake of a gel sample was measured at room temperature. A swollen sample was removed from the solvent. After the water on the surface was absorbed gently with filter paper, the sample was immediately weighed. Then, the sample was returned to the medium. The mass swelling ratios (M_s) was calculated as follows:

$$M_\mathrm{s}(\%) = \frac{m_t - m_0}{m_0} \times 100\% \tag{2}$$

where m_t, m_0, and ($m_\mathrm{t} - m_0$) are the masses of a swollen sample at a given time, dry gel, and absorbed water, respectively.

The equilibrium water content W_e in swollen samples was calculated as:

$$W_\mathrm{e}(\%) = \frac{m_\infty - m_0}{m_0} \times 100\% \tag{3}$$

where m_∞ is the weight of the swollen hydrogel at equilibrium [16].

2.5. Drug Loading and Release

The drug release kinetics is important for the application of the gel to drug delivery. Doxorubicin hydrochloride (DOX) was chosen as an anti-cancer model drug. The DOX loading was carried out by dispersing 10 mg of PVA gel in 3 mL DOX solution at a concentration of 0.02 mg/mL at room temperature in the dark. The mixture of PVA gel in DOX was shaken (80 rpm) at room temperature for 48 h to facilitate DOX uptake. The optical density of residual DOX in the supernatant was measured at 479 nm by UV-vis spectrophotometer (Cary 50, VARIAN, Palo Alto, CA, USA). The drug loading was determined as the difference between the initial DOX concentration and the DOX concentration in the supernatant. After the supernatant was removed, the release profile was obtained by reimmersing the gel loaded with DOX in 3 mL of water under gentle stirring. The concentration of DOX in the particle-free solution was determined at fixed time intervals by UV-vis spectrophotometry.

3. Results and Discussion

3.1. Reaction Mechanism of Ni-NP PVA Gel

Liquid phase reduction has some advantages over other synthetic methods for magnetic nanomaterials. Using some popular reducing agents, liquid phase reduction was applied to reduce magnetic metal ions to magnetic metal [12]. In this kind of reaction, hydrides are usually used for reducing agents. It is difficult to handle the sensitivity of hydrides to the mild environment. No special laboratory condition is required for these strong reactants, except for the moisture. Hydrides are also penetrative to some polymers, so the particles can still be reduced even with protective coatings.

$NaBH_4$ is a particularly powerful reducing agent in liquid phase reduction. It is soluble in both methanol and water. The mechanism of reduction for Ni using $NaBH_4$ is complicated. In the reaction, a black metal powder of Ni-NPs formed due to an instantaneous $Ni^{2+} \rightarrow Ni$ co-reduction reaction with $NaBH_4$ [17]. The reduction of nickel ions using $NaBH_4$ followed the equation

$$NiCl_2 + 2NaBH_4 + 6H_2O \rightarrow Ni + 2B(OH)_3 + 2NaCl + 7H_2\uparrow$$

The byproducts of $B(OH)_3$ and NaCl remained dissolved in the aqueous solution and were removed after the washing process in fresh water.

Poly(vinyl alcohol) (PVA) is a good stabilizer for small metal particles in chemical synthesis to prevent the agglomeration and precipitation [18]. The embedding of the particles is also advantageous for the PVA casting. The Ni-NP PVA hydrogel was formed by the embedding of Ni-NPs into PVA aqueous solution. The Ni-NP remained in gel form within the matrix, as sketched in Scheme 1. Figure 1a,b shows photographs of the obtained PVA gel and Ni-NP PVA gel, respectively. Figure 1c,d shows photographs of the Ni-NPs and Ni-NP PVA gel synthesized by the same reduction reaction in the magnet field. When the Ni-NPs and the Ni-NP hydrogels were exposed to the field of a permanent NbFeB magnet, they were be attracted to the external magnet. This simple analysis demonstrated the magnetic properties of the polymers containing Ni-NPs.

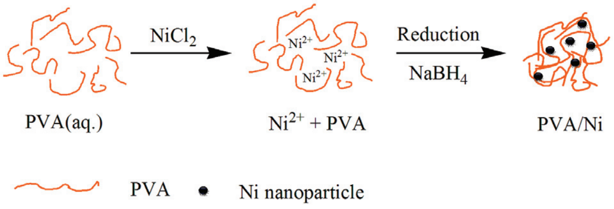

Scheme 1. One step preparation of PVA/Ni magnetic gel.

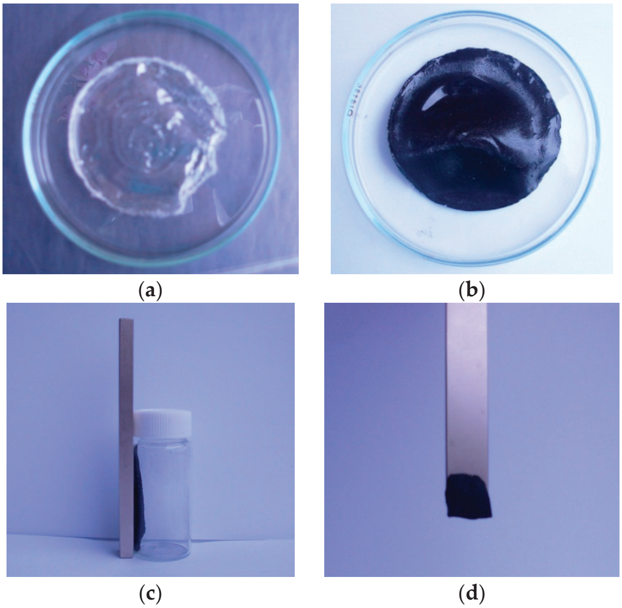
(**a**) (**b**) (**c**) (**d**)

Figure 1. Photographs of (**a**) PVA gel; (**b**) PVA/Ni magnetic gel; (**c**) Ni-nanoparticle (NPs) in the magnet field; (**d**) PVA/Ni magnetic gel in the magnet field.

3.2. Structural and Morphological Properties

To explore the sample morphology, FE-SEM micrographs are presented. Figure 2a–f shows Ni-NPs, PVA gel, and PVA gel with magnetite particles. The surface of Ni-NP PVA gel is rough (Figure 2c) compared to the surface of PVA gel (Figure 2b). The neat PVA gel showed a very smooth surface. Figure 2c shows a micrograph of a Ni PVA gel with pores of about 50 nm. Ni-NPs' formation was evident from the presence of spherical particles over the PVA gel (Figure 2e) compared to the pure Ni-NPs formed by the same reduction reaction in aqueous solution (Figure 2a). From the image in Figure 2c, it can be seen that the magnetic particles are distributed in a compact PVA matrix. The EDX spectrum of PVA gel containing 2.3% Ni (Figure 2d) confirmed the presence of Ni-NPs. The EDX results revealed the percentage of Ni in PVA to be 10.97 wt.%. It is, thus, presumed that Ni-NPs have good dispersion in PVA gel. Compare the FE-SEM micrograph of PVA gel containing 2.3% Ni (Figure 2c) with 4.5% Ni (Figure 2e); the higher the amounts of magnetic nanoparticles, the rougher the surface of the Ni-NP PVA gel is. The EDX results (Figure 2f) revealed the percentage of Ni in PVA to be 41.15 wt.%.

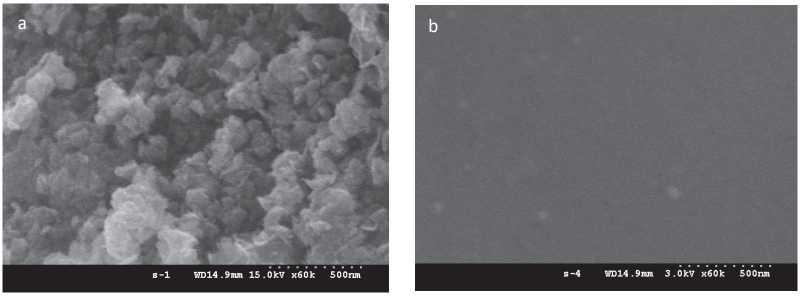

Figure 2. *Cont.*

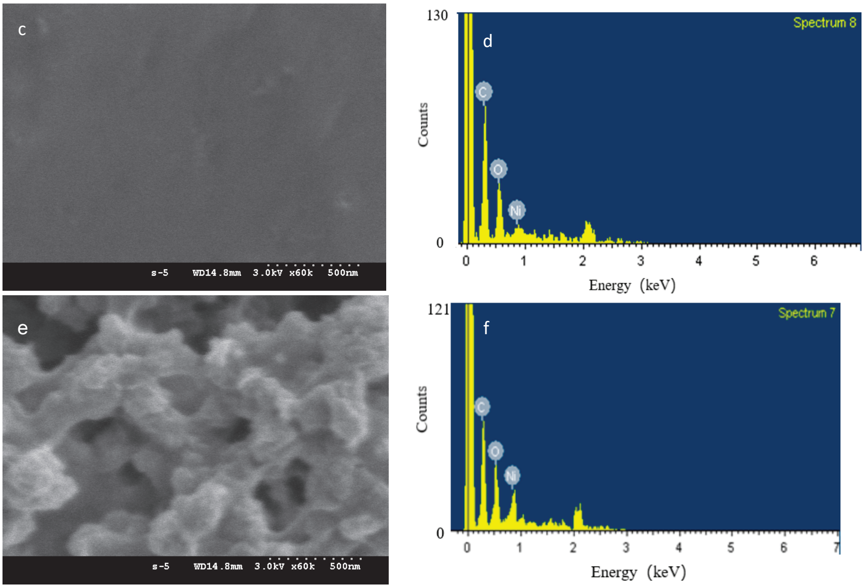

Figure 2. FESEM micrograph of (**a**) Ni-NPs; (**b**) PVA gel; (**c**) PVA gel containing 2.3% Ni; (**d**) EDX spectrum of PVA gel containing 2.3% Ni; (**e**) PVA gel containing 4.5% Ni; and (**f**) EDX spectrum of PVA gel containing 4.5% Ni.

Figure 3 shows the XRD spectra of PVA gel without or with Ni-NPs of different concentrations, and pure Ni-NPs obtained by the reduction reaction of nickel chloride with sodium borohydride. The XRD pattern of Ni-NPs (Figure 3d) shows that the products are metallic nickel. The average crystallite sizes were calculated from the peak broadening of XRD patterns by the Scherrer equation. The average size of the Ni-NPs was 7.0 nm. The X-ray diffractograms indicate a crystalline structure with some amorphosity of the disordered surface layers. The XRD spectra of Ni-NPs for 2θ values from 10° to 80° is similar to the literature, despite that an additional peak, the largest, at 2θ = 11.98° (intensity I_p = 100 u), was not mentioned [19]. The XRD Patterns do not correspond to face centered cubic (fcc) nickel with space group $Fm\bar{3}m$, but are indexed for a tetragonal crystal structure with space group 14/mcm [17]. Those peaks at 2θ = 24.96° (I_p = 7.0 u), 2θ = 34.06° (I_p = 16.2 u), 2θ = 36.03° (I_p = 3.7 u), 2θ = 45.04° (I_p = 6.8 u), 2θ = 60.00° (I_p = 8.7 u), and 2θ = 71.96° (I_p = 2.2 u) are attributed to (110), (002), (200), (211), (310), and (321) facets of the tetragonal crystal structure of Ni, respectively. The lattice parameters are a = 0.4887 nm and c = 0.4516 nm for the nickel nanoparticle sample.

Figure 3a–c compares the X-ray diffractograms of PVA gel containing different amounts of Ni-NPs. The interplaner distance was calculated. XRD patterns of the pure PVA gel (Figure 3a) indicate the characteristic peak for poly(vinyl alcohol) at a 2θ value of 19.82 with the inter planner distance of 0.4476. The same phenomenon has been observed by Clémenson et al. [20]. PVA, known to be semicrystalline in nature, shows a single broad peak. The relatively sharp and broad peak centered on about 19 indicates that the semicrystalline nature of the polymer PVA contains crystalline and amorphous regions. It is clear from Figure 3b,c that the peaks representing the tetragonal crystal structure of Ni in XRD disappear, indicating the conversion of nickel nanoparticle to the amorphous Ni-NP PVA gel. For both PVA gel with 1.5 mol% Ni and 2.3 mol% Ni-NPs, a broad peak centered on a 2θ value of about 19 is observed. It suggests the characteristic peak of PVA gel, indicating that the Ni-NP PVA polymer intercalation occurs with the formation of Ni-NPs within the polymer matrix. The amorphous broad band decreased for PVA gel containing 2.3% Ni, indicating the metal interacts with the polymer chain [21]. From the Figure 3a–c, comparing the XRD spectra of the bulk Ni-NPs, the smaller spectral intensity of the diffraction peak of PVA in the composite is due to the presence of a higher content of Ni-NPs in hydrogels.

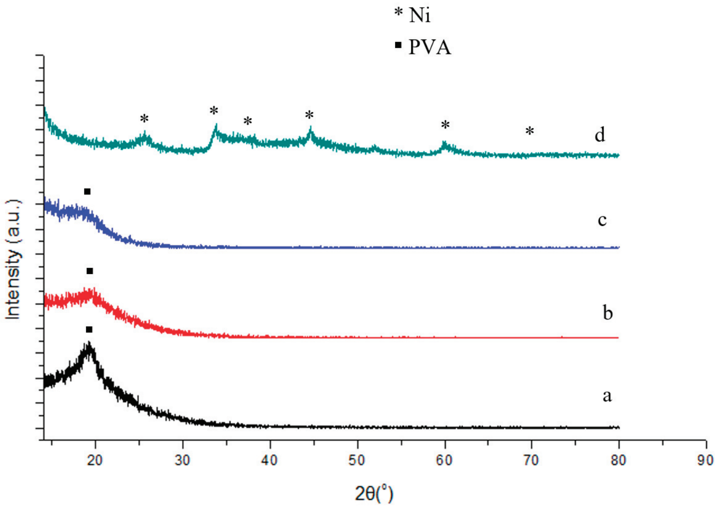

Figure 3. XRD patterns for PVA gel containing (**a**) 0% Ni; (**b**) 1.5% Ni; (**c**) 2.3% Ni; and (**d**) pure Ni nanoparticles.

3.3. Magnetic Properties

The magnetic properties of PVA gel with or without Ni-NPs of different concentration, and pure Ni-NPs were measured. Figure 4 shows the magnetization curves versus external magnetic field for neat PVA gel, or PVA gel with Ni-NPs of different concentration and pure Ni-NPs. Magnetization as a function of increasing external field up to 50 kOe at temperature of 5 K has been measured for selected samples. It can be found that the magnetization of pure Ni-NPs is obviously higher than other samples. The magnetic properties of Ni-NP PVA gel significantly changed with the composite formation. The magnetization of Ni-NP PVA gel is far weaker than that of the pure Ni-NPs. The greater the amount of Ni the Ni-NP PVA gel contains, the higher the value the magnetic moment shows at the same magnetic field. In contrast, the curve of the neat PVA gel is mostly flat. It is well known that the polymer is antimagnetic [22]. As shown in Figure 4, the curve of Ni-NPs shows that the magnetic moment does not reach full saturation even at 50 kOe. Among all these samples, the maximum magnetic moment value is 68.6 emu/g for pure Ni-NPs. The magnetization of the Ni-NPs and Ni-NP PVA gel samples increases quickly as the intensity of applied magnetic field increased below 10 kOe. The magnetization of the samples containing Ni increases slowly to reach saturation when the magnetic field above 10 kOe increases. The saturated magnetizations of the PVA gel containing 2.3 mol% Ni and PVA gel containing 4.5 mol% Ni at 50 kOe are 5.1 and 12.9 emu/g, respectively. Generally, the saturation of the magnetic moment increases with a higher amount of Ni-NPs. This is in agreement with the results of SEM and XRD.

In order to better understand the magnetic behavior, the samples were measured in the zero-field-cooled (ZFC) and field-cooled states (FC). The ZFC and FC measurements were performed by cooling the nanoparticles at zero field or in the presence of an external field. To obtain the ZFC measurement, the samples were cooled to 5 K in the absence of an external field. An external magnetic field of 1000 Oe was then applied to the samples. The magnetization was measured as the temperature was increased. The samples were then immediately cooled to 5 K in the presence of a magnetic field of 1000 Oe for the FC measurement. Figure 5a–c compares the magnetization versus temperature measured under ZFC and FC conditions for PVA gel without or with Ni-NPs of different concentration, and pure Ni-NPs, respectively. The effect of cooling is clearly observed. ZFC and FC magnetization curves split below T = 84, 54, and 35 K for PVA gels containing 2.3% Ni, 4.5% Ni, and the pure Ni gel, respectively. The difference in the magnetic moment signals is due to a two times larger amount of Ni in sample of PVA gel containing 4.5% Ni with respect to sample PVA gel containing 2.3% Ni, and the pure Ni without PVA. Samples of Ni-NP PVA gels and pure Ni nanoparticles present a significant magnetic irreversibility. The blocking temperature (T_B) of a magnetic nanoparticle can be measured where the FC and the ZFC curves diverge. The ZFC magnetization curve exhibits a peak around T = 15 K. This temperature indicates a collective freezing of magnetic moments. The signal of a magnetic moment is relatively weaker when the amount of Ni in the sample is lower. On the other hand, no temperature dependence is observed for the PVA without Ni sample. It is confirmed that pure PVA is diamagnetic. The results establish the role of Ni loading within the PVA polymer for the magnetic moments. Figure 5a–c indicates that for all the samples containing Ni, the temperature dependence of the magnetic moment does not follow Curie's law at temperatures above 100 K. The difference between PVA gel and Ni-NP PVA gel suggests that magnetic response of the Ni particles manifests a certain degree of magnetic interaction [23].

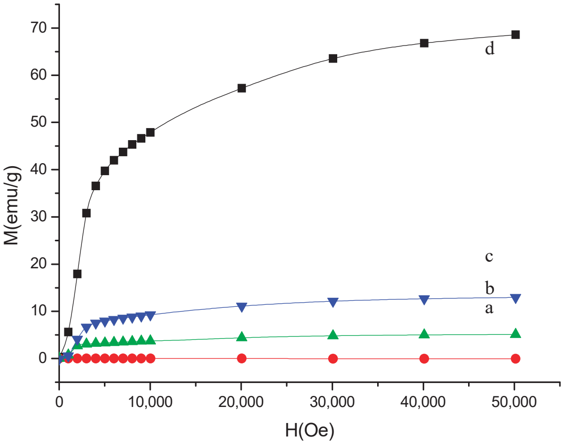

Figure 4. Magnetization curves of the PVA gel containing (**a**) 0% Ni; (**b**) 2.3% Ni; (**c**) 4.5% Ni; and (**d**) pure Ni nanoparticles.

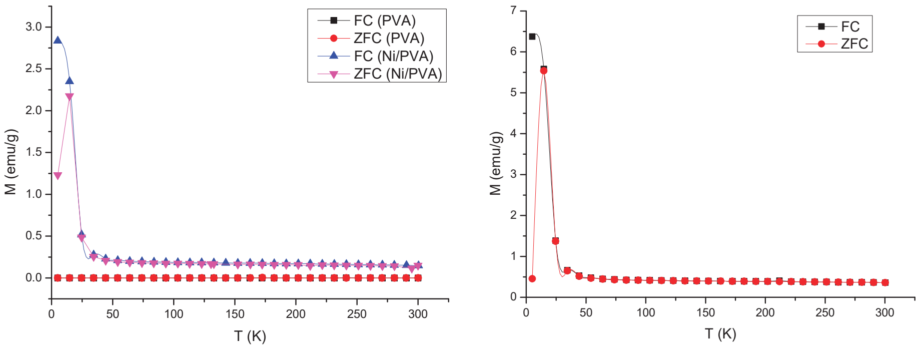

(**a**) (**b**)

Figure 5. *Cont.*

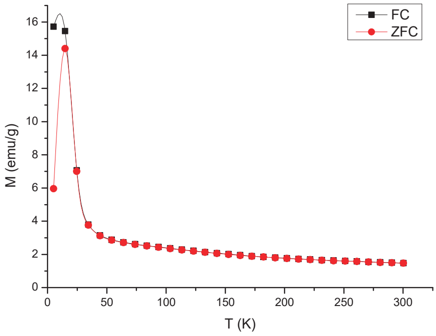

(c)

Figure 5. Field-cooling (FC) and zero-field-cooling (ZFC) magnetic moment curves measured for samples: (**a**) PVA gels containing 2.3% Ni; (**b**) 4.5% Ni; and (**c**) pure Ni nanoparticles. The lower curve of each sample represents the ZFC measurement and the upper one represents the FC measurement.

3.4. Thermogravimetric Analysis

To study the thermal changes in the PVA gels containing Ni, the samples were thermally characterized by TGA and DSC. A typical TGA curve of the PVA gel containing Ni is presented (Figure 6). The thermogram suggests that weight loss mainly occurs in three steps. First step corresponds to the loss of water molecules and slow removal of impurities from room temperature to 192 °C with a total weight loss of 14% in a PVA gel containing Ni. The second step corresponds to the removal of oligomers and the decomposition of PVA in the range of 266–294 °C with a weight loss of 29% [22]. The third step corresponds to the degradation of polymeric backbone in the range of 385–986 °C with a weight loss of 48% in the sample. At last, about 5% weight residue remained at a temperature above 986 °C, due to the Ni magnet. There is nearly no residue that remained above 986 °C in the PVA alone. This result is consistent with Khanna et al. [18]. Figure 6 shows the DSC thermogram of the PVA gel containing Ni [24].

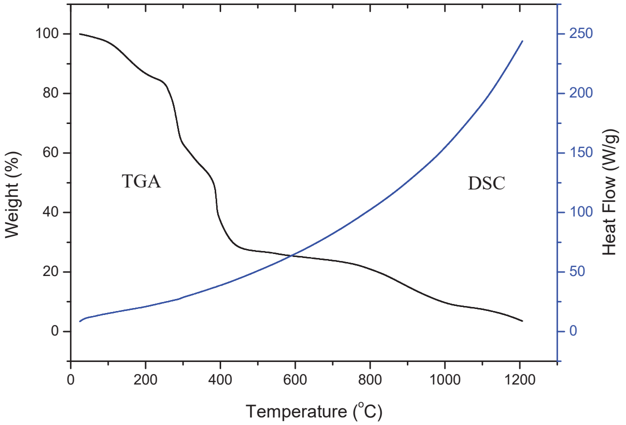

Figure 6. TGA curve and DSC plot of Ni-NP PVA gel.

3.5. Swelling Studies

Swelling experiments can yield important information concerning the stability of PVA gels in solution [25]. It can also be used to trigger drug release by controlling the hydrogel swelling properties. Water uptake was measured to determine the swelling abilities of the hydrogels. This is most commonly used to evaluate the effects of different synthesis methods of PVA on water transport. The swelling kinetic curves of the hydrogels are shown in Figures 7 and 8. Figure 7 shows the dimension changes as a function of the exposure time for different PVA gels containing nickel in the amounts of 0 mol%, 1.5 mol%, 2.3 mol%, and 4.5 mol%. The mass change as a function of time from 5 min to 24 h for different hydrogels in water is shown in Figure 7. From Figures 7 and 8, the samples attained their maximum swelling ratio at about 16 h. The results of the dimension changes are in agreement with the results of the mass changes. The equilibrium water contents in swollen samples (W_e) were 364.60%, 312.36%, 230.16%, and 166.67% for neat PVA gel, and PVA gels with 1.5 mol%, 2.3 mol%, and 4.5 mol% Ni-NPs, respectively. From both Figures 7 and 8, it can be observed that the swelling ratio decreases as the amount of Ni-NPs in a PVA gel increases. The NPs have effect an on the swelling properties of the PVA gel by a simply physical method. The interaction of the PVA chains with Ni-NPs might induce the formation of low-mobility regions that can act as additional physical cross-linking points. The swelling ratio decreases with the presence of NPs, pointing to an increase of the physical crosslinking density as reported for the formation of PVA ferrogels through a freezing–thawing procedure [26].

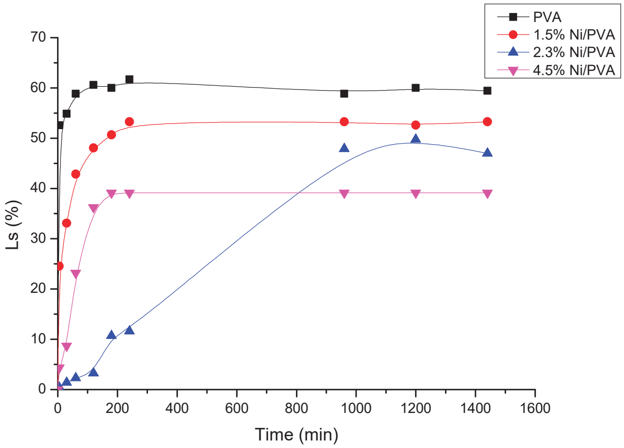

Figure 7. Dimension change (L_s) versus immersion time for PVA gel and PVA/Ni magnetic gel.

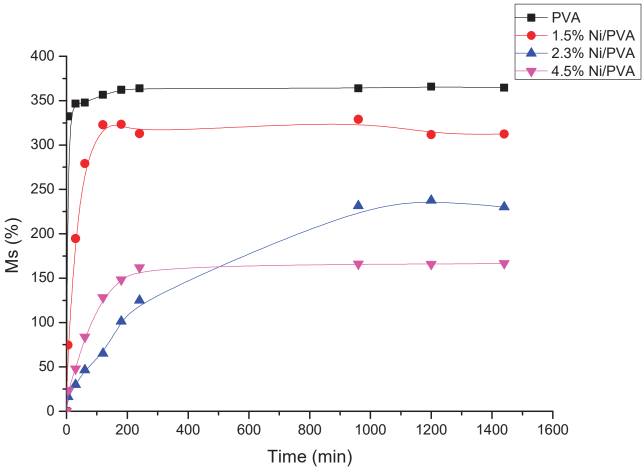

Figure 8. Water absorption (M_s) as a function of the exposure time for PVA/Ni magnetic gel.

3.6. Drug Loading and Release

To design the magnetic polymer for the anti-cancer drug delivery system, a well-known anti-cancer drug was needed. It was convenient to investigate the drug release properties in vitro. Furthermore, regarding swollen polymers—the drug is in an aqueous environment; its water solubility becomes an important consideration. As one of the most common anti-cancer drugs, DOX was chosen in this study to model the release action of anti-cancer drug from Ni-NP PVA gel. Most of the DOX was up-taken about in 24 h. A loading capacity of about 96% of the drug weight was determined. This result was used for the evaluation of the cumulative release of DOX. To investigate the drug delivery properties, Ni-NP PVA gels with a cargo amount of 5.8 mg/g were studied.

The release kinetics measured for Ni-NP PVA gel under two different conditions of 25 °C and 37 °C is shown in Figure 9. Both curves were measured by the UV-vis absorbance in water. From the figure, the curve with temperature of 25 °C shows a relatively low cumulative release of DOX. The corresponding cumulative release rapidly achieves the level of about 10% in 10 h. About 15% of the drug was released in 48 h. The release rate was much higher with the temperature of 37 °C. The corresponding cumulative release rapidly achieved the level of about 39% in 10 h. In total, 73% of drug was released in 48 h. This probably manifests through the fact that the Ni-NP PVA gel is made from simply physical cross-linking. This kind of gel is flexible when put in wet or very humid conditions under high temperatures. To study the release behaviors of the Ni-NP PVA gel, the cumulative release ratio (M_t/M_∞) was calculated based on the classic Korsmeyer-Peppas equation [27]. M_t/M_∞ is the fraction of drug released after time t relative to the amount of drug released at infinite time. There are two stages in the drug release curve. The initial diffusion of drugs mainly happened in the outermost layer of the Ni-NP PVA gel. At that stage, the drug released rapidly. At the second stage, the release was under diffusion's control and the drug released relatively slowly.

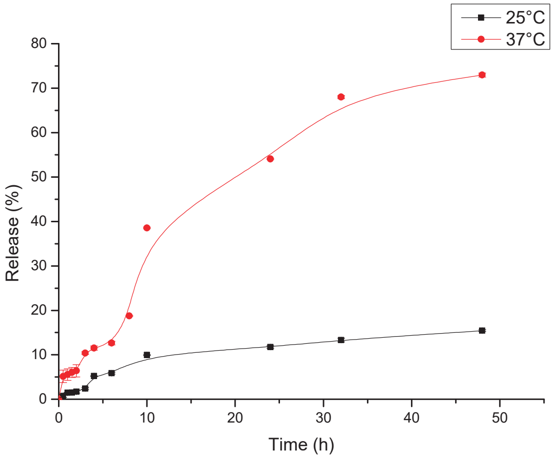

Figure 9. Drug release profiles of Ni-NP PVA gel in water.

4. Conclusions

The magnetic hydrogels have sparked particular interest in the anti-cancer drug delivery applications. PVA is a type of biocompatible material used for biomedicine. In this work, a new kind of nickel nanoparticle-based magnetic PVA gel was synthesized by a one-step procedure. The nickel nanoparticles and cross-linked mPVA gels were formed simultaneously. The structural and morphological properties of Ni-NP PVA gel were measured by FE-SEM and X-ray diffraction. The surface of Ni-NP PVA gel was rougher than that of the neat PVA gel. The amount of Ni-NPs detected was consistent with the theoretical value. The peak of PVA in the XRD spectra was weaker than that of Ni-NP PVA gel. The magnetic and thermal properties were also measured. With a higher amount of Ni-NPs, Ni-NP PVA gel had higher magnetic moments. There are noteworthy features for the Ni-NP PVA gel in terms of ferromagnetism and thermally stability. All measurements confirmed the good formation of the Ni-NP PVA gel. The release of DOX showed diffusion control in vitro. With a higher temperature, the release rate of DOX was higher. The Ni-NP PVA gels are expected to be applied for controlled drug delivery. The novel, simple synthetic method can be used to form other magnetic gels for biotechnology.

Author Contributions: Conceptualization, K.-P.L.; methodology, A.I.G.; data curation, J.L.; writing—original draft preparation, J.L.; visualization, J.L.; supervision, K.-P.L.; project administration, K.-P.L. and A.I.G.; funding acquisition, K.-P.L.

Funding: This research received no external funding.

Conflicts of Interest: The authors declare no conflict of interest.

References

1. Teodorescu, M.; Bercea, M.; Morariu, S. Biomaterials of PVA and PVP in medical and pharmaceutical applications: Perspectives and challenges. *Biotechnol. Adv.* **2019**, *37*, 109–131. [CrossRef] [PubMed]
2. DeMerlis, C.; Schoneker, D. Review of the oral toxicity of polyvinyl alcohol (PVA). *Food Chem. Toxicol.* **2003**, *41*, 319–326. [CrossRef]
3. Aisida, S.O.; Akpa, P.A.; Ahmad, I.; Maaza, M.; Ezema, F.I. Influence of PVA, PVP and PEG doping on the optical, structural, morphological and magnetic properties of zinc ferrite nanoparticles produced by thermal method. *Phys. B Condens. Matter* **2019**, *571*, 130–136. [CrossRef]
4. Arruebo, M.; Fernández-Pacheco, R.; Ibarra, M.R.; Santamaría, J. Magnetic nanoparticles for drug delivery. *Nano Today* **2007**, *2*, 22–32. [CrossRef]
5. Weeber, R.; Hermes, M.; Schmidt, A.M.; Holm, C. Polymer architecture of magnetic gels: A review. *J. Phys. Condens. Matter* **2018**, *30*, 063002. [CrossRef] [PubMed]
6. Veloso, S.R.S.; Ferreira, P.M.T.; Martins, J.A.; Coutinho, P.J.G.; Castanheira, E.M.S. Magnetogels: Prospects and main challenges in biomedical applications. *Pharmaceutics* **2018**, *10*, 145. [CrossRef]
7. Indira, T.K.; Lakshmi, P.K. Magnetic nanoparticles: A review. *Int. J. Pharm. Sci. Nanotechnol.* **2010**, *3*, 1035–1042.
8. Hoare, T.R.; Kohane, D.S. Hydrogels in drug delivery: Progress and challenges. *Polymer* **2008**, *49*, 1993–2007. [CrossRef]
9. Mok, H.; Zhang, M. Superparamagnetic iron oxide nanoparticle-based delivery systems for biotherapeutics. *Expert Opin. Drug Deliv.* **2013**, *10*, 73–87. [CrossRef]
10. De France, K.J.; Xu, F.; Hoare, T. Structured macroporous hydrogels: Progress, challenges, and opportunities. *Adv. Healthc. Mater.* **2018**, *7*, 17. [CrossRef]
11. Klostergaard, J.; Seeney, C.E. Magnetic nanovectors for drug delivery. *Nanomed. Nanotechnol. Biol. Med.* **2012**, *8*, S37–S50. [CrossRef] [PubMed]
12. McBain, S.C.; Yiu, H.H.; Dobson, J. Magnetic nanoparticles for gene and drug delivery. *Int. J. Nanomed.* **2008**, *3*, 169.
13. Hanf, A.; Oelze, M.; Manea, A.; Li, H.; Münzel, T.; Daiber, A. The anti-cancer drug doxorubicin induces substantial epigenetic changes in cultured cardiomyocytes. *Chem. Biol. Interact.* **2019**, *313*, 108834. [CrossRef] [PubMed]
14. Zhou, P.; Wu, S.; Hegazy, M.; Li, H.; Xu, X.; Lu, H.; Huang, X. Engineered borate ester conjugated protein-polymer nanoconjugates for pH-responsive responsive drug delivery. *Mater. Sci. Eng. C Mater. Biol. Appl.* **2019**, *104*, 109914. [CrossRef]
15. Fernandes, T.; Santos, E.; Madriaga, V.; Bessa, I.; Nascimento, V.; Garcia, F.; Ronconi, C. A self-assembled AMF-responsive nanoplatform based on Pillar[5]arene and superparamagnetic nanoparticles for controlled release of doxorubicin. *J. Braz. Chem. Soc.* **2019**, *30*, 2452–2463. [CrossRef]
16. Rao, K.K.; Ha, C.S. pH Sensitive hydrogels based on acryl amides and their swelling and diffusion characteristics with drug delivery behavior. *Polym. Bull.* **2009**, *62*, 167–181.

17. Riveiro, J.M.; Roy, A.; Srinivas, V.; Ram, S.; De Toro, J.A. Effect of interstitial oxygen on the crystal structure and magnetic properties of Ni nanoparticles. *J. Appl. Phys.* **2004**, *96*, 6782.
18. Khanna, P.; Singh, N.; Charan, S.; Subbarao, V.; Gokhale, R.; Mulik, U. Synthesis and characterization of Ag/PVA nanocomposite by chemical reduction method. *Mater. Chem. Phys.* **2005**, *93*, 117–121. [CrossRef]
19. Srinivas, V.; Barik, S.; Bodo, B.; Karmakar, D.; Rao, T.C. Magnetic and electrical properties of oxygen stabilized nickel nanofibers prepared by the borohydride reduction method. *J. Magn. Magn. Mater.* **2008**, *320*, 788–795. [CrossRef]
20. Clemenson, S.; Léonard, D.; Sage, D.; David, L.; Espuche, E. Metal nanocomposite films prepared In Suite from PVA and silver nitrate. Study of the nanostructuration process and morphology as a function of the in suite routes. *J. Polym. Sci. Part A Polym. Chem.* **2008**, *46*, 2062–2071. [CrossRef]
21. Bhajantri, R.; Ravindrachary, V.; Harisha, A.; Crasta, V.; Nayak, S.P.; Poojary, B. Microstructural studies on $BaCl_2$ doped poly(vinyl alcohol). *Polymer* **2006**, *47*, 3591–3598. [CrossRef]
22. Reddy, K.R.; Lee, K.P.; Gopalan, A.I.; Kang, H.D. Organosilane modified magnetite nanoparticles/poly (aniline-co-o/m-aminobenzenesulfonic acid) composites: Synthesis and characterization. *React. Funct. Polym.* **2007**, *67*, 943–954. [CrossRef]
23. Couto, G.G.; Klein, J.J.; Schreiner, W.H.; Mosca, D.H.; De Oliveira, A.J.; Zarbin, A.J.; Zarbin, A.J.G. Nickel nanoparticles obtained by a modified polyol process: Synthesis, characterization, and magnetic properties. *J. Colloid Interface Sci.* **2007**, *311*, 461–468. [CrossRef] [PubMed]
24. Reddy, C.S.; Sharma, A.; Rao, V.N. Electrical and optical properties of a polyblend electrolyte. *Polymer* **2006**, *47*, 1318–1323. [CrossRef]
25. Hassan, C.M.; Peppas, N.A. Structure and morphology of freeze/thawed PVA hydrogels. *Macromolecules* **2000**, *33*, 2472–2479. [CrossRef]
26. Gonzalez, J.S.; Hoppe, C.E.; Muraca, D.; Sánchez, F.H.; Alvarez, V.A. Synthesis and characterization of PVA ferrogels obtained through a one-pot freezing-thawing procedure. *Colloid Polym. Sci.* **2011**, *289*, 1839–1846. [CrossRef]
27. Zhou, L.; He, B.; Zhang, F. Facile one-pot synthesis of iron oxide nanoparticles cross-linked magnetic poly(vinyl alcohol) gel beads for drug delivery. *ACS Appl. Mater. Interfaces* **2011**, *4*, 192–199. [CrossRef]

coatings

MDPI

Article

Proteomic Analysis of Biomaterial Surfaces after Contacting with Body Fluids by MALDI-ToF Mass Spectroscopy

Makoto Hirohara [1,†], Tatsuhiro Maekawa [1,†], Evan Angelo Quimada Mondarte [1], Takashi Nyu [1], Yoshiki Mizushita [1] and Tomohiro Hayashi [1,2,3,*]

[1] Department of Materials Science and Engineering, School of Materials and Chemical Technology, Tokyo Institute of Technology, 4259 Nagatsuta-cho, Midori-ku, Yokohama, Kanagawa 226-8502, Japan; hirohara.m.aa@m.titech.ac.jp (M.H.); maekawa.t.af@m.titech.ac.jp (T.M.); mondarte.e.aa@m.titech.ac.jp (E.A.Q.M.); nyutaa7@gmail.com (T.N.); shiki.mizu.3322@gmail.com (Y.M.)

[2] Surface and Interface Science Laboratory, RIKEN, 2-1 Hirosawa, Wako, Saitama 351-0198, Japan

[3] JST-PRESTO, 4-1-8 Hon-cho, Kawaguchi, Saitama 332-0012, Japan

[*] Correspondence: tomo@mac.titech.ac.jp; Tel.: +81-45-924-5400

[†] These authors contributed equally to this work.

Received: 22 October 2019; Accepted: 17 December 2019; Published: 22 December 2019

Abstract: We developed a method to identify proteins adsorbed on solid surfaces from a solution containing a complex mixture of proteins by using Matrix-Assisted Laser Desorption/Ionization-Time of Flight mass (MALDI-ToF mass) spectroscopy. In the method, we performed all procedures of peptide mass fingerprint method including denaturation, reduction, alkylation, digestion, and spotting of matrix on substrates. The method enabled us to avoid artifacts of pipetting that could induce changes in the composition. We also developed an algorithm to identify the adsorbed proteins. In this work, we demonstrate the identification of proteins adsorbed on self-assembled monolayers (SAMs). Our results show that the composition of proteins on the SAMs critically depends on the terminal groups of the molecules constituting the SAMs, indicating that the competitive adsorption of protein molecules is largely affected by protein-surface interaction. The method introduced here can provide vital information to clarify the mechanism underlying the responses of cells and tissues to biomaterials.

Keywords: protein identification; matrix-assisted laser desorption/ionization-time of flight; proteomics; quartz crystal microbalance; self-assembled monolayer

---

1. Introduction

Scaffolding protein in extracellular matrices (ECM) plays a significant role in determining cellular responses. There are many situations where the scaffolding proteins govern the cellular responses—biodevices implanted in a body [1], patterning of cells on solid substrates [2], and general cell culturing in dishes, among others. For the thorough understanding of the mechanism underlying the cellular behavior, we need to clarify the properties of the layer of the scaffolding proteins [3,4].

Investigation of the adsorbed proteins has been done mostly in terms of the amount of adsorption. They are measured with surface plasmon resonance (SPR) spectroscopy [5], quartz crystal microbalance (QCM) [6–8], and surface acoustic wave spectroscopy (SAW) [9–11] for real-time adsorption kinetic measurements; and X-ray photoelectron spectroscopy (XPS) [12,13], Fourier transform infrared absorption spectroscopy (FTIR) [14–16], and fluorescence microscopy with labeling molecules [17,18] for samples in dry state after adsorption.

In contrast with the number of proteins in the scaffolding layer, the composition of proteins in the protein layers formed on biomaterials after contacting body fluids or cell-culturing media has not been intensively studied even though this information is essential for the understanding of the mechanism underlying the responses of the adhered cells to materials. In general, the identification of proteins in solution is carried out by a peptide mass fingerprint method [19]. In this method, the proteins in the solution are separated first by electrophoresis [20]. Then, the separated proteins are fragmented into peptides by digestion with trypsin. Finally, the proteins can be identified from the pattern of the peaks in the Matrix Assisted Laser Desorption/Ionization-Time of Flight mass (MALDI-ToF mass) spectrum. However, in the case of the scaffolding proteins on the surface of biomaterials, especially on small surface areas, this procedure is difficult to employ because the total amount of adsorbed proteins is often not enough for a reliable and efficient separation by electrophoresis which, in general, requires ~20–30 μg of proteins.

Several works that overcame the problem have been reported. One is the usage of nanoparticles to acquire a large interfacial area between materials and proteins [21]. However, this approach is not universal because many biomaterials cannot be fabricated in the form of nanoparticles. Another is the proteomic analysis of membrane filters for hemodialysis wherein the proteins adsorbed on the membrane filters after hemodialysis were collected by an eluting solvent and then isolated by electrophoresis followed by MALDI-ToF mass measurements [22,23]. Like the first example, this approach also has the merit of having a larger interfacial area. Unfortunately, this method cannot be employed for biomaterials with a flat surface. Moreover, proteins with relatively high hydrophobicity can easily adhere to the walls of pipets resulting in the change in the composition of the protein and thus greatly affects the results especially for a small collection of proteins [24]. Therefore, it is important to perform all steps of the proteomic analysis directly on the surface of the materials. Although this approach was already performed by Kirschhofer et al., who have succeeded in the identification of the adsorbed proteins, the proteins used in their reports consist of only three kinds with known compositions [25].

In this work, we performed the full peptide mass fingerprint method on the biomaterial surfaces and obtained mass spectra by MALDI-ToF mass spectroscopy of the adsorbed proteins from the more complex protein serum. To extract the composition of the adsorbed proteins from the resulting complex spectra, we developed an algorithm to give assignments to the peaks by collating the experimental and theoretical peak positions of peptide fragmented from the serum proteins. Furthermore, we established a method to evaluate the molar ratio between proteins in the scaffolding layer. In general, the composition of proteins strongly depends on the analytical techniques used [26–29]. To solve this problem, we thereby employed a method to evaluate molar ratios between proteins by using the results obtained from original standard samples with a known molar ratio. We believe that our method may shed light on the role of the scaffolding layer in determining the fates of cells or tissues after being in contact with biomaterials.

2. Materials and Methods

2.1. Self-Assembled Monolayers and Their Substrates

Metal substrates for self-assembled monolayers (SAMs) of alkanethiols were prepared by thermal evaporation under vacuum (base pressure: 4×10^{-6} Pa). A 5-nm Ge (adhesion promoter) was first deposited on a glass plate (18×18 mm^2, Matsunami glass inc. Ltd., Oosaka, Japan) followed by the deposition of 100-nm Au film. The glass plates underwent prior cleaning by sonication in ethanol, then in pure water, and lastly dried with nitrogen gas.

Fabrication of the SAMs was carried out by immersing the substrates in a thiol solution in ethanol (0.1 mM) for 24 h. We used five kinds of thiols in this work (Table 1) [Sigma-Aldrich (St. Louis, MI, USA) and ProChimia Surfaces (Gdansk, Poland)]. After the immersion, the samples were carefully rinsed with pure ethanol to remove the physisorbed thiol molecules from the surface.

Table 1. Thiols used in this work and their chemical structures.

Abbreviation	Chemical Structure of the Thiol Molecules
C8	$HS–(CH_2)_7–CH_3$
COOH	$HS–(CH_2)_{11}–COOH$
OH	$HS–(CH_2)_{11}–OH$
NH2	$HS–(CH_2)_{11}–NH_2$
EG3–OH	$HS–(CH_2)_{11}–(O–CH_2–CH_2)_3–OH$

2.2. QCM Measurements

The amounts of proteins adsorbed onto the SAMs from protein solution and fetal bovine serum (FBS) (Equitech-Bio Inc, Kerrville, TX, USA, lot number: SFBM30-2485) were measured by QCM (D300 Q-Sense, Gothenburg, Sweden). The sensors were cleaned by UV-Ozone treatment, followed by rinsing with ethanol and pure water. The fabrication of the SAMs on the Au-coated QCM sensors was done with the same procedure as the case of the Au/Ge/glass substrates. For the adsorption of bovine serum albumin (BSA) (Sigma-Aldrich, St. Louis, MI, USA) and fibrinogen (Biogenesis, Poole, England), we prepared the protein solution by dissolving the proteins in phosphate buffer saline (PBS) (Sigma Aldrich, St. Louis, MI, USA) at a concentration of 1 mg/mL. For the adsorption of proteins from the serum, the FBS was diluted to 20% in volume with PBS.

In the QCM measurements, the measurement cell was first filled with PBS for background measurements, then the protein or serum solution was injected. After the frequency shift was equilibrated, PBS was injected again for rinsing. All measurements were performed at 25 °C We calculated the amount of the adsorbed protein from the Sauerbrey equation (Equation (1))

$$\Delta m = -\frac{C \cdot \Delta f}{n}, \tag{1}$$

where C, Δf, n are the conversion constant (17.7 ng cm^{-2} Hz^{-1}), change in the resonant frequency and overtone number (n = 3 in this work), respectively.

2.3. Formation of Protein Layer on SAMs from FBS for Peptide Mass Fingerprinting

To form a layer of serum proteins on the SAMs, 50 μL of the 20% (v/v) FBS were placed on the SAMs for 24 h at room temperature. Then, the SAMs were rinsed with PBS buffer and dried in air.

2.4. Digestion of the Serum Proteins Adsorbed on the SAMs

The procedure of the preparation of samples for MALDI-ToF mass measurements (denaturation, reduction, alkylation, digestion, and spotting of a matrix) is summarized in Figure 1. A mixture of 25 μL of 10 mM ammonium bicarbonate aqueous solution (Wako, Osaka, Japan), 25 μL of 2,2,2-trifluoroethanol (Wako, Osaka, Japan), and 10 μL of 20 mM dithiothreitol aqueous solution (Sigma-Aldrich, St. Louis, MI, USA) was placed on the dried protein layer then was left still in an oven at 60 °C under atmospheric pressure for 45 min to denature and reduce the adsorbed proteins. Then, the sample was taken out from the oven, cooled to room temperature, added with 40 μL of 20 mM iodoacetamide (Sigma-Aldrich, St. Louis, MI, USA) aqueous solvent to allow alkylation, and was allowed to stand at room temperature for 1 h. In order to quench the iodoacetamide aqueous solvent, 10 μL of an aqueous dithiothreitol solution used in the reduction was added and then dried at 60 °C under vacuum. Next, the proteins underwent digestion with trypsin (Promega, Madison, WI, USA). A 200 μL of trypsin-acetic acid solution was prepared by dissolving 20 μg trypsin in 1 mM acetic acid (Promega, Madison, WI, USA). A 10-μL aliquot of the trypsin-acetic acid solution was mixed with 30 μL of a 10 mM ammonium hydrogen carbonate aqueous solution, and 10 μL of the mixture was dropped onto the sample and kept for 4 h. To stop the digestion, 50 μL of 10% trichloroacetic acid (Wako, Osaka, Japan) was added and then the samples were dried in a desiccator at 60 °C. The digestion of proteins in 20% (v/v) FBS was performed with the same procedure.

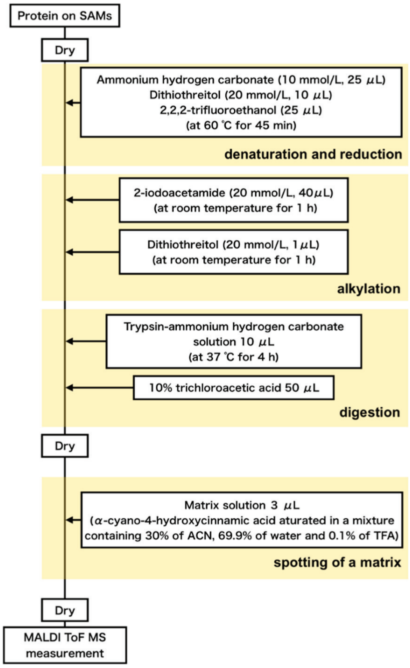

Figure 1. Flow of preparation of samples for MALDI-ToF mass spectroscopic measurements.

The samples were fixed on a slide glass coated with an indium tin oxide (ITO) film with carbon tape. To be able to check if the samples are of the same height level, a commercial peptide solution (Peptide Calibration Standard II: PCS II) (Bruker, Billerica, MA, USA) was placed on all the samples. After that, the matrix solution (α-cyano-4-hydroxycinnamic acid (Sigma-Aldrich, St. Louis, MI, USA)) saturated in a mixture containing 30% of acetonitrile (Wako, Osaka, Japan), 69.9% of water and 0.1% of trifluoracetic acid (TFA) (Wako, Osaka, Japan) is placed on the samples to be measured then dried. The height of the samples was adjusted by placing blank substrates with the same thickness as a spacer at the corners (Figure 2).

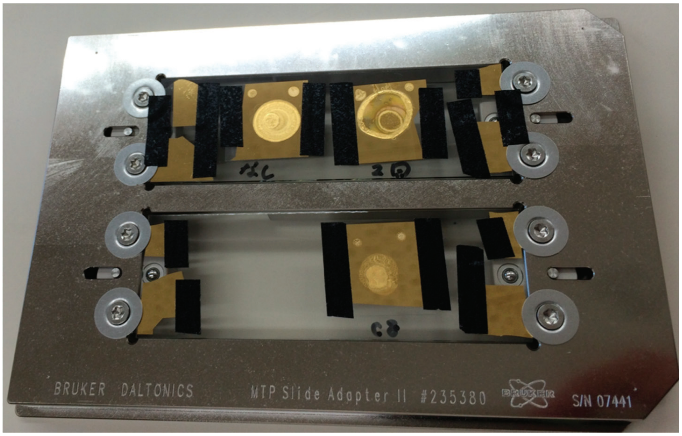

Figure 2. Samples (protein/SAM/Au/Ge/glass) fixed on a MALDI target plate after all the processes presented in Figure 1.

2.5. Standard Samples to Calibrate Peak Intensity

A mixture of proteins of interest with a known ratio was prepared to calibrate the effect of ionization of peptides, which is dependent on the peptide sequence, on their intensities in mass spectra. In this work, we dissolved BSA, vitronectin, and fibronectin in PBS and prepare the mixed solution at a molar ratio of 1:1.29:0.255 (weight ratio of 1:1:1). This solution was spotted on an ITO substrate and processed as the same procedure as the case of serum proteins on the SAMs.

2.6. MALDI-ToF Mass Spectroscopic Measurements

We used a commercial MALDI-ToF mass spectrometer (ultrafleXtreme, Bruker Daltonics, Billerica, MA, USA) for our measurements. Mass spectra in the range of 500 to 4000 Da were measured in the positive-ion reflector mode with 5000 laser shots with raster. FlexAnalysis software (Bruker Daltonics, Billerica, MA, USA) was used to assign peaks. For each sample, 10 spectra obtained at different positions of the substrates were accumulated after the calibration of m/z values (linear offset in m/z) using the fragment peak from BSA (m/z = 927.49). We prepared two samples for each SAM and measured 15 spectra for each sample giving a total of 30 spectra for each SAM.

2.7. Analysis of the Obtained Mass Spectra

2.7.1. Finding m/z Values Unique for Proteins of Interest

From the complex spectra we obtained, we attempted to find m/z values unique for each protein. Basing on the top 20 abundant proteins plus the proteins associated with cell adhesion (fibronectin and vitronectin) (Table 2) in FBS, we constructed a list of all possible fragments after digestion using a WEB-based database of ExPASy (https://www.expasy.org/) [30,31]. We omitted m/z values that are close to each other within 0.5 Δm/z. Furthermore, we also removed m/z values that are close ($0 \leq$ m/z < 3) to that of the isotopes of the peptide fragments of BSA, because BSA is dominant (around 60%) in serum and even the isotopes of its fragments exhibit peaks with considerable intensity. Finally, from the remaining m/z values for each protein, we selected the one with the highest intensity in the spectra and denote as the 'reference m/z' hereafter (Figure 3).

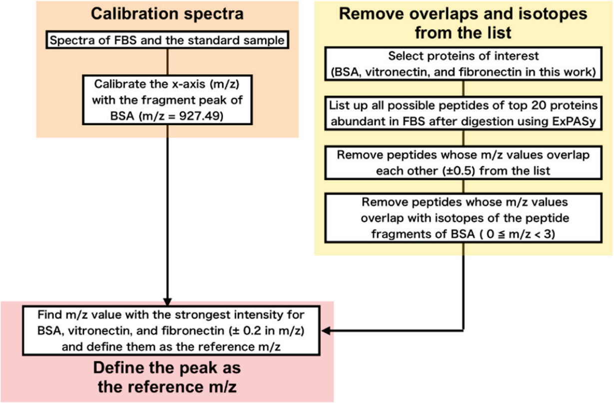

Figure 3. Procedure for determination of the reference m/z values.

Table 2. Proteins of interest in serum (abundant and those with RGD moieties), their molecular weights, and reference m/z obtained by the procedure presented in Figure 3.

Protein	Molecular Weight	Reference m/z
Serum albumin	69,293	927.493
Alpha-1-antiproteinase	46,104	873.468
Plasminogen	91,216	1426.640
Cone cGMP-specific 3′,5′-cyclic phosphodiesterase subunit alpha′	98,798	1476.690
Lactoperoxidase	80,642	1423.830
NADH-ubiquinone oxidoreductase 75 kDa subunit	79,468	2048.070
Alpha-2-HS-glycoprotein	38,419	2058.130
Kininogen-2	68,710	1998.000
hemiferrin	24,091	1715.900
Integrin beta-1	88,094	1436.670
Prothrombin	70,506	1716.890
Apolipoprotein A-I	30,276	1772.920
Antithrombin-III	52,347	2062.050
Beta-2-glycoprotein 1	38,252	1475.770
Alpha-2-antiplasmin	54,711	1728.820
Protein AMBP	39,235	2058.930
Hemoglobin fetal subunit beta	15,859	1434.670
Alpha 1-antichymotrypsin	28,571	2210.180
Apolipoprotein A-II	11,202	657.324
Hemoglobin subunit alpha	15,184	2986.440
fibronectin	272,154	1323.710
vitronectin	53,615	946.489

2.7.2. Conversion from Peak Intensities to Molar Ratio

The peak intensity in the mass spectrum linearly correlates to the concentration of the peptide in the sample [32]. However, the dependence of the signal intensity on the sequences of peptide must be calibrated. In this work, we employ Equation (2) to evaluate molar ratios,

$$M_{a/b} = \frac{I_a}{I_b} \cdot K_{a/b}, \tag{2}$$

where I, M, and K are the intensities of the reference peaks, molar ratio between two proteins, and coefficients to calibrate the intensity and molar ratios, respectively. Using the standard sample with known composition, $K_{\text{vitronectin/BSA}}$ and $K_{\text{fibronectin}/\text{BSA}}$ were calculated to be 0.302 and 1.51, respectively.

3. Results and Discussion

First, we verified whether the processes of the digestion affect the spectral patterns. Figure 4 compares the spectra obtained from proteins digested in different environments—on substrate and in solution. The overall intensity of the spectrum (a) is about 10 times weaker than that of the spectrum (b), which is rationalized by the total amounts of BSA molecules measured. The peak positions assigned to the fragments of BSA and the relative ratio between the peaks of the fragments are consistent, indicating that the digestion of BSA on C8-SAM provides the same result as in solution. It should be noted that there is disagreement in the peak intensity of the other peaks. A possible reason is a different ratio among BSA, trypsin, and other chemicals in the different environments of digestion.

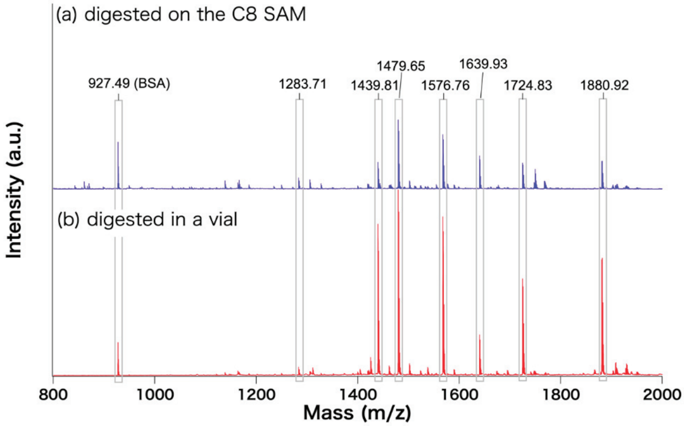

Figure 4. MALDI-ToF mass spectra of digested BSA. (**a**) BSA adsorbed on the C8 SAM then digested (procedure shown in Figure 2) (**b**) BSA was digested in a vial and measured on an C8 SAM.

The results of the adsorption tests with proteins of single composition (Figure 5) showed that EG3-OH exhibited strong resistance to fibrinogen and BSA, whereas the other SAMs adsorbed these proteins. These results are consistent with previous findings reported from our group and others [33–38] showing that SAMs of oligo(ethyleneglycol)-terminated alkanethiols exhibit strong protein-resistance to various proteins at relatively low concentrations of protein solution (typically < 2 mg/mL). In contrast with the adsorption of single protein at low concentration, the results of adsorption tests with the serum diluted to 20% with PBS revealed that all the SAMs used in this work adsorbed serum proteins. Considering that the adsorption amount of about 100 ng/cm^2 corresponds to a monolayer of fibrinogen [35], all the SAMs were certainly covered with a layer of serum proteins. It should also be noted that this concentration of serum employed in this work is often used for cell culturing. There is strong dependence of the amounts of adsorbed proteins on both the concentration and composition of the proteins in the original solution [39]. This is one of the good examples that demonstrate that conventional protein adsorption assays cannot predict the protein adsorption from serum or other body fluids.

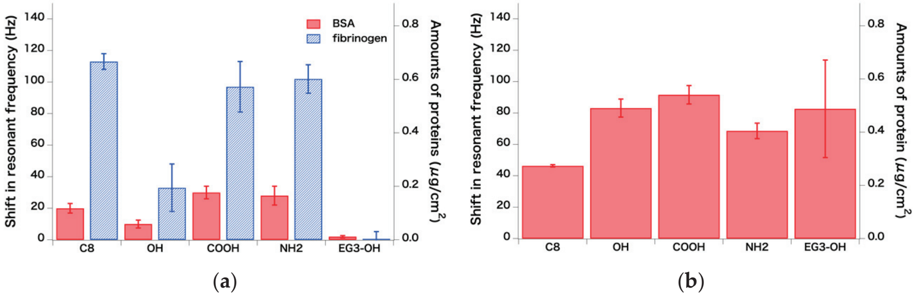

(**a**) (**b**)

Figure 5. Amounts of adsorbed proteins and changes in the resonant frequency measured by QCM. (**a**) Adsorption of BSA and fibrinogen from 1 mg/mL solution in PBS (n = 4) and (**b**) adsorption of serum proteins from 20% serum diluted with PBS (n = 3). Error bars and n denote standard deviation and the number of measurements, respectively.

After the confirmation of the formation of the protein layers on the SAMs by QCM-D, we processed the adsorbed protein as the procedure shown in Figure 1. Figure 6a–e shows mass spectra of digested adsorbed proteins on the SAMs. In contrast with the peaks assigned to BSA, the patterns of other peaks, e.g., in the ranges of m/z = 1300–1400 and 1600–1700 are different depending on the SAMs. This indicates that the composition of proteins other than BSA is different depending on the terminal groups of the molecules constituting the SAMs.

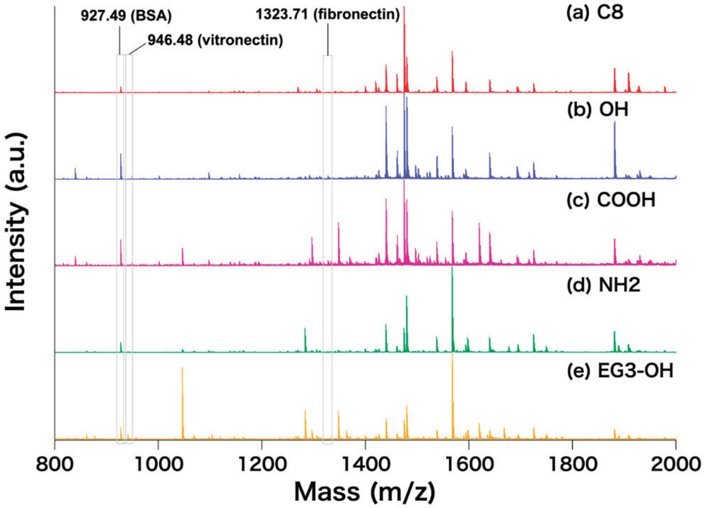

Figure 6. MALDI-ToF mass spectra of fragmented proteins on the SAMs; (**a**) C8, (**b**) OH, (**c**) COOH, (**d**) NH2, and (**e**) EG3-OH SAMs. The locations of the reference m/z of BSA, vitronectin and fibronectin are shown (m/z = 927.49, 946.48 and 1323.71 for BSA, vitronectin, and fibronectin, respectively).

The relative peak intensities of the reference m/z for each protein with respect to that for BSA for each SAM are summarized in Table 3. Although we cannot discuss the exact amount of proteins from peak intensities, the change in the composition of proteins after adsorption from serum onto SAMs can be easily seen from the results. The final composition of the adsorbed proteins on materials is a result of competitive adsorption of serum proteins (Vroman effect) [40,41]. In theoretical models proposed so far, small proteins adsorb first because of their high mobility and replaced with larger ones. However, the complexity of the problem includes a wide variety of protein-protein and protein-surface interactions. Moreover, the conformational changes of proteins after adsorption complicates the issue. Therefore, it is very difficult to correlate the composition with the physicochemical properties of the SAMs. It should also be noted that we also compared the compositions of vitronectin and fibronectin with respect to BSA obtained by the conventional methods, which incorporate pipetting processes, and our method (Table S1), clearly indicating the effect of pipetting on the ratio of the peak intensities.

The main finding here is that the compositions of vitronectin and fibronectin on the SAMs, which provide RGD moieties essential for cell adhesion, are higher than in serum (Figure 7). The evaluation of the exact amounts of the serum proteins requires standard samples containing the proteins. Unfortunately, many of the proteins listed in Tables 2 and 3 were not available, and we were not able to evaluate the exact amounts by combining with the results of QCM-D. But fortunately, there have been several works that attempted to predict peak intensities of peptides from their sequences by using techniques of informatics [42–44]. These approaches may realize the exact evaluation of the protein composition in the future.

Table 3. Relative peak intensity of the reference m/z for each protein with respect to that of BSA in FBS and on the SAMs. Errors denote a standard deviation of 30 spectra (two substrates for each SAM with 15 spectra each at different positions).

Protein	**Relative Peak Intensity of the Reference m/z for Each Protein with Respect to that for BSA**					
	FBS	**C8**	**OH**	**COOH**	**NH2**	**EG3-OH**
Serum albumin	1.00	1.00	1.00	1.00	1.00	1.00
Alpha-1-antiproteinase	0.00719 ± 0.00421	0.212 ± 0.138	0.0843 ± 0.0333	0.109 ± 0.076	0.172 ± 0.084	0.111 ± 0.056
Plasminogen	0.950 ± 0.526	2.59 ± 1.81	0.746 ± 0.609	1.31 ± 0.50	1.54 ± 0.69	0.846 ± 0.314
Cone cGMP-specific 3′,5′-cyclic phosphodiesterase subunit alpha′	0.0639 ± 0.0442	1.24 ± 0.82	0.279 ± 0.177	0.298 ± 0.186	0.972 ± 0.537	1.17 ± 0.77
Lactoperoxidase	0.0132 ± 0.0075	0.166 ± 0.171	0.0575 ± 0.0308	0.0692 ± 0.0269	0.311 ± 0.539	0.222 ± 0.160
NADH-ubiquinone oxidoreductase 75 kDa subunit	0.0763 ± 0.0658	1.62 ± 2.03	0.101 ± 0.063	0.231 ± 0.157	0.533 ± 0.247	0.242 ± 0.062
Alpha-2-HS-glycoprotein	1.02 ± 0.97	0.707 ± 0.775	0.0908 ± 0.0489	0.152 ± 0.150	0.317 ± 0.194	0.179 ± 0.029
Kininogen-2	0.0118 ± 0.0055	0.135 ± 0.112	0.0731 ± 0.0489	0.0916 ± 0.0345	0.137 ± 0.088	0.103 ± 0.045
Hemiferrin	0.138 ± 0.123	0.155 ± 0.050	0.114 ± 0.057	0.142 ± 0.062	0.110 ± 0.039	0.100 ± 0.020
Integrin beta-1	0.0117 ± 0.00609	0.123 ± 0.039	0.114 ± 0.047	0.140 ± 0.052	0.0825 ± 0.0347	0.0676 ± 0.0361
Prothrombin	0.125 ± 0.118	0.212 ± 0.111	0.241 ± 0.075	0.234 ± 0.107	0.121 ± 0.057	0.143 ± 0.081
Apolipoprotein A-I	0.0242 ± 0.0237	0.157 ± 0.079	0.0925 ± 0.0457	0.107 ± 0.070	0.143 ± 0.108	0.0798 ± 0.0403
Antithrombin-III	0.0641 ± 0.0715	2.56 ± 2.17	0.786 ± 0.296	0.757 ± 0.676	1.01 ± 0.51	0.482 ± 0.122
Beta-2-glycoprotein 1	0.582 ± 0.481	0.117 ± 0.061	0.0784 ± 0.0327	0.128 ± 0.064	0.0953 ± 0.0403	0.0948 ± 0.0556
Alpha-2-antiplasmin	0.0355 ± 0.0297	0.256 ± 0.133	0.129 ± 0.038	0.153 ± 0.097	0.159 ± 0.092	0.0913 ± 0.0375
Protein AMBP	0.0596 ± 0.0383	0.204 ± 0.077	0.0859 ± 0.0331	0.131 ± 0.056	0.108 ± 0.038	0.0894 ± 0.0375
Hemoglobin fetal subunit beta	0.0187 ± 0.0064	0.154 ± 0.121	0.0531 ± 0.0277	0.0703 ± 0.031	0.151 ± 0.082	0.216 ± 0.158
Alpha 1-antichymotrypsin	0.00869 ± 0.00451	0.192 ± 0.062	0.475 ± 0.310	0.467±0.191	0.208 ± 0.068	0.130 ± 0.054
Apolipoprotein A-II	0.00390 ± 0.00420	0.227 ± 0.263	0.110 ± 0.047	0.109±0.072	0.133 ± 0.061	0.115 ± 0.044
Hemoglobin subunit alpha	0.00598 ± 0.00580	0.166 ± 0.145	0.212 ± 0.121	0.346 ± 0.334	0.136 ± 0.064	0.125 ± 0.124
Fibronectin	0.00317 ± 0.00226	0.100 ± 0.051	0.0620 ± 0.0259	0.0803 ± 0.0365	0.0461 ± 0.0241	0.0451 ± 0.0176
Vitronectin	0.00297±0.00160	0.132 ± 0.129	0.0563 ± 0.0379	0.0761 ± 0.0329	0.0396 ± 0.0249	0.0435 ± 0.0200

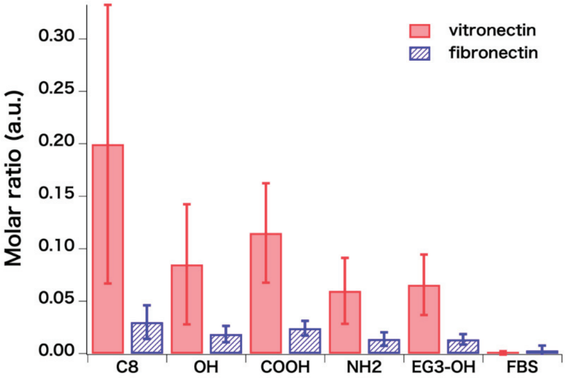

Figure 7. Evaluated molar ratios of vitronectin and fibronectin with respect to BSA ($n = 30$). Error bars and n denote standard deviation and the number of spectra analyzed, respectively.

4. Summary and Conclusions

In this paper, we proposed a new method to evaluate the composition of adsorbed proteins on solid surfaces. In this method, we perform denaturation, alkylation, digestion, and measurements without the collection of proteins. This method enables us to collect all the peptide fragments without the artifact of pipetting. To find reference m/z values used to evaluate the protein composition, we first looked for the m/z value unique for the proteins of interest by listing up m/z values of all possible fragments of the top 20 proteins abundant in serum and the interesting proteins, i.e., those with RGD moieties. Then, we determined a correlation factor to evaluate molar ratios between the proteins from peak intensities by using standard samples with the known composition of proteins.

Our results clearly showed that the composition of the proteins adsorbed from serum onto SAMs critically depends on the terminal groups of the molecules constituting the SAMs as a result of the

Vroman effect (competitive adsorption of proteins onto surfaces). Moreover, in this work, we evaluated the ratios of vitronectin and fibronectin to BSA. The compositions of vitronectin and fibronectin govern the adhesion of cells that have integrin-mediated adhesion systems since RGD moieties of the proteins provide binding sites for integrins. We found a clear correlation between cell adhesion and the compositions of vitronectin and fibronectin. This finding will be published elsewhere.

Supplementary Materials: The following are available online at http://www.mdpi.com/2079-6412/10/1/12/s1. For quality assessment of identification of proteins. Here we simply show the matching ratio between theoretical m/z values and experimentally observed peak positions, since we removed some of the m/z values and cannot employ ROC plot analysis. In the case of the standard sample, which contains BSA, fibronectin, and vitronectin, more than 95% of the theoretical fragment m/z values were observed in the spectra. In the case of serum proteins, the matching rate is lower (Table S2). If the matching rate is larger than 25%, it can be considered to be marginally matched [45]. Therefore, we consider that the identification is satisfactory in this work.

Author Contributions: M.H. and T.M. did all the experiments and analysis. T.N. and E.A.Q.M. contributed to the coding of the software. Y.M. and T.H. designed this project and optimized the experimental conditions. All authors have read and agreed to the published version of the manuscript.

Funding: The author (T.H.) acknowledges the financial supports by KAKENHI (19H02565, 17K20095 and 15KK0184) and JST- PRESTO.

Acknowledgments: The authors appreciate the help of Ms. Kazue Taki for the administration of this project.

Conflicts of Interest: The authors declare no conflict of interest.

References

1. Tanaka, M.; Hayashi, T.; Morita, S. The roles of water molecules at the biointerface of medical polymers. *Polym. J.* **2013**, *45*, 701–710. [CrossRef]
2. Kane, R.S.; Takayama, S.; Ostuni, E.; Ingber, D.E.; Whitesides, G.M. Patterning proteins and cells using soft lithography. *Biomaterials* **1999**, *20*, 2363–2376. [CrossRef]
3. Flaim, C.J.; Chien, S.; Bhatia, S.N. An extracellular matrix microarray for probing cellular differentiation. *Nat. Methods* **2005**, *2*, 119–125. [CrossRef] [PubMed]
4. Watt, F.M.; Huck, W.T. Role of the extracellular matrix in regulating stem cell fate. *Nat. Rev. Mol. Cell Biol.* **2013**, *14*, 467–473. [CrossRef] [PubMed]
5. Silin, V.V.; Weetall, H.; Vanderah, D.J. SPR Studies of the Nonspecific Adsorption Kinetics of Human IgG and BSA on Gold Surfaces Modified by Self-Assembled Monolayers (SAMs). *J. Colloid Interface Sci.* **1997**, *185*, 94–103. [CrossRef] [PubMed]
6. Nakata, S.; Kido, N.; Hayashi, M.; Hara, M.; Sasabe, H.; Sugawara, T.; Matsuda, T. Chemisorption of proteins and their thiol derivatives onto gold surfaces: Characterization based on electrochemical nonlinearity. *Biophys. Chem.* **1996**, *62*, 63–72. [CrossRef]
7. Caruso, F.; Furlong, D.N.; Kingshott, P. Characterization of Ferritin Adsorption onto Gold. *J. Colloid Interface Sci.* **1997**, *186*, 129–140. [CrossRef]
8. Hook, F.; Rodahl, M.; Kasemo, B.; Brzezinski, P. Structural changes in hemoglobin during adsorption to solid surfaces: Effects of pH, ionic strength, and ligand binding. *Proc. Natl. Acad. Sci. USA* **1998**, *95*, 12271–12276. [CrossRef]
9. Renken, J.; Dahint, R.; Grunze, M.; Josse, F. Multifrequency evaluation of different immunosorbents on acoustic plate mode sensors. *Anal. Chem.* **1996**, *68*, 176–182. [CrossRef]
10. Cavic, B.A.; Thompson, M. Adsorptions of plasma proteins and their elutabilities from a polysiloxane surface studied by an on-line acoustic wave sensor. *Anal. Chem.* **2000**, *72*, 1523–1531. [CrossRef]
11. Gizeli, E.; Bender, F.; Rasmusson, A.; Saha, K.; Josse, F.; Cernosek, R. Sensitivity of the acoustic waveguide biosensor to protein binding as a function of the waveguide properties. *Biosens. Bioelectron.* **2003**, *18*, 1399–1406. [CrossRef]
12. Labarre, D.; Vauthier, C.; Chauvierre, C.; Petri, B.; Muller, R.; Chehimi, M.M. Interactions of blood proteins with poly(isobutylcyanoacrylate) nanoparticles decorated with a polysaccharidic brush. *Biomaterials* **2005**, *26*, 5075–5084. [CrossRef] [PubMed]

13. Zenhausern, F.; Adrian, M.; Descouts, P. Solution structure and direct imaging of fibronectin adsorption to solid surfaces by scanning force microscopy and cryo-electron microscopy. *J. Electron Microsc.* **1993**, *42*, 378–388.
14. Lestelius, M.; Liedberg, B.; Lundstrom, I.; Tengvall, P. In vitro plasma protein adsorption and kallikrein formation on 3-mercaptopropionic acid, L-cysteine and glutathione immobilized onto gold. *J. Biomed. Mater. Res.* **1994**, *28*, 871–880. [CrossRef] [PubMed]
15. Caruso, F.; Furlong, D.N.; Ariga, K.; Ichinose, I.; Kunitake, T. Characterization of polyelectrolyte-protein multilayer films by atomic force microscopy, scanning electron microscopy, and Fourier transform infrared reflection-absorption spectroscopy. *Langmuir* **1998**, *14*, 4559–4565. [CrossRef]
16. Schwendel, D.; Dahint, R.; Herrwerth, S.; Schloerholz, M.; Eck, W.; Grunze, M. Temperature dependence of the protein resistance of poly- and oligo(ethylene glycol)-terminated alkanethiolate monolayers. *Langmuir* **2001**, *17*, 5717–5720. [CrossRef]
17. Model, M.A.; Healy, K.E. Quantification of the surface density of a fluorescent label with the optical microscope. *J. Biomed. Mater. Res.* **2000**, *50*, 90–96. [CrossRef]
18. Beverloo, H.B.; Vanschadewijk, A.; Bonnet, J.; Vandergeest, R.; Runia, R.; Verwoerd, N.P.; Vrolijk, J.; Ploem, J.S.; Tanke, H.J. Preparation and microscopic visualization of multicolor luminescent immunophosphors. *Cytometry* **1992**, *13*, 561–570. [CrossRef]
19. Pappin, D.J.; Hojrup, P.; Bleasby, A.J. Rapid identification of proteins by peptide-mass fingerprinting. *Curr. Biol.* **1993**, *3*, 327–332. [CrossRef]
20. Scheler, C.; Lamer, S.; Pan, Z.; Li, X.P.; Salnikow, J.; Jungblut, P. Peptide mass fingerprint sequence coverage from differently stained proteins on two-dimensional electrophoresis patterns by matrix assisted laser desorptiodionization-mass spectrometry (MALDI-MS). *Electrophoresis* **1998**, *19*, 918–927. [CrossRef]
21. Sempf, K.; Arrey, T.; Gelperina, S.; Schorge, T.; Meyer, B.; Karas, M.; Kreuter, J. Adsorption of plasma proteins on uncoated PLGA nanoparticles. *Eur. J. Pharm. Biopharm.* **2013**, *85*, 53–60. [CrossRef] [PubMed]
22. Urbani, A.; Lupisella, S.; Sirolli, V.; Bucci, S.; Amoroso, L.; Pavone, B.; Pieroni, L.; Sacchetta, P.; Bonomini, M. Proteomic analysis of protein adsorption capacity of different haemodialysis membranes. *Mol. BioSyst.* **2012**, *8*, 1029–1039. [CrossRef] [PubMed]
23. Urbani, A.; Sirolli, V.; Lupisella, S.; Levi-Mortera, S.; Pavone, B.; Pieroni, L.; Amoroso, L.; Di Vito, R.; Bucci, S.; Bernardini, S.; et al. Proteomic investigations on the effect of different membrane materials on blood protein adsorption during haemodialysis. *Blood Transfus.* **2012**, *10*, s101–s112. [CrossRef] [PubMed]
24. Kristensen, K.; Henriksen, J.R.; Andresen, T.L. Adsorption of cationic peptides to solid surfaces of glass and plastic. *PLoS ONE* **2015**, *10*, 1–17. [CrossRef] [PubMed]
25. Kirschhofer, F.; Rieder, A.; Prechtl, C.; Kuhl, B.; Sabljo, K.; Woll, C.; Obst, U.; Brenner-Weiss, G. Quartz crystal microbalance with dissipation coupled to on-chip MALDI-ToF mass spectrometry as a tool for characterising proteinaceous conditioning films on functionalised surfaces. *Anal. Chim. Acta* **2013**, *802*, 95–102. [CrossRef] [PubMed]
26. Zheng, X.Y.; Baker, H.; Hancock, W.S.; Fawaz, F.; McCaman, M.; Pungor, E. Proteomic analysis for the assessment of different lots of fetal bovine serum as a raw material for cell culture. Part IV. Application of proteomics to the manufacture of biological drugs. *Biotechnol. Prog.* **2006**, *22*, 1294–1300. [CrossRef]
27. Shannahan, J.H.; Brown, J.M.; Chen, R.; Ke, P.C.; Lai, X.; Mitra, S.; Witzmann, F.A. Comparison of nanotube-protein corona composition in cell culture media. *Small* **2013**, *9*, 2171–2181. [CrossRef]
28. Sakulkhu, U.; Mahmoudi, M.; Maurizi, L.; Coullerez, G.; Hofmann-Amtenbrink, M.; Vries, M.; Motazacker, M.; Rezaee, F.; Hofmann, H. Significance of surface charge and shell material of superparamagnetic iron oxide nanoparticle (SPION) based core/shell nanoparticles on the composition of the protein corona. *Biomater. Sci.* **2015**, *3*, 265–278. [CrossRef]
29. Strojan, K.; Leonardi, A.; Bregar, V.B.; Krizaj, I.; Svete, J.; Pavlin, M. Dispersion of nanoparticles in different media importantly determines the composition of their protein corona. *PLoS ONE* **2017**, *12*, 1–21. [CrossRef]
30. Artimo, P.; Jonnalagedda, M.; Arnold, K.; Baratin, D.; Csardi, G.; De Castro, E.; Duvaud, S.; Flegel, V.; Fortier, A.; Gasteiger, E.; et al. ExPASy: SIB bioinformatics resource portal. *Nucleic Acids Res.* **2012**, *40*, W597–W603. [CrossRef]
31. Available online: https://www.expasy.org/ (accessed on 22 December 2019).
32. Bucknall, M.; Fung, K.Y.C.; Duncan, M.W. Practical quantitative biomedical applications of MALDI-TOF mass spectrometry. *J. Am. Soc. Mass Spectrom.* **2002**, *13*, 1015–1027. [CrossRef]

33. Chang, R.; Asatyas, S. Water near bioinert self-assembled monolayers. *Polym. J.* **2018**, *50*, 563–571. [CrossRef]
34. Hayashi, T.; Tanaka, Y. Mechanism underlying bioinertness of self-assembled monolayers of oligo(ethyleneglycol)-terminated alkanethiols on gold: protein adsorption, platelet adhesion, and surface forces. *Phys. Chem. Chem. Phys.* **2012**, *14*, 10196–10206. [CrossRef] [PubMed]
35. Sekine, T.; Tanaka, Y. Evaluation of Factors To Determine Platelet Compatibility by Using Self-Assembled Monolayers with a Chemical Gradient. *Langmuir* **2015**, *31*, 7100–7105. [CrossRef]
36. Harder, P.; Grunze, M. Molecular conformation in oligo(ethylene glycol)-terminated self-assembled monolayers on gold and silver surfaces determines their ability to resist protein adsorption. *J. Phys. Chem. B* **1998**, *102*, 426–436. [CrossRef]
37. Sekine, T.; Asatyas, S. Surface force and vibrational spectroscopic analyses of interfacial water molecules in the vicinity of methoxy-tri(ethylene glycol)-terminated monolayers: mechanisms underlying the effect of lateral packing density on bioinertness. *J Biomater Sci Polym Ed* **2017**, *28*, 1231–1243. [CrossRef]
38. Hayashi, T.; Hara, M. Nonfouling self-assembled monolayers: mechanisms underlying protein and cell resistance. *Curr. Phys. Chem.* **2011**, *1*, 90–98. [CrossRef]
39. Yang, Z.; Jaeckisch, S.M. Enhanced binding of Aspergillus fumigatus spores to A549 epithelial cells and extracellular matrix proteins by a component from the spore surface and inhibition by rat lung lavage fluid. *Thorax* **2000**, *55*, 579–584. [CrossRef]
40. Cuypers, P.A.; Willems, G.M. Adsorption kinetics of protein mixtures. A tentative explanation of the Vroman effect. *Ann. N. Y. Acad. Sci.* **1987**, *516*, 244–252. [CrossRef]
41. Leonard, E.F.; Vroman, L. Is the Vroman effect of importance in the interaction of blood with artificial materials? *J. Biomater. Sci. Polym. Ed* **1991**, *3*, 95–107. [CrossRef]
42. Yang, D.; Ramkissoon, K. High-accuracy peptide mass fingerprinting using peak intensity data with machine learning. *J. Proteome Res.* **2008**, *7*, 62–69. [CrossRef] [PubMed]
43. Timm, W.; Scherbart, A. Peak intensity prediction in MALDI-TOF mass spectrometry: a machine learning study to support quantitative proteomics. *Bmc Bioinformatics* **2008**, *9*, 443. [CrossRef] [PubMed]
44. Gay, S.; Binz, P.A. Peptide mass fingerprinting peak intensity prediction: extracting knowledge from spectra. *Proteomics* **2002**, *2*, 1374–1391. [CrossRef]
45. Stead, D.A.; Preece, A. Universal metrics for quality assessment of protein identifications by mass spectrometry. *Mol. Cell. Proteomics* **2006**, *5*, 1205–1211. [CrossRef]

coatings

Article

Chemical and Biological Roles of Zinc in a Porous Titanium Dioxide Layer Formed by Micro-Arc Oxidation

Masaya Shimabukuro [1], Yusuke Tsutsumi [2,3], Kosuke Nozaki [1], Peng Chen [2], Risa Yamada [1], Maki Ashida [2], Hisashi Doi [2], Akiko Nagai [4] and Takao Hanawa [2,*]

[1] Graduate School of Medical and Dental Sciences, Tokyo Medical and Dental University, 1-5-45 Yushima, Bunkyo-ku, Tokyo 113-8549, Japan; shimabukuro.met@tmd.ac.jp (M.S.); k.nozaki.fpro@tmd.ac.jp (K.N.); r.yamada.fpro@tmd.ac.jp (R.Y.)

[2] Institute of Biomaterials and Bioengineering, Tokyo Medical and Dental University, 2-3-10 Kanda-Surugadai, Chiyoda-ku, Tokyo 101-0062, Japan; TSUTSUMI.Yusuke@nims.go.jp (Y.T.); chen.met@tmd.ac.jp (P.C.); ashida.met@tmd.ac.jp (M.A.); doi.met@tmd.ac.jp (H.D.)

[3] Research Center for Structural Materials, National Institute for Materials Science (NIMS), 1-2-1 Sengen, Tsukuba, Ibaraki 305-0047, Japan

[4] Department of Anatomy, School of Dentistry, Aichi Gakuin University, 1-100 Kusumoto, Chikusa-ku, Nagoya 464-8650, Japan; aknagai@dpc.agu.ac.jp

* Correspondence: hanawa.met@tmd.ac.jp; Tel./Fax: +81-3-5280-8006

Received: 12 October 2019; Accepted: 27 October 2019; Published: 29 October 2019

Abstract: This study investigated the time transient effect of zinc (Zn) in the porous titanium dioxide formed by micro-arc oxidation (MAO) treatment routinely performed for Zn-containing electrolytes. The aim of our analysis was to understand the changes in both the chemical and biological properties of Zn in physiological saline. The morphology of the Zn-incorporated MAO surface did not change, and a small amount of Zn ions were released at early stages of incubation in saline. We observed a decrease in Zn concentration in the oxide layer because its release and chemical state (Zn^{2+} compound to ZnO) changed over time during incubation in saline. In addition, the antibacterial property of the Zn-incorporated MAO surface developed at late periods after the incubation process over a course of 28 days. Furthermore, osteogenic cells were able to proliferate and were calcified on the specimens with Zn. The changes related to Zn in saline had non-toxic effects on the osteogenic cells. In conclusion, the time transient effect of Zn in a porous titanium dioxide layer was beneficial to realize dual functions, namely the antibacterial property and osteogenic cell compatibility. Our study suggests the importance of the chemical state changes of Zn to control its chemical and biological properties.

Keywords: zinc; titanium oxide; micro-arc oxidation; antibacterial activity; osteogenic cell compatibility

1. Introduction

Recent studies have reported that biomaterial-associated infections caused by the formation of biofilms on biomaterial surfaces were a major cause of failure in implant surgeries [1–6]. The biofilms are generally formed as a result of bacterial adhesion, growth, colony formation, extracellular polysaccharides, quorum sensing signals, and formation of nutrition channels. Biofilms can weaken the effect of antibiotic agents due to the presence of a wide variety of bacterial species and the barrier effect of the extracellular polysaccharide [7–12]. After the formation of biofilms, it becomes almost impossible to remove the matured biofilms from implanted devices in the human body. The only way of preventing sepsis is by retrieval of the device on which the biofilm was formed from the patient. To avoid this, it is necessary to inhibit biofilm formation during implantation of devices in advance. Prosthetic joint infection is divided into early infection (within three weeks after surgery) and late-onset infection (around three to eight weeks after surgery); this period is considered the incubation stage [13]. Moreover, infections associated with hip implants have been reported in the case of dental treatments [14,15]. Thus, the long-term antibacterial activity of the implant material is strongly desired. An ideal biomaterial surface with antibacterial activity can not only prevent the initial stages of infection such as bacterial adhesion, but also inhibit subsequent bacterial growth at later stages.

Recent studies on antibacterial surfaces have used various surface treatments with silver (Ag) species [16–23]. Ag is a well-known antibacterial agent and its effects on various bacteria have been studied extensively. Many researchers have reported that Ag can strongly influence various kinds of fungal and bacterial strains, including multidrug-resistant bacteria [23–27]. In addition to the efficacy of Ag for bacteria, copper, zinc (Zn), gallium, selenium and silicon have been recently used as antibacterial elements owing to their good antibacterial activity [23,28–35]. Among them, Zn is one of the most important trace elements in living organisms and an effective antibacterial element [30,31,36–42]. Therefore, we expected that the application of Zn for the surface modification of implant devices might offer antibacterial activity as effective as that of Ag.

Titanium (Ti) and its alloys are widely used as major implant materials owing to their excellent mechanical properties and biocompatibility [43]. Recent studies related to the bio-functionalization of a Ti surface has been widely reported and well-summarized elsewhere [44]. Among them, Micro-arc oxidation (MAO) is an electrochemical surface treatment technique performed in a specific electrolyte under high voltage. After MAO, the surface of the substrate metal is covered by a connective-porous oxide layer. The resultant oxide layer formed by MAO treatment contained additional elements that were contained in the electrolyte solution. Therefore, MAO treatment improved the osteogenic cell compatibility of titanium (Ti) when the electrolyte contained calcium and phosphate ions [45–51]. The biocompatibility of MAO coatings has been demonstrated by numerous in vitro and in vivo tests [52–57].

Several studies have focused on the incorporation of Zn onto a Ti surface by MAO treatment [58–64]. Hu et al. [59], Zhang et al. [61], Zhang et al. [62] and Du et al. [63] reported that Zn-incorporated TiO_2 coatings showed good antibacterial activity against both *Escherichia coli* (*E. coli*) and *Staphylococcus aureus*. Moreover, Zhao et al. [60] reported that a Zn coating on a Ti surface showed bacteriostatic activity against *Streptococcus mutans*. These experiments provide adequate evidence to demonstrate that MAO-treated Ti in the electrolyte with Zn inhibited both bacterial adhesion as well as growth. In addition, Hu et al. [59], Zhao et al. [60] and Zhang et al. [64] reported that suitable amounts of Zn could promote adhesion, proliferation, and differentiation of osteogenic cells (e.g., rat bone marrow stem cells, MG63 cells and MC3T3-E1 cells). Thus, Zn plays a key role in the development of both antibacterial activity and osteogenic cell compatibility, and the incorporation of Zn by MAO treatment is a promising approach for surface treatment to achieve antibacterial activity in orthopedic and dental implants. Nevertheless, little attention has been given to the chemical and biological changes of Zn in the MAO coatings on their bio-function. Therefore, for the prevention of late-onset infections and the application of Zn to medical and dental implants, it is important to evaluate the long-term behavior of Zn in the body.

The purpose of this study was to investigate the long-term behavior of Zn-incorporated surface oxide produced by MAO for the prevention of late-onset infections. We investigated the time transient effect of Zn on chemical property, antibacterial activity, and osteogenic cell compatibility. The detailed chemical state of Zn in physiological saline was characterized by X-ray photoelectron spectroscopy (XPS). The change in antibacterial activity of the specimens before and after incubation for four weeks in saline was evaluated by the ISO method using *E. coli* as typical gram-negative facultative anaerobic bacteria. In addition, calcification by the cells on the specimens were evaluated at 14 and 28 days after seeding. In this study, we considered different time points and investigated changes in the chemical and biological properties of the Zn-incorporated MAO surface in a simulated body fluid environment.

2. Materials and Methods

2.1. Specimen Preparation

Commercially pure Ti (CP Ti; Rare Metallic, Tokyo, Japan) with grade 2 was used as a substrate material in this study. Two kinds of CP Ti disks with diameters 8 mm and 25 mm were obtained by cutting from a rod of CP Ti. The surfaces of these disks were mechanically polished using #150, #320, #600, and #800 grid SiC abrasive papers, followed by ultra-sonication in acetone and ethanol for 10 min. The disks were then stored in an auto-dry desiccator till further use. Each Ti disk was then fixed onto a polytetrafluoroethylene holder with an O-ring. The area in contact with the electrolyte was 39 mm^2 (7.0 mm in diameter) or 398 mm^2 (22.5 mm in diameter). Details of the working electrode were as described earlier [65]. An AISI304 type stainless steel plate was used as a counter electrode. The base composition of the electrolyte for MAO treatment was 100 mM calcium glycerophosphate and 150 mM calcium acetate. Varying concentrations of $ZnCl_2$ (0, 0.5, 1.0, and 2.5 mM) were added to the base electrolyte. After pouring the electrolyte into the electrochemical cell, both electrodes were connected to a DC power supply (PL-650-0.1, Matsusada Precision Inc., Shiga, Japan) and a positive voltage with a constant current density of 251 Am^{-2} was applied for 10 min. The resultant voltage during the MAO treatment was 400 V at all conditions. After the MAO treatment, the surfaces were thoroughly washed in ultrapure water in order to remove any electrolyte solution remaining in the porous oxide layer. A major part of the Ti disk was MAO-treated; an annular untreated area was 0.5 mm from the margin. All surface characterization described below was performed in a MAO-treated area.

2.2. Incubation in Saline

The specimens treated in the electrolyte that had various concentrations of Zn were immersed in physiological saline (0.9% NaCl) for 28 days. Saline is the simplest simulated body fluid, which is suitable for long-period measurement. Moreover, chloride ion (Cl^-) is unexceptionally contained in all simulated body fluids. The specimens were fixed onto a polyethylene container to allow the release of Zn ions from the surface into physiological saline. Incubation was performed at 37 °C in a humidified chamber under constant shaking (100 rpm). Every 7th day, the pooled solution was changed with fresh physiological saline. After immersion, the immersed specimens were used further for surface characterization, evaluation of antibacterial activity, and quantification of Zn ions.

2.3. Surface Characterization and Evaluation of Zinc Ion Release

Scanning electron microscopy with energy dispersive X-ray spectrometry (SEM/EDS; S-3400NX, Hitachi High-Technologies Corp., Tokyo, Japan) was used to observe the surface morphology and composition before and after incubation. X-ray diffraction (XRD, BRUKER D8 DISCOVER, Bruker AXS KK, Yokohama, Japan) was performed to characterize the crystal structure of the specimens before and after incubation. The diffractometer was used with Cu-Kα radiation (40 keV, 40 mA). XPS was performed using a spectrometer (JPS-9010MC, JEOL, Tokyo, Japan) with Mg Kα X-ray source (energy: 1253.6 eV; acceleration voltage: 10 kV; current: 10 mA). The pressure of the measurement chamber was 1×10^{-7} Pa. All binding energies mentioned in this paper are relative to the Fermi level. The spectrometer was calibrated against Au $4f_{7/2}$ of pure gold, Ag $3d_{5/2}$ of pure silver, and Cu $2p_{3/2}$ of pure copper. Spectra were obtained using an analysis area of 1 mmϕ with a pass energy of 20 eV. The detection angle to the specimen surface was 90°. The binding energies were calibrated with C 1s photoelectron energy region peak derived from contaminating carbon (285.0 eV). To calculate the integrated intensity of peaks, the background was subtracted from the measured spectrum according to Shirley's method [66]. The chemical state changes of Zn were determined by the modified Auger parameter (α′) on the Wagner plot with those of typical Zn compounds. The α′ of each specimen was calculated using the following Equation (1).

$$\alpha' = E_K(\mathrm{Zn\ L_3M_{45}M_{45}}) + E_B(\mathrm{Zn\ 2p_{3/2}}) \quad (1)$$

Equation (1) contains both kinetic energy of Zn $L_3M_{45}M_{45}$, E_K(Zn $L_3M_{45}M_{45}$) and binding energy of Zn $2p_{3/2}$, E_B(Zn $2p_{3/2}$). The composition of the specimens were calculated according to a method described previously [67]. The photoionization cross-section of empirical data [68,69] and theoretically calculated data [70] were used for quantification. Inductively coupled plasma-atomic emission spectrometry (ICP-AES, ICPS-7000 ver. 2, Shimadzu Corp., Kyoto, Japan) was used to quantify Zn ion release from the Zn incorporated surface. The amounts of Zn ions released into the pooled solution were quantified each week.

2.4. Evaluation of Antibacterial Activity

The antibacterial activity was evaluated according to ISO 22196: 2007 method. To examine the antibacterial activity of the specimens, we employed *E. coli* (NBRC3972). The experiment was approved by the Pathogenic Organisms Safety Management Committee of the Tokyo Medical and Dental University (22012-025c). *E. coli* is a representative gram-negative rod-shaped bacterium commonly found in the gut. *E. coli* was cultured in Luria-Bertani (LB) broth (LB-Medium, MP Biomedicals, CA, USA) at 37 °C for 24 h. The optical density of the bacterial suspensions were measured at 600 nm using an ultraviolet-visible (UV–vis) spectrometer (V-550, JASCO, Tokyo, Japan) and diluted to obtain concentrations of 4.9×10^6 colony-forming units (CFUs) mL^{-1}. Prior to the antibacterial activity testing, all specimens were sterilized with 70% ethanol, washed with distilled water, and dried. Drops of bacterial suspension were added on all specimens, which were subsequently covered with a sterilized plastic film and incubated at 37 °C for 24 h ($n = 3$). Bacterial cells were then collected from all the incubated specimens; the obtained suspensions were diluted, pipetted onto nutrient agar plates, and incubated overnight at 37 °C. The number of viable bacteria was determined by counting the number of colonies formed.

2.5. Calcification by Osteogenic Cells

As described in our previous work [71], MC3T3-E1 cells (RIKEN BioResource Center, Tsukuba, Japan) were maintained in a cell culture medium: alpha modification of Eagle's minimum essential medium (α-MEM; GIBCO, Grand island, CA, USA) supplemented with 10% fetal bovine serum (FBS; GIBCO), 10 U mL^{-1} penicillin, 100 mg mL^{-1} streptomycin, and 0.25 mg mL^{-1} amphotericin B (GIBCO). All specimens were sterilized in 70% ethanol for 20 min and thoroughly rinsed with deionized water before in vitro testing. The cells were seeded on to the sterilized specimens with an approximate initial density of 10,000 cells cm^{-2}. As a control, cells were also seeded on MAO-treated Ti without Zn. The cells were incubated at 37 °C in a fully humidified atmosphere under 5% CO_2. For induction of osteogenic differentiation, a cell culture medium supplemented with 2 mM β-glycerophosphate (Calbiochem, Darmstadt, Germany) and 50 mg mL^{-1} L-ascorbic acid (Wako Pure Chemical Industries, Osaka, Japan) was used when 100% confluence was reached for all the specimens. The medium used for induction was named as the differentiation-inducing medium. The differentiation-inducing medium was changed every three days.

After the seeding for the 1st, 2nd, and 3rd day, the cells attached to each specimen were harvested with trypsin/EDTA, re-suspended in a cell culture medium, and transferred to 96-well microplates. Then, the Cell Counting Kit-8 assay (CCK-8, Dojindo Laboratories, Kumamoto, Japan) was added to each 96-well microplate, which contained cell suspension, and the reaction was continued for 4 h at 37 °C. The absorbance of the samples was measured at 450 nm using a microplate reader (ChroMate Microplate Reader, Awareness Technology, Palm, FL, USA). The reference wavelength was set at 630 nm. In this evaluation, the tissue culture polystyrene (TCPS) was used as a control specimen for quantification of the number of attached cells on each specimen. The cells that were attached to the TCPS were harvested by treatment with Trypsin/EDTA followed by re-suspension of cells in the cell culture medium. Cell suspensions were diluted serially. The number of cells in the cell suspension harvested from TCPS were counted by Trypan blue (Trypan Blue Stain 0.4%; Gibco) using a hemocytometer. Then, standard curves for cell number calibration and for light absorbance were constructed and were used for quantification of the number of attached cells on each specimen.

The calcification of MC3T3-E1 cells on each specimen was evaluated by the calcified deposits by a color change reaction after alizarin red S staining. After the removal of media from all the specimens, cells were rinsed three times with phosphate-buffered saline. Cells were then fixed with 4% formalin for 1 h and rinsed three times with ultra-pure water. Each specimen was stained with 1% alizarin red S solution (adjusted to pH 4.2 with ammonium hydroxide) at room temperature for 30 min. After removing the alizarin red S solution, cells were repeatedly rinsed with ultrapure water. When the specimens were fully dry, the surface of each specimen was studied using an optical microscope (OLYMPUS SZX12, Olympus, Tokyo, Japan).

2.6. Statistical Analysis

Data obtained by surface characterization were calculated from three independent specimens. The results of biological tests are shown from at least two independent tests. Each test was performed using at least three independent specimens. All values are presented as means ± SD, and commercial statistical software KaleidaGraph (Version 4.1.1, Synergy Software, Reading, PA) was used for statistical analysis. One-way analysis of variance (ANOVA) was used following multiple comparisons with Student–Newman–Keuls method to assess the data, and $P < 0.05$ was considered to indicate statistical significance.

3. Results

3.1. Surface Characterization and Evaluation of Zinc Ion Release

Figure 1 shows SEM images of the MAO-treated Ti surface treated in the electrolyte with 2.5 mM Zn before (A) and after (B) incubation in saline. Typical connective porous morphology after MAO treatment was observed. There was no difference in the surface morphology among the specimens before and after incubation in saline for 28 days according to our SEM data under the indicated magnification. In addition, the pore size on the specimens before incubation was 5.3 ± 2.3 µm and on the specimens after incubation during 28 days was 4.8 ± 2.1 µm. There were no significant differences in the pore size among the specimens before and after incubation.

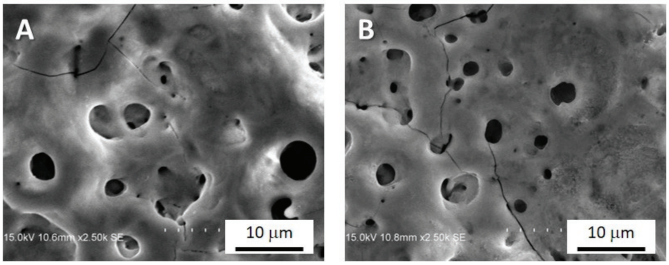

Figure 1. Scanning electron microscopy (SEM) images of specimens before (**A**) and after (**B**) incubation in saline during 28 days. These images show the connective porous oxide layer on a Titanium (Ti) surface formed by micro-arc oxidation (MAO) treatment using Zinc-containing electrolyte.

XRD spectra obtained from the MAO-treated Ti surface treated in the electrolyte with 2.5-mM Zn before and after incubation has been shown in Figure 2. The peaks originating from α-Ti and anatase TiO_2 were detected from each specimen. Moreover, the peaks originating from Zn were undetected. There was no difference in the crystal structure among the specimens before and after incubation in saline for 28 days.

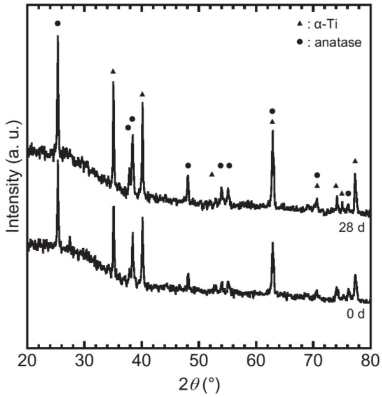

Figure 2. X-ray diffraction (XRD) spectra of the Zn-incorporated specimens before and after incubation in saline during 28 days.

XPS survey spectra of the MAO-treated Ti surface in the electrolyte with 2.5 mM Zn before and after incubation in saline has been shown in Figure 3A. In addition to peaks originating from C, O, P, Ca, and Ti, those originating from Zn and Na were detected. Narrow scan spectra around Zn 2p electron energy region is shown in Figure 3B. The binding energies of Zn $2p_{3/2}$ peaks obtained from all specimens were 1022.2–1022.6 eV, indicating that Zn existed as Zn^{2+}. Phosphorus was found to exist as phosphate species and calcium existed as a divalent ion, because binding energies of the corresponding peaks of P 2p and Ca $2p_{3/2}$ were 134.1 ± 0.2 eV and 347.8 ± 0.2 eV, respectively. The binding energy of Ti $2p_{3/2}$ peak was 459.0 ± 0.1 eV, indicating that Ti existed as TiO_2.

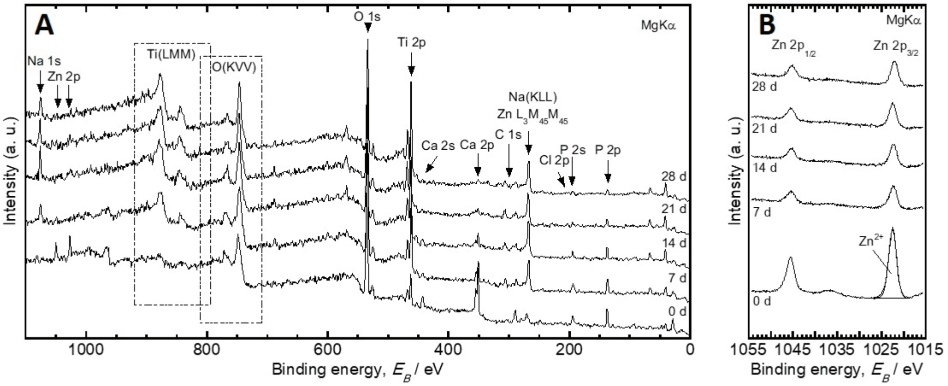

Figure 3. X-ray photoelectron spectroscopy (XPS) spectra of survey (**A**) and Zn 2p photoelectron energy region (**B**) from specimens immersed in saline for 0–28 days.

Figure 4 depicts the Wagner plot of Zn in the oxide layer incubated for 0–28 days based on Zn $2p_{3/2}$ peaks and Zn $L_3M_{45}M_{45}$ Auger peaks and reference plots from Zn^{2+} compounds as reported by previous studies [72–75]. The chemical state of an element was determined by comparison of its binding energy with modified Auger parameter values on the Wagner plot. According to the Wagner plot of Zn, the binding energy decreased, and the Auger parameter increased with incubation time. Moreover, since the value of the Auger parameter finally converged to 2010.2 eV, it became clear that the chemical state of Zn incorporated in titanium dioxide by MAO approached to that of ZnO with increasing incubation times.

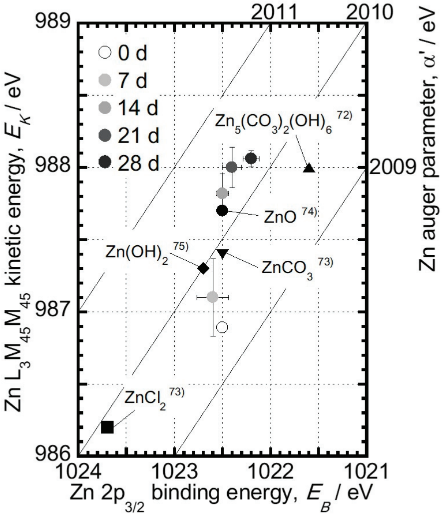

Figure 4. Wagner plot of Zn in the oxide layer incubated for 0–28 days based on Zn $2p_{3/2}$ photoelectron peaks and Zn $L_3M_{45}M_{45}$ Auger peaks (n = 3). Each parameter of Zn^{2+} compounds were plotted according to previous studies [72–75].

Figure 5 shows the change in the Zn concentration in the oxide layer at each incubation time, as determined by XPS. The concentration of Zn was relatively small even before the incubation; thus, the amount of Zn incorporated during MAO treatment was small. The amount of Zn dramatically decreased to about 0.8% by the incubation in saline from 0 to 7 days and was maintained for 28 days.

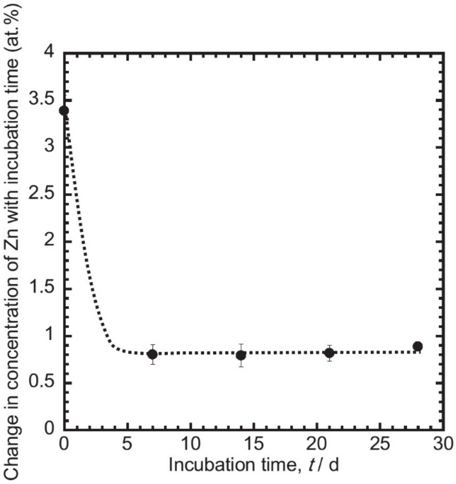

Figure 5. Change in the concentration of Zn in the oxide layer with incubation time determined by XPS (n = 3).

Figure 6 shows the amount of Zn ions released from the oxide layer into saline, as determined by ICP-AES. The amount of Zn ions released within the first 7 days was the highest and thereafter Zn was not detected. In summary, there was no observed release of Zn ions after 7 days.

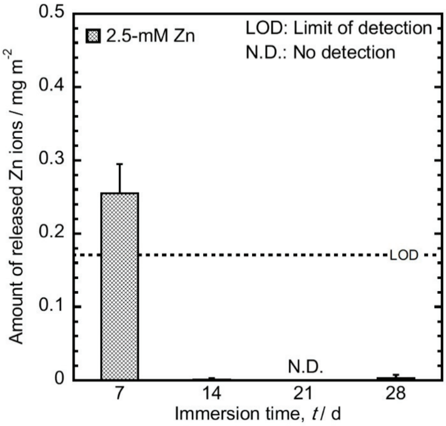

Figure 6. The amount of Zn ions released into saline every week from Ti MAO-treated in the electrolyte containing 2.5-mM Zn ($n = 3$).

3.2. Evaluation of Antibacterial Activity

Figure 7 shows the normalized CFU count for *E. coli* or antibacterial effects of MAO-treated Ti in the electrolyte containing various concentrations of Zn. The vertical axis represents the normalized bacterial number, defined as the bacterial number on each of the specimens divided by that of the control, MAO-treated Ti in the electrolyte without Zn. The normalized bacterial number that was below 1 (shown as dashed line in the figure) implied that the tested specimens had antibacterial activity. Before incubation, there was no significant difference in *E. coli* counts among the specimens. On the other hand, after incubation for 28 days, antibacterial effects against *E. coli* were observed. This effect was independent of the concentration of Zn in the electrolyte for MAO treatment, indicating that antibacterial activity of Zn developed after incubation in saline.

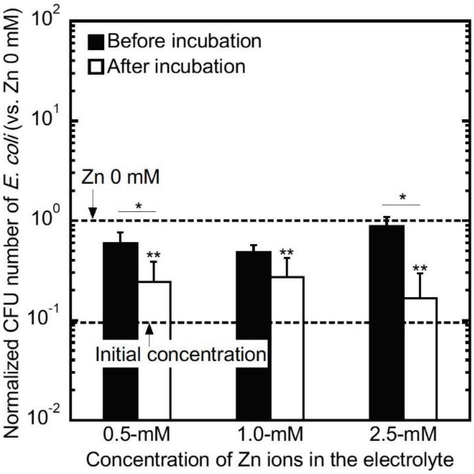

Figure 7. Antibacterial effects of Ti MAO-treated in the electrolyte containing various concentrations of Zn. Data are shown as the mean ± SD. *: Significant difference between specimens before and after incubation, **: Significant difference against the specimen without Zn ($n \geq 3$, $P < 0.05$).

3.3. Calcification by Osteogenic Cells

Figure 8 shows the number of MC3T3-E1 cells on MAO-treated Ti in the electrolyte containing various concentrations of Zn with varying culture times. The number of viable cells on all specimens increased with culture time. The Zn concentrations in the electrolyte did not differ significantly among specimens.

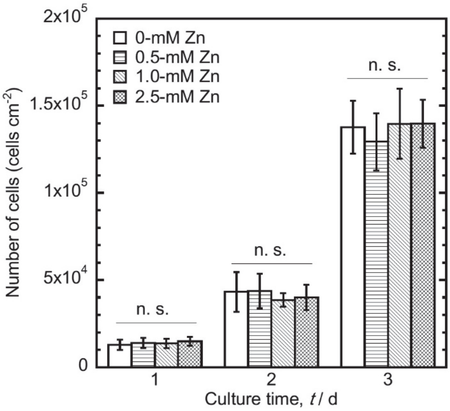

Figure 8. Number of MC3T3-E1 cells on Ti MAO-treated in the electrolyte containing various concentrations of Zn with culture time. Data are shown as the mean ±SD. n.s.: No significant difference ($n \geq 5$, $P < 0.05$).

Figure 9 shows photographs of alizarin red S staining of calcified deposits by MC3T3-E1 cells on each specimen cultured for 14 and 28 days. In case of MAO-treated specimens, we observed that only the central part (7 mm in diameter) was covered with the oxide layer formed by MAO treatment while the margins (0.5 mm) were not treated. Calcified cells were observed in all the specimens. However, untreated Ti showed bare metal-colored parts that indicated the presence of incompletely calcified cells. On the other hand, all MAO-treated specimens showed completely stained surfaces. There was no segregation seen for calcified and non-calcified areas on the MAO-treated surface. In addition, there were no visual differences among the MAO-treated specimens with and without Zn.

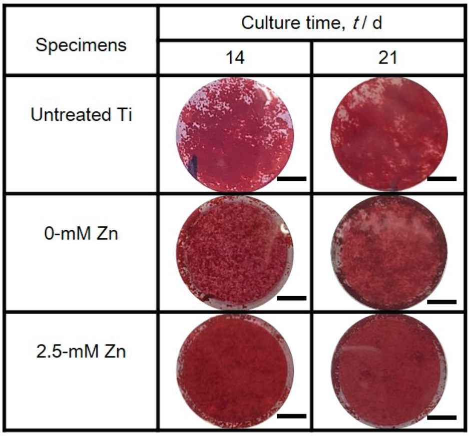

Figure 9. Color scale stained by alizarin red S of calcified deposits by MC3T3-E1 cells on each specimen cultured for 14 and 28 days. Scale bar represents 2 mm.

4. Discussion

The morphology and crystal structure of the porous oxide layer formed by MAO treatment did not show any changes during incubation in saline (Figures 1 and 2); this property is highly advantageous for implant surfaces.

The peaks originating from Zn were not detected from the specimens by XRD. The amount of Zn incorporated during MAO treatment was 3.5%, and decreased with incubation (Figure 5). Therefore, we believe that XRD peaks originating from Zn were relatively small compared with Ti, which was not detected by XRD.

The chemical state and concentration of Zn in the oxide layer changed during incubation in saline (Figures 3–5). In addition, the Zn ions were released into saline during the 7-day incubation period; thereafter, no Zn ions were eluted (Figure 6). These phenomena indicate that Zn incorporated into specimens would be released only during the initial stages of implantation in vivo. The concentration of Zn in the oxide layer decreased with the release of Zn ions during the first 7 days and was maintained at 0.8 at % in the subsequent period. In other words, despite the presence of Zn in the oxide layer, no Zn ions were released from the surface from 7 to 28 days. This indicated that the released Zn ion was adsorbed on the surface of the oxide layer to form zinc oxide as an insoluble corrosion product of Zn. The insoluble corrosion product of Zn was converted to ZnO to achieve chemical stabilization of Zn in saline. In other words, Zn incorporated into the oxide layer by MAO treatment changed the chemical state by interaction with saline and was finally stabilized by conversion into ZnO. Moreover, ZnO was already generated on the surface of oxide layer in the 14-day incubation (Figure 4). Therefore, it was considered that Zn ions did not elute during the 14–28 days period due to both the conversion into ZnO and stabilization in saline.

The specimens incubated in saline exhibited antibacterial activity against *E. coli*, while the specimens before incubation did not (Figure 7). Ti incorporated with Zn in the surface oxide layer formed by MAO treatment exhibited late-onset antibacterial activity against *E. coli*. The release of Zn ions were observed only during the initial stages of the incubation process (0–7 days). This indicated that Zn ions itself did not have any antibacterial activity. Du et al. [76] reported that the minimum inhibitory concentration (MIC) for Zn ions against *E. coli* was 768 $\mu g \cdot mL^{-1}$. The maximum concentration of Zn ions released from the specimens in this study was smaller than the previously reported MIC of Zn ions. For this reason, development of antibacterial activity by other factors needs to be considered. Prasanna et al. [77] reported that ZnO could produce reactive oxygen species (ROS) in the dark, owing to singly ionized oxygen vacancy in the crystal lattice of ZnO, and that generation of ROS contributed to its antibacterial properties. This study clearly revealed that Zn was finally converted to ZnO and was stabilized by interactions in saline. Therefore, the development of the late-onset antibacterial activity of Zn was due to the generation of ZnO in saline. In other words, this study proved that the chemical state of Zn incorporated in the oxide layer played a key role in the development of its antibacterial activity. Therefore, we believed that antibacterial activity was developed when ZnO was generated. According to Figure 4, we considered that the specimens incubated in saline during 14–21 days could exhibit the antibacterial activity, while the specimens incubated in saline during 0–7 days may not affect to bacteria. On the other hand, it is believed that bacteria interact with titanium dioxide through surface siderophores, and the oxides provide a template for biofilm formation [78,79]. For this reason, it is expected that bacteria can be captured by the interaction between the porous titanium dioxide and the siderophore on the cell surface, and killed by ZnO. We believe that Zn-incorporation for a Ti surface by MAO treatment may be suitable for realizing both bacterial capture ability and antibacterial activity, namely a 'trap-killing' system [80].

The MAO-treated specimens containing Zn showed no toxic effects on proliferation of osteogenic cells (Figure 8). Moreover, the calcification of cells on MAO-treated specimens with Zn were at the same level as that on the specimen without Zn. Therefore, the existence of a slight amount of Zn did not affect the osteogenic property of cells and proliferation was normal. The porous oxide layer consisted not only of titanium oxide but also incorporated Ca, P, and Zn (Figure 3). Relatively large amounts of Ca and P were contained in the oxide layer of MAO-treated Ti-based alloy at 7.6 and 10.0 at %, respectively [81]. Ca and P are the main mineral components in bone tissues and are present as calcium–phosphate compounds. The presence of Ca and P in the porous oxide layer formed by MAO treatment enhances the activity of osteogenic cells [47]. In our previous study, MAO-treated specimens containing a small amount of Ag showed osteogenic cell compatibility, which accelerated the calcification process by MC3T3-E1 cells without any cytotoxicity [22]. Therefore, we predicted that Zn-containing specimens in this study might have the same calcification ability.

In addition, a specific antibacterial activity of Zn, which was incorporated in the oxide layer was observed. Zn-incorporated oxide layer formed by MAO exhibited late-onset antibacterial activity and osteogenic cell compatibility, namely dual function. The amount of Zn ions released during 7 days incubation (0.02 ppm) was much less than IC_{50} for MC3T3-E1 cells reported by Yamamoto et al. [82]. Moreover, our results indicated that the small amount of ZnO generation did not affect osteogenic cells. In other words, the time transient effect of a suitable amount of Zn was effective for only bacteria. Therefore, MAO treatment of Ti using Zn made it possible to exhibit both late-onset antibacterial activity and osteogenic cell compatibility on Zn-containing TiO_2 layer. In addition, our study proposed the importance of the chemical state of Zn in the oxide layer for the development of antibacterial properties of Zn. Our results have suggested that due to the time transient effect of Zn in TiO_2, its chemical and biological properties could be easily changed and this property could be adapted for achieving changes in simulated body fluids (Figure 10). In particular, we suggest the importance of the chemical state changes of Zn in the various environments to control its chemical and biological properties. We hope that in future, that the outcome of the present study would be useful in the design of bio-functional implants related to Zn and contribute to the development of antibacterial biomaterials.

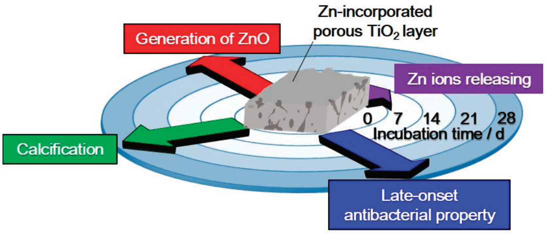

Figure 10. The schematic illustration of time transient effect of Zn in the porous titanium dioxide layer on chemical and biological properties.

5. Conclusions

This study investigated the time transient effect of Zn in titanium dioxide with incubation in saline. Although the morphology of the porous oxide layer formed by MAO treatment did not change, the chemical state of Zn in the oxide layer changed to ZnO during incubation in saline. Moreover, the antibacterial activity of the specimen with Zn developed in the late stages after the incubation process in saline for 28 days. We propose that the generation of ZnO in the oxide layer played a key role in development of antibacterial activity. In addition, the Zn-incorporated specimen did not exhibit any cytotoxicity in MC3T3-E1 cells and did not hinder the proliferation and calcification of cells. Therefore, MAO treatment of Ti using Zn is suitable for realizing both late-onset antibacterial activity and osteogenic cell compatibility.

Author Contributions: Conceptualization, M.S., Y.T., A.N. and T.H.; formal analysis, M.S., Y.T., K.N. and P.C.; investigation, M.S., K.N., R.Y. and M.A.; methodology, M.S., K.N., P.C. and H.D.; project administration, Y.T., A.N. and T.H.; supervision, A.N. and T.H.; validation, M.S., Y.T., K.N. and R.Y.; writing – original draft, M.S.; writing – review and editing, T.H.

Funding: This research received no external funding.

Acknowledgments: This study was supported by the Research Center for Biomedical Engineering, Tokyo Medical and Dental University, Project "Creation of Life Innovation Materials for Interdisciplinary and International Researcher Development" and project "Cooperative project amount medicine, dentistry, and engineering for medical innovation-Construction of creative scientific research of the viable material via integration of biology and engineering" by the Ministry of Education, Culture, Sports, Science and Engineering, Japan.

Conflicts of Interest: The authors declare no conflict of interest

References

1. Grainger, D.W.; van der Mei, H.C.; Jutte, P.C.; van den Dungen, J.J.A.M.; Schultz, M.J.; van der Laan, B.F.A.M.; Zaat, S.A.J.; Busscher, H.J. Critical factors in the translation of improved antimicrobial strategies for medical implants and devices. *Biomaterials* **2013**, *34*, 9237–9243. [CrossRef] [PubMed]
2. Busscher, H.J.; van der Mei, H.C.; Subbiahdoss, G.; Jutte, P.C.; van den Dungen, J.J.A.M.; Zaat, S.A.J.; Schultz, M.J.; Grainger, D.W. Biomaterial-associated infection: Locating the finish line in the race for the surface. *Sci. Transl. Med.* **2012**, *4*, 153. [CrossRef] [PubMed]
3. Dibart, S.; Warbington, M.; Su, M.F.; Skobe, Z. In vitro evaluation of the implant-abutment bacterial seal: The locking taper system. *Int. J. Oral Maxillofac. Implant.* **2005**, *20*, 732–737.
4. Glauser, R.; Schupbach, P.; Gottlow, J.; Hammerle, C.H. Periimplant soft tissue barrier at experimental one-piece mini-implants with different surface topography in humans: A light-microscopic overview and histometric analysis. *Clin. Implant Dent. Relat. Res.* **2005**, *7*, S44–S51. [CrossRef] [PubMed]
5. Tesmer, M.; Wallet, S.; Koutouzis, T.; Lundgren, T. Bacterial colonization of the dental implant fixture-abutment interface: An in vitro study. *J. Periodontol.* **2009**, *80*, 1991–1997. [CrossRef] [PubMed]
6. MacKintosh, E.E.; Patel, J.D.; Marchant, R.E.; Anderson, J.M. Effects of biomaterial surface chemistry on the adhesion and biofilm formation of staphylococcus epidermidis in vitro. *J. Biomed. Mater. Res. A* **2006**, *78A*, 836–842. [CrossRef]
7. Hobley, L.; Harkins, C.; MacPhee, C.E.; Stanley-Wall, N.R. Giving structure to the biofilm matrix: An overview of individual strategies and emerging common themes. *FEMS Microbiol. Rev.* **2015**, *39*, 649–669. [CrossRef]
8. Lindsay, D.; von Holy, A. Bacterial biofilms within the clinical setting: What healthcare professionals should know. *J. Hosp. Infect.* **2006**, *64*, 313–325. [CrossRef]
9. Fux, C.A.; Costerton, J.W.; Stewart, P.S.; Stoodley, P. Survival strategies of infectious biofilms. *Trends Microbiol.* **2005**, *13*, 34–40. [CrossRef]
10. Stewart, P.S.; Costerton, J.W. Antibiotic resistance of bacteria in biofilms. *Lancet* **2001**, *358*, 135–138. [CrossRef]
11. Hoiby, N.; Bjarnsholt, T.; Givskov, M.; Molin, S.; Ciofu, O. Antibiotic resistance of bacterial biofilms. *Int. J. Antimicrob. Agents* **2010**, *34*, 322–332. [CrossRef] [PubMed]
12. Koo, H.; Allan, R.N.; Howlin, R.P.; Stoodley, P.; Hall-Stoodley, L. Targeting microbial biofilms: Current and prospective therapeutic strategies. *Nat. Rev. Microbiol.* **2017**, *15*, 740–755. [CrossRef] [PubMed]
13. Conventry, M.B. Treatment of infections occurring in total hip surgery. *Orthop. Clin. North Am.* **1975**, *6*, 991–1003.
14. LaPorte, D.M.; Waldman, B.J.; Mont, M.A.; Hungerford, D.S. Infections associated with dental procedures in total hip arthroplasty. *J. Bone Joint Surg. Br.* **1999**, *81B*, 56–59. [CrossRef]
15. Rubin, R.; Salvati, E.A.; Lewis, R. Infected total hip-replacement after dental procedures. *Oral Surg. Oral Med. Oral Pathol. Oral Radiol. Endod.* **1976**, *41*, 18–23. [CrossRef]
16. Koerner, R.J.; Butterworth, L.A.; Mayer, I.V.; Dasbach, R.; Busscher, H.J. Bacterial adhesion to titanium-oxy-nitride (TiNOX) coatings with different resistivities: A novel approach for the development of biomaterials. *Biomaterials* **2002**, *23*, 2835–2840. [CrossRef]
17. Gao, A.; Hang, R.Q.; Huang, X.B.; Zhao, L.Z.; Zhang, X.Y.; Wang, L.; Tang, B.; Ma, S.L.; Chu, P.K. The effects of titania nanotubes with embedded silver oxide nanoparticles on bacteria and osteoblasts. *Biomaterials* **2014**, *35*, 4223–4235. [CrossRef]
18. Zhao, L.Z.; Wang, H.R.; Huo, K.F.; Cui, L.Y.; Zhang, W.R.; Ni, H.W.; Zhang, Y.M.; Wu, Z.F.; Chu, P.K. Antibacterial nano-structured titania coating incorporated with silver nanoparticles. *Biomaterials* **2011**, *32*, 5706–5716. [CrossRef]
19. Cao, H.L.; Liu, X.Y.; Meng, F.H.; Chu, P.K. Biological actions of silver nanoparticles embedded in titanium controlled by micro-galvanic effects. *Biomaterials* **2011**, *32*, 693–705. [CrossRef]

20. Mei, S.L.; Wang, H.Y.; Wang, W.; Tong, L.P.; Pan, H.B.; Ruan, C.S.; Ma, Q.L.; Liu, M.Y.; Yang, H.L.; Zhang, L.; et al. Antibacterial effects and biocompatibility of titanium surfaces with graded silver incorporation in titania nanotubes. *Biomaterials* **2014**, *35*, 4255–4265. [CrossRef]
21. Gasqueres, C.; Schneider, G.; Nusko, R.; Maier, G.; Dingeldein, E.; Eliezer, A. Innovative antibacterial coating by anodic spark deposition. *Surf. Coat. Technol.* **2012**, *206*, 3410–3414. [CrossRef]
22. Shimabukuro, M.; Tsutsumi, Y.; Yamada, R.; Ashida, M.; Chen, P.; Doi, H.; Nozaki, K.; Nagai, A.; Hanawa, T. Investigation of realizing both antibacterial property and osteogenic cell compatibility on titanium surface by simple electrochemical treatment. *ACS Biomater. Sci. Eng.* **2019**, in press. [CrossRef]
23. Cochis, A.; Azzimonti, B.; Della Valle, C.; De Giglio, E.; Bloise, N.; Visai, L.; Cometa, S.; Rimondini, L.; Chiesa, R. The effect of silver or gallium doped titanium against the multidrug resistant acinetobacter baumannii. *Biomaterials* **2016**, *80*, 80–95. [CrossRef] [PubMed]
24. Rai, M.K.; Deshmukh, S.D.; Ingle, A.P.; Gade, A.K. Silver nanoparticles: The powerful nanoweapon against multidrug-resistant bacteria. *J. Appl. Microbiol.* **2012**, *112*, 841–852. [CrossRef]
25. Lara, H.H.; Ayala-Nunez, N.V.; Turrent, L.D.I.; Padilla, C.R. Bactericidal effect of silver nanoparticles against multidrug-resistant bacteria. *World J. Microbiol. Biotechnol.* **2010**, *26*, 615–621. [CrossRef]
26. Prakash, P.; Gnanaprakasam, P.; Emmanuel, R.; Arokiyaraj, S.; Saravanan, M. Green synthesis of silver nanoparticles from leaf extract of mimusops elengi, linn. for enhanced antibacterial activity against multi drug resistant clinical isolates. *Colloids Surf. B Biointerfaces* **2013**, *108*, 255–259. [CrossRef]
27. Chernousova, S.; Epple, M. Silver as antibacterial agent: Ion, nanoparticle, and metal. *Angew. Chem. Int. Ed. Engl.* **2013**, *52*, 1636–1653. [CrossRef]
28. Cloutier, M.; Mantovani, D.; Rosei, F. Antibacterial coatings: Challenges, perspectives, and opportunities. *Trends Biotechnol.* **2015**, *33*, 637–652. [CrossRef]
29. Lemire, J.A.; Harrison, J.J.; Turner, R.J. Antimicrobial activity of metals: Mechanisms, molecular targets and applications. *Nat. Rev. Microbiol.* **2013**, *11*, 371–384. [CrossRef]
30. Samani, S.; Hossainalipour, S.M.; Tamizifar, M.; Rezaie, H.R. In vitro antibacterial evaluation of sol–gel-derived Zn-, Ag-, and (Zn + Ag)-doped hydroxyapatite coatings against methicillin-resistant staphylococcus aureus. *J. Biomed. Mater. Res. A* **2013**, *101*, 222–230. [CrossRef]
31. Jin, G.; Qin, H.; Cao, H.; Qian, S.; Zhao, Y.; Peng, X.; Zhang, X.; Liu, X.; Chu, P.K. Synergistic effects of dual Zn/Ag ion implantation in osteogenic activity and antibacterial ability of titanium. *Biomaterials* **2014**, *35*, 7699–7713. [CrossRef] [PubMed]
32. Kelson, A.B.; Carnevali, M.; Truong-Le, V. Gallium-based anti-infectives: Targeting microbial iron-uptake mechanisms. *Curr. Opin. Pharmacol.* **2013**, *13*, 707–716. [CrossRef] [PubMed]
33. Tran, P.A.; Webster, T.J. Antimicrobial selenium nanoparticle coatings on polymeric medical devices. *Nanotechnology* **2013**, *24*, 155101. [CrossRef] [PubMed]
34. Rodriguez-Valencia, C.; Lopez-Alvarez, M.; Cochon-Cores, B.; Pereiro, I.; Serra, J.; Gonzalez, P. Novel selenium-doped hydroxyapatite coatings for biomedical applications. *J. Biomed. Mater. Res. A* **2013**, *101*, 853–861. [CrossRef] [PubMed]
35. Zhang, W.; Li, Y.; Niu, J.F.; Chen, Y.S. Photogeneration of reactive oxygen species on uncoated silver, gold, nickel, and silicon nanoparticles and their antibacterial effects. *Langmuir* **2013**, *29*, 4647–4651. [CrossRef] [PubMed]
36. Applerot, G.; Lipovsky, A.; Dror, R.; Perkas, N.; Nitzan, Y.; Lubart, R.; Gedanken, A. Enhanced antibacterial activity of nanocrystalline ZnO due to increased ROS-mediated cell injury. *Adv. Funct. Mater.* **2009**, *19*, 842–852. [CrossRef]
37. Storrie, H.; Stupp, S.I. Cellular response to zinc-containing organoapatite: An in vitro study of proliferation, alkaline phosphatase activity and biomineralization. *Biomaterials* **2005**, *26*, 5492–5499. [CrossRef]
38. Jones, N.; Ray, B.; Ranjit, K.T.; Manna, A.C. Antibacterial activity of ZnO nanoparticle suspensions on a broad spectrum of microorganisms. *FEMS Microbiol. Lett.* **2008**, *279*, 71–76. [CrossRef]
39. Dastjerdi, R.; Montazer, M. A review on the application of inorganic nano-structured materials in the modification of textiles: Focus on anti-microbial properties. *Colloids Surf. B Biointerfaces* **2010**, *79*, 5–18. [CrossRef]
40. Raghupathi, K.R.; Koodali, R.T.; Manna, A.C. Size-dependent bacterial growth inhibition and mechanism of antibacterial activity of zinc oxide nanoparticles. *Langmuir* **2011**, *27*, 4020–4028. [CrossRef]

41. Padmavathy, N.; Vijayaraghavan, R. Enhanced bioactivity of ZnO nanoparticles-an antimicrobial study. *Sci. Technol. Adv. Mater.* **2008**, *9*, 035004. [CrossRef] [PubMed]
42. Su, Y.C.; Cockerill, I.; Wang, Y.D.; Qin, Y.X.; Chang, L.Q.; Zheng, Y.F.; Zhu, D.H. Zinc-based biomaterials for regeneration and therapy. *Trends Biotechnol.* **2019**, *37*, 428–441. [CrossRef] [PubMed]
43. Hanawa, T. Titanium–tissue interface reaction and its control with surface treatment. *Front Bioeng. Biotechnol.* **2019**, *7*, 170. [CrossRef] [PubMed]
44. Hanawa, T. A comprehensive review of techniques for biofunctionalization of titanium. *J. Periodontal. Implant. Sci.* **2011**, *41*, 263–272. [CrossRef]
45. Ha, J.Y.; Tsutsumi, Y.; Doi, H.; Nomura, N.; Kim, K.H.; Hanawa, T. Enhancement of calcium phosphate formation on zirconium by micro-arc oxidation and chemical treatments. *Surf. Coat. Technol.* **2011**, *205*, 4948–4955. [CrossRef]
46. Song, W.H.; Ryu, H.S.; Hong, S.H. Antibacterial properties of Ag (or Pt)-containing calcium phosphate coating formed by micro-arc oxidation. *J. Biomed. Mater. Res. A* **2009**, *88A*, 246–254. [CrossRef]
47. Li, L.H.; Kim, H.W.; Kim, Y.W.; Kim, H.E.; Heo, S.J.; Koak, J.Y. Improved biological performance of Ti implants due to surface modification by micro-arc oxidation. *Biomaterials* **2004**, *25*, 2867–2875. [CrossRef]
48. Li, Y.; Lee, I.S.; Cui, F.Z.; Choi, S.H. The biocompatibility of nanostructured calcium phosphate coated on micro-arc oxidized titanium. *Biomaterials* **2008**, *29*, 2025–2032. [CrossRef]
49. Suh, J.Y.; Janga, B.C.; Zhu, X.; Ong, J.L.; Kim, K.H. Effect of hydrothermally treated anodic oxide films on osteoblast attachment and proliferation. *Biomaterials* **2003**, *24*, 347–355. [CrossRef]
50. Son, W.W.; Zhu, X.; Shin, H.I.; Ong, J.L.; Kim, K.H. In vivo histological response to anodized and anodized/hydrothermally treated titanium implants. *J. Biomed. Mater. Res. B Appl. Biomater.* **2003**, *66B*, 520–525. [CrossRef]
51. Kim, D.Y.; Kim, M.; Kim, H.E.; Koh, Y.H.; Kim, H.W.; Jang, J.H. Formation of hydroxyapatite within porous TiO_2 layer by micro-arc oxidation coupled with electrophoretic deposition. *Acta Biomater.* **2009**, *5*, 2196–2205. [CrossRef] [PubMed]
52. Wang, Y.; Yu, H.J.; Chen, C.Z.; Zhao, Z.H. Review of the biocompatibility of micro-arc oxidation coated titanium alloys. *Mater. Des.* **2015**, *85*, 640–652. [CrossRef]
53. Wang, L.; Shi, L.; Chen, J.J.; Shi, Z.F.; Ren, L.; Wang, Y.J. Biocompatibility of Si-incorporated TiO_2 film prepared by micro-arc oxidation. *Mater. Lett.* **2014**, *116*, 35–38. [CrossRef]
54. Zhang, R.F.; Qiao, L.P.; Qu, B.; Zhang, S.F.; Chang, W.H.; Xiang, J.H. Biocompatibility of micro-arc oxidation coatings developed on Ti6Al4V alloy in a solution containing organic phosphate. *Mater. Lett.* **2015**, *153*, 77–80. [CrossRef]
55. Chen, H.T.; Chung, C.J.; Yang, T.C.; Chiang, I.P.; Tang, C.H.; Chen, K.C.; He, J.L. Osteoblast growth behavior on micro-arc oxidized β-titanium alloy. *Surf. Coat. Technol.* **2010**, *205*, 1624–1629. [CrossRef]
56. Cimenoglu, H.; Gunyuz, M.; Kose, G.T.; Baydogan, M.; Ugurlu, F.; Sener, C. Micro-arc oxidation of Ti_6Al_4V and Ti_6Al_7Nb alloys for biomedical applications. *Mater. Charact.* **2011**, *62*, 304–311. [CrossRef]
57. The in vitro and in vivo performance of a strontium-containing coating on the low-modulus $Ti_{35}Nb_2Ta_3Zr$ alloy formed by micro-arc oxidation. *J. Mater. Sci. Mater. Med.* **2015**, *26*, 203. [CrossRef]
58. He, X.J.; Zhang, X.Y.; Wang, X.; Qin, L. Review of Antibacterial activity of titanium based implants' surface fabricated by micro-arc oxidation. *Coatings* **2017**, *7*, 45. [CrossRef]
59. Hu, H.; Zhang, W.; Qiao, Y.; Jiang, X.; Liu, X.; Ding, C. Antibacterial activity and increased bone marrow stem cell functions of Zn-incorporated TiO_2 coatings on titanium. *Acta. Biomater.* **2012**, *8*, 904–915. [CrossRef]
60. Zhao, B.H.; Zhang, W.; Wang, D.N.; Feng, W.; Liu, Y.; Lin, Z.; Du, K.Q.; Deng, C.F. Effect of Zn content on cytoactivity and bacteriostasis of micro-arc oxidation coatings on pure titanium. *Surf. Coat. Technol.* **2013**, *228*, S428–S432. [CrossRef]
61. Zhang, L.; Gao, Q.; Han, Y. Zn and Ag co-doped anti-microbial TiO_2 coatings on Ti by micro-arc oxidation. *J. Mater. Sci. Technol.* **2016**, *32*, 919–924. [CrossRef]
62. Zhang, X.Y.; Wang, H.Z.; Li, J.F.; He, X.J.; Hang, R.Q.; Huang, X.B.; Tian, L.H.; Tang, B. Corrosion behavior of Zn-incorporated antibacterial TiO_2 porous coating on titanium. *Ceram. Int.* **2016**, *42*, 17095–17100. [CrossRef]
63. Du, Q.; Wei, D.Q.; Liu, S.; Cheng, S.; Hu, N.; Wang, Y.M.; Li, B.Q.; Jia, D.C.; Zhou, Y. The hydrothermal treated Zn-incorporated titania based microarc oxidation coating: Surface characteristics, apatite-inducing ability and antibacterial ability. *Surf. Coat. Technol.* **2013**, *352*, 489–500. [CrossRef]

64. Zhang, X.X.; Yang, L.; Lu, X.Q.; Lv, Y.; Jiang, D.; Yu, Y.; Peng, Z.; Dong, Z.H. Characterization and property of dual-functional Zn-incorporated TiO_2 micro-arc oxidation coatings: The influence of current density. *J. Alloy. Compd.* **2019**, *810*, 151893. [CrossRef]
65. Tanaka, Y.; Kobayashi, E.; Hiromoto, S.; Asami, K.; Imai, H.; Hanawa, T. Calcium phosphate formation on Ti by low-voltage electrolytic treatments. *J. Mater. Sci. Mater. Med.* **2007**, *18*, 797–806. [CrossRef] [PubMed]
66. Shirley, D.A. High-Resolution X-Ray Photoemission Spectrum of the Valence Bands of Gold. *Phys. Rev. B* **1972**, *5*, 552–556. [CrossRef]
67. Asami, K.; Hashimoto, K.; Shimodaira, S. XPS determination of compositions of alloy surfaces and surface oxides on mechanically polished iron–chromium alloys. *Corros. Sci.* **1977**, *17*, 713–723. [CrossRef]
68. Asami, K.; Chen, S.C.; Habazaki, H.; Kawashima, A.; Hashimoto, K. A photoelectrochemical and ESCA study of passivity of amorphous nickel-valve metal alloys. *Corros. Sci.* **1990**, *31*, 727–732. [CrossRef]
69. Hashimoto, K.; Kasaya, M.; Asami, K.; Masumoto, T. Electrochemical and XPS studies on corrosion behavior of amorphous Ni–Cr–P–B alloys. *Corros. Eng.* **1977**, *26*, 445–452. [CrossRef]
70. Scofield, J.H. Hartree-Slater subshell photoionization cross-sections at 1254 and 1487 eV. *J. Electron. Spectrosc. Relat. Phenom.* **1976**, *8*, 129–137. [CrossRef]
71. Oya, K.; Tanaka, Y.; Moriyama, Y.; Yoshioka, Y.; Kimura, T.; Tsutsumi, Y.; Doi, H.; Nomura, N.; Noda, K.; Kishida, A.; et al. Differences in the bone differentiation properties of MC3T3-E1 cells on polished bulk and sputter-deposited titanium specimens. *J. Biomed. Mater. Res. A* **2010**, *94A*, 611–618. [CrossRef] [PubMed]
72. Moretti, G.; Fierro, G.; Jacono, M.L.; Porta, P. Characterization of CuO–ZnO catalysts by X-ray photoelectron spectroscopy: Precursors, calcined and reduced samples. *Surf. Interface. Anal.* **1989**, *14*, 325–336. [CrossRef]
73. Dake, L.S.; Baer, D.R.; Zachara, J.M. Auger parameter measurements of zinc compounds relevant to zinc transport in the environment. *Surf. Interface Anal.* **1989**, *14*, 71–75. [CrossRef]
74. Gaarenstroom, S.W.; Winograd, N. Initial and final state effects in the ESCA spectra of cadmium and silver oxides. *J. Chem. Phys.* **1977**, *67*, 3500–3506. [CrossRef]
75. Deroubaix, G.; Marcus, P. X-ray photoelectron spectroscopy analysis of copper and zinc oxides and sulphides. *Surf. Interface Anal.* **1992**, *18*, 39–46. [CrossRef]
76. Du, W.L.; Niu, S.S.; Xu, Y.L.; Xu, Z.R.; Fan, C.L. Antibacterial activity of chitosan tripolyphosphate nanoparticles loaded with various metal ions. *Carbohydr. Polym.* **2009**, *75*, 385–389. [CrossRef]
77. Prasanna, V.L.; Vijayaraghavan, R. Insight into the mechanism of antibacterial activity of ZnO: Surface defects mediated reactive oxygen species even in the dark. *Langmuir* **2015**, *31*, 9155–9162. [CrossRef]
78. McWhirter, M.J.; Bremer, P.J.; Lamont, I.L.; McQuillan, A.J. Siderophore-Mediated covalent bonding to metal (Oxide) surfaces during biofilm initiation by pseudomonas aeruginosa bacteria. *Langmuir* **2003**, *19*, 3575–3577. [CrossRef]
79. Sharma, S.; Sharma, R.K.; Gaur, K.; Torres, J.F.C.; Loza-Rosas, S.A.; Torres, A.; Saxena, M.; Julin, M.; Tinoco, A.D. Fueling a hot debate on the application of TiO_2 nanoparticles in Sunscreen. *Materials* **2019**, *12*, 2317. [CrossRef]
80. Jia, Z.J.; Xiu, P.; Li, M.; Xu, X.C.; Shi, Y.Y.; Cheng, Y.; Wei, S.C.; Zheng, Y.F.; Xi, T.F.; Cai, H.; et al. Bioinspired anchoring AgNPs onto micro-nanoporous TiO_2 orthopedic coatings: Trap-killing of bacteria, surface-regulated osteoblast functions and host responses. *Biomaterials* **2016**, *75*, 203–222. [CrossRef]
81. Tsutsumia, Y.; Niinomi, M.; Nakai, M.; Tsutsumi, H.; Doi, H.; Nomura, N.; Hanawa, T. Micro-arc oxidation treatment to improve the hard-tissue compatibility of Ti–29Nb–13Ta–4.6Zr alloy. *Appl. Surf. Sci.* **2012**, *262*, 34–38. [CrossRef]
82. Yamamoto, A.; Honma, R.; Sumita, M. Cytotoxicity evaluation of 43 metal salts using murine fibroblasts and osteoblastic cells. *J. Biomed. Mater. Res.* **1998**, *39*, 331–340. [CrossRef]

coatings

MDPI

Article

Icariin/Aspirin Composite Coating on TiO_2 Nanotubes Surface Induce Immunomodulatory Effect of Macrophage and Improve Osteoblast Activity

Aobo Ma †, Yapeng You †, Bo Chen, Wanmeng Wang, Jialin Liu, Hui Qi, Yunkai Liang, Ying Li * and Changyi Li *

School of Dentistry, Tianjin Medical University, Tianjin 300070, China; maaobo@tmu.edu.cn (A.M.); youyapeng@tmu.edu.cn (Y.Y.); chenbo@tmu.edu.cn (B.C.); wangwanmeng@tmu.edu.cn (W.W.); liujialin@tmu.edu.cn (J.L.); qihui@tmu.edu.cn (H.Q.); liangyunkai@tmu.edu.cn (Y.L.)
* Correspondence: yingli@tmu.edu.cn (Y.L.); lichangyi@tmu.edu.cn (C.L.);
Tel.: +86-22-23332034 (Y.L.); +86-22-23332003 (C.L.)
† These authors contributed equally to this work.

Received: 24 March 2020; Accepted: 22 April 2020; Published: 24 April 2020

Abstract: Surface coating modification of titanium-based alloys is an efficient way to accelerate early osseointegration in dental implant fields. Icariin (ICA) is a traditional Chinese medicine that has bone activating functions, while aspirin (ASP) is a classical non-steroidal anti-inflammatory drug with good antipyretic and analgesic capabilities. Moreover, poly(lactic–co–glycolic acid) (PLGA) has attracted great attention due to its excellent biocompatibility and biodegradability. We superimposed an ASP/PLGA coating onto ICA loaded TiO_2 nanotubes structure so as to establish an icariin/aspirin composite coating on TiO_2 nanotubes surface. Scanning electron microscopy, X-ray photoelectron spectroscopy, a contact angle test and a drug release test confirmed the successful preparation of the NT–ICA–ASP/PLGA substrate, with a sustained release pattern of both ICA and ASP. Compared to those cultured on the Ti surface, macrophage cells on the NT-ICA-ASP/PLGA substrate displayed decreased M1 proinflammatory and enhanced M2 proregenerative genes and proteins expression, which implied activated immunomodulatory effect. Moreover, when cultured with conditioned medium from macrophages, osteoblast cells on the NT-ICA-ASP/PLGA substrate revealed improved cell proliferation, adhesion and osteogenic genes and proteins expression, compared with those on the Ti surface. The abovementioned results suggest that the established NT-ICA-ASP/PLGA substrate is a promising candidate for functionalized coating material in Ti implant surface modification.

Keywords: icariin; aspirin; composite coating; TiO_2 nanotubes; immunomodulatory effect; macrophage; osteoblast activity

---

1. Introduction

Dental implant dentures are the preferred treatment option for patients with dentition defect and edentulous jaws [1]. Titanium and titanium—based alloys have become the main steam material for dental implants due to their excellent mechanical properties and biocompatibility [2]. However, the biological inertness of pure titanium impairs the rapid bonding between dental implant and bone tissue, even causes implant failure [3]. Therefore, surface modification of Ti-based implant materials has become the main way to enhance cell activity, exert antibacterial effect and so as to promote osseointegration [4]. Various strategies have been employed for improving surface characteristics of dental implant, including physical, chemical and biological methods [5].

Among them, the application of protein growth factor on implant surface has been proved to be an effective way for enhancing osteogenesis and could accelerate osseointegration at the implant–tissue interface, such as bone morphogenetic protein–2 [6–8]. However, the lack of chemical stability of growth factor proteins hinders their wide application in implant surface modification [8,9]. In addition, inflammation reaction generated during the drilling, screwing and inserting processes of implant surgery may hamper bonding strength between implant and surrounding bone tissue [10]. In order to overcome the drawbacks, it becomes imperative to develop a new surface modification method, which could load osteogenic drug with chemical stability and subside inflammation accompanied with implant surgery at the same time.

Epimedium is widely used in traditional Chinese medicine and has the kidney invigorating and bone activating functions [11]. Icariin (ICA), an inexpensive and chemically stable monomer components of Epimedium [12,13], retains the osteogenic function of Epimedium and has antiatherosclerotic, anti-inflammatory and anticancer capabilities [14]. At the same time, icariin can promote the proliferation activity of osteoblasts and inhibit the formation of osteoclasts. Therefore, it is widely used in the treatment of osteoporosis [15]. In addition, icariin is also a promising osteoinductive compound for bone tissue engineering [11,16]. We previously reported that the icariin-functionalized coating on TiO_2 nanotubes surface promote osteoblast function and accelerate osseointegration [17]. Moreover, recently the anti-inflammatory [18,19] and immunoregulatory [20] functions of ICA has also been raised. Therefore, ICA becomes an ideal candidate drug for Ti-based implant surface modification to regulate immune response and promote bone formation at the same time.

Aspirin (ASP) is a well-established non-steroidal anti-inflammatory drug (NSAID), with chemical stability and an inexpensive price. In addition to its long-term application as an antipyretic and analgesic for postoperative pain relief [21], ASP is also reported to substantially improve immunomodulatory function, manifested as regulatory T cells upregulation and Th17 cells downregulation in vitro [22]. In addition, systemic use of ASP revealed enhanced bone regeneration in vivo [23]. Moreover, some scholars have recently demonstrated that low doses of ASP can regulate the balance between bone resorption and bone formation in osteoporosis caused by ovariectomy [24–26]. Evidence from both in vitro cell culture tests and in vivo animal studies also revealed that ASP has a protective effect on bones by promoting the proliferation of osteoblast precursor cells and differentiation of osteoblasts [27]. Therefore, in the present work, we further superimposed ASP on the ICA-loaded TiO_2 nanotubes surface, in order to simultaneously resolve acute inflammation after implant insertion and improve osteogenesis.

Due to the lack of immobilization sites for drug molecules on the pristine Ti surface, we fabricated TiO_2 nanotubes on Ti surface as the reservoir for drug storage and delivery. Prepared by anodization, TiO_2 nanotubes are widely used as a surface modification method for dental implants [28]. It is well-accepted that nanostructured morphology can promote osteoblast adhesion, proliferation, differentiation activity and accelerate osseointegration around the implant [29]. However, since the end of nanotubes are in an open state, loading drug on TiO_2 nanotubes surface may cause undesired early burst release of the drug [30]. To solve this problem, it is necessary to find a coating material combined with nanotube architecture so as to endow the modified surface with a controlled drug release platform.

In order to effectively overcome the initial fast drug release of the simple TiO_2 nanotubes surface, various coatings were applied to acquire sustained drug release capacity on the nanotubes surface [31,32]. Among them, poly(lactic-co-glycolic acid), often shortened to PLGA, is one of the important materials for preparing controlled drug release coatings. A large amount of literature have reported different types of PLGA-based drug delivery systems (DDSs), such as nanoparticles, microspheres, implants, nanogels, nanofibers, rods, films, etc. [33,34]. The PLGA controlled release coating can load a variety of substances from hydrophilic to lipophilic drugs, from micromolecule to macromolecule and from single molecules to multiple molecules [35].

Therefore, in the present study, TiO_2 nanotubes structure were first prepared on the Ti surface and then loaded with ICA. Afterwards, the ASP/PLGA coating is employed to cover the pre-existed ICA loaded nanotubes surface. Thus, we constructed the icariin/aspirin composite coating on TiO_2

nanotubes surface, abbreviated as NT–ICA–ASP/PLGA substrate. Scanning electron microscope (SEM), X-ray photoelectron spectroscopy (XPS) and contact angle test were utilized for characterization of the physical and chemical features of the established icariin/aspirin composite coating on TiO_2 nanotubes surface. While the drug release tests were used to evaluate the release profiles of ICA and ASP, respectively.

Previously, researchers have made great effort on titanium surface modification to improve osteogenic properties in mesenchymal stem cells or osteoblast cells. However, the discrepancies of biological responses between in vitro and in vivo experiments exist when evaluating implant materials so far. It implies that the complexity of the in vivo environment has not been fully understood and some important factors, including immunomodulatory factors, are often ignored [36,37]. Among all the immune cells, macrophages play a central role in inflammation reaction [38,39]. Macrophage cells were also one of the cell types, which firstly contact with implant materials after insertion [40]. Therefore, in the present work, we intend to simultaneously explore the immunomodulatory function and osteogenic effect of the icariin/aspirin composite coating on TiO_2 nanotubes surface. At first, we examined the immunomodulatory effect of the established NT–ICA–ASP/PLGA substrate using macrophage cells. Then, we employed the indirect coculture system including macrophage conditioned media (CM) and osteoblast cells to evaluate the osteogenic function of the constructed NT–ICA–ASP/PLGA substrate.

Our hypothesis is that icariin/aspirin composite coating on the TiO_2 nanotubes surface could improve osteogenic effect of osteoblast cells through regulating the polarized status of macrophages. By exerting immunomodulatory function of macrophages at the interface between implant and surround bone tissue, an immune microenvironment that favors bone formation is created. The combined effects of icariin and aspirin may synergistically accelerate osseointegration of the dental implant.

2. Materials and Methods

2.1. Chemicals and Reagents

ICA and ASP was provided by Sigma-Aldrich (St. Louis, MO, USA). PLGA (Resomer RG 503, lactide:glycolide 50:50, ester terminated, Mw 24,000–38,000) was provided by Sigma-Aldrich Phosphate buffered saline (PBS) was obtained from Solarbio, Inc. (Beijing, China). Ammonium fluoride (NH_4F) and ethylene glycol (EG) were provided by Tianjin FengChuan Chemical Reagent Co., Ltd (Tianjin, China).

2.2. Specimen Preparation and Surface Characterization

2.2.1. TiO_2 Nanotubes Fabrication

To prepare the TiO_2 nanotubes surface, titanium (Ti) discs with diameter of 15 mm and thickness of 1 mm were fabricated from commercially produced titanium plate (Grade 2, ASTM F67 unalloyed Ti; 99.7% Ti; 0.14% O; 0.09% Fe; 0.04% C; 0.02% N; 0.008% H; 0.002% other elements), which were purchased from Baoji Titanium Industry (Baoji, China). Ti discs were polished by 320, 800, 1500 and 2000 grit sand paper in sequence, ultrasonically washed with acetone, ethanol and deionized water in turn for 10 min, and then dried in air. The solvent of the electrolyte is ethylene glycol (EG), the solute is 0.16 mol/L NH_4F, with 10% deionized water by volume added. The TiO_2 nanotubes discs were fabricated under a voltage of 40 V for 1 h by high-voltage DC power supply (Dongwen High Voltage Power Supply Factory, Tianjin, China). After reaction, discs were ultrasonically cleaned by the EG solution. Later, the discs were rinsed with deionized water for 3 times, and left to dry naturally to obtain the TiO_2 nanotubes (NT) surface.

2.2.2. Construction of Icariin/Aspirin Composite Coating on the TiO_2 Nanotubes Surface

To fabricate the NT–ICA surface, ICA was dissolved in anhydrous methanol, with the concentration adjusted to 1.15 mg/mL, then the solution was mixed by vortex oscillators for 2 min. The NT slices were placed in the wells of a 24–well plate, one well for each slice, then 1 mL prefabricated ICA solution was added to each well, sealed with parafilm membrane and left to stand for 24 h at 4 °C. After that, the excess liquid was sucked out and air-dried to obtain the NT-ICA surface.

To construct the Ti-PLGA and NT-ICA-PLGA surfaces, we dissolved 30 mg of PLGA powder in 1 mL acetone solution, mixed thoroughly by vortex. We spread 100 µL mixed solution evenly on the surface of the Ti and the NT–ICA slices, dried naturally and repeated four times to obtain the Ti–PLGA and NT-ICA-PLGA surfaces, respectively.

To establish the NT–ASP/PLGA and NT–ICA–ASP/PLGA substrates, we took 30 mg PLGA and 10 mg ASP powder into a 15 mL centrifuge tube, add 1 mL acetone solution, and mix thoroughly by vortex. Then apply 100 µL of the mixed solution of ASP, PLGA and acetone to the surface of the NT and NT–ICA slices and left to dry naturally. Repeat the coating step four times to obtain the NT–ASP/PLGA and NT–ICA–ASP/PLGA substrates, respectively.

2.2.3. Surface Characterization

Observe the macro surface morphology of Ti, Ti–PLGA, NT, NT–ICA, NT–ICA-PLGA, NT–ASP/PLGA and NT-ICA-ASP/PLGA surfaces with stereomicroscope (S9i; Leica Microsystem, Tokyo, Japan). The micro surface topography of various surfaces was observed using a scanning electron microscope (SEM, Zeiss Merlin Compact; ZEISS, Jena, Germany), the working distance was 22.4–27.8 mm. X-ray photoelectron spectroscopy (XPS, AXIS Nova; Kratos Analytical, Manchester, UK) was used for analyzing the elemental composition of each sample's constituents. At room temperature, the wettability of the sample surfaces were evaluated by contact angle measurement using deionized water. The droplet volume used was 2 µL, and a contact angle goniometer (JGW-360A, Chongda Intelligent Technology, Xiamen, China) was used to acquire droplet images. Values of initial contact angle were analyzed using image analysis software (version 1.0, Anglem, Chongda Intelligent Technology, Xiamen, China). Three different positions were measured for each sample, and values were determined as mean ± standard deviation, $n = 3$.

2.3. Icariin and Aspirin Drug Release Amount Measurement

The drug release profiles of two drugs ICA and ASP were detected by the high performance liquid chromatography system (HPLC; 1100 Series; Agilent Technologies, Santa Clara, CA, USA). The MS 105 electronic balance (Mettler-Toledo., Greifensee, Zurich, Switzerland) of 0.01 mg accuracy was used to accurately weigh the ICA and ASP reference substance. Anhydrous methanol was used to prepare the standard solution used in the standard curve by half dilution method. The standard solution concentrations of ICA and ASP are 0, 0.5, 1, 2, 4, 8 and 16 µg/mL and 0, 2.5, 5, 10, 20, 40 and 80 µg/mL, respectively. The samples were immersed in PBS (pH 7.4) at 37 °C for drug release experiments. Various samples were immersed in 10 mL PBS and incubated for 24 h, and then the solution was daily collected for analysis by the HPLC system. After that, fresh PBS solution was added to replace the extracted solution. The test periods for ICA and ASP lasted for 30 and 8 days, respectively. The total amount of drug loaded on the sample was calculated according to the accumulated amount of drug released until the end of the test period used in this experiment. The drug cumulative release percentage was calculated by dividing the accumulated amount of released drug at each time point by the total amount of drug loaded. Data are collected from three separate experiments and expressed as mean ± SD ($n = 3$).

2.4. Behaviors of RAW 264.7 Cells Cultured on Different Surfaces

2.4.1. Cell Culture of Macrophage Cells

All samples were sterilized by irradiation with 25 kGy Cobalt 60 for 30 min and placed in 24–well plate. RAW 264.7 macrophage cells (American Type Culture Collection, ATCC, Manassas, VA, USA) were cultured in Dulbecco's modified eagle medium (DMEM, Gibco, Carlsbad, CA, USA) supplemented with 10% fetal bovine serum (FBS, Gibco, Carlsbad, CA, USA) and 1% (*v/v*) streptomycin/penicillin (Gibco, Carlsbad, CA, USA) in a 5% CO_2 incubator (Thermo Fisher Scientific, Waltham, MA, USA) at 37 °C. Culture medium was daily changed and cells were stimulated with Lipopolysaccharides (LPS; Sigma Aldrich, St Louis, MO, USA) at the concentration of 1 μg/mL for the first three days. All samples were sterilized by irradiation with 25 kGy Cobalt 60 for 30 min.

2.4.2. Proinflammatory (M1) and Proregenerative (M2) Marker Gene Expression

The gene expression levels of proinflammatory (M1) and proregenerative (M2) markers in RAW 264.7 macrophage cells cultured on different substrates were analyzed by quantitative real-time polymerase chain reaction (qPCR). RAW 264.7 macrophage cells were seeded on all surfaces at a density of 1×10^4 cells/well for 3 days. Then, total RNA was extracted by TRIzol (Thermo Fisher Scientific, Waltham, MA, USA). The RNA concentration and purity were measured at 260 nm by Nanodrop spectrophotometer (NanoDrop Technologies, Wilmington, DE, USA). Mouse mRNA encoding genes for tumor necrosis factor-alpha (TNF–a), interleukin-1β (IL–1β), transforming growth factor-beta (TGF–β) and heme oxygenase-1 (HO–1) were selected, glyceraldehyde–3–phosphate dehydrogenase (GAPDH) was amplified in parallel with the target genes and used as an internal control. Reverse transcription and qPCR were performed. Then relative gene expression levels were determined using the relative threshold cycle (CT) method and reported as $2^{-\Delta\Delta Ct}$. Primers used for both the target genes and the housekeeping gene were shown in Table 1. For every interested gene, the cDNA amplification was performed in triplicate by a single sample. The results were from three independent tests.

Table 1. Primers for proinflammatory (M1) and proregenerative (M2) marker genes.

Gene	Gene Bank ID	DNA Primer	Sequence	Size (bp)
TNF–α	NM_001278601.1	Forward	5′-TGCCTATGTCTCAGCCTCTTC-3′	117
		Reverse	5′-GAGGCCATTTGGGAACTTCT-3′	
IL–1β	NM_008361.4	Forward	5′-TGTGCAAGTGTCTGAAGCAGC-3′	129
		Reverse	5′-TGGAAGCAGCCCTTCATCTT-3′	
TGF–β	NM_011577.2	Forward	5′-TTGCTTCAGCTCCACAGAGA-3′	183
		Reverse	5′-TGGTTGTAGAGGGCAAGGAC-3′	
HO–1	NM_010442.2	Forward	5′-GCCGAGAATGCTGAGTTCATG-3′	86
		Reverse	5′-TGGTACAAGGAAGCCATCACC-3′	
GAPDH	NM_008084.3	Forward	5′-GGTGAAGGTCGGTGTGAACG-3′	233
		Reverse	5′-CTCGCTCCTGGAAGATGGTG-3′	

2.4.3. Enzyme-Linked Immunosorbent (ELISA) Assay

The proinflammatory (M1) and proregenerative (M2) marker protein expression levels in RAW 264.7 macrophage cells incubated with all kinds of samples were further measured by enzyme-linked immunosorbent (ELISA) assay. RAW 264.7 macrophage cells were seeded on different surfaces at a density of 1×10^4 cells/well for 3 days. The supernatants were then collected and measured immediately. The concentrations of proteins including tumor necrosis factor-alpha (TNF-a), interleukin–1β (IL–1β), transforming growth factor-beta (TGF–β) and heme oxygenase–1 (HO–1) were determined by ELISA kits (ImmunoWay Biotechnology, Plano, TX, USA). Three different slices were measured for each group. Three independent experiments were repeated.

2.5. Behaviors of MC3T3-E1 Cells on Various Surfaces in Conditioned Medium (CM)

2.5.1. Collection and Preparation of CM

RAW 264.7 macrophages were seeded on various surfaces at a density of 1×10^4 cells/well for 14 days. Cells were stimulated with LPS (1 μg/mL) for the first three days, and culture medium supernatant were collected daily and changed with new medium. The collected supernatant was centrifuged at 1500 rpm for 15 min, and then filtered through a 0.22 μm filter. Then, the filtered supernatant was mixed with DMEM containing 10% FBS and 1% penicillin/streptomycin at a volume ratio of 1:1 to obtain the conditioned medium (CM), and stored at 4 °C for later use.

2.5.2. Cell Culture of Osteoblast Cells

MC3T3-E1 preosteoblast cells (ATCC, Manassas, VA, USA) were first cultured in the DMEM supplemented with 10% FBS and 1% (*v/v*) streptomycin/penicillin in a 5% CO_2 incubator at 37 °C. After 4 h of inoculation, cells were seeded on different surfaces at a density of 1×10^4 cells/well and the CM prepared in 2.5.1 was used for cell culture. Various samples were disinfected through irradiation with 25 kGy Cobalt 60 for 30 min.

2.5.3. Cell Proliferation

The cell proliferation ability of RAW 264.7 macrophage cells incubated with various substrates were measured using cell counting kit-8 assay (CCK-8, New Cell and Molecular Biotech, Suzhou, Zhejiang, China). Cells were cultured with all kinds of substrates in 24–well plates at a density of 1×10^4 cells/well for 7 days. At 1, 3, 5 and 7 d, 1 mL of culture medium containing 100 μL CCK-8 solution was distributed to each well. After incubation for 2 h in the incubator, 100 μL reserved solution was transferred into a new 96-well plate, and then measured by a microplate reader (Cytation 5, Bio-Tek, Winooski, VT, USA) at 450 nm. The values were measured and recorded as mean ± standard deviation, $n = 3$. The cell proliferation tests were repeated three times.

2.5.4. Cell Morphology

To examine cell morphology on various surfaces, MC3T3–E1 cells were incubated with different surfaces for 24 h before observation. Then, all samples were rinsed twice with PBS, fixed with 2.5% glutaraldehyde solution (Solarbio, Beijing, China) at 4 °C overnight. Then the fixed cells were rinsed by PBS for three times, 10 min each time. Afterwards, samples were further fixed by 1% osmic acid away from light for 1 h and then dehydrated using sequential ethanol solutions (30%, 50%, 75%, 90%, 95% and 100% (*v/v*)). Subsequently, various substrates were dried by critical point dryer (EM CPD030, Leica Microsystems, Wetzlar, Germany, the working distance was 8.3–9.4 mm. Lastly, cells grown on various samples were observed by SEM (SU8010, Hitachi, Tokyo, Japan). The typical images from three independent slices were shown for each group.

2.5.5. Osteogenic-Related Gene Expression

To detect the osteogenic-related gene expression levels in MC3T3-E1 cells incubated with different substrates, MC3T3–E1 cells were cultured for 14 days and the culture medium was changed daily. At 14 d, cells on the samples were extracted by TRIzol. Expression levels of mouse mRNA encoding genes for alkaline phosphatase (ALP), collagen type 1 alpha 1 (COL1A1), osteopontin (OPN) and osteocalcin (OCN) were detected, with the housekeeping gene *GAPDH* used as the internal control. Reverse transcription and quantitative real-time polymerase chain reaction were performed and data were calculated by the $2^{-\Delta\Delta Ct}$ method. Primers used for the target genes and the housekeeping genes were shown in Table 2. The cDNA amplification of each gene of interest was conducted in triplicate by one sample and data were reported from three separate tests.

Table 2. Primers for osteogenesis-related genes.

Gene	Gene Bank ID	DNA Primer	Sequence	Size (bp)
ALP	NM_007431.3	Forward Reverse	5′-ATCTTTGGTCTGGCTCCCATG-3′ 5′-TTTCCCGTTCACCGTCCAC-3′	106
COL1A1	NM_007742.4	Forward Reverse	5′-TAAGGGTCCCCAATGGTGAGA-3′ 5′-GGGTCCCTCGACTCCTACAT-3′	203
OPN	NM_001204203.1	Forward Reverse	5′-CTCACATGAAGAGCGGTGAG-3′ 5′-TCTCCTGGCTCTCTTTGGAA-3′	174
OCN	NM_007541.3	Forward Reverse	5′-GGACCATCTTTCTGCTCACTCTG-3′ 5′-GTTCACTACCTTATTGCCCTCCTG-3′	131
GAPDH	NM_008084.3	Forward Reverse	5′-GGTGAAGGTCGGTGTGAACG-3′ 5′-CTCGCTCCTGGAAGATGGTG-3′	233

2.5.6. Western Blot Test

The osteogenic-related protein expression levels in MC3T3–E1 cells cultured with various surfaces were examined by Western blot test after 14 days of incubation. MC3T3–E1 cells were cultured for 14 days and medium changed daily. Cells were then harvested on ice, washed twice using PBS, and 200 μL lysis buffer supplemented with protease inhibitor were added to each well. After being incubated on ice for 10 min, cell extracts were subjected to centrifuge with 12,000 rpm at 4 °C for 15 min. Protein samples were separated by SDS-PAGE and then transferred to polyvinylidene fluoride (PVDF) membranes. After blocking using skim milk powder (5 g/100mL, Solarbio, Beijing, China) for 1 h, PVDF membranes were hybridized with specific antibodies of ALP (1:1000, ab229126), COL1A1 (1:1000, ab6308), OPN (1:1000, ab63856) and OCN (1:1000, ab93876) from Abcam, Cambridge, UK, respectively overnight at 4 °C. Data of expression levels from interested proteins were compared with that of internal control beta-Actin (1:1000, ab8226, Abcam, Cambridge, UK) to normalize loaded protein amount of different samples. The membranes were washed three times, and then incubated with goat anti-mouse secondary antibody at 1:5,000 dilution for 1 h. The protein bands were visualized using chemiluminescence imaging system (ChemiDoc$^{\mathrm{TM}}$ XRS+ workstation, Hercules, CA, USA). The relative intensity of the protein bands was quantified using image analysis software (Image Pro-Plus 6.0, Media Cybernetics, Silver Spring, MD, USA).

2.6. Statistical Analysis

All experiments were performed three times and the data were expressed as means ± standard deviations (SD). The one-way ANOVA combined with Tukey post hoc test was applied to examine the statistical difference between different samples. All differences considered to be significant when $p < 0.05$.

3. Results

3.1. Surface Characterization

First, the macro surface morphology of various surfaces was observed with stereomicroscope (S9i; Leica Microsystem, Tokyo, Japan) and shown in Figure 1. The Ti slice looks silver and the Ti-PLGA surface observed a transparent film covering the original Ti surface, suggesting that PLGA can form thin film materials on the prepared surface. For the NT surface, a faint gray-green color was seen after anodic oxidation. Whereas, the surface of NT–ICA samples had obvious yellow color, with scattered icariin particles deposited. The NT–ICA–PLGA surface obtained by dripping the PLGA solution on the surface of the NT–ICA sample was still yellow, but the original ICA particles were covered and difficult to identify. Since ASP and PLGA are both white, the NT–ASP/PLGA surface revealed a white-color film on the faint gray-green color NT base material. While for the NT–ICA–ASP/PLGA substrate, a white-color film covering yellow base of NT-ICA was seen.

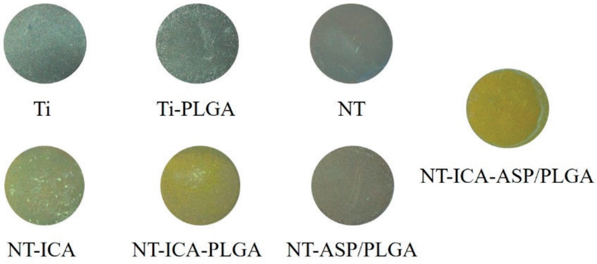

Figure 1. Macro surface morphology of various surfaces was observed under stereomicroscope (S9i; Leica Microsystem, Tokyo, Japan) and representative images were shown (10 ×).

Second, the micro surface morphology of all samples was observed using a scanning electron microscope (SEM, Zeiss Merlin Compact; ZEISS, Jena, Germany). As shown in Figure 2, scratch marks were seen on the surface of Ti after gradient polishing. After loading the PLGA coating, the Ti–PLGA group displayed a smooth and uniform surface. After the anodizing process, nanotubes with uniform and controllable diameter and length can be detected on the surface of NT group. The diameter of nanotubes was 100 ± 5 nm, while the length of which was 3 ± 0.5 μm. On the surface of the NT–ICA group, scattered granular substances of ICA were observed. For the NT–ICA–PLGA surface, ICA was completely enwrapped by the uniform smooth film of PLGA coating, with many needle-like configurations indicating the existence of ICA. While on the NT–ASP/PLGA substrate, short needle-like ASP crystals were observed in the PLGA coating layer. The morphology of NT–ICA–ASP/PLGA surface combined the common features of NT–ASP/PLGA and NT–ICA–PLGA surfaces, and displayed both the configuration of ICA and ASP in the PLGA coating.

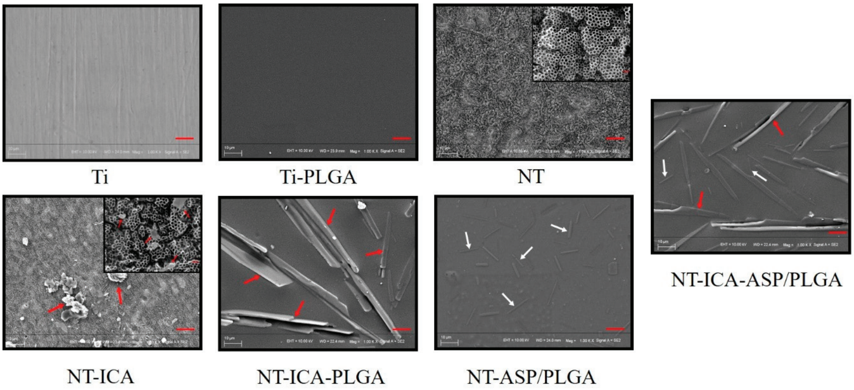

Figure 2. Surface micromorphology images of different substrates were obtained with scanning electron microscope (SEM, Zeiss Merlin Compact; ZEISS, Jena, Germany). Red and white arrows indicate icariin (ICA) and aspirin (ASP), respectively; 1000×, scale bar = 10 μm. Insets of images of NT and NT-ICA substrates were magnified SEM graphs (30,000×, scale bar = 200 nm).

XPS results were used to determine the elemental composition of different samples. All binding energies were referenced to the C 1s spectrum peak (284.8 eV) as an internal reference after calibrating peak position. As shown in Figure 3 and Table 3, the spectra of the Ti and NT mainly include C1s, O1s and Ti2p3. For the NT-ICA surface, increased peak of C1s may originate from ICA ($C_{33}H_{40}O_{15}$), while the decreased peak of Ti2p3 may be explained by the partial coverage of the TiO_2 nanotubes structure by ICA, compared to the NT surface.

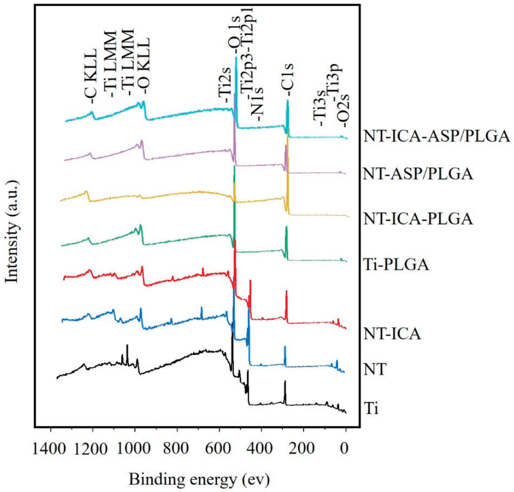

Figure 3. X-ray photoelectron spectroscopy (XPS) analysis displaying chemical composition of different surfaces.

Table 3. Chemical compositions of samples measured by XPS.

Substrates	C%	N%	O%	Ti%
Ti	47.19 ± 0.05	3.57 ± 0.01	39.27 ± 0.05	9.97 ± 0.02
Ti–PLGA	61.17 ± 0.05	0.34 ± 0.01	38.49 ± 0.03	0
NT	38.2 ± 0.03	2.97 ± 0.01	43.19 ± 0.03	15.63 ± 0.02
NT–ICA	50.49 ± 0.03	2.16 ± 0.01	39.47 ± 0.02	7.87 ± 0.02
NT–ICA–PLGA	90.66 ± 0.05	0	9.34 ± 0.02	0
NT–ASP/PLGA	72.3 ± 0.05	0	27.71 ± 0.02	0
NT–ICA–ASP/PLGA	64.53 ± 0.01	0	35.47 ± 0.05	0

In addition, the disappearance of the Ti peak on the Ti–PLGA, NT–ICA–PLGA, NT–ASP/PLGA and NT–ICA–ASP/PLGA surfaces indicate that the PLGA coating totally overspread the original Ti and nanotubes structures. As we known, PLGA ($[C_5H_8O_5]_n$), ICA ($C_{33}H_{40}O_{15}$) and ASP ($C_9H_8O_4$) are all composed of C, H and O. Due to the small photoionization cross section of H, the signal of H is too weak for XPS to be detected. Therefore, only C and O could be detected on the Ti–PLGA, NT–ICA–PLGA, NT–ASP/PLGA and NT–ICA–ASP/PLGA surfaces by XPS analysis. Moreover, since both icariin and aspirin have higher C and lower O element content than PLGA, the increased C and decreased O element content observed in NT–ICA–PLGA, NT-ASP/PLGA and NT–ICA–ASP/PLGA groups compared to the Ti–PLGA group may be explained by the successful loading of ICA and ASP.

In addition to surface topography and chemical composition, hydrophilicity is also an essential factor, which affects the biological compatibility of materials. Figure 4 showed that the contact angle of Ti was 89.5 ± 0.6°, while after the application of PLGA coating, the contact angles decreased to Ti–PLGA (69.5 ± 0.6°), NT–ICA–PLGA (58.9 ± 0.8°), NT–ASP/PLGA (69.8 ± 0.5°) and NT–ICA–ASP/PLGA (64.5 ± 1.6°), respectively, with statistical significance. This indicates that PLGA coating could improve the wettability of surfaces, compared to pure Ti surface. Moreover, the contact angles of the NT and NT–ICA groups were 19.5 ± 3.0° and 21.3 ± 1.0°, respectively, even lower than those of various PLGA coated substrates, with statistical significance. This phenomenon suggested that the titanium nanotube structure fabricated after anodization could substantially enhance the hydrophilicity of surfaces. In this experiment, we only detected the initial contact angles. In a follow-up experiment, we will further test the frequency acquisition of the droplet images and monitor the time dependence of the water contact angle so as to obtain more kinetic constant and exponential parameters of material and evaluate hydrophilicity of the material much more accurately.

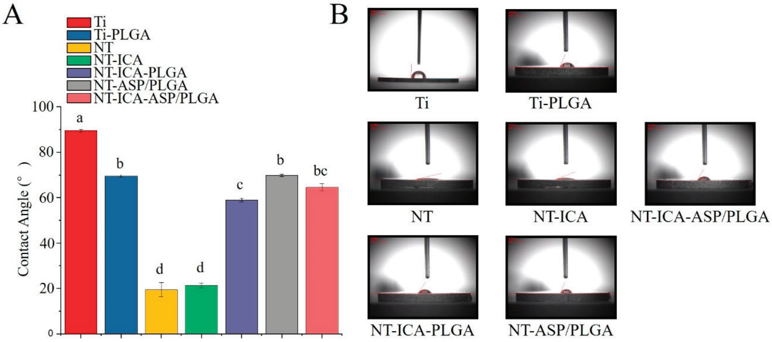

Figure 4. Contact angles of various surfaces. (**A**) Contact angle degree of different surfaces. Different lowercase letters indicate statistically significant differences between different groups ($p < 0.05$). Data are expressed as mean ± SD, $n = 3$ replicates each group. (**B**) Images of contact angles on different surfaces.

3.2. In Vitro Drug Release Profile

The drug release pattern of ICA in the NT-ICA-ASP/PLGA surface is shown in Figure 5A. A sustained release profile of ICA was seen during the 30 days detection period. At the same time, the daily concentration of ICA always maintained within the range of 0.1–1 × 10^{-5} mol/L per day, which was proved to be effective concentration of icariin to promote MC3T3–E1 cells osteogenesis in our preliminary experiment (data not shown). Taken into consideration of this point, the addition of ICA in the NT–ICA–ASP/PLGA surface is expected to exert continued osteogenic function during the release period.

As shown in Figure 5B, the release profile of ASP also displayed controlled release pattern during the release period, and finally reached a plateau at day 7. In addition, the release concentration of ASP maintained between 0.2 and 4 mM during day 1–5, within the effective concentration of anti-inflammatory and proregenerative function of ASP by our preliminary data (data not shown). Therefore, we hypothesized that the addition of ASP in the coating may promote RAW 264.7 macrophage cells to change from M1 to M2 polarization status.

Meanwhile, the release kinetics of both ICA and ASP in the NT–ICA–ASP/PLGA surface were assessed by fitting the release profiles of the two drugs to the Korsmeyer−Peppas model [41]. The mechanism of ICA and ASP release from the established surface during dissolution investigations in PBS was determined using Equation (1):

$$\frac{M_t}{M_\infty} = kt^n \tag{1}$$

where $\frac{M_t}{M_\infty}$ is the fractional drug release at denoted time point t, k is a kinetic constant reflecting the structural and geometric properties of the drug/carrier system, and n is the release exponent, which relies on the release mechanism. As shown in Figure 6, the first 10 days of ICA release profile was used for simulation and the release exponent n was 1 ± 0.0251, which is close to a desirable time-dependent release mechanism, as indicated by Korsmeyer et al. [41]. While for ASP, since there were relatively less time points for simulation, we selected the first 4 days for simulation and the diffusional release exponent n value was 0.5438 ± 0.0725, which implied a drug release mechanism approximately controlled by anomalous (non-Fickian) diffusion. As illustrated in Figure 6, the data fit the model well as the correlation coefficient R^2 of ICA and ASP release curves are 0.9946 and 0.9485, respectively. In addition, the kinetic constant of ICA and ASP were 5.9699 ± 0.2496 and 47.5629 ± 3.2833, respectively, which indicated different structural and geometric properties of the two kinds of drugs in the drug/carrier system. The drug release percentage scatter diagrams as a function of time and sketch view of the established substrate were shown in Figure 6A–C. The sustained release mechanism of ICA may partly be interpreted by its poor water solubility [42] and the existence of the outside ASP/PLGA coating, which generate a viscous layer that further retarded the drug diffusion to the solvent, similar to a previous report [43]. In the future, drug release amount at more time points, especially for ASP, are needed to be measured to evaluate the kinetic mechanism much accurately.

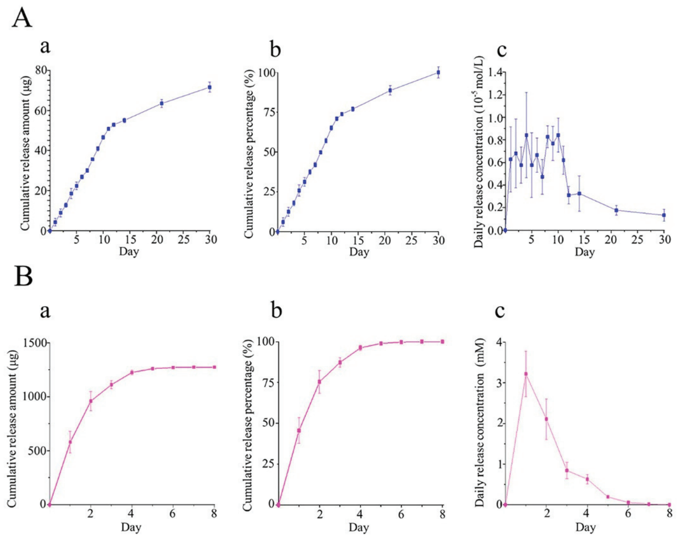

Figure 5. In vitro release profile of ICA (**A**) and ASP (**B**) on the NT-ICA-ASP/PLGA surface. (**a**) Cumulative release amount curve. (**b**) Cumulative release percentage curve. (**c**) Daily release concentration curve. Data are expressed as mean ± SD (*n* = 3).

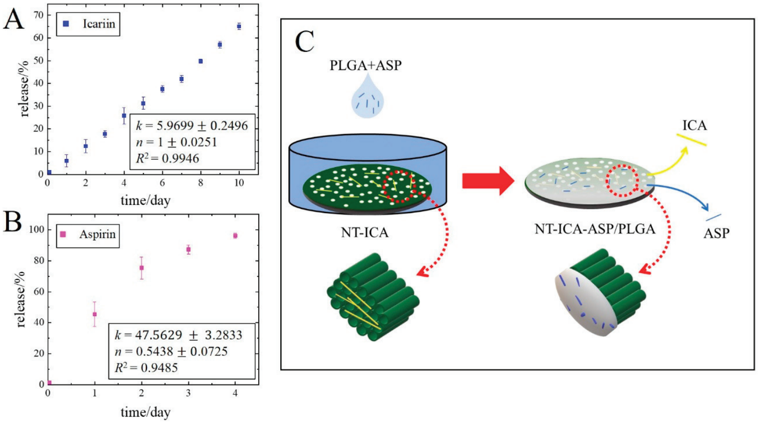

Figure 6. (**A**) ICA release behaviors in the first ten days. (**B**) ASP release behaviors in the first four days. (**C**) Sketch view of the NT–ICA–ASP/PLGA release system.

3.3. Polarization Status of RAW 264.7 Cells Cultured on Different Surfaces

3.3.1. Proinflammatory (M1) and Proregenerative (M2) Marker Genes Expression

Quantitative real-time polymerase chain reaction (qPCR) was performed to detect expression levels of proinflammatory (M1) and proregenerative (M2) gene markers in RAW 264.7 macrophage cells incubated with different substrates. The results were displayed in Figure 7. In the physiological healing of wound, the inflammatory phase last hours to days. Therefore, the initial several days after dental implant insertion was crucial for ideal osseointegration. Since the drug release curve of ASP revealed a relative steady release profile during day 2–4, we selected day 3 to evaluate the polarization of macrophages. As shown in Figure 7, M1 proinflammatory genes IL-1β and TNF-α expression levels decreased in cells cultured on the NT surface, compared with those on the pristine Ti surface, indicating that the 100 nm diameter NT used in this experiment could inhibit inflammatory reaction at the gene level. Whereas the Ti−PLGA surface evoked higher proinflammatory genes expression than Ti surface. It indicated that although PLGA is a non-toxic and harmless material that can be absorbed by the human body, it could promote inflammatory reaction in RAW 264.7 cells during the early period after implantation. However, the decreased M1 proinflammatory gene levels in cells incubated with the NT-ICA-PLGA surface, compared with those with the Ti-PLGA surface implied that ICA may exert anti-inflammatory function. In particular, the addition of ASP, a well-established non-steroidal anti-inflammatory drug, obviously decreased proinflammatory gene expression in macrophage cells cultured on NT−ASP/PLGA and NT−ICA−ASP/PLGA substrates, compared with the Ti surface.

The M2 proregenerative marker genes expression in RAW 264.7 macrophage cells cultured on various surfaces were further evaluated. After 3 days of incubation, the addition of PLGA coating on the Ti−PLGA surface did not change TGF-β and HO-1 gene expression levels much, compared with Ti surface. It indicated that PLGA had no significant effect on induction of macrophages towards M2 polarized status. Previously, ICA has been reported to exert anti-inflammatory effect by elevated cytoprotective gene expression HO−1 [44,45]. Therefore, the observed highest HO−1 gene level on the NT−ICA surface may be attributed to the burst release of ICA occurred during the first 3 days, which evoked the substantially increased HO−1 gene expression. Most importantly, TGF−β and HO−1 gene levels in cells on the NT−ICA, NT−ICA−PLGA, NT−ASP/PLGA and NT−ICA−ASP/PLGA substrates were obviously higher than those on the Ti surface, with statistical significance. These results suggest that both ICA and ASP could induce M2 polarization of macrophage, which endowed the NT−ICA−ASP/PLGA substrate with superior proregenerative immunomodulatory ability.

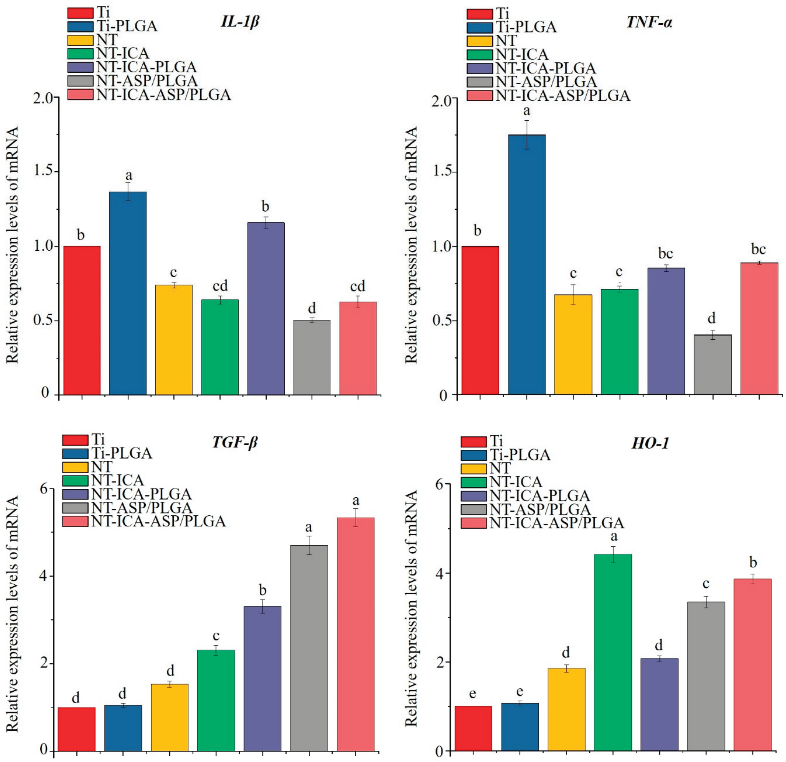

Figure 7. Real-time PCR results of interleukin-1β (IL-1β), tumor necrosis factor-alpha (TNF-a), transforming growth factor-beta (TGF-β) and heme oxygenase-1 (HO-1) gene expression levels in the RAW 264.7 cells on different substrates after 3 days of incubation. Different lowercase letters indicate statistically significant differences between different groups ($p < 0.05$). Data are mean ± SD, $n = 3$ replicates each group.

3.3.2. Enzyme-Linked Immunosorbent (ELISA) Assay

We further examined the proinflammatory (M1) and proregenerative (M2) marker protein expression levels by ELISA assay. As shown in Figure 8, decreased IL−1β and TNF−α and increased TGF−β and HO−1 protein levels were observed in cells cultured on the NT surface, compared with those on the Ti surface, displaying that the nanotube structure could reduce inflammation and induce regeneration. On the contrary, proinflammatory IL−1β and TNF−α protein levels were enhanced, while the proregenerative TGF−β and HO−1 protein levels do not change much in cells on the Ti−PLGA surface, compared with the Ti surface. It showed that the PLGA coating could induce M1 inflammatory reaction, but failed to induce M2 polarization in macrophages. After the addition of ICA and ASP, M1 proinflammatory IL−1β and TNF-α protein levels reduced, whereas TGF−β and HO−1 protein levels elevated in cells on the NT−ICA, NT−ICA−PLGA, NT−ASP/PLGA and NT−ICA−ASP/PLGA substrates, compared to the original Ti surface, with statistical significance. In particular, NT-ASP/PLGA and NT−ICA−ASP/PLGA groups had relatively lower M1 and higher M2 proteins secretion than the other groups.

Combined the results from gene and protein detection in RAW 264.7 cells, similar to the NT−ASP/PLGA surface, the NT−ICA−ASP/PLGA substrate also exhibited a superior ability of inflammation inhibition and regeneration enhancement than other surfaces. It implies that the combination of ASP and ICA on the NT−ICA−ASP/PLGA surface could achieve anti-inflammatory and proregenerative function.

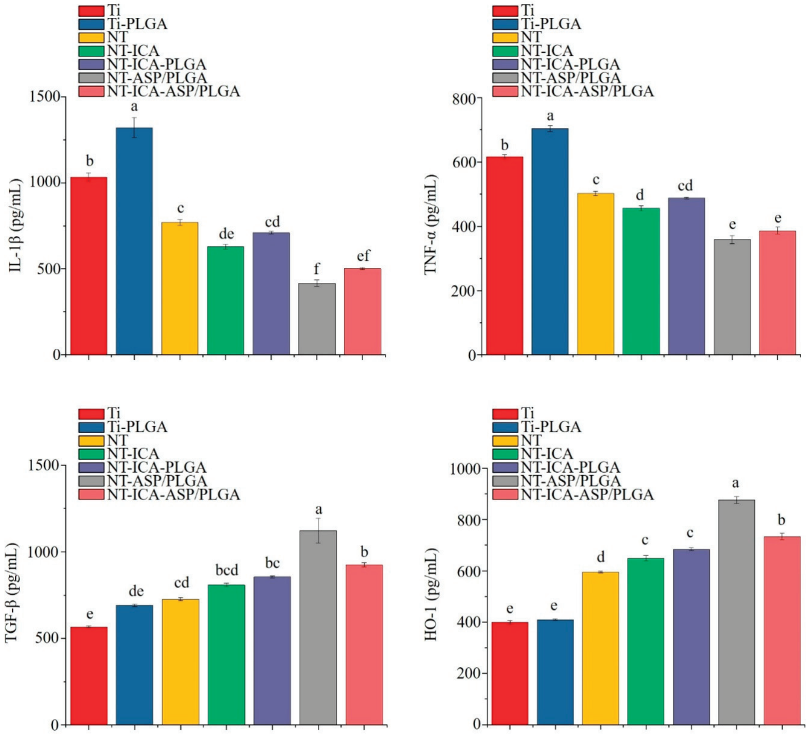

Figure 8. ELISA results representing the RAW 264.7 cytokine secretion on different substrates after 3 days of culture. Different lowercase letters indicate statistically significant differences between different groups ($p < 0.05$). Data are mean ± SD, $n = 3$ replicates each group.

3.4. Behaviors of MC3T3-E1 Cells on Various Surfaces in Conditioned Medium (CM)

3.4.1. Cell Proliferation

The proliferation of MC3T3-E1 cells seeded on all samples was assessed by CCK-8 assay. Figure 9 showed cell numbers cultured on different surfaces after 1, 3, 5 and 7 days of incubation. At day 1 and 3, there was no statistical significance in the cell proliferation capacity of each group although a tendency of a higher cell proliferation rate on the NT−ICA−ASP/PLGA substrate was seen, compared with the Ti group. After 5 and 7 days of incubation, cells cultured on NT−ASP/PLGA and NT−ICA−ASP/PLGA substrates revealed higher cell proliferation ability compared with that on the pristine Ti, $p < 0.05$. This suggests the relative strong effect of aspirin to promote osteoblast proliferation under the existence of CM from macrophage cells. Interestingly, the proliferation rate of cells on the NT−ASP/PLGA group was moderately higher than that on the NT−ICA−ASP/PLGA group, although there was no statistical difference. This phenomenon may be explained by that the NT−ICA−ASP/PLGA substrate had an additional prodifferentiation effect on osteoblasts than the NT−ASP/PLGA surface, due to the existence of ICA. It is well accepted that during cell life activity, higher proliferation activity is often inhibited when cell differentiation is promoted and vice versa [12,46]. Therefore, the slightly inhibited cell proliferation of the NT−ICA−ASP/PLGA group may imply its enhanced cell differentiation due to the additional prodifferentiation effect of released ICA, compared to the NT−ASP/PLGA group.

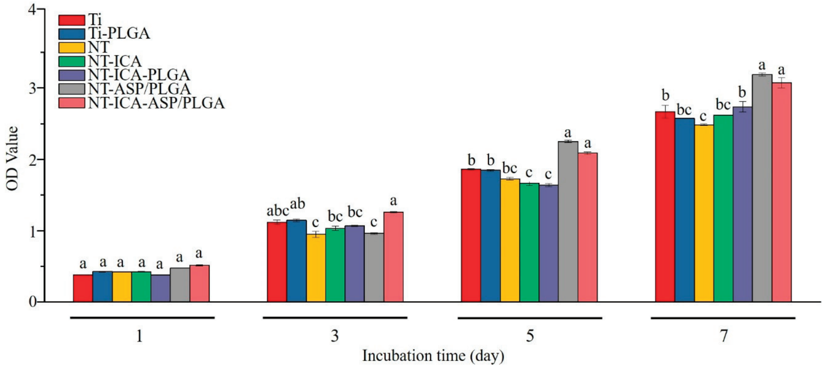

Figure 9. The CCK-8 results of MC3T3−E1 cells cultured on different surfaces for 1, 3, 5 and 7 days. Different lowercase letters indicate statistically significant differences between different groups ($p < 0.05$). Data are mean ± SD, $n = 3$ replicates each group.

3.4.2. Cell Morphology

Cell morphologies of MC3T3−E1 osteoblast cells on different samples after 24 h of incubation were acquired with scanning electron microscope (SEM, SU8010, Hitachi, Tokyo, Japan) and shown in Figure 10. After 24 h of incubation, cells attached along the direction of scratch marks on the pure Ti surface. While on the NT and NT−ICA substrates, cells revealed well-distributed morphology, with filopodia stretching into the nanotubular structures, which implies good cell adhesion induced by the nanostructure. In addition, cells on the Ti−PLGA, NT−ICA−PLGA, NT−ASP/PLGA and NT−ICA−ASP/PLGA substrates displayed a spread-out morphology, towards different directions. This can be explained by that PLGA improved cell adhesion to some extent, similar with previous report [47]. In particular, for the NT−ICA−ASP/PLGA substrate, cells extend towards all directions, which revealed the satisfied cell adhesion ability.

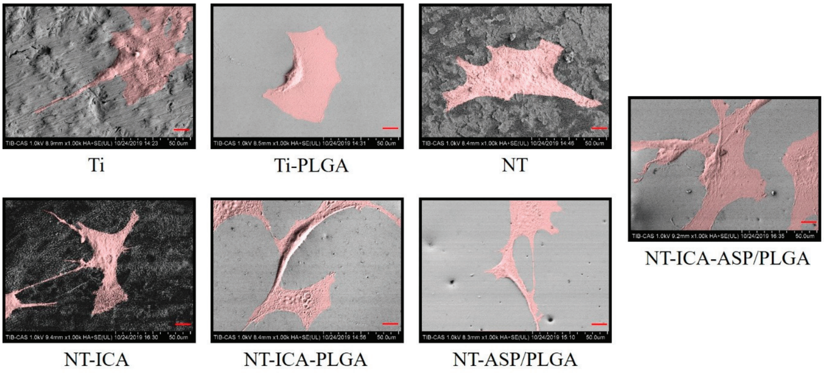
Ti

Ti-PLGA

NT

NT-ICA-ASP/PLGA

NT-ICA

NT-ICA-PLGA

NT-ASP/PLGA

Figure 10. Images of MC3T3−E1 cells showing the representative morphology on different substrates after 24 h of culture were obtained with scanning electron microscope (SEM, SU8010, Hitachi, Tokyo, Japan). The pseudo colored pink cells indicate morphology of MC3T3−E1 cells; 1000×, scale bar = 10 µm.

3.4.3. Osteogenesis-Related Gene Expression

Figure 11 shows osteogenesis-related genes expression of MC3T3−E1 cells cultured on different surfaces after 14 days of culture under the condition of macrophage CM. Gene expression levels of ALP, COL1A1 and OCN all increased on osteoblast cells cultured on the NT−ICA−PLGA, NT−ASP/PLGA and NT−ICA−ASP/PLGA substrates, compared with that on the pristine Ti and Ti-PLGA surfaces,

$p < 0.05$. It's worth noting that the NT−ICA−ASP/PLGA substrate showed highest expression levels for all of the osteogenesis-related genes examined than the other surfaces, with statistical significance. These results suggested that the employment of ICA and ASP could both improve osteoblast differentiation, and the superior osteogenic function of the NT−ICA−ASP/PLGA substrate lies in the synergistic function of ICA and ASP.

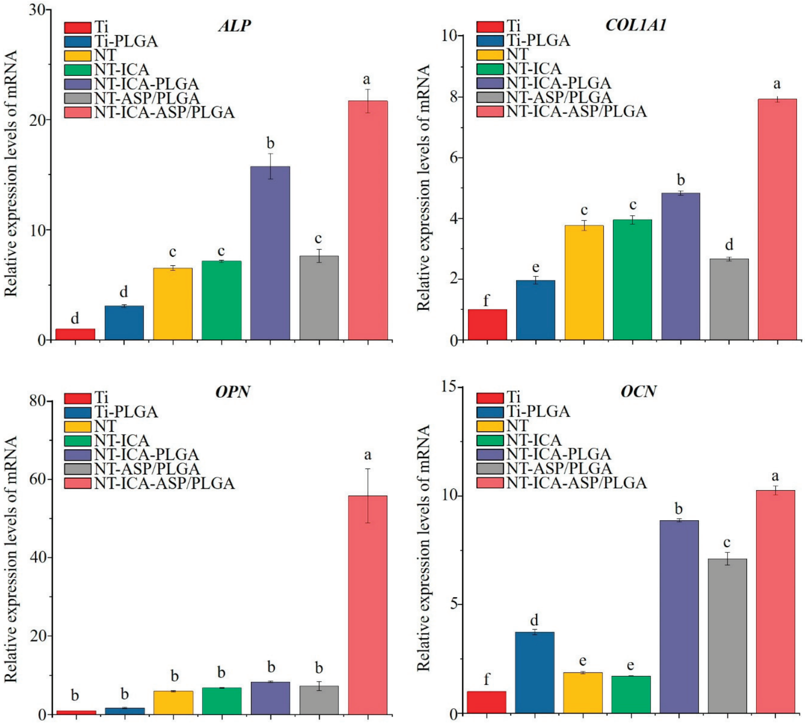

Figure 11. Real-time PCR results representing the gene expression levels of alkaline phosphatase (ALP), collagen type 1 alpha 1 (COL1A1), osteopontin (OPN) and osteocalcin (OCN) in MC3T3-E1 cells after 14 days of culture on different samples. Different lowercase letters indicate statistically significant differences between different groups ($p < 0.05$). Data are mean ± SD, $n = 3$ replicates each group.

3.4.4. Western Blot Test

Western blot analysis was used to evaluate the protein expression levels in MC3T3-E1 cells cultured on different samples for 14 days. Figure 12A,B displayed Western blot bands and quantitative analysis, respectively.

Consistent with the gene expression levels, the protein expression levels of ALP, COL1A1 and OCN were all higher in cells incubated with NT−ICA−PLGA, NT−ASP/PLGA and NT−ICA−ASP/PLGA substrates, compared to that on the original Ti and Ti-PLGA surfaces. Especially, NT−ICA−ASP/PLGA substrate revealed enhanced expression levels for all of the osteogenic proteins determined in this experiment than those on the other surfaces, $p < 0.05$. The optimal osteogenesis-related protein expression of the NT−ICA−ASP/PLGA substrate is attributed to the combined effects of both ICA and ASP to facilitate bone formation in osteoblast cells.

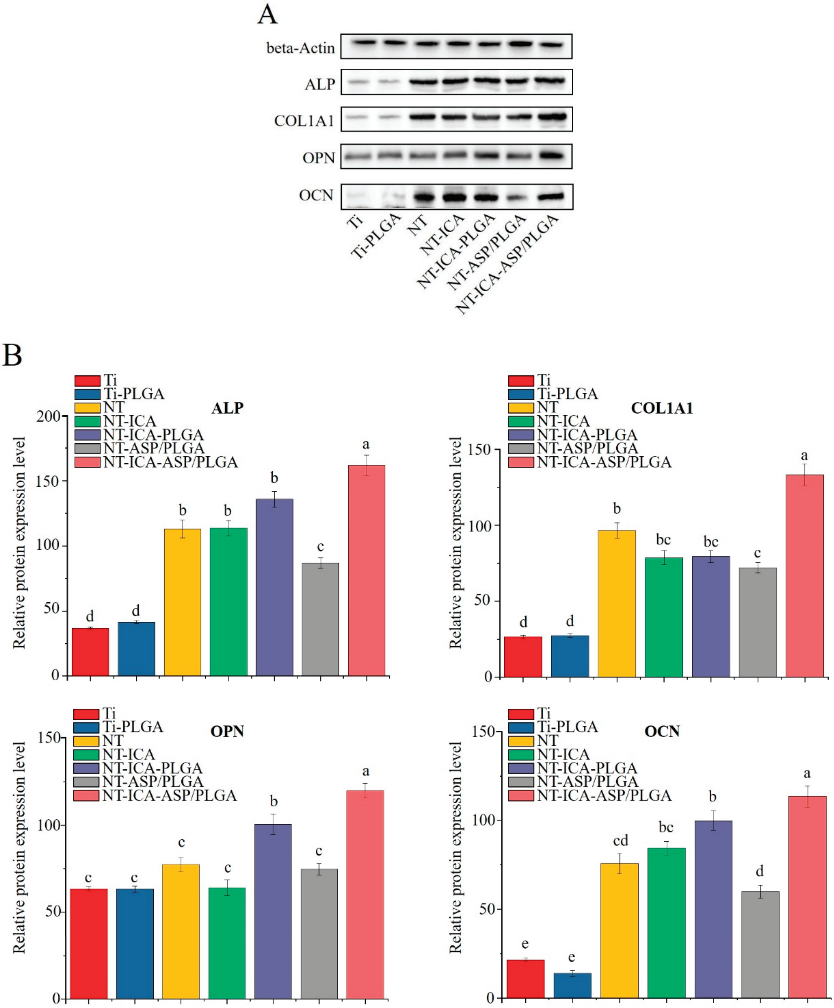

Figure 12. (**A**) Western blot showing the protein expression levels of ALP, COL1A1, OPN and OCN and beta-Actin in MC3T3-E1 cells after 14 days of culture on different samples. (**B**) The corresponding gray-scale values of proteins levels in the 7 groups. Different lowercase letters indicate statistically significant differences between different groups ($p < 0.05$). Data are mean ± SD, $n = 3$ replicates each group.

4. Discussion

Numerous strategies have been implemented to integrate bioactive molecules into the implant surface so as to promote osseointegration. Previously, most investigators endeavored to optimize dental implant materials to promote osteogenic differentiation in mesenchymal stem cells or osteoblast cells and have developed satisfied implant materials to a certain degree. However, only promoting bone formation in osteoblast cells is not enough to fulfill implant osseointegration in vivo. The reason is that after implant were inserted in to the bone tissue, in addition to its interaction with osteoblast, immune cells, such as macrophages, also play an important role in osseointegration [48]. In order to uncover the close relationship between skeletal and immune system, we applied the icariin/aspirin composite coating on TiO_2 nanotubes surface, named as the NT-ICA-ASP/PLGA substrate, and explore its immunomodulatory effect on macrophage and osteogenic activity in osteoblast cells. We hypothesized that the NT–ICA–ASP/PLGA substrate could induce immunoregulatory function in macrophages and provide an immune microenvironment, which is favorable for osteogenesis in osteoblast cells.

In the current work, the NT-ICA-ASP/PLGA substrate was fabricated. The SEM, XPS detection and contact angle tests confirmed the successful preparation of the icariin/aspirin functionalized coating on TiO_2 nanostructured surface. The established NT–ICA–ASP/PLGA substrate achieved controlled release of both ICA and ASP, with satisfied hydrophilicity. The drug release curves revealed that the releasing period of aspirin is about 7 days, while icariin achieved a sustained release period until 30 days.

To maintain the controlled release of the two kinds of drugs, we firstly prepared TiO_2 nanotubes on the surface of pure titanium by anodization. It is well established that 70–100 nm diameter nanotubes could induce improved cell adhesion, differentiation toward osteoblasts [49–51]. Previously, we have chosen 80 nm diameter nanotubes for the fabrication of functionalized coating [17]. In the present study, we selected a 100 nm diameter of TiO_2 nanotubes for further functionalization study after taking two reasons into considerations. First, as a drug loading reservoir, the larger diameter of the nanotubes, the stronger ability to load drugs [52]; second, 100 nm diameter nanotubes displayed highest ability of protein adsorption, which is critical in mediating cell attachment and proliferation so as to promote bone formation [53,54]. In view of this, we selected 100 nm diameter nanotube as a drug carrier, hoping that it will balance the drug-loading capacity and osteogenic ability at the same time. Another thing should be clarify is that we changed the anodization parameters, compared to our past article [17]. In our previous work, HF was used as an electrolyte, while in the present experiment we employed the reaction system composed of NH_4F, ethylene glycol and water. The reason that we adopted this new method lies in that it can increase the viscosity of the electrolyte and reduce the activity of fluoride ions in order to acquire much controllable and orderly aligned nanotubes with uniform diameter [55]. In present work, we analyzed the bioactivity, gene expression and immune regulatory responses of the established icariin/aspirin composite coating on 100 nm diameter TiO_2 nanotubes. In the future, we will continue to evaluate the influence of different sizes of TiO_2 nanotubes on the biological behaviors of the coated surface.

We further used PLGA to avoid the initial burst release of drug from the TiO_2 nanotubes surface. PLGA is commonly applied in bone tissue engineering because of its favorable mechanical properties and drug-loading capacity [56,57] and used in wound dressings due to its excellent bonding ability [58]. PLGA has also been employed as coating materials on the surface of titanium implants [59,60]. Serving as biodegradable material [61], PLGA polymer-coated nanotube displayed longer drugs release period compared to chitosan-coated nanotubes [62]. In addition, compared with protein growth factor, icariin and aspirin were both chemical stable and heat-resistant drugs [63,64]. More importantly, since we adopted the dip-coating method for preparation of the PLGA coating onto the NT–ICA–ASP/PLGA substrate, this mild coating method could further protect icariin and aspirin from denaturation during the coating procedure and achieve sustained and multiple release of two kinds of drugs at the same time. Therefore, in this way, we successfully superimposed the ASP/PLGA coating onto the ICA loaded TiO_2 nanotubes structure so as to obtain the established NT–ICA–ASP/PLGA substrate. In the future, we will further detect the interfacial adhesion strength between the coating and titanium substrate.

We have previously reported that ICA and TiO_2 nanotubes structures could exert osteogenic effects synergistically [17]. In the present work, apart from its well-established osteogenic effect, we also intend to explore other functions of ICA. Although there is less report about this issue, it has been revealed that icariin could exert anti-inflammatory function [18]. Icariin and its derivate have demonstrated anti-inflammatory effects in macrophage cell lines, human myeloid cells, and a mouse model of inflammation. Additionally the anti-inflammatory effect was concomitant with a down-regulation of IL–10, IL–6 and TNF–α [19]. Other researchers also found that icariin possess significant therapeutic effect on rheumatoid arthritis (RA) clinically [9]. Moreover, the mechanism of icariin to prevent RA might be related to its immunoregulatory function, which was mediated through the decrease in the cell number of immune cells Th17. Additionally, icariin administration could inhibit IL–17 production [20]. Taking the above-mentioned factors into consideration, we attempt to discover the anti-inflammatory and immunoregulatory functions of ICA in this work. In the present study, during inflammation markers detection, we discovered decreased IL–1β gene expression and inhibited IL–1β and TNF–α protein levels on the NT–ICA and NT–ICA–ASP/PLGA surfaces, compared to Ti surface. Moreover, enhanced gene and protein levels of M2 phenotype markers TGF–β and HO–1 were also observed on ICA–loaded surfaces, compared with Ti and Ti–PLGA substrates. These results confirmed the anti-inflammatory and immunoregulatory functions of ICA.

Aspirin (ASP), a classic non-steroidal anti-inflammatory drug, remains the first-line clinical drug due to its good antipyretic and analgesic capabilities and extremely low drug side effects [65]. Some researchers showed that ASP down-regulate iNOS and TNF-α expression in macrophage cells in vitro and improve bone regeneration in vivo by inhibiting LPS-induced macrophage activation in the early stages of inflammation [66]. In addition, aspirin may be a promising option for preventing and curing osteoclastic bone destruction, including peri-implant osteolysis [67]. Another researcher also proved that on the surface of titanium primed with phase-transited lysozyme, a coating loaded with aspirin could promote osseointegration [68]. In our experiment, compared with Ti surface, NT–ASP/PLGA and NT–ICA–ASP/PLGA surfaces displayed decreased IL-1β gene level and reduced IL–1β and TNF–α protein levels, with upregulated TGF–β and HO–1 gene and protein expression levels, $p < 0.05$. As expected, our results confirmed the anti-inflammatory and immunoregulatory functions of ASP, with the established NT–ICA–ASP/PLGA substrate exhibiting decreased M1 inflammatory and increased M2 proregenerative effects at the same time.

It is well known that macrophages are the main effector cells of the inflammatory response, and have great plasticity. When stimulated by different signals, they can show a M1 or M2 phenotype [38,39]. The timely transformation of M1–type to M2–type macrophages effectively promotes the regression of inflammation and tissue repair [69,70]. Generally speaking, classically activated macrophages (M1) secrete a variety of proinflammatory factors, such as TNF–α, IL–1β, IL–6, etc. While the alternatively activated M2 phenotype macrophages generate anti-inflammatory or immunoregulatory cytokines such as TGF–β and IL–10 [71]. In addition, heme oxygenase HO–1, the derivable isoform of the heme-degrading enzyme HO, plays an important role in inflammation and immunoregulation of homeostasis. Myeloid HO–1 expression modulates macrophage polarization to M2 [72,73]. Furthermore, high HO-1 level increased the expression of osteonectin, OPG and BMP–2, and increase osteoblast function and differentiation [74]. In our experiment, down-regulated M1 proinflammatory and up-regulated M2 proregenerative genes and proteins expression were shown on the novel icariin/aspirin composite coating covered TiO_2 nanotubes surface, compared with pure Ti surface. These results indicated that the NT–ICA–ASP/PLGA substrate revealed optimal ability, which could inhibit inflammation and enhance regeneration simultaneously, probably attributed to the synergistic effects of ICA and ASP.

Recently, osteoimmunomodulation (OIM) has been raised to emphasize the importance of immune response during osteogenesis at biomaterial–tissue interface. As the concept of OIM has been gradually accepted, more and more attention has been paid to the positive regulation of immune response at implant–tissue interface so as to accelerate implant osseointegration [75]. After implant insertion, inflammation should be properly regulated to achieve faster bone integration, particularly for patients who are suffering from systemic diseases, which were adverse to bone formation [76,77]. By regulating the early inflammatory response of macrophages, tissue repair can be enhanced, thereby promoting the early rapid formation of bone tissue around the implant.

In order to evaluate OIM, we firstly extracted conditioned media (CM) from macrophage cells incubated with various implant materials. Then the extracted CM was added to osteoblast cells to simulate the immune microenvironment around the implant site. Thus, the indirect coculture system composed of sample slices, macrophage CM and osteoblast cells is ready to evaluate the effects of immune cells on osteoblast differentiation. Our results suggested that in the coculture system, osteoblast cells on the NT–ASP/PLGA and NT–ICA–ASP/PLGA substrates displayed increased cell proliferation, compared with the other groups at day 5 and 7. Moreover, cells showed well–spread morphology on the NT–ICA–ASP/PLGA substrate, suggesting good cell adhesion on the modified substrate. In addition, we also detected the osteogenic gene and protein levels in the coculture system. During the osteoblast cell differentiation process, an early increase in alkaline phosphatase (ALP) was observed. Then followed by an augment in collagen type 1 and OPN, with osteocalcin expressed later [78]. We measured expression levels of the abovementioned four typical marker genes, including *ALP*, *COL*, *OPN* and *OCN*, which expressed at different stages of osteoblast differentiation and osteogenesis. As predicted, the highest gene levels were observed on the NT–ICA–ASP/PLGA substrate, implying the collaborative pro-osteogenic effect of ICA and ASP at the genetic level. Not only that, both ICA and ASP modified surfaces revealed relatively higher protein levels of osteogenic proteins than pure Ti surface. Especially, the NT–ICA–ASP/PLGA substrate demonstrated the highest expression levels for all of the osteogenesis-related proteins. It is well-accepted that enhanced gene and protein expression levels related to osteoblast cell differentiation may accelerate osseointegration at the implant–tissue interface. The advanced expression levels of both osteogenesis-related genes and proteins on the NT-ICA-ASP/PLGA substrate implied its superior ability to induce osteoblast cells differentiation. The optimal effect of the NT-ICA-ASP/PLGA substrate might be ascribed to the synergistic effects of ICA and ASP, which is in line with its excellent cell proliferation and adhesion results.

5. Conclusions

In view of the concept of OIM, it is especially to be expected to fabricate an implant material, which possesses both early immune regulatory property and long-term osteogenic ability. Both ICA and ASP are candidate drugs for implant surface modification with multiple function including anti-inflammation, immunoregulation and osteogenesis. Taken into consideration of the factors mentioned above, we constructed the NT–ICA–ASP/PLGA substrate. The novel substrate could trigger an effective and timely shift of macrophage from the inflammatory reaction stage to restorative stage. The established NT–ICA–ASP/PLGA surface endowed the modified surface with immunomodulatory function in macrophages and osteogenic effect in osteoblast cells at the same time. This study provides a very promising strategy for fabricating functionalized coating on titanium-based alloys to improve implant osseointegration.

Author Contributions: Conceptualization, Y.L. (Ying Li) and C.L.; Data curation, A.M. and Y.Y.; Funding acquisition, Y.L. (Ying Li) and C.L.; Investigation, A.M., Y.Y., B.C., and W.W.; Methodology, A.M., Y.Y., J.L., H.Q., and Y.L. (Yunkai Liang); Project administration, Y.L. (Ying Li) and C.L; Writing—original draft, A.M. and Y.Y.; Writing—review and editing, Y.L. (Ying Li). All authors have read and agreed to the published version of the manuscript.

Funding: This research was funded by National Natural Science Foundation of China, Grant No. 81870809, 81500886, 31470920 and Tianjin Natural Science Foundation Grant No. 16JCYBJC28700.

Acknowledgments: We sincerely acknowledge Baoe Li from the School of Materials Science and Engineering, Hebei University of Technology, for her precious technical support and discussions. We also thank Huanhuan Zhai from Tianjin Institute of Industrial Biotechnology, Chinese Academy of Sciences, for her important work in preparing SEM images.

Conflicts of Interest: The authors declare no conflict of interest.

References

1. Elani, H.W.; Starr, J.R.; Da Silva, J.D.; Gallucci, G.O. Trends in Dental Implant Use in the U.S., 1999–2016, and Projections to 2026. *J. Dent. Res.* **2018**, *97*, 1424–1430. [CrossRef] [PubMed]
2. Krishna, B.V.; Bose, S.; Bandyopadhyay, A. Low stiffness porous Ti structures for load-bearing implants. *Acta Biomater.* **2007**, *3*, 997–1006. [CrossRef] [PubMed]

3. Rani, V.V.; Vinoth-Kumar, L.; Anitha, V.C.; Manzoor, K.; Deepthy, M.; Shantikumar, V.N. Osteointegration of titanium implant is sensitive to specific nanostructure morphology. *Acta Biomater.* **2012**, *8*, 1976–1989. [CrossRef] [PubMed]
4. Qing, Y.; Cheng, L.; Li, R.; Liu, G.; Zhang, Y.; Tang, X.; Wang, J.; Liu, H.; Qin, Y. Potential antibacterial mechanism of silver nanoparticles and the optimization of orthopedic implants by advanced modification technologies. *Int. J. Nanomed.* **2018**, *13*, 3311–3327. [CrossRef] [PubMed]
5. Yang, B.C.; Zhou, X.D.; Yu, H.Y.; Wu, Y.; Bao, C.Y.; Man, Y.; Cheng, L.; Sun, Y. Advances in titanium dental implant surface modification. *Hua Xi Kou Qiang Yi Xue Za Zhi* **2019**, *37*, 124–129. [CrossRef]
6. Li, Y.; Song, Y.; Ma, A.; Li, C. Surface Immobilization of TiO_2 Nanotubes with Bone Morphogenetic Protein-2 Synergistically Enhances Initial Preosteoblast Adhesion and Osseointegration. *BioMed Res. Int.* **2019**, *2019*, 5697250. [CrossRef]
7. Agarwal, R.; Garcia, A.J. Biomaterial strategies for engineering implants for enhanced osseointegration and bone repair. *Adv. Drug Deliv. Rev.* **2015**, *94*, 53–62. [CrossRef]
8. Lai, M.; Cai, K.; Zhao, L.; Chen, X.; Hou, Y.; Yang, Z. Surface functionalization of TiO_2 nanotubes with bone morphogenetic protein 2 and its synergistic effect on the differentiation of mesenchymal stem cells. *Biomacromolecules* **2011**, *12*, 1097–1105. [CrossRef]
9. Ren, L.; Pan, S.; Li, H.; Li, Y.; He, L.; Zhang, S.; Che, J.; Niu, Y. Effects of aspirin-loaded graphene oxide coating of a titanium surface on proliferation and osteogenic differentiation of MC3T3-E1 cells. *Sci. Rep.* **2018**, *8*, 15143. [CrossRef]
10. Thomas, M.V.; Puleo, D.A. Infection, inflammation, and bone regeneration: A paradoxical relationship. *J. Dent. Res.* **2011**, *90*, 1052–1061. [CrossRef]
11. Zhang, X.; Liu, T.; Huang, Y.; Wismeijer, D.; Liu, Y. Icariin: Does it have an osteoinductive potential for bone tissue engineering? *Phytother. Res.* **2014**, *28*, 498–509. [CrossRef] [PubMed]
12. Song, Y.; Ma, A.; Ning, J.; Zhong, X.; Zhang, Q.; Zhang, X.; Hong, G.; Li, Y.; Sasaki, K.; Li, C. Loading icariin on titanium surfaces by phase-transited lysozyme priming and layer-by-layer self-assembly of hyaluronic acid/chitosan to improve surface osteogenesis ability. *Int. J. Nanomed.* **2018**, *13*, 6751–6767. [CrossRef] [PubMed]
13. Wu, T.; Shu, T.; Kang, L.; Wu, J.; Xing, J.; Lu, Z.; Chen, S.; Lv, J. Icaritin, a novel plant-derived osteoinductive agent, enhances the osteogenic differentiation of human bone marrow- and human adipose tissue-derived mesenchymal stem cells. *Int. J. Mol. Med.* **2017**, *39*, 984–992. [CrossRef] [PubMed]
14. Ma, X.N.; Zhou, J.; Ge, B.F.; Zhen, P.; Ma, H.P.; Shi, W.G.; Cheng, K.; Xian, C.J.; Chen, K.M. Icariin induces osteoblast differentiation and mineralization without dexamethasone in vitro. *Planta Med.* **2013**, *79*, 1501–1508. [CrossRef]
15. Song, L.; Zhao, J.; Zhang, X.; Li, H.; Zhou, Y. Icariin induces osteoblast proliferation, differentiation and mineralization through estrogen receptor-mediated ERK and JNK signal activation. *Eur. J. Pharmacol.* **2013**, *714*, 15–22. [CrossRef]
16. Zhao, J.; Ohba, S.; Komiyama, Y.; Shinkai, M.; Chung, U.I.; Nagamune, T. Icariin: A potential osteoinductive compound for bone tissue engineering. *Tissue Eng. Part A* **2010**, *16*, 233–243. [CrossRef]
17. Ma, A.; Shang, H.; Song, Y.; Chen, B.; You, Y.; Han, W.; Zhang, X.; Zhang, W.; Li, Y.; Li, C. Icariin-Functionalized Coating on TiO_2 Nanotubes Surface to Improve Osteoblast Activity In Vitro and Osteogenesis Ability In Vivo. *Coatings* **2019**, *9*, 327. [CrossRef]
18. Zhou, J.; Wu, J.; Chen, X.; Fortenbery, N.; Eksioglu, E.; Kodumudi, K.N.; Pk, E.B.; Dong, J.; Djeu, J.Y.; Wei, S. Icariin and its derivative, ICT, exert anti-inflammatory, anti-tumor effects, and modulate myeloid derived suppressive cells (MDSCs) functions. *Int. Immunopharmacol.* **2011**, *11*, 890–898. [CrossRef]
19. Shao, H.; Shen, J.; Wang, M.; Cui, J.; Wang, Y.; Zhu, S.; Zhang, W.; Yang, H.; Xu, Y.; Geng, D. Icariin protects against titanium particle-induced osteolysis and inflammatory response in a mouse calvarial model. *Biomaterials* **2015**, *60*, 92–99. [CrossRef]
20. Chi, L.; Gao, W.; Shu, X.; Lu, X. A natural flavonoid glucoside, icariin, regulates Th17 and alleviates rheumatoid arthritis in a murine model. *Mediat. Inflamm.* **2014**, *2014*, 392062. [CrossRef]
21. Derry, S.; Moore, R.A. Single dose oral aspirin for acute postoperative pain in adults. *Cochrane Database Syst. Rev.* **2012**, *18*, CD002067. [CrossRef] [PubMed]

22. Tang, J.; Xiong, J.; Wu, T.; Tang, Z.; Ding, G.; Zhang, C.; Wang, S.; Liu, Y. Aspirin treatment improved mesenchymal stem cell immunomodulatory properties via the 15d-PGJ2/PPARgamma/TGF-beta1 pathway. *Stem Cells Dev.* **2014**, *23*, 2093–2103. [CrossRef] [PubMed]
23. Cao, Y.; Xiong, J.; Mei, S.; Wang, F.; Zhao, Z.; Wang, S.; Liu, Y. Aspirin promotes bone marrow mesenchymal stem cell-based calvarial bone regeneration in mini swine. *Stem Cell Res.* **2015**, *6*, 210. [CrossRef] [PubMed]
24. Xie, Y.; Pan, M.; Gao, Y.; Zhang, L.; Ge, W.; Tang, P. Dose-dependent roles of aspirin and other non-steroidal anti-inflammatory drugs in abnormal bone remodeling and skeletal regeneration. *Cell Biosci.* **2019**, *9*, 103. [CrossRef]
25. Shi, S.; Yamaza, T.; Akiyama, K. Is aspirin treatment an appropriate intervention to osteoporosis? *Future Rheumatol.* **2008**, *3*, 499–502. [CrossRef]
26. Yamaza, T.; Miura, Y.; Bi, Y.; Liu, Y.; Akiyama, K.; Sonoyama, W.; Patel, V.; Gutkind, S.; Young, M.; Gronthos, S.; et al. Pharmacologic stem cell based intervention as a new approach to osteoporosis treatment in rodents. *PLoS ONE* **2008**, *3*, e2615. [CrossRef]
27. Wei, S.; Li, Y.; Bai, Y.; Pan, J.; Wang, H.; Li, H.; Xu, X.; Fu, X.; Shi, R.; Luo, Z.; et al. A hybrid 3D-printed aspirin-laden liposome composite scaffold for bone tissue engineering. *J. Mater. Chem. B* **2018**, *7*. [CrossRef]
28. Maher, S.; Mazinani, A.; Barati, M.R.; Losic, D. Engineered titanium implants for localized drug delivery: Recent advances and perspectives of Titania nanotubes arrays. *Expert Opin. Drug Deliv.* **2018**, *15*, 1021–1037. [CrossRef]
29. Ahn, T.K.; Lee, D.H.; Kim, T.S.; Jang, G.C.; Choi, S.; Oh, J.B.; Ye, G.; Lee, S. Modification of Titanium Implant and Titanium Dioxide for Bone Tissue Engineering. *Adv. Exp. Med. Biol.* **2018**, *1077*, 355–368. [CrossRef]
30. Gulati, K.; Ivanovski, S. Dental implants modified with drug releasing titania nanotubes: Therapeutic potential and developmental challenges. *Expert Opin. Drug Deliv.* **2017**, *14*, 1009–1024. [CrossRef]
31. Rasouli, R.; Barhoum, A.; Uludag, H. A review of nanostructured surfaces and materials for dental implants: Surface coating, patterning and functionalization for improved performance. *Biomater. Sci.* **2018**, *6*, 1312–1338. [CrossRef] [PubMed]
32. Wang, Q.; Huang, J.Y.; Li, H.Q.; Chen, Z.; Zhao, A.Z.; Wang, Y.; Zhang, K.Q.; Sun, H.T.; Al-Deyab, S.S.; Lai, Y.K. TiO_2 nanotube platforms for smart drug delivery: A review. *Int. J. Nanomed.* **2016**, *11*, 4819–4834. [CrossRef]
33. Kapoor, D.N.; Bhatia, A.; Kaur, R.; Sharma, R.; Kaur, G.; Dhawan, S. PLGA: A unique polymer for drug delivery. *Ther. Deliv.* **2015**, *6*, 41–58. [CrossRef] [PubMed]
34. Danhier, F.; Ansorena, E.; Silva, J.M.; Coco, R.; Le Breton, A.; Preat, V. PLGA-based nanoparticles: An overview of biomedical applications. *J. Control. Release* **2012**, *161*, 505–522. [CrossRef] [PubMed]
35. Pagels, R.F.; Prud'homme, R.K. Polymeric nanoparticles and microparticles for the delivery of peptides, biologics, and soluble therapeutics. *J. Control. Release* **2015**, *219*, 519–535. [CrossRef] [PubMed]
36. Wang, J.; Meng, F.; Song, W.; Jin, J.; Ma, Q.; Fei, D.; Fang, L.; Chen, L.; Wang, Q.; Zhang, Y. Nanostructured titanium regulates osseointegration via influencing macrophage polarization in the osteogenic environment. *Int. J. Nanomed.* **2018**, *13*, 4029–4043. [CrossRef]
37. Zhang, R.; Liu, X.; Xiong, Z.; Huang, Q.; Yang, X.; Yan, H.; Ma, J.; Feng, Q.; Shen, Z. The immunomodulatory effects of Zn-incorporated micro/nanostructured coating in inducing osteogenesis. *Artif. CellsNanomed. Biotechnol.* **2018**, *46*, 1123–1130. [CrossRef]
38. Oishi, Y.; Manabe, I. Macrophages in inflammation, repair and regeneration. *Int. Immunol.* **2018**, *30*, 511–528. [CrossRef]
39. Peiseler, M.; Kubes, P. Macrophages play an essential role in trauma-induced sterile inflammation and tissue repair. *Eur. J. Trauma Emerg. Surg. Off. Publ. Eur. Trauma Soc.* **2018**, *44*, 335–349. [CrossRef]
40. Minutti, C.M.; Knipper, J.A.; Allen, J.E.; Zaiss, D.M. Tissue-specific contribution of macrophages to wound healing. *Semin. Cell Dev. Biol.* **2017**, *61*, 3–11. [CrossRef]
41. Korsmeyer, R.W.; Gurny, R.; Doelker, E.; Buri, P.; Peppas, N.A. Mechanisms of solute release from porous hydrophilic polymers. *Int. J. Pharm.* **1983**, *15*, 25–35. [CrossRef]
42. Sun, X.; Wei, J.; Lyu, J.; Bian, T.; Liu, Z.; Huang, J.; Pi, F.; Li, C.; Zhong, Z. Bone-targeting drug delivery system of biomineral-binding liposomes loaded with icariin enhances the treatment for osteoporosis. *J. Nanobiotechnol.* **2019**, *17*, 10. [CrossRef] [PubMed]
43. Lisuzzo, L.; Cavallaro, G.; Parisi, F.; Milioto, S.; Fakhrullin, R.; Lazzara, G. Core/Shell Gel Beads with Embedded Halloysite Nanotubes for Controlled Drug Release. *Coatings* **2019**, *9*, 70. [CrossRef]
44. Zheng, Y.; Zhu, G.; He, J.; Wang, G.; Li, D.; Zhang, F. Icariin targets Nrf2 signaling to inhibit microglia-mediated neuroinflammation. *Int. Immunopharmacol.* **2019**, *73*, 304–311. [CrossRef] [PubMed]

45. El-Shitany, N.A.; Eid, B.G. Icariin modulates carrageenan-induced acute inflammation through HO-1/Nrf2 and NF-kB signaling pathways. *Biomed. Pharmacother. Biomed. Pharmacother.* **2019**, *120*, 109567. [CrossRef] [PubMed]
46. Zhao, L.; Mei, S.; Chu, P.K.; Zhang, Y.; Wu, Z. The influence of hierarchical hybrid micro/nano-textured titanium surface with titania nanotubes on osteoblast functions. *Biomaterials* **2010**, *31*, 5072–5082. [CrossRef] [PubMed]
47. Zhao, W.; Li, J.; Jin, K.; Liu, W.; Qiu, X.; Li, C. Fabrication of functional PLGA-based electrospun scaffolds and their applications in biomedical engineering. *Mater. Sci. Eng. C Mater. Biol. Appl.* **2016**, *59*, 1181–1194. [CrossRef]
48. Chen, Z.; Klein, T.; Murray, R.Z.; Crawford, R.; Chang, J.; Wu, C.; Xiao, Y. Osteoimmunomodulation for the development of advanced bone biomaterials. *Mater. Today* **2016**, *19*, 304–321. [CrossRef]
49. Cheng, Y.; Yang, H.; Yang, Y.; Huang, J.; Wu, K.; Chen, Z.; Wang, X.; Lin, C.; Lai, Y. Progress in TiO_2 nanotube coatings for biomedical applications: A review. *J. Mater. Chem. B* **2018**, *6*, 1862–1886. [CrossRef]
50. von Wilmowsky, C.; Bauer, S.; Roedl, S.; Neukam, F.W.; Schmuki, P.; Schlegel, K.A. The diameter of anodic TiO_2 nanotubes affects bone formation and correlates with the bone morphogenetic protein-2 expression in vivo. *Clin. Oral Implant. Res.* **2012**, *23*, 359–366. [CrossRef]
51. Yu, W.-Q.; Jiang, X.-Q.; Zhang, F.-Q.; Xu, L. The effect of anatase TiO_2 nanotube layers on MC3T3-E1 preosteoblast adhesion, proliferation, and differentiation. *J. Biomed. Mater. Res. A* **2010**, *94A*, 1012–1022. [CrossRef] [PubMed]
52. Torres, C.C.; Campos, C.H.; Diáz, C.; Jiménez, V.A.; Vidal, F.; Guzmán, L.; Alderete, J.B. PAMAM-grafted TiO_2 nanotubes as novel versatile materials for drug delivery applications. *Mater. Sci. Eng. C Mater. Biol. Appl.* **2016**, *65*, 164–171. [CrossRef] [PubMed]
53. Yang, W.; Xi, X.; Ran, Q.; Liu, P.; Hu, Y.; Cai, K. Influence of the titania nanotubes dimensions on adsorption of collagen: An experimental and computational study. *Mater. Sci. Eng. C Mater. Biol. Appl.* **2014**, *34*, 410–416. [CrossRef] [PubMed]
54. Kulkarni, M.; Mazare, A.; Park, J.; Gongadze, E.; Killian, M.S.; Kralj, S.; von der Mark, K.; Iglic, A.; Schmuki, P. Protein interactions with layers of TiO_2 nanotube and nanopore arrays: Morphology and surface charge influence. *Acta Biomater.* **2016**, *45*, 357–366. [CrossRef] [PubMed]
55. Ya, J.; An, L.; Liu, Z.; E, L.; Zhao, W.; Zhao, D.; Liu, C. Investigation of surface morphologies of TiO_2 nanotube arrays by anodization in ethylene glycol electrolytes. *J. Optoelectron. Adv. Mater.* **2011**, *13*, 684–688.
56. Bao, H.; Lv, F.; Liu, T. A pro-angiogenic degradable Mg-poly(lactic-co-glycolic acid) implant combined with rhbFGF in a rat limb ischemia model. *Acta Biomater.* **2017**, *64*, 279–289. [CrossRef] [PubMed]
57. Mehrasa, M.; Asadollahi, M.A.; Ghaedi, K.; Salehi, H.; Arpanaei, A. Electrospun aligned PLGA and PLGA/gelatin nanofibers embedded with silica nanoparticles for tissue engineering. *Int. J. Biol. Macromol* **2015**, *79*, 687–695. [CrossRef]
58. Daristotle, J.L.; Lau, L.W.; Erdi, M.; Hunter, J.; Djoum, A., Jr.; Srinivasan, P.; Wu, X.; Basu, M.; Ayyub, O.B.; Sandler, A.D.; et al. Sprayable and biodegradable, intrinsically adhesive wound dressing with antimicrobial properties. *Bioeng. Transl. Med.* **2020**, *5*, e10149. [CrossRef]
59. Yang, Y.; Ren, S.; Zhang, X.; Yu, Y.; Liu, C.; Yang, J.; Miao, L. Safety and efficacy of PLGA(Ag-Fe3O4)-coated dental implants in inhibiting bacteria adherence and osteogenic inducement under a magnetic field. *Int. J. Nanomed.* **2018**, *13*, 3751–3762. [CrossRef]
60. Kazek-Kesik, A.; Nosol, A.; Plonka, J.; Smiga-Matuszowicz, M.; Golda-Cepa, M.; Krok-Borkowicz, M.; Brzychczy-Wloch, M.; Pamula, E.; Simka, W. PLGA-amoxicillin-loaded layer formed on anodized Ti alloy as a hybrid material for dental implant applications. *Mater. Sci. Eng. C Mater. Biol. Appl.* **2019**, *94*, 998–1008. [CrossRef]
61. Kumari, A.; Yadav, S.K.; Yadav, S.C. Biodegradable polymeric nanoparticles based drug delivery systems. *Colloids Surf. B-Biointerfaces* **2010**, *75*, 1–18. [CrossRef] [PubMed]
62. Gulati, K.; Ramakrishnan, S.; Aw, M.S.; Atkins, G.J.; Findlay, D.M.; Losic, D. Biocompatible polymer coating of titania nanotube arrays for improved drug elution and osteoblast adhesion. *Acta Biomater.* **2012**, *8*, 449–456. [CrossRef] [PubMed]
63. Wu, T.; Nan, K.; Chen, J.; Jin, D.; Jiang, S.; Zhao, P.; Xu, J.; Du, H.; Zhang, X.; Li, J.; et al. A new bone repair scaffold combined with chitosan/hydroxyapatite and sustained releasing icariin. *Chin. Sci. Bull.* **2009**, *54*, 2953–2961. [CrossRef]

64. Banerjee, P.K.; Amidon, G.L. Physicochemical property modification strategies based on enzyme substrate specificities I: Rationale, synthesis, and pharmaceutical properties of aspirin derivatives. *J. Pharm. Sci.* **1981**, *70*, 1299–1303. [CrossRef] [PubMed]
65. Vane, J.R.; Botting, R.M. The mechanism of action of aspirin. *Thromb Res.* **2003**, *110*, 255–258. [CrossRef]
66. Liu, Y.; Fang, S.; Li, X.; Feng, J.; Du, J.; Guo, L.; Su, Y.; Zhou, J.; Ding, G.; Bai, Y.; et al. Aspirin inhibits LPS-induced macrophage activation via the NF-kappaB pathway. *Sci. Rep.* **2017**, *7*, 11549. [CrossRef]
67. Shi, J.; Wang, Z.; Guo, X.; Shen, J.; Sun, H.; Bai, J.; Yu, B.; Wang, L.; Zhou, W.; Liu, Y.; et al. Aspirin inhibits osteoclast formation and wear-debris-induced bone destruction by suppressing mitogen-activated protein kinases. *J. Cell. Physiol.* **2020**, *235*, 2599–2608. [CrossRef]
68. Zhang, W.; Lu, X.; Yuan, Z.; Shen, M.; Song, Y.; Liu, H.; Deng, J.; Zhong, X.; Zhang, X. Establishing an osteoimmunomodulatory coating loaded with aspirin on the surface of titanium primed with phase-transited lysozyme. *Int. J. Nanomed.* **2019**, *14*, 977–991. [CrossRef]
69. Brown, B.N.; Ratner, B.D.; Goodman, S.B.; Amar, S.; Badylak, S.F. Macrophage polarization: An opportunity for improved outcomes in biomaterials and regenerative medicine. *Biomaterials* **2012**, *33*, 3792–3802. [CrossRef]
70. Miron, R.J.; Bosshardt, D.D. OsteoMacs: Key players around bone biomaterials. *Biomaterials* **2016**, *82*, 1–19. [CrossRef]
71. Shapouri-Moghaddam, A.; Mohammadian, S.; Vazini, H.; Taghadosi, M.; Esmaeili, S.A.; Mardani, F.; Seifi, B.; Mohammadi, A.; Afshari, J.T.; Sahebkar, A. Macrophage plasticity, polarization, and function in health and disease. *J. Cell. Physiol.* **2018**, *233*, 6425–6440. [CrossRef] [PubMed]
72. Vijayan, V.; Wagener, F.; Immenschuh, S. The macrophage heme-heme oxygenase-1 system and its role in inflammation. *Biochem. Pharm.* **2018**, *153*, 159–167. [CrossRef] [PubMed]
73. Zhang, M.; Nakamura, K.; Kageyama, S.; Lawal, A.O.; Gong, K.W.; Bhetraratana, M.; Fujii, T.; Sulaiman, D.; Hirao, H.; Bolisetty, S.; et al. Myeloid HO-1 modulates macrophage polarization and protects against ischemia-reperfusion injury. *JCI Insight* **2018**, *3*. [CrossRef] [PubMed]
74. Barbagallo, I.; Vanella, A.; Peterson, S.J.; Kim, D.H.; Tibullo, D.; Giallongo, C.; Vanella, L.; Parrinello, N.; Palumbo, G.A.; Di Raimondo, F.; et al. Overexpression of heme oxygenase-1 increases human osteoblast stem cell differentiation. *J. Bone Min. Metab.* **2010**, *28*, 276–288. [CrossRef] [PubMed]
75. Hotchkiss, K.M.; Reddy, G.B.; Hyzy, S.L.; Schwartz, Z.; Boyan, B.D.; Olivares-Navarrete, R. Titanium surface characteristics, including topography and wettability, alter macrophage activation. *Acta Biomater.* **2016**, *31*, 425–434. [CrossRef]
76. Aghaloo, T.; Pi-Anfruns, J.; Moshaverinia, A.; Sim, D.; Grogan, T.; Hadaya, D. The Effects of Systemic Diseases and Medications on Implant Osseointegration: A Systematic Review. *Int. J. Oral Maxillofac. Implant.* **2019**, *34*, s35–s49. [CrossRef]
77. Smeets, R.; Henningsen, A.; Jung, O.; Heiland, M.; Hammacher, C.; Stein, J.M. Definition, etiology, prevention and treatment of peri-implantitis-a review. *Head Face Med.* **2014**, *10*, 34. [CrossRef]
78. Eleniste, P.P.; Patel, V.; Posritong, S.; Zero, O.; Largura, H.; Cheng, Y.H.; Himes, E.R.; Hamilton, M.; Baughman, J.; Kacena, M.A.; et al. Pyk2 and Megakaryocytes Regulate Osteoblast Differentiation and Migration Via Distinct and Overlapping Mechanisms. *J. Cell Biochem.* **2016**, *117*, 1396–1406. [CrossRef]

coatings

MDPI

Article

The Bioactive Polypyrrole/Polydopamine Nanowire Coating with Enhanced Osteogenic Differentiation Ability with Electrical Stimulation

Yuan He [1], Lingfeng Dai [1,2], Xiuming Zhang [1], Yanan Sun [1], Wei Shi [1,*] and Dongtao Ge [1,*]

[1] Department of Biomaterials, College of Materials, Xiamen University, Xiamen 361005, China; 20720140153722@stu.xmu.edu.cn (Y.H.); dlf@fjirsm.ac.cn (L.D.); zhangxiuming@xmu.edu.cn (X.Z.); sunyanan@xmu.edu.cn (Y.S.)

[2] Quanzhou Institute of Equipment Manufacturing Haixi Institutes, Chinese Academy of Science, Quanzhou 362000, China

* Correspondence: shiwei@xmu.edu.cn (W.S.); gedt@xmu.edu.cn (D.G.)

Received: 11 November 2020; Accepted: 3 December 2020; Published: 5 December 2020

Abstract: Polypyrrole (PPy) is a promising conducting polymer in bone regeneration; however, due to the biological inertia of the PPy surface, it has poor cell affinity and bioactivity. Based on the excellent adhesion capacity, biocompatibility, and bioactivity of polydopamine (PDA), the PDA is used as a functional coating in tissue repair and regeneration. Herein, we used a two-step method to construct a functional conductive coating of polypyrrole/polydopamine (PPy/PDA) nanocomposite for bone regeneration. PPy nanowires (NWs) are used as the morphologic support layer, and a layer of highly bioactive PDA is introduced on the surface of PPy NWs by solution oxidation. By controlling the depositing time of PDA within 5 h, the damage of nano morphology and conductivity of the PPy NWs caused by the coverage of PDA deposition layer can be effectively avoided, and the thin PDA layer also significantly improve the hydrophilicity, adhesion, and biological activity of PPy NWs coating. The PPy/PDA NWs coating performs better biocombaitibility and bioactivity than pure PPy NWs and PDA, and has benefits for the adhesion, proliferation, and osteogenic differentiation of MC3T3-E1 cells cultured on the surface. In addition, PPy/PDA NWs can significantly promote the osteogenesis of MC3T3-E1 in combination with micro galvanostatic electrical stimulation (ES).

Keywords: PPy/PDA nanocomposite; nanowires; polydopamine; electrical stimulation

1. Introduction

Conducting polymers (CPs) especially polypyrrole (PPy) with excellent conductivity, long-term stability and biocompatibility have been widely applied in many fields [1–3]. In particular, the conductivity of CPs enables their use as sensors [4], controlled drug release [5,6], and functional tissue repair materials [7,8]. Moreover, CPs with nano morphology, which mimics the natural morphology of the extracellular matrix (ECM), can be easily fabricated via electrochemical and chemical polymerization on various substrates, and makes it an outstanding coating used in the biomedical field [9,10]. Actually, many studies confirmed that the PPy applied with electrical stimulation (ES) could promote the expression of proliferation and differentiation for tissue regeneration such as bone and nerves [11–13]. However, PPy does not display functional groups to help it adhere to surfaces [14]; therefore, generating composite materials with PPy and other adhesive polymers can effectively enhance the functionality of PPy-containing coatings.

Polydopamine (PDA) could be synthesized by the self-oxidative polymerization of dopamine (DA), which is the most abundant catecholamine neurotransmitter in the brain. PDA has excellent biocompatibility and biological activity [15]. The rich functional groups, especially the catechol compounds, offers PDA astonishing adhesive ability on a variety of materials [16,17]. Many studies focusing on the use of PDA as a surface functional modification material to improve the biocompatibility and surface modifiability of other materials were reported [18]. However, the PDA has poor conductivity without electrical signal response. Moreover, the inescapable fact is that the oxidative polymerization of dopamine (DA) is uncontrollable, which means it is very difficult to control the morphology [19,20], and the condition for preparing the PDA coating with nano morphology is quite harsh.

At present, many researchers are attentive to the preparation of PPy/PDA composites, which can solve the drawbacks of the above-mentioned materials. This kind of composites can be fabricated via one-pot or two-step method to avoid the disadvantages of pure PPy and PDA [21–24]. By controlling reaction conditions, the pyrrole (PY) and DA composite material has both good morphology, conductivity, and bioactivity. Zhao et al. have demonstrated that the copolymer of DA-PPy performs improved water dispersibility, improved electrical conductivity and film adhesion than pure PPy [17,25]. Electrochemical method has more advantages than chemical polymerization in the preparation of nanostructured conducting coatings with better controllability and uniformity of thickness and morphology. By precise regulating the concentration of PY and DA, PDA/PPy composite coatings with nanowires and vesicular structure morphology with enhanced conductivity, adhesion and cell affinity have been successfully prepared via a one-pot electrochemical polymerization [26–28]. In the one-pot reaction system of PY and DA, the concentration of PY and DA both have obvious effects on the morphology and conductivity of the copolymer. The concentration of dopamine and the polymerization potential need to be precisely controlled in order to obtain the copolymer with nano morphology. Compared with the co-polymerization of PPy/PDA, the reaction condition for preparing PPy/PDA composite coatings by a two-step method is relatively simple, as for the reaction condition of preparation pure PPy coating with various nano structure and size morphology can be controlled more easily and precisely by electrochemical deposition [29,30]. However, in order to better control the morphology and conductivity of the products, the most reported study on preparation of PPy/PDA composites via a two-step method is always setting fabrication of PPy layer as the final step to ensure the excellent conductivity [23,31]. Taking the PDA as the outer layer is more beneficial to improve the biocompatibility of PPy/PDA composites, and the key point is to precisely control the thickness of PDA deposition. The best result is that the deposition of PDA on the surface of PPy NWs will not significantly change the nano morphology of the first layer, nor reduce the conductivity.

In this study, the PDA modified PPy/PDA nanowire (NW) coating is synthesized by a two-step reaction (Figure 1). The first layer is preparation PPy NWs coating by electrochemical polymerization as the template, and the PDA layer is following deposited on each PPy NWs surface by solution oxidation. By regulating the deposition time of PDA, the influence of different PDA depositing time on the conductivity of PPY/PDA NWs coating is studied, and the optimal PDA deposition time is determined. The morphology, chemical structure, hydrophilicity, adhesiveness are further characterized. The cell affinity and bioactivity of the PPy/PDA NWs coating on MC3T3-E1 cell are further evaluated. The PPy/PDA NWs coating provides enhanced hydrophilicity and adhesiveness. The introduced PDA layer indeed improves the cell adhesion, proliferation, and differentiation of MC3T3-E1. Combined with ES, the PPy/PDA NWs coating shows better osteogenic activity to accelerate maturation of MC3T3-E1 cells.

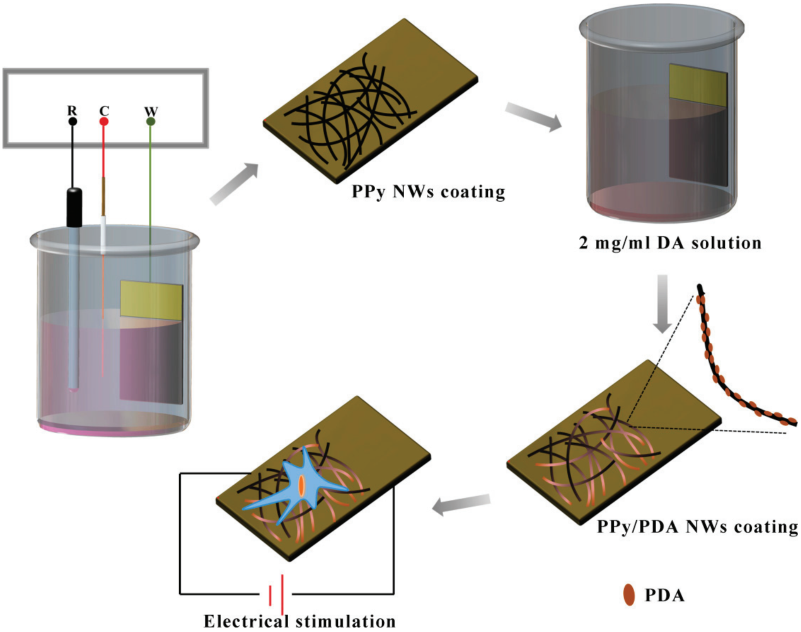

Figure 1. Illustration of preparation of PPy/PDA NWs coating and the synergistic effect with electrical stimulation on MC3T3-E1.

2. Materials and Methods

2.1. Materials

Pyrrole (PY, 98%) and sodium p-toluenesulfonate were purchased from J & K Chemical Ltd. (Beijing, China) Dopamine hydrochloride (98%), Vitamin C and β-glycerophosphate were bought from Sigma-Aldrich (Shanghai, China). Tris(dydroxymethyl) aminomethane (Tris-HCl, 99%) was purchased from Sangon Biotech Co. Ltd. (Shanghai, China). Other used inorganic salt reagents such as sodium chloride (NaCl), potassium chloride (KCl), disodium hydrogen phosphate (Na_2HPO_4), sodium dihydrogen phosphate (NaH_2PO_4), hydrochloric acid (HCl) were bought from SINOPHARM (Beijing, China). Monocrystal silicon wafer (p-type, 0.5 mm) was taken from Xiamen Zhongli Technology Co. Ltd. (Xiamen, China).

Before used, pyrrole need to be purified by distillation under the protection of N_2 gas and stored in the refrigerator at −20 °C for future use. Other reagents can be used directly without additional treatment. The water used in experiments was ultrapure water (18.2 MΩ).

Monocrystal silicon wafers were first cleaned via boiled in Piranha solution (H_2SO_4:H_2O_2 = 4:1) for 15 min and washed in hot water, then dried by nitrogen for further use. Next, a 500 nm thick of oxide layer was formed on the silicon surface by thermal diffusion oxidation. Finally, 50 nm titanium and 100 nm gold layer were fabricated in the silicon wafer surface via magnetron sputter. The Au/Ti/Si wafer was diced for further experiment.

2.2. Synthesis of PPy/PDA Nanowires (NWs) Coating

The PPy/PDA NWs coating was fabricated via a two-step method. In brief, the first step was the polymerization of PPy NWs layer by electrochemical deposition, and the second step was the deposition of PDA layer on the surfaces of PPy NWs via solution oxidation.

First, Pyrrole monomers could be polymerized with proper oxidation potential to form PPy. In this manuscript, the PPy NWs coating was directly fabricated by electrochemical polymerized on the Au/Ti/Si wafer under a potential at 0.8 V for 200 s with CHI660D electrochemical workstation (Chen Hua Instrument Company, Shanghai, China). The electropolymerization process of pyrrole was carried out in a traditional three-electrode system, in which the Au/Ti/Si wafer was the working electrode, a platinum wire was the counter electrode and a saturated calomel electrode (SCE, INESA Scientific Instrument Co. Ltd., Shanghai, China) was the reference electrode. The pyrrole monomer was dissolved in the electrolyte of 0.2 M PBS solution (pH = 7.4) containing 0.14 M of pyrrole and 0.085 M sodium p-toluenesulfonate. After 200 s, a uniform layer of PPy NWs can be deposited on the surface of the Au/Ti/Si substrate.

Second, the PDA layer was directly deposited on the PPy NWs by immersing the PPy NWs substrate into the fresh 2 mg/mL DA alkaline Tris-HCl solution (10 mM, pH = 8.50). The whole reaction vessel was opened and standing at room temperature for 5 h. Finally, the PPy/PDA NWs coated substrate was fished out and cleaned with distilled water.

The pure PPy NWs coating was fabricated by electrochemical polymerized the same as the first step. The Pure PDA coating was obtained on Au/Ti/Si substrate by direct immersing the bare Au/Ti/Si substrate in the fresh 2 mg/mL DA alkaline Tris-HCl solution (10 mM, pH = 8.50) for 5 h. The fabricated PPy/PDA NWs, PPy NWs, and PDA coatings were carefully washed with distilled water and dried in vacuum at 50 °C for further use.

2.3. Characterization

The morphologies of PPy NWs and PPy/PDA NWs were observed by scanning electron microscopy (SEM, SU-70, Hitachi, Tokyo, Japan) at an accelerating voltage of 10.0 kV and transmission electron microscopy (TEM, JME-2100, JEOL, Tokyo, Japan) under 200 kV accelerating voltage. The chemical composition of pure PDA, PPy, and PPy/PDA were characterized by Fourier transform infrared spectroscopy (FTIR, Nicolet IN10, Thermo Scientific, Waltham, MA, USA) with potassium bromide (KBr) tablet method. The static contact angle of different coating samples was measured by a contact angle meter (JC2000A, Shanghai Zhongchen digital technic apparatus Co. Ltd, Shanghai, China) with 2 μL water dropped at five different positions for each sample. Each sample randomly tested three parallel specimen. The electrical conductivity of the PPy and PPy/PDA NWs coatings was evaluated by a four-point probe apparatus (SZ83, Suzhou Baishen Technology Co. Ltd, Suzhou, China). Adhesion ability of PPy NWs and PPy/PDA NWs coating with the substrate was tested with ScotchTM MagicTM Tape 810 (3M, Saint Paul, MN, USA) and each sample was repeated three times in the same direction. Cyclic voltammetry (CV) was conducted in the 0.9% NaCl solution with a CHI660D electrochemical workstation. The voltage test ranging from −0.9–0.5 V at the scan rate of 10 mV/s.

2.4. Cell Culture

The mouse embryonic osteoblast precursor cells (MC3T3-E1) was bought at the Wuhan Cell Bank of Chinese Academy of Sciences Basic Science Cell Center. MC3T3-E1 cells were cultured in the alpha-modified minimum essential medium (α-MEM, Gibco, Waltham, MA, USA) supplemented with 10% FBS (Gibco, Waltham, MA, USA) and 1% penicillin and streptomycin (Hyclone, Chicago, IL, USA) in the saturated humidity incubator with 5% CO_2 at 37 °C. During the normal subculture of cells, the medium was changed every two days.

2.5. Effect of Surface Morphology on MC3T3-E1 Adhesion and Proliferation and Differentiation

Three different morphology substrates including PPy NWs, PDA and PPy/PDA NWs coatings on Au/Ti/Si wafers and bare Au/Ti/Si wafers were first sterilized by soaking in 75% ethanol for 24 h and following immersing in distilled water for another 24 h. The bare Au/Ti/Si wafer was the control group. Before the experiment, all substrates were further irradiated under UV radiation for another 2 h.

The sterilized substrates with different morphology were placed in the 24-well plate and washed with PBS. Then 1 mL of MC3T3-E1 (2×10^4 cells/mL) suspension was seeded to each well and then cultured in cell incubator (5% CO_2, 37 °C).

2.5.1. MTT Test

To test the adhesion and proliferation ability of MC3T3-E1 cell on different substrates, the MTT assay was used to evaluate the cell viability after cells were seeded and cultured for 4, 6, 8, 12, 24, and 48 h, respectively. In brief, at the tested time point, the cell culture was carefully removed and washed with PBS twice. 500 μL fresh culture medium containing 10% MTT working solution (5 mg/mL) was added to each well and continued to incubate for another 4 h. Next, the working solution was completely removed and incubated with 500 μL DMSO to dissolve the formazan crystal under 37 °C. Finally, the optical density was tested at 570 nm using a Microplate reader (Infinity 200 pro, Tecan, Männedorf, Switzerland). Each sample was set four-parallel experiments.

2.5.2. Cell Morphology

The cell morphology of adhesion and proliferation was observed via Fluorescence microscope (Leica DM2500, Leica Camera, Wetzlar, Germany). By staining the filamentous actin (F-actin) of the MC3T3-E1 cytoskeleton, the cell spreading morphology on substrates could be observed. Generally, after MC3T3-E1 cells were cultured for 12 and 24 h, cells were rinsed with PBS and then fixed with 4% paraformaldehyde solution for 15 min. After washed with PBS, cells were continued treated with 0.1% TritonX-100 solution to enhance the permeability of cell membrane. Next, the cell was incubated in 1% BSA solution for 20 min and washed with PBS. Followed above treatments, cells were finally stained with 5 U/mL Alexa Fluor 568 phalloidin solution for 30 min in the dark environment. Samples were observed by using a fluorescence microscope.

The morphology of MC3T3-E1 cell on different substrates was further watched with SEM. After cultured for 12 h, cells were fixed and dehydrated with gradient ethanol successively. After drying, samples were sputter-coated with gold before SEM testing.

2.5.3. Total Protein Content and Alkaline Phosphatase Activity

The MC3T3-E1 cell proliferation and differentiation activities were further measured by testing the total protein content and alkaline phosphatase (ALP) activity in the period of cell proliferation and differentiation. After MC3T3-E1 cell was seeded and cultured on different substrates for 24 h, the culture medium was changed to induced medium, which additionally added 1% Vitamin C (5 mg/mL) and β-glycerophosphate (1 M). The cells were cultured normally and the fresh induced medium was changed every 2 days.

The total protein content and ALP activity were tested at 3, 7 and 14 d. At each time point, cells in each group were washed with PBS and lysed on ice by incubation with 0.1% TritonX-100-PMSF pyrolysis liquid for 3 min, then centrifuged at 4 °C for 10 min. The supernatant was collected for further protein content and ALP activity detections. Total protein content measured by using a commercial BCA protein Assay Reagen Kit (Beyotime Institute of Biotechnology, Shanghai, China) and tested absorption signal at 562 nm. The ALP activity was tested using the commercial ALP Assay Kit (Beyotime Institute of Biotechnology, Shanghai, China), and measured the absorption intensity at 405 nm. Each sample was set four-parallel experiments.

2.6. Effect of Electrical Stimulation on MC3T3-E1 Adhesion and Proliferation and Differentiation

Micro constant current electrical stimulation signal (10 μA) was directly applied on the surface of different substrates (PPy NWs and PPy/PDA NWs) via an electrochemical workstation. ES was applied from the 12 h after cells inoculation and lasted for 2 h per day for 14 days. The cell proliferation and mineralization activity detection were the same as described in the above part.

2.7. Statistical Analysis

Quantitative results were presented as mean ± standard deviation. Statistical differences among groups were analyzed by ANOVA followed by Turkey's posttest. $p < 0.05$ was considered a significant difference and represented by *, and $p < 0.01$ was considered a highly significant difference and represented by #.

3. Results and Discussion

3.1. Characterization of PPy/PDA NWs

The PPy/PDA NWs was fabricated via a two-step method. First, PPy NWs coating was electrochemical polymerized on the surface of Au/Ti/Si wafer. Under the constant voltage of 0.8 V, after 200 s, the gold electrode surface could be covered with a layer of black PPy coating completely without revealing the color of the substrate, which mean the PPy coating could effectively cover the substrate with sufficient thickness. SEM images further showed the detailed morphology of obtained PPy NWs (Figure 2a). The PPy coating had nanowire morphology. PPy NWs were slender and uniform, and tightly wound with each other. The high magnification SEM and TEM images (Figure 2c,e) detailed showed the structure of PPy NWs, the surface of PPy NWs was smooth with a diameter of about 40–60 nm. Next, after immersing PPy NWs coating into the fresh dopamine (DA) alkaline solution for several hours, a layer of PDA could be formed on PPy NWs. The PDA coated PPy NWs composites retained the former nanowire morphology with uniform size (Figure 2b,d). While compared with pure PPy NWs, the surface roughness of PPy/PDA nanowires increased, and the PDA protrusion structure adhered to the surface of PPy nanowire could be observed clearly by TEM image (Figure 2f). At the same time, the diameter of PPy/PDA NWs also increased to about 80–100 nm, indicating that PDA could be successfully polymerized on the surface of each single PPy nanowire, and the PPy/PDA had core-shell structure.

PPy has excellent electrical conductivity and electrochemical activity. Many studies were conducted to prepare responsive coatings with electrical conductivity based on the electrical conductivity of PPy. As a bioactive material, PDA can significantly improve the bioactivity of the composite. However, PDA has poor conductivity. In alkaline solution, the thickness of PDA increases with the reaction, and after reacted for 24 h, the thickness of PDA could reach above 50 nm [32]. In addition, an excessively thick layer of PDA deposition covered on PPy NWs not only concealed the nano-scale morphology of PPy/PDA composite, but also significantly reduced the conductivity of the material. Therefore, it was very important to control the depositing thickness of PDA effectively on PPy NWs surface in order to ensure the maximum retention of excellent nano morphology and conductivity. As Figure 3 indicated, by controlling the PDA depositing time, the morphology and conductivity of the PPy/PDA nanocomposite performed regular changes. Within 5 h of PDA polymerization, the morphology of the PPy NWs could be well maintained and no obvious PDA aggregates were observed. With the prolongation of deposition time, a large number of PDA random aggregates were adhered on the surface of PPy NWs. When the deposition time prolonged to 15 h, PDA particles even filled into the gap of PPy NWs, and the nanostructure morphology was gradually disappeared. At 20 h, PDA almost completely covered the whole PPy NWs coating (Figure 3a). At the same time, the conductivity change of PPy/PDA coating also displayed cliff fall after deposition time above 5 h (Figure 3b). Therefore, the deposition time of PDA was chosen at 5 h. Under this condition, the PPy/PDA nanocomposite coating could retain both good nanowire morphology and conductivity (about 1 $\text{S}\cdot\text{cm}^{-1}$).

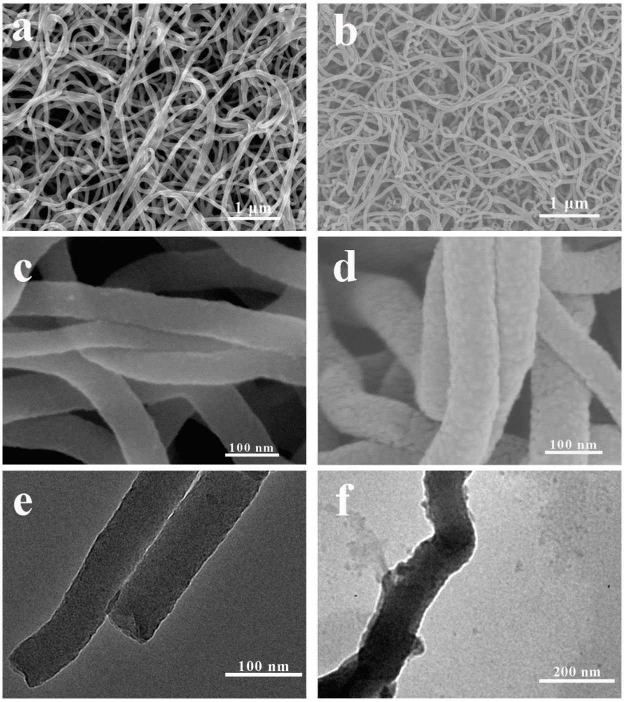

Figure 2. SEM images of PPy NWs (**a**) and PPy/PDA NWs (**b**). High resolution SEM images of PPy NWs (**c**) and PPy/PDA NWs (**d**). TEM images of PPy NWs (**e**) and PPy/PDA NWs (**f**).

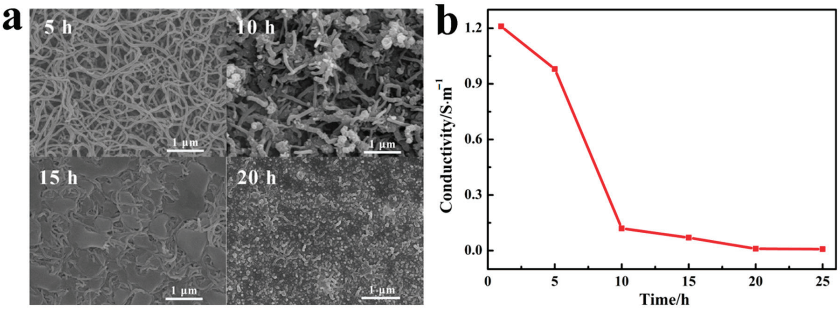

Figure 3. (**a**) SEM images of PPy/PDA NWs with different deposition time of PDA. (**b**) The conductivity of PPy/PDA NWs with different deposition time of PDA.

Comparing the FTIR spectra of pure PDA, PPy and PPy/PDA nanocomposite, it could be seen that the PPy/PDA nanocomposite possessed characteristic peaks of both pure PDA and PPy (Figure 4a): the broad peak around 3400 cm^{-1} was belonging to the N–H and O–H stretching vibrations, where PDA and PPy both have a broad peak. The peak at 1544 cm^{-1} was the characteristic peak of PPy attributed to the symmetric stretching vibrations of pyrrole ring [33]; and the characteristic peaks of PDA at 1615 and 1488 cm^{-1} ascribing to C=C and C=N/N–H stretching vibrations in aromatic amine species were also appeared [34,35], which further indicated the PDA was successfully deposited on the surface of PPy NWs to form a composite structure. Furthermore, the change of element proportion could also prove the successful modification of PDA by XPS analysis (Figure 4b). PY and DA monomers have the same elemental composition, but there is a significant difference in the N/C ratio between PY and DA. PY (1:4) has higher theoretical N/C ratio than that of DA (1:8). After polymerization, it could be seen that the N/C ratio of PPy NWs coating (0.164) was higher than that of pure PDA coating (0.094). In addition, after PDA deposited, the N/C ratio in PPy/PDA NWs coating decreased to 0.14, which further demonstrated that PDA was successfully deposited on the surface of PPy NWs.

PDA had better hydrophilicity than PPy due to rich hydrophilic groups. The contact angle measurement displayed the change of surface hydrophilicity after PDA deposition (Figure 4c). For the bare Au surface, it had large hydrophobicity, which the average contact angle was more than 90°. After the Au surface was covered by PPy NWs or pure PDA, the water contact angle decreased more than 30°, and nanowire morphology was more conducive to the decrease of contact angle. The PPy/PDA NWs coating had the minimum water contact angle, which was only 16°. The excellent hydrophilicity of PPy/PDA composite mainly came from both the rough porous nanostructure and a large number of exposed hydrophilic groups such as ammonia hydroxyl groups on the surface of PDA.

PDA have astonishing adhesion ability, which can adhere to a variety of materials. We used the 3M tape to test the adhesion ability of different coatings with the substrate by tear test (Figure 4d). The result demonstrated that the deposited layer of PDA could even enhance the adhesion property of the PPy/PDA NWs coating with the Au surface compared with pure PPy NWs. After several instances of the tear test, PPy/PDA NWs coating still adhered to the substrate firmly with almost no material loss. Therefore, the enhancement of surface hydrophilicity and the increase of adhesion stability with substrates made PPY/PDA NWs a better coating material than pure PPy NWs.

The PPy/PDA NWs had good conductivity. The electrochemical property was measured by cyclic voltammetry in 0.9% NaCl solution (Figure 4e). Pure PDA was hardly conductive and had no obvious electrochemical activity. After PDA deposited, compared with pure PPy NWs, the electrochemical activity of PPy/PDA NWs did not decrease significantly. However, compared with pure PPy NWs, the redox peak of PPy/PDA NWs was slightly shifted, indicating that PDA was not only successfully modified on the surface of PPy, but also interacted with PPy.

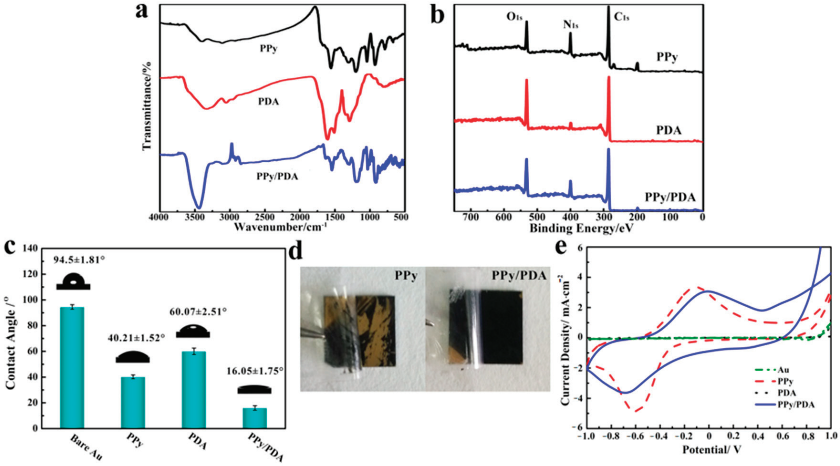

Figure 4. (**a**) FITR spectra of pure PPy NWs, PDA and PPy/PDA nanocomposite NWs. (**b**) XPS spectra of PPy NWs, PDA and PPy/PDA nanocomposite NWs. (**c**) The water contact angle of different material substrates. (**d**) The adhesion test of pure PPy NWs and PPy/PDA NWs. (**e**) Cyclic voltammogramms of different materials in 0.9% NaCl solution at the scan rate of 10 mV/s.

The above experiments demonstrated that via a two-step method, the PPy/PDA NWs nanocomposite coating was obtained. Compared with pure PPy NWs, PPy/PDA can effectively increase the hydrophilicity of the coating and the firmness of adhesion with the substrate materials while retaining the excellent nanostructure, conductivity, and electrochemical activity. PDA has excellent biocompatibility and bioactivity. It has been confirmed that PDA can promote osteoblast cell adhesion and biomineralization [14]. We speculated that this nano-structured PPy/PDA NWs might have excellent promoting effect on osteogenesis than pure PDA and PPy.

3.2. Effect of PPy/PDA NWs Coating on MC3T3-E1 Activity

When contacting with materials, in the beginning 8–12 h, the main behavior of cells is to interact with the material and then adhere to the surface of material. The morphology, structure and chemical microenvironment of the materials all have significant effects on anchorage-dependent cell adhesion. SEM images showed that at the initial 12 h after cells were seeded, MC3T3-E1 cell could adhere and spread well on pure PPy NWs, PDA and PPy/PDA NWs coatings (Figure 5a). MTT test indicated that compared with bare Au, all modified coatings including pure PPy NWs, PDA and PPy/PDA NWs could promote the adhesion and proliferation of MC3T3-E1 cells, and the PPy/PDA NWs coating performed most effective facilitation (Figure 5b). SEM and fluorescence images detailed showed the morphology of MC3T3-E1 cells adhesion and spreading on the surface of different materials (Figure 5a). After 12 h, most cells on PPy NWs coating performed spindle and fibrous shape with some pseudo feet anchored on near PPy NWs. On the other hand, cells on the surface of PDA were flat and full spreading, and there were lots of pseudopods linked cells with each other, which proved that PDA can promote cell spreading better than PPy NWs, while MC3T3-E1 cells grew on PPy/PDA NWs coating were well spreading than pure PPy NWs. Most cells on PPy/PDA NWs surface were spreading flat, and pseudopodia filaments of cells were dispersed into surrounding nanowires and adhered closely to the substrate. Moreover, MC3T3-E1 cells were interconnected with each other through a large number of pseudopods. After 12 h of inoculation, the adherent cells entered the fast proliferative phase (Figure 5a,b). MC3T3-E1 cells on all substrates were grew well, and cells on PPy/PDA NWs coating had the fastest growth rate, which ensured that the PPy/PDA NWs coating had excellent biocompatibility and bioactivity and was more benefit for cell adhesion and proliferation than pure PPy NWs and PDA.

For the PPy/PDA NWs nanocomposite, the PDA deposition introduced abundant active functional groups on the inert surface of PPy, which facilitated early cell recognition and anchoring adhesion process. Moreover, the morphology of nanowires was closer to the natural extracellular matrix (ECM) morphology and the primary growth environment of osteoblasts, which significantly promoted the adhesion and proliferation of MC3T3-E1 cells on the surface. Therefore, the PPy/PDA NWs coating took the advantages of both nano morphology came from PPy NWs and excellent biological active inherited from PDA, and had the best value for cell adhesion and proliferation than pure PPy NWs and PDA.

In the procedure of culture osteoblasts for 14 days, it can be divided into three stages [36]. First, the adhesion between cells and matrix was mainly carried out within 12 h after cells were seeded. After 2–3 days, the cells entered the rapid proliferation stage. In this stage, large amounts of protein and DNA were synthesized. Finally, after 6–9 days, the cell proliferation basically stopped and began to enter the mineralization stage. At this stage, the metabolic activity of cells was still vigorous, and the activity of osteoblast markers represented by alkaline phosphatase (ALP) increased significantly, and osteoblasts began to enter differentiating and mature process.

The content of total protein in cells could be used to describe the proliferation and metabolic activity of cells. By testing the total protein content of MC3T3-E1 that cells grew on different coatings (Figure 5c), it could be found that the proliferation and metabolism activity of MC3T3-E1 cells growing on the surface of PPy NWs, PDA and PPy/PDA NWs coatings were all more vigorous than that of the control group (bare Au), and the cell on the PPy/PDA NWs coating maintained the highest protein content during the 14 days throughout, which indicated the PPy/PDA NWs coating could promote the cell rapid proliferation and metabolism activity than pure PPy NWs and PDA.

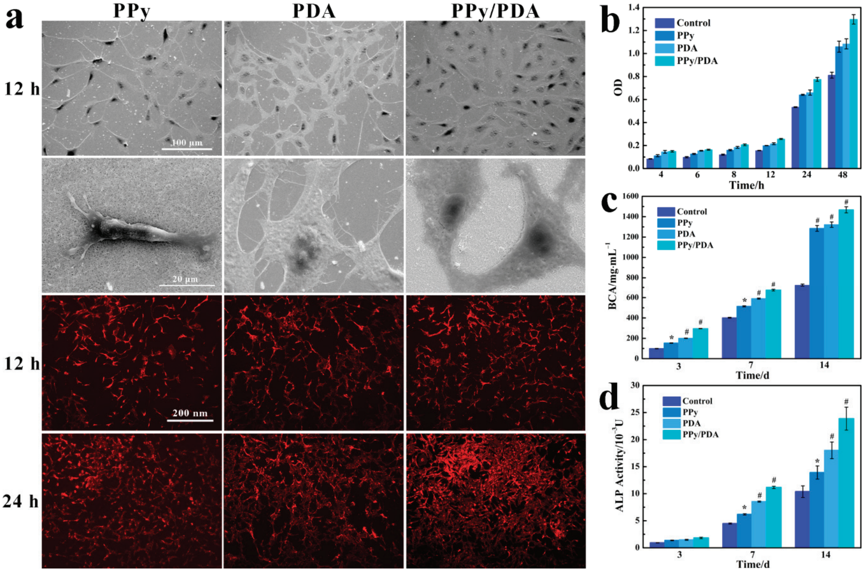

Figure 5. (**a**) SEM and fluorescence images of MC3T3-E1 cells on PPy NWs, PDA and PPy/PDA NWs cultured for 12 h and 24 h. (**b**) Proliferation of MC3T3-E1 cells on different coatings. (**c**) The protein content of MC3T3-E1 cells cultured on different coatings. (**d**) The ALP activity of MC3T3-E1 cells cultured on different coatings. * $p < 0.05$, and # $p < 0.01$.

The ALP activity, the early marker of osteogenic differentiation, could evaluate the osteogenic activity of MC3T3-E1 cells cultured on different coatings. As the result indicated (Figure 5d), at the initial stage of three days, the ALP activity of cells grown on four kind of coatings were all at low level without obvious difference. At this time, t cells were mainly in the rapid proliferation phase with low osteogenic activity. After 7 days, cells gradually entered the mineralization stage and the ALP activity in all group increased, and the PPy/PDA NWs group had the highest ALP activity. After 14 days, the advantage of ALP activity in PPy/PDA NWs group continued to expand, indicating that PDA/PPy NWs could significantly promote the mineralization and osteogenesis of MC3T3-E1 cells.

Above results demonstrated that the PPy/PDA NWs nanocomposite coating was not only helpful to the rapid adhesion of cells on the surface of materials, but also conducive the osteogenic activity for new bone formation.

3.3. Synergistic Effect of PPy/PDA NWs Coating with Electrical Stimulation on MC3T3-E1 Activity

In the process of bone formation and bone remodeling, electrical microenvironment around the bone cells occurs. Many studies confirmed that a small amount of electrical stimulation (ES) can significantly promote the proliferation and differentiation of osteoblasts at the cellular and tissue level [37,38]. PPy has good conductivity, and could be fabricated as a conductive coating to apply ES on cells sensitive to electrical signals. Our previous study have demonstrated that MC3T3-E1 cells shows better osteogenic activity on the surface of PPy coating with ES [39]. The PPy/PDA NWs was well maintained the excellent conductivity of PPy NWs layer, and performed better osteogenic differentiation activity than pure PPy NWs. Next, we used a self-made device to apply a constant current electrical stimulation (10 μA) to MC3T3-E1 cells through the PPy/PDA coating, and to study the synergistic effect of PPy/PDA NWs and ES working together on MC3T3-E1 cells.

After 12 h of the MC3T3-E1 cell culture, the constant ES was applied on cells for 2 h a day until 14 days. It could be seen that continuous ES can significantly increase the adhesion and proliferation of MC3T3-E1 cell (Figure 6a), the number of MC3T3-E1 cells on PPy/PDA NWs coatings was almost doubled higher after ES was applied. Additionally, the total protein content and ALP activity tests relating to the proliferation and osteogenesis activity of MC3T3-E1 cells both revealed that the ES could promote the osteogenic differentiation of MC3T3-E1 cells (Figure 6b,c). It was noticeable that the total protein content and ALP activity value of MC3T3-E1 cells with ES at 7 days was very close to that of the cells without ES at 14 days, which proved that the PPy/PDA NWs coating together with ES addition could accelerate the cells entering the mature stage of osteogenic differentiation.

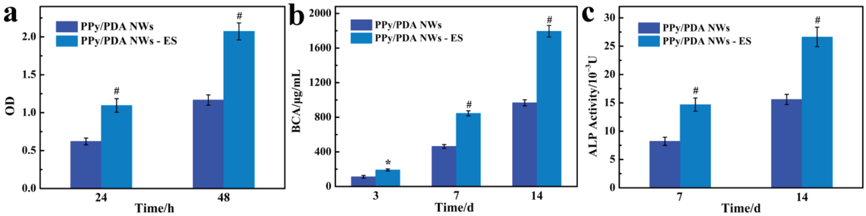

Figure 6. (**a**) The effect of ES on the proliferation of MC3T3-E1 cells on PPy/PDA NWs coating. (**b**) The effect of ES on the total protein content of MC3T3-E1 cells cultured on PPy/PDA NWs coating. (**c**) The effect of ES on the ALP activity of MC3T3-E1 cells cultured on PPy/PDA NWs coating. * $p < 0.05$, and # $p < 0.01$.

4. Conclusions

We successfully fabricated the PPy/PDA NWs coating via a simple two-step method. By well controlling the depositing time of PDA within 5 h, the PPy/PDA NWs nanocomposite retained the nano morphology, conductivity, and electrochemical activity from the PPy NWs layer. Moreover, the introduction of the PDA deposition layer significantly improved the hydrophilicity and bioactivity of the material surface. In vitro experiments further proved that the PPy/PDA NWs composite coating had better biocompatibility and osteogenic differentiation ability than pure PPy NWs and PDA. MC3T3-E1 cells could quickly adhere and anchor on the surface of PPy/PDA NWs coating, and enter the proliferation and differentiation process. Furthermore, external applied ES with PPy/PDA NWs coating had the synergistic effect in stimulating the osteogenesis of MC3T3-E1 cell. Therefore, the PPy/PDA NWs composite is a potential coating with enhanced biocompatibility and biological activity in bone regeneration and repairing.

Author Contributions: L.D., Y.H., W.S. and D.G. designed the experiments; L.D. and Y.H. undertook the most experiments; Y.H. and L.D. completed the data and imaging preparation and edition; Y.H. wrote the manuscript; D.G., W.S., X.Z. and Y.S. gave valuable suggestions and revised the manuscript. All authors have read and agreed to the published version of the manuscript.

Funding: This work was supported by the National Nature Foundation of China (31870986), the National Nature Science Foundation of China (31271009, 81271689), the Fundamental Research Funds for the Central Universities (2011121001), the Natural Science Foundation of Fujian Province (2011J01331), the Program for New Century Excellent Talents in University, and the Program for New Century Excellent Talents in Fujian Province University.

Acknowledgments: We acknowledge the analysis and testing center of Xiamen University.

Conflicts of Interest: The authors declare no conflict of interest.

References

1. Wu, J.-G.; Chen, J.-H.; Liu, K.-T.; Luo, S.-C. Engineering antifouling conducting polymers for modern biomedical applications. *ACS Appl. Mater. Interfaces* **2019**, *11*, 21294–21307. [CrossRef] [PubMed]
2. Hackett, A.J.; Malmström, J.; Travas-Sejdic, J. Functionalization of conducting polymers for biointerface applications. *Prog. Polym. Sci.* **2017**, *70*, 18–33. [CrossRef]
3. Hardy, J.G.; Lee, J.Y.; Schmidt, C.E. Biomimetic conducting polymer-based tissue scaffolds. *Curr. Opin. Biotechnol.* **2013**, *24*, 847–854. [CrossRef] [PubMed]

4. Xia, L.; Wei, Z.; Wan, M. Conducting polymer nanostructures and their application in biosensors. *J. Colloid Interface Sci.* **2010**, *341*, 1–11. [CrossRef]
5. Boehler, C.; Oberueber, F.; Asplund, M. Tuning drug delivery from conducting polymer films for accurately controlled release of charged molecules. *J. Control Release* **2019**, *304*, 173–180. [CrossRef]
6. Jiang, S.; Sun, Y.; Cui, X.; Huang, X.; He, Y.; Ji, S.; Shi, W.; Ge, D. Enhanced drug loading capacity of polypyrrole nanowire network for controlled drug release. *Synth. Met.* **2013**, *163*, 19–23. [CrossRef]
7. Mihardja, S.S.; Sievers, R.E.; Lee, R.J. The effect of polypyrrole on arteriogenesis in an acute rat infarct model. *Biomaterials* **2008**, *29*, 4205–4210. [CrossRef]
8. Bu, Y.; Xu, H.; Li, X.; Xu, W.; Yin, Y.-X.; Dai, H.; Wang, X.-B.; Huang, Z.-J.; Xu, P.-H. A conductive sodium alginate and carboxymethyl chitosan hydrogel doped with polypyrrole for peripheral nerve regeneration. *RSC Adv.* **2018**, *8*, 10806–10817. [CrossRef]
9. Lee, J.Y.; Bashur, C.A.; Goldstein, A.S.; Schmidt, C.E. Polypyrrole-coated electrospun PLGA nanofibers for neural tissue applications. *Biomaterials* **2009**, *30*, 4325–4335. [CrossRef]
10. Harjo, M.; Torop, J.; Järvekülg, M.; Tamm, T.; Kiefer, R. Electrochemomechanical behavior of polypyrrole-coated nanofiber scaffolds in cell culture medium. *Polymers* **2019**, *11*, 1043. [CrossRef]
11. Hu, W.-W.; Hsu, Y.-T.; Cheng, Y.-C.; Li, C.; Ruaan, R.-C.; Chien, C.-C.; Chung, C.-A.; Tsao, C.-W. Electrical stimulation to promote osteogenesis using conductive polypyrrole films. *Mater. Sci. Eng. C* **2014**, *37*, 28–36. [CrossRef] [PubMed]
12. Zhou, Z.; Chen, J.; Zhou, L.; Tu, L.; Fan, L.; Zhang, F.; Dai, C.; Liu, Y.; Ning, C.; Du, J.; et al. Polypyrrole nanocones and dynamic piezoelectric stimulation-induced stem cell osteogenic differentiation. *ACS Biomater. Sci. Eng.* **2019**, *5*, 4386–4392. [CrossRef]
13. Hardy, J.G.; Sukhavasi, R.C.; Aguilar, D.; Villancio-Wolter, M.K.; Mouser, D.J.; Geissler, S.A.; Nguy, L.; Chow, J.K.; Kaplan, D.L.; Schmidt, C.E. Electrical stimulation of human mesenchymal stem cells on biomineralized conducting polymers enhances their differentiation towards osteogenic outcomes. *J. Mater. Chem. B* **2015**, *3*, 8059–8064. [CrossRef]
14. Zhou, T.; Yan, L.; Xie, C.; Li, P.; Jiang, L.; Fang, J.; Zhao, C.; Ren, F.; Wang, K.; Wang, Y.; et al. A mussel-inspired persistent ROS-scavenging, electroactive, and osteoinductive scaffold based on electrochemical-driven in situ nanoassembly. *Small* **2019**, *15*, 1805440. [CrossRef] [PubMed]
15. Cheng, S.; Wang, D.; Ke, J.; Ma, L.; Zhou, J.; Shao, H.; Zhu, H.; Liu, L.; Zhang, Y.; Peng, F.; et al. Improved in vitro angiogenic behavior of human umbilical vein endothelial cells with oxidized polydopamine coating. *Colloids Surf. B* **2020**, *194*, 111176. [CrossRef]
16. Waite, J.H. The adhesive proteins secreted by mussels are the inspiration behind a versatile approach to the surface modification of a wide range of inorganic and organic materials, resulting in the fabrication of multifunctional coatings for a variety of applications. *Nat. Mater.* **2008**, *7*, 8–9. [CrossRef]
17. Zhang, W.; Pan, Z.; Yang, F.K.; Zhao, B. A facile in situ approach to polypyrrole functionalization through bioinspired catechols. *Adv. Funct. Mater.* **2015**, *25*, 1588–1597. [CrossRef]
18. Zeng, X.; Luo, M.; Liu, G.; Wang, X.; Tao, W.; Lin, Y.; Ji, X.; Nie, L.; Mei, L. Polydopamine-modified black phosphorous nanocapsule with enhanced stability and photothermal performance for tumor multimodal treatments. *Adv. Sci.* **2018**, *5*, 1800510. [CrossRef]
19. Zhang, P.-B.; Hu, W.; Wu, M.; Gong, L.; Tang, A.; Xiang, L.; Zhu, B.; Zhu, L.-P.; Zeng, H. Cost-effective strategy for surface modification via complexation of disassembled polydopamine with Fe(III) ions. *Langmuir* **2019**, *35*, 4101–4109. [CrossRef]
20. Ponzio, F.; Bertani, P.; Ball, V. Role of surfactants in the control of dopamine–eumelanin particle size and in the inhibition of film deposition at solid–liquid interfaces. *J. Colloid Interface Sci.* **2014**, *431*, 176–179. [CrossRef]
21. Zhang, W.; Yang, F.K.; Pan, Z.; Zhang, J.; Zhao, B. Bio-inspired dopamine functionalization of polypyrrole for improved adhesion and conductivity. *Macromol. Rapid Commun.* **2014**, *35*, 350–354. [CrossRef] [PubMed]
22. Kim, S.; Jang, L.K.; Park, H.S.; Lee, J.Y. Electrochemical deposition of conductive and adhesive polypyrrole-dopamine films. *Sci. Rep.* **2016**, *6*, 30475. [CrossRef] [PubMed]
23. Pan, J.; Yang, M.; Luo, L.; Xu, A.; Tang, B.; Cheng, D.; Cai, G.; Wang, X. Stretchable and highly sensitive braided composite yarn@polydopamine@polypyrrole for wearable applications. *ACS Appl. Mater. Interfaces* **2019**, *11*, 7338–7348. [CrossRef] [PubMed]

24. Kim, S.; Jang, L.K.; Jang, M.; Lee, S.; Hardy, J.G.; Lee, J.Y. Electrically conductive polydopamine-polypyrrole as high performance biomaterials for cell stimulation in vitro and electrical signal recording in vivo. *ACS Appl. Mater. Interfaces* **2018**, *10*, 33032–33042. [CrossRef] [PubMed]
25. Zhang, W.; Zhou, Y.; Feng, K.; Trinidad, J.; Yu, A.; Zhao, B. Morphologically controlled bioinspired dopamine-polypyrrole nanostructures with tunable electrical properties. *Adv. Electron. Mater.* **2015**, *1*, 1500205. [CrossRef]
26. Xie, C.; Li, P.; Han, L.; Wang, Z.; Zhou, T.; Deng, W.; Wang, K.; Lu, X. Electroresponsive and cell-affinitive polydopamine/polypyrrole composite microcapsules with a dual-function of on-demand drug delivery and cell stimulation for electrical therapy. *NPG Asia Mater.* **2017**, *9*, 358. [CrossRef]
27. Wang, Z.; Zhou, L.; Yu, P.; Liu, Y.; Chen, J.; Liao, J.; Li, W.; Chen, W.; Zhou, W.; Yi, X.; et al. Polydopamine-assisted electrochemical fabrication of polypyrrole nanofibers on bone implants to improve bioactivity. *Macromol. Mater. Eng.* **2016**, *301*, 1288–1294. [CrossRef]
28. Tan, J.; Zhang, Z.; He, Y.; Yue, Q.; Xie, Z.; Ji, H.; Sun, Y.; Shi, W.; Ge, D. Electrochemical synthesis of conductive. superhydrophobic and adhesive polypyrrole-polydopamine nanowires. *Synth. Met.* **2017**, *234*, 86–94. [CrossRef]
29. Huang, J.; Wang, K.; Wei, Z. Conducting polymernanowire arrays with enhanced electrochemical performance. *J. Mater. Chem.* **2010**, *20*, 1117–1121. [CrossRef]
30. Debiemme-Chouvy, C. Template-free one-step electrochemical formation of polypyrrole nanowire array. *Electrochem. Commun.* **2009**, *11*, 298–301. [CrossRef]
31. Ma, F.-F.; Zhang, D.; Zhang, N.; Huang, T.; Wang, Y. Polydopamine-assisted deposition of polypyrrole on electrospun poly(vinylidene fluoride) nanofibers for bidirectional removal of cation and anion dyes. *Chem. Eng. J.* **2018**, *354*, 432–444. [CrossRef]
32. Lee, H.; Dellatore, S.M.; Miller, W.M.; Messersmith, P.B. Mussel-inspired surface chemistry for multifunctional coatings. *Science* **2007**, *318*, 426–430. [CrossRef] [PubMed]
33. Liu, S.; Pan, T.; Wang, R.; Yue, Y.; Shen, J. Anti-corrosion and conductivity of the electrodeposited graphene/polypyrrole composite coating for metallic bipolar plates. *Prog. Org. Coat* **2019**, *136*, 105237. [CrossRef]
34. Luo, R.; Tang, L.; Wang, J.; Zhao, Y.; Tu, Q.; Weng, Y.; Shen, R.; Huang, N. Improved immobilization of biomolecules to quinone-rich polydopamine for efficient surface functionalization. *Colloids Surf. B* **2013**, *106*, 66–73. [CrossRef] [PubMed]
35. Zangmeister, R.A.; Morris, T.A.; Tarlov, M.J. Characterization of polydopamine thin films deposited at short times by autoxidation of dopamine. *Langmuir* **2013**, *29*, 8619–8628. [CrossRef]
36. Qqarles, L.D.; Yohay, D.A.; Lever, L.W.; Caton, R.; Wenstrup, R.J. Distinct proliferative and differentiated stages of murine MC3T3-El cells in culture: An in vitro model of osteoblast development. *J. Bone Miner. Res.* **1992**, *7*, 683–692. [CrossRef]
37. Lirani-Galvão, A.P.R.; Chavassieux, P.; Portero-Muzy, N.; Bergamaschi, C.T.; Silva, O.L.; Carvalho, A.B.; Lazaretti-Castro, M.; Delmas, P.D. Low-intensity electrical stimulation counteracts the effects of ovariectomy on bone tissue of rats: Effects on bone microarchitecture, viability of osteocytes, and nitric oxide expression. *Calcif. Tissue Int.* **2009**, *84*, 502–509. [CrossRef]
38. Lirani-Galvão, A.P.R.; Lazaretti-Castro, M.; Portero-Muzy, N.; Bergamaschi, C.T.; Silva, O.L.; Carvalho, A.B.; Delmas, P.D.; Chavassieux, P. Is nitric oxide a mediator of the effects of low-intensity electrical stimulation on bone in ovariectomized rats? *Calcif. Tissue Int.* **2010**, *87*, 52–59. [CrossRef]
39. He, Y.; Wang, S.; Mu, J.; Dai, L.; Zhang, Z.; Sun, Y.; Shi, W.; Ge, D. Synthesis of polypyrrole nanowires with positive effect on MC3T3-E1 cell functions through electrical stimulation. *Mater. Sci. Eng. C* **2017**, *71*, 43–50. [CrossRef]

coatings

MDPI

Article

Corrosion Behavior and Biological Activity of Micro Arc Oxidation Coatings with Berberine on a Pure Magnesium Surface

Liting Mu [1,2], Zhen Ma [1], Jingyan Wang [1], Shidan Yuan [1] and Muqin Li [1,*]

[1] School of Materials Science and Engineering, Jiamusi University, Jiamusi 154007, China; muliting@163.com (L.M.); mz252930179@163.com (Z.M.); jmsdxclwjy@163.com (J.W.); jmsdxysd@163.com (S.Y.)

[2] School of Pharmacy, Jiamusi University, Jiamusi 154007, China

* Correspondence: limuqin@jmsu.edu.cn; Tel.: +86-454-8618-702

Received: 1 August 2020; Accepted: 22 August 2020; Published: 28 August 2020

Abstract: Bone tissue repair materials can cause problems such as inflammation around the implant, slow bone regeneration, and poor repair quality. In order to solve these problems, a coating was prepared by ultrasonic micro-arc oxidation and self-assembly technology on a pure magnesium substrate. We studied the effect of berberine on the performance of the ultrasonic micro-arc oxidation/polylactic acid and glycolic acid copolymer/berberine (UMAO/PLGA/BR) coating. The chemical and morphological character of the coating was analyzed using scanning electron microscopy, X-ray diffraction, and X-ray photoelectron spectroscopy. The corrosion properties were studied by potentiodynamic polarization and electrochemical impedance spectroscopy in a simulated body fluid. The cumulative release of drugs was tested by high-performance liquid chromatography. The results indicate that different amounts of BR can seal the corrosion channel to different extents. These coatings have a self-corrosion current density (Icorr) at least one order of magnitude lower than the UMAO coatings. When the BR content is 3.0 g/L, the self-corrosion current density of the UMAO/PLGA/BR coatings is the lowest (3.14×10^{-8} A/cm^2) and the corrosion resistance is improved. UMAO/PLGA/BR coatings have excellent biological activity, which can effectively solve the clinical problem of rapid degradation of pure magnesium and easy infection.

Keywords: pure magnesium; ultrasonic micro-arc oxidation; berberine; corrosion resistance

---

1. Introduction

Traumatic bone repair materials have become a research hotspot in the field of orthopedics. They are mainly derived from autologous and allogeneic bone grafts [1]. The source of autologous bone grafting materials is limited, complications are prone to occur after surgery, and the success rate is low. Allogeneic bone graft materials are expensive and prone to rejection. The degradation of allogeneic bone is slow, resulting in a smaller volume of new bone. In order to solve the above problems, material researchers are trying to find suitable human bone repair materials. With the development of biodegradable materials, metal bone repair biomaterials are undergoing a revolution. The properties of metal biomaterials have changed from being biologically inert to having biological activity and multiple biological functions [2,3]. Magnesium and magnesium alloys are characterized by good osteoinductivity, spontaneous degradability, and excellent biological safety. Their mechanical properties are similar to those of human cortical bone, and the biological properties of the graft are similar to those of natural bone, which has attracted a great amount of attention in the bone repair materials field [4,5]. The degradable properties of magnesium will eliminate the need for a second surgery to remove the implant. Thus, magnesium and magnesium alloy bone repair materials would not only further reduce the pain and burden for patients, but also increase the application of these advanced materials [6]. However, a series of biological problems have been discovered during the clinical application of pure magnesium, such as osteolysis around the implant, easy loosening of the implant, rapid degradation, and hemolytic infection, which limit the application of pure medical magnesium and magnesium alloys [7–9].

Therefore, researchers should study composite coatings with antibacterial, anti-inflammatory, and bone growth promotion effects, and then adjust and control the degradation rate and biological characteristics of pure medical magnesium to solve the fundamental problem of magnesium implants and make magnesium more suitable as an implant material [10]. In recent years, ultrasonic micro-arc oxidation (UMAO) has been shown to be an effective surface modification technology that can effectively reduce the degradation rate of materials [11,12]. UMAO can effectively improve the corrosion resistance of magnesium alloys. However, the micropores and microcracks of the UMAO surface may cause undesirable rapid and unexpected degradation of magnesium and its alloys [13]. Therefore, scholars have tried to compound other surface modification technologies on the UMAO surface [14–16]. Li [17] reported using KH550 as a silane coupling agent to modify the surface of the ultrasonic micro-arc oxidation coating on pure magnesium. The organic film of the Si–O–Mg bond formed on the surface helps to reduce the pores in the UMAO coating and improve its corrosion resistance. In order to further improve the bone growth around the implant, as well as the antibacterial and anti-inflammatory effects, Peng [18] prepared a phytic acid puerarin solution on the UMAO coating by dip coating. The composite coating has better corrosion resistance than UMAO. It also accelerates the mineralization of apatite and improves the biological activity. Wang [19] prepared an UMAO/chitosan/citrin coating on a pure Mg substrate. They found that the Chinese herbal extract coating enhanced the corrosion resistance and biological activity of pure Mg, and also enhanced the adhesion and proliferation of osteoblasts. However, the coating drug released quickly and the concentration was low. Furthermore, its ability to promote bone growth, as well as its antibacterial and anti-inflammatory effects, did not reach the expected effect.

The most difficult problem with these coatings in bone injury is the low drug concentration at the lesion site. If the drug concentration around the local implant is maintained in a reasonable range, it will be slowly released around the implantation area at a certain rate within a certain period of time to achieve the purpose of the treatment. At present, long-acting sustained-release drug-loaded artificial bone is considered feasible [20,21]. The preparation of drug-loaded artificial bone usually includes methods such as the vacuum adsorption freeze-drying method and the compression molding method. The above methods can achieve the effect of sustained drug release. However, studies have found that the release of drugs is too fast or the drug-carrying materials cannot be degraded or they degrade very slowly, which limits the application [22–24]. Polylactic acid glycolic acid copolymer (PLGA) is a degradable functional polymer organic compound, usually used as a carrier for drug release [25]. PLGA is widely used in the fields of pharmaceutical and medical engineering materials, mainly because it is biocompatible, non-toxic, shows controllable degradation, and produces harmless metabolites in the body. It also has excellent coating-forming properties. At the same time, PLGA as a biomedical material has been certified by the U.S. Food and Drug Administration. Sevostyanov [26] studied the coating of PLGA-containing triple anti-tuberculosis patients' bones, which can stably and slowly release drugs and maintain the local drug concentration at a high level in the lesion. Qian [27] found that the degradation of PLGA in the human body is acidic, and magnesium is degraded to alkaline. After degradation, the environment is neutralized to a certain extent. Wu [28] prepared magnesium-enhanced PLGA copolymer composites by extraction and oil bath methods, and found that the pH of the environment during the degradation process is normal, does not affect bone growth, and can effectively regulate the strength and characteristics of the material according to the location and characteristics of the repaired bone degradation rate.

Until now, PLGA has mostly been used as a carrier for the preparation of slow-release Western medicines. At present, the focus of attention has shifted from synthetic medicine to natural medicine

(Chinese medicine), mainly because traditional Chinese medicine has the characteristics of stable action, low toxicity, and natural materials. Traditional Chinese medicine plays a positive role in promoting the growth of osteoblasts, has antibacterial and anti-inflammatory effects, and is able to regulate the differentiation and biological activity of osteoblasts. Berberine (BR), the main active component of the Chinese medicine coptis, has a variety of biological activities, such as inhibiting inflammation, promoting bone formation, and inhibiting osteoclasts [29,30]. However, few reports have focused on combining PLGA and BR to form a composite sustained-release drug coating to enhance the biological activity and corrosion resistance of magnesium alloys [31].

In this study, by modifying the surface of pure magnesium, we obtain a PLGA/BR multi-element composite functional coating that has antibacterial function, promotes bone growth, and can control the degradation rate, and the structural characteristics, corrosion resistance, and biological activity of the composite coating are systematically evaluated.

2. Materials and Methods

2.1. Materials and Drugs

Mg (Technology Co., Ltd., Yi'an, China) was cut into 10 × 10 × 1 mm sample cubes. The molecular weight of PLGA (polylactic acid/glycolic acid, 50:50) was 90,000 (Daigang Biological Engineering Co., Ltd., Jinan, China), and the berberine content was 99% (China Institute for Food and Drug Control).

2.2. Sample Preparation

Sandpaper was used to polish the samples to a smooth surface; which were then soaked and degreased with ethanol for 30 min; and then cleaned with deionized water, dried, and sealed for later use. The following electrolytes were used in UMAO: $Na_2SiO_3{\cdot}9H_2O$ (15 g/L), KOH (10 g/L), KF (8 g/L), and $C_{10}H_{14}N_2Na_2O_8$ (1 g/L). The working parameters for the UMAO treatment were as follows: first, a pulse width of 50 μs, a pulse frequency of 500 Hz, an auxiliary ultrasonic frequency of 60 kHz, an ultrasonic power of 50 W, a voltage of 300 V, and an oxidation time of 7 min; and second, a regulated voltage of 260 V and an oxidation time of 3 min, cleaned with deionized water and dried in air.

The composite coating was prepared by immersion in 3 mol/L NaOH solution at 60 °C for 1 h, referred to as alkali treatment. Then, 500 mg of PLGA was dissolved in 10 mL of dichloromethane under ultrasound for 30 min. BR-loaded solutions in concentrations of 1.5 g/L, 3.0 g/L, and 6.0 g/L were prepared ultrasonically using the 50 g/L PLGA solution as the solvent for 30 min, giving a self-assembly solution. The sample was immersed in the self-assembly solution for 3 min. Then, the sample was removed from the solution in the vertical direction at a speed of 5 cm/min and dried in air. UMAO/PLGA/BR coatings were marked as 1.5, 3.0, and 6.0 g/L, respectively.

2.3. Coating Characterization

The microstructure and elemental composition of the coatings were characterized by scanning electron microscopy (SEM, JSM-7800JJEOL, Tokyo, Japan) and energy dispersive spectroscopy (EDAX, FALCON60S, Mahwah, NJ, USA). The phases in the coatings were identified by X-ray diffraction (XRD, D8 ADVANCE, BRUKER, Karlsruhe, Germany) with Cu Kα radiation in the 2θ range of 10° to 90°. The contact angle of the coatings was measured by a contact angle meter (JC2000C1, Zhongchen, Shanghai, China). The micro-roughness of the coatings was observed by German Bruker atomic force microscopy (AFM, BRUKER, Karlsruhe, Germany). X-ray photoelectron spectroscopy (XPS, ESCALAB250XI, Thermo Fisher Scientific, Waltham, MA, USA) was used to qualitatively analyze the presence of elements, carbon components, and chemical bonds on the sample surface. The excitation source was Al Kα, the test power was 300 W, and C1s (binding energy 284.8 eV) was used before the test to correct the charge displacement of each element in the test. For the XPS peak, software was used to fit the peaks of the high-resolution XPS spectra of the corrected elements.

2.4. Electrochemical Test

The electrochemical impedance spectroscopy (EIS) and the Tafel curve measurements of the coating were performed by a VersaSTAT 3 electrochemical workstation in the simulated body fluid (SBF) solution at 37 °C to evaluate the corrosion behavior of the coating. SBF [32] composition is shown in Table 1. All reagents comply with American Chemical Society standards (ACS). The frequency range of EIS measurements was 10^{-1}–10^4 Hz. ZsimpWin software was used to perform equivalent circuit fitting on the impedance results.

Table 1. Chemical composition and reagents grade (ACS, American Chemical Society standards) and purity used for preparation of simulated body fluid (SBF).

No.	Chemical Formula	Amount	Reagent Grade	Purity	Manufacturer
1	NaCl	8.035 g/L	ACS reagent	≥99.90%	Comeo Co., Ltd., Tianjin, China
2	$NaHCO_3$	0.355 g/L	Bio Reagent	≥99.50%	
3	KCl	0.225 g/L	ACS reagent	≥99.50%	
4	$K_2HPO_4{\cdot}3H_2O$	0.231 g/L	ACS reagent	≥99.90%	
5	$MgCl_2{\cdot}6H_2O$	0.311 g/L	ACS reagent	≥98.00%	
6	1.0M-HCl	39 mL	ACS reagent	≥37.00%	
7	$CaCl_2$	0.292 g/L	ACS reagent	≥99.90%	
8	Na_2SO_4	0.072 g/L	ACS reagent	≥99.90%	
9	$(CH_2OH)_3CNH_2$	6.118 g/L	Standard & Buffer	≥99.90%	

2.5. Immersion Tests

The temperature of the experiment was maintained at 37.0 ± 0.5 °C using a constant temperature water bath and soaked for 3, 7, and 14 days. The degradation and corrosion resistance of the composite bio-coating was identified by SEM. The morphology and composition of the sample before and after immersion were analyzed and studied.

2.6. Slow-Release Drug Measurement

A high-performance liquid chromatography (HPLC) method was established for the qualitative analysis of berberine standard products. The chromatographic conditions were selected as follows: column: Hypersil GOLD C_{18} (100 × 2.1 mm, 1.9 μm); mobile phase: 0.1% formic acid–acetonitrile/0.1% formic acid water (A/B = 30:70); flow rate: 0.3 mL/min, temperature: 40 °C; injection volume: 10 μL; detection wavelength: 345 nm. A constant temperature method was used for the in vitro drug release test. The samples were sealed and placed in an eppendorf (EP) tube, added to a simulated body fluid with a pH of 7.4, and placed in a 37 °C incubator to simulate the growth environment. Samples were taken after 1, 3, 5, 7, 9, 11, 13, 15, 17, 19, 21, 23, 25, 27, 29, and 31 d. Then, 40 μL of the sample was added to 360 μL methanol, and the same amount of simulated body fluid was added to the EP tube. The sample was injected into the HPLC, the peak area was recorded at 345 nm, and the cumulative release of BR was calculated using the peak area. The time was the abscissa and the cumulative release rate was the ordinate to draw the release curve, and analyze the results.

3. Results and Discussion

3.1. SEM Analysis

The surface morphologies of the various coatings were characterized by SEM, as shown in Figure 1. The surface of the UMAO coating had a porous honeycomb structure typical of the micro-arc oxidation process [33,34], as shown in Figure 1a. The porous structure of the coating surface became a channel for body fluids to etch the substrate, which corroded the pure Mg substrate. The surface of the UMAO/PLGA/BR coatings was covered by PLGA/BR coating (Figure 1b–d). When the BR content was 1.5 g/L, the morphology of the micro-arc oxidation began to be obscured. When the content of BR was

3.0 g/L and 6.0 g/L, the surface morphology of the coating changed significantly. Most of the micro-arc oxidation morphology was filled by PLGA/BR, so the pore size and number were reduced, with better compactness. As the amount of the drug increased, the morphology of the micro-arc oxidation was more completely covered. As PLGA was acidic after degradation, the coating had some holes, and the degraded magnesium could be neutralized with PLGA degradation that was produced to avoid a local pH that was too low or too high [35].

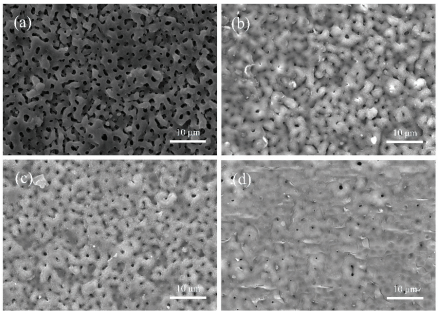

Figure 1. Scanning electron microscopy (SEM) cross-sectional morphologies of various coatings: (**a**) ultrasonic micro-arc oxidation (UMAO); (**b**) UMAO/polylactic acid and glycolic acid copolymer (PLGA)/berberine (BR)1.5; (**c**) UMAO/PLGA/BR3.0; (**d**) UMAO/PLGA/BR6.0.

The cross-sectional morphologies of the coatings with different amounts of BR were characterized by SEM, as shown in Figure 2. Obvious through holes were seen in the UMAO coating section, and the coating thickness was 4.8 μm (Figure 2a). UMAO/PLGA/BR coatings had obvious double-layer superimposed structures, and the interface between the UMAO layer and the PLGA/BR layer was very clear. When the concentration of BR was 1.5 g/L, UMAO through holes were reduced, and the coating thickness was 5.4 μm (Figure 2b). At 3.0 g/L of BR, the UMAO through holes were significantly reduced, and the coating thickness was 7.7 μm (Figure 2c). Compared with the research of Peng [18], the coating thickness increases and the coating becomes denser. At 6.0 g/L of BR, the coating was dense and the coating thickness was 6.0 μm (Figure 2d). Comparative analysis of the cross-sectional morphology of the coating showed that, with the increase of the amount of BR, the thickness of the coating first increased and then decreased, but the overall coating thicknesses increased and the corrosion channels were better filled. When the BR drug content reached 3.0 and 6.0 g/L, the cross sections of the coatings were denser, and the bonding effect between the coatings was better.

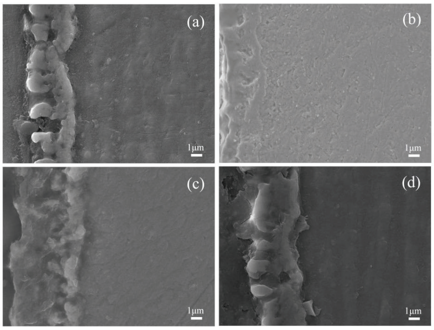

Figure 2. SEM cross-sectional morphologies of various coatings: (**a**) UMAO; (**b**) UMAO/PLGA/BR1.5; (**c**) UMAO/PLGA/BR3.0; (**d**) UMAO/PLGA/BR6.0.

3.2. Phase Analysis of the Coatings

All the samples were investigated from the phase structural point of view. The phase structures of the various coatings were characterized by XRD, as shown in Figure 3. Contrasted with international centre diffraction data (ICDD). The UMAO coating mainly consisted of MgO (ICDD file no. 65-0476) and Mg_2SiO_4 (ICDD file no. 83-1807) phase [36,37]. MgO and Mg_2SiO_4 phase were detected UMAO/PLGA/BR coatings. In addition, owing to the thin film, the Mg phase was detected in various coatings (ICDD file no. 35-0821).

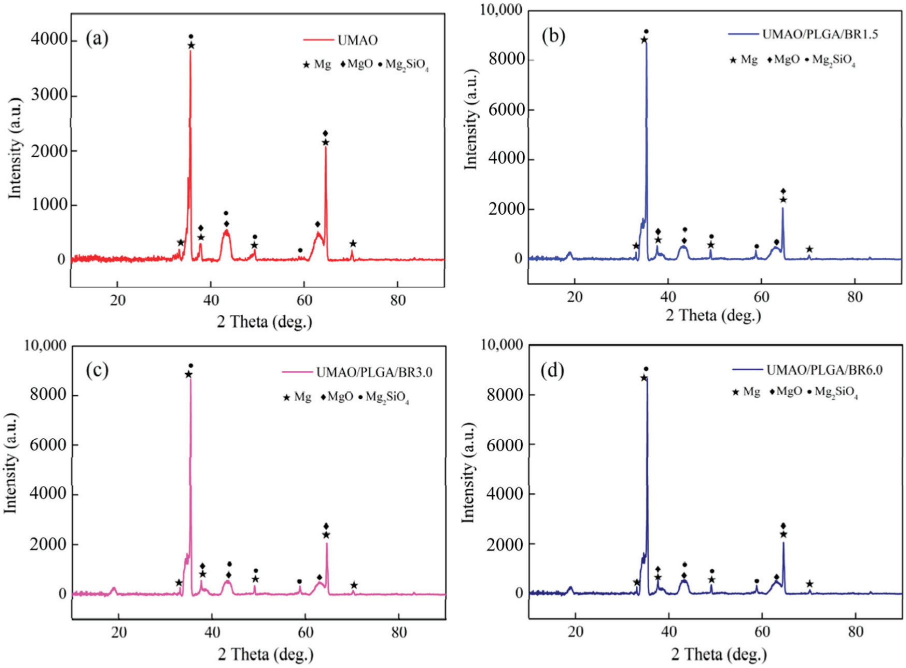

Figure 3. X-ray diffraction (XRD) patterns of coatings with various BR contents: (**a**) UMAO; (**b**) UMAO/PLGA/BR1.5; (**c**) UMAO/PLGA/BR3.0; (**d**) UMAO/PLGA/BR6.0.

3.3. Contact Angle Analysis

The wettability of the various coatings was determined by the static water contact angle, as shown in Figure 4. The five contact angles measured by various coatings are shown in Table 2. The water contact angle on the UMAO coating was 20.63 ± 0.56° (Figure 4a). Because the surface of the UMAO coating had higher porosity, the contact angle of the coating was smaller. The water contact angles of the UMAO/PLGA/BR (1.5 g/L), UMAO/PLGA/BR (3.0 g/L), and UMAO/PLGA/BR (6.0 g/L) coatings were 68.12 ± 0.96°, 69.73 ± 0.83°, and 70.46 ± 0.89°, respectively (Figure 4b–d). After UMAO self-assembled BR treatment, the contact angle of the coating increased significantly, restricting the entry of corrosive media and improving the corrosion resistance of the coating [38]. However, the angle was less than 90°, and the hydrophilic coating did not affect cell adhesion.

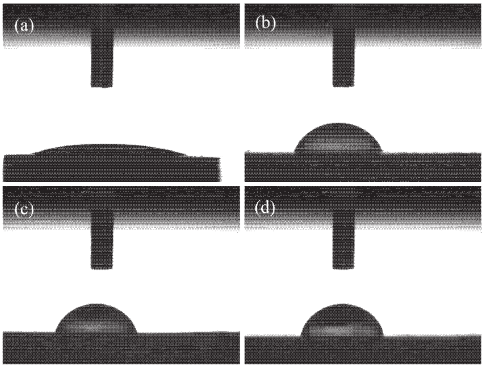

Figure 4. Contact angles of UMAO and coatings with BR on pure magnesium: (**a**) UMAO; (**b**) UMAO/PLGA/BR1.5; (**c**) UMAO/PLGA/BR3.0; (**d**) UMAO/PLGA/BR6.0.

Table 2. Contact angle of various coatings. UMAO, ultrasonic micro-arc oxidation; BR, berberine.

Sample	**UMAO**	**BR (1.5 g/L)**	**BR (3.0 g/L)**	**BR (6.0 g/L)**
contact angle 1	20.13°	67.42°	70.23°	71.35°
contact angle 2	20.07°	69.08°	69.53°	69.64°
contact angle 3	20.93°	68.42°	68.90°	71.12°
contact angle 4	21.19°	67.16°	69.43°	70.62°
contact angle 5	20.83°	68.52°	70.56°	69.57°
average value	20.63 ± 0.56°	68.12 ± 0.96°	69.73 ± 0.83°	70.46 ± 0.89°

3.4. Coating Roughness

The micro-roughness of the coatings was observed by German Bruker atomic force microscopy (AFM). The roughnesses of the coatings with different amounts of BR are shown in Figure 5. The BR changed the micro-roughness of the various coatings. The surface of the UMAO membrane was densely populated with raised cells and hills, the size was obviously increased, and the roughness arithmetic (Ra) value was larger (Figure 5a). The surface roughness of BR (1.5 g/L) showed a downward trend, which effectively eliminated the bumps on the surface of the UMAO and reduced the surface roughness of the coating (Figure 5b). With the increase in BR content, the surface roughness value showed an increasing trend. At 3.0 g/L of BR, the bulges and depressions on the film surface increased, and the roughness of the coating became larger (Figure 5c). The surface roughness at 6.0 g/L of BR became smaller. This was because BR further filled the holes in the coating surface and the coating became flat (Figure 5d). It was seen that the amount of BR added greatly affected the Ra value of the UMAO/PLGA/BR coating. The specific roughness values are shown in Table 3.

Table 3. Roughness values of various coatings.

Sample	**UMAO**	**BR (1.5 g/L)**	**BR (3.0 g/L)**	**BR (6.0 g/L)**
Roughnesses (nm)	246	92.4	190	145

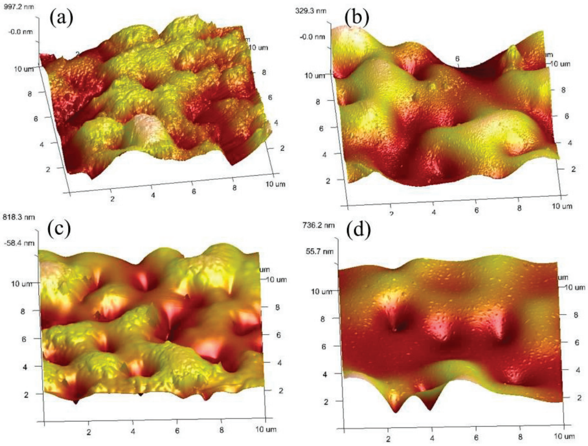

Figure 5. Atomic force microscopy (AFM) images of coatings with various BR contents: (**a**) UMAO; (**b**) UMAO/PLGA/BR1.5; (**c**) UMAO/PLGA/BR3.0; (**d**) UMAO/PLGA/BR6.0.

3.5. XPS Analysis

XPS measurements were carried out to characterize the composition of the coatings, as shown in Figure 6. Figure 6a illustrates the XPS survey spectra of the different coatings. The chemical composition and element state of the composite coatings were determined. The BR (1.5), BR (3.0), and BR (6.0) coatings all produced spectral peaks of Mg, C, O elements, and this result was consistent with the surface morphology of the coating.

Figure 6b–d illustrate the fine fitting spectra of the O, C, and N elements of the BR (3.0) coating. Using the BR (3.0) coating as an example, the peaks of the UMAO/PLGA/BR coating were analyzed. The fine fitting spectrum of the BR (3.0) coating is shown in Figure 6b–d. According to the further peak analysis of O 1*s* (shown in Figure 6b), the distinctive peak at 530.8 eV in its fine spectrum is the binding energy of the oxygen element in the Mg–O bond [39]. Figure 6b illustrates the O 1*s* XPS pattern for the UMAO/PLGA/BR coating, in which the Mg–O bond was present at a binding energy of 530.8 eV and the O element of the –OH was present at a binding energy of 531.4 eV. Figure 6c illustrates the fine spectrum of C 1*s*. There were two characteristic peaks at 286.3 eV and 284.6 eV in the fine spectrum of C 1*s*. The characteristic peak at 286.3 eV was attributed to the binding energy of C elements in –C–O– in PLGA. The characteristic peak at 284.6 eV was attributed to the binding energy of the C element in –C–H and –C–C– in PLGA and the binding energy of the C=C functional group C in BR [40,41]. Figure 6d illustrates the fine spectrum of N 1*s*. The characteristic peaks at 398.6 eV and 399.7 eV were attributed to C–N in BR [42]. It was further seen that, after changing the amount of BR, UMAO/PLGA/BR coating materials were self-assembled on the surface of the pure magnesium substrate.

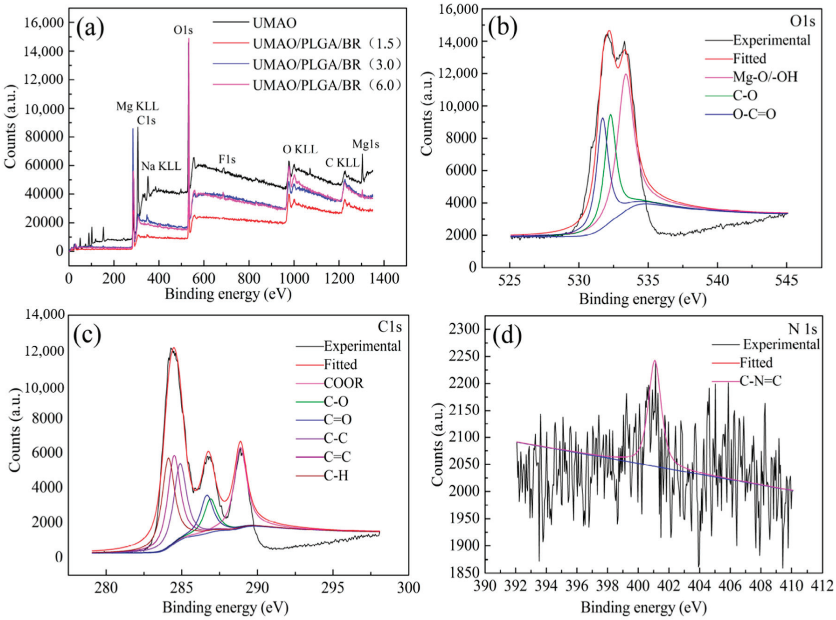

Figure 6. X-ray photoelectron spectroscopy (XPS) spectra of coatings with various BR additions: (**a**) survey spectrum; (**b**) O 1*s* spectra; (**c**) C 1*s* spectra; (**d**) N 1*s* spectra.

3.6. Corrosion Resistance

The polarization curves of the UMAO, 1.5 g/L, 3.0 g/L, and 6.0 g/L samples are shown in Figure 7. Relevant electrochemical values were obtained by fitting. The corrosion current density (Icorr) of the UMAO, UMAO/PLGA/BR (1.5 g/L), UMAO/PLGA/BR (3.0 g/L), and UMAO/PLGA/BR (6.0 g/L) coatings was 2.26×10^{-6}, 3.33×10^{-7}, 3.14×10^{-8}, and 1.26×10^{-7} A/cm^2, respectively. The more positive corrosion voltage (Ecorr), smaller corrosion rate (CR) and Icorr demonstrate that BR (3.0 g/L) improves the corrosion resistance of Mg by forming the modified structure as described previously [43]. The corresponding fitting parameters are shown in Table 4.

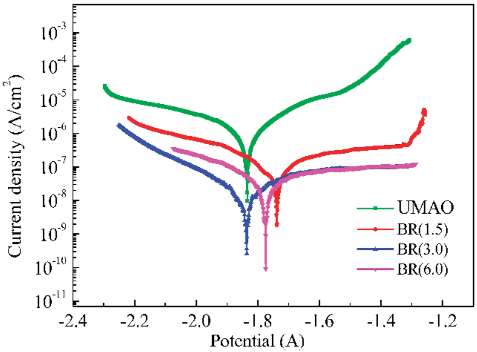

Figure 7. Potentiodynamic polarization curves of various samples.

The Icorr of UMAO/PLGA/BR coatings with different BR content was at least one order of magnitude lower than that of UMAO. For the coating prepared by Zhang [44], the corrosion current of magnesium alloy in simulated body fluid was 2.05 × 10^{-6} A/cm^2. This illustrates that coatings with different amounts of BR protected magnesium substrates more effectively than UMAO coatings. In addition, among the drug-loaded coatings, the UMAO/PLGA/BR (3.0 g/L) coating had the lowest Icorr value. It is well known that the Ecorr can describe the thermodynamic property, so the corrosion resistance cannot be evaluated in terms of Ecorr [45]. It can be concluded that the UMAO/PLGA/BR (3.0 g/L) coating showed a lower corrosion rate and corrosion current density compared with other coatings. It was inferred that the corrosion resistance of the 3.0 g/L coating was the best.

Table 4. Corrosion current densities and corrosion potentials for different coatings in SBF at 37 ± 1 °C. Icorr, corrosion current density; Ecorr, corrosion voltage; CR, corrosion rate.

Sample	UMAO	BR (1.5 g/L)	BR (3.0 g/L)	BR (6.0 g/L)
Ecorr (V)	−1.834 ± 0.007	−1.741 ± 0.006	−1.872 ± 0.007	−1.769 ± 0.006
Icorr (A/cm^2)	(2.26 ± 0.02) × 10^{-6}	(3.33 ± 0.019) × 10^{-7}	(3.14 ± 0.017) × 10^{-8}	(1.26 ± 0.023) × 10^{-7}
CR (mm/yr)	5.16 × 10^{-3}	7.60 × 10^{-4}	7.17 × 10^{-5}	2.88 × 10^{-4}

To further analyze the corrosion behavior of the various coatings, EIS measurements were performed in the SBF, as shown in Figure 8. The EIS measurements were analyzed using ZsimpWin software and fitted to the appropriate equivalent circuit. The symbols represent the experimental data, and the solid lines represent the fitted data. Figure 8a shows the Nyquist plots of the samples. The Nyquist plot of the UMAO coating is composed of a capacitive loop. The capacitive loop at the high frequency is attributed to the resistance and capacitance of the electrolyte penetrating through the UMAO layer [46]. The Nyquist plots of the UMAO/PLGA/BR coatings are composed of widened capacitive loops. The capacitive loop is attributed to the resistance and capacitance of the electrolyte penetrating through the PLGA/BR layer at the medium frequency [47]. The radii of the semicircles corresponding to the UMAO/PLGA/BR coating were visibly larger than those of the UMAO coating. These results reveal that the UMAO/PLGA/BR coating has a higher impedance value and higher corrosion resistance.

Figure 8b shows the impedance modulus |Z| of different coatings, which were 4.20 × 10^4 (UMAO), 5.24 × 10^5 (BR 1.5 g/L), 1.68 × 10^6 (BR 3.0 g/L), and 1.41 × 10^6 (BR 6.0 g/L) Ω·cm^2. The impedance modulus of the drug-loaded coatings was an order of magnitude higher than that of the UMAO coating. However, after the addition of 6.0 g/L BR, the impedance modulus value of the UMAO/PLGA/BR coating did not continue to increase. Because the solution was a suspension when 6.0 g/L of BR was added, it was not conducive to the formation of self-assembled coatings. As we all know, good corrosion resistance between the coating and the electrolyte corresponds to a higher R value [48,49]. The results showed that, when the amount of BR was 3.0 g/L, the coating had higher resistance and better corrosion resistance.

The Bode plots of the coatings with different amounts of BR are shown in Figure 8c. The shapes were similar. Both coatings have two time constants distributed at a low frequency (10^{-1}–10^2 Hz) and a high frequency (10^2–10^4 Hz). The low-frequency time constant is the response of the UMAO coating, and the high-frequency time constant is the response of the PLGA and PLGA/BR layers [46].

The time constant of the high frequency zone was ascribed to the PLGA/BR layer, and the time constant of the low frequency zone was ascribed to the UMAO layer. The phase angles of BR (1.5), BR (3.0), and BR (6.0) coatings were 65°, 68°, and 62°, respectively. When the amount of BR added reached 3.0 g/L, the phase angle of the coating was the largest and the corrosion resistance was the highest. The Nyquist diagram of the composite coating was consistent with the results of the Bode diagram, indicating that the BR (3.0) coating had good corrosion resistance.

The equivalent circuit used to fit the electrochemical impedance plot of the coatings is shown in Figure 8d. The corresponding fitting parameters are shown in Table 5. In the circuit, Rs is the solution resistance, R_1 is the resistance of the UMAO coating, and R_2 is the resistance of the PLGA/BR coating. CPE_1(capacitance of coating) and CPE_2 are constant phase angle components of electric double layer capacitors, which represent the capacitive reactance of the UMAO dense layer coating and the

PLGA/BR drug-loaded layer, respectively. In UMAO, R_2 and CPE_2 represent load transfer resistance and interface electric double layer capacitance, respectively. The impedance of the drug-loaded coating was greater than that of the UMAO coating, indicating that the drug-loaded coating could prevent corrosion more effectively [50].

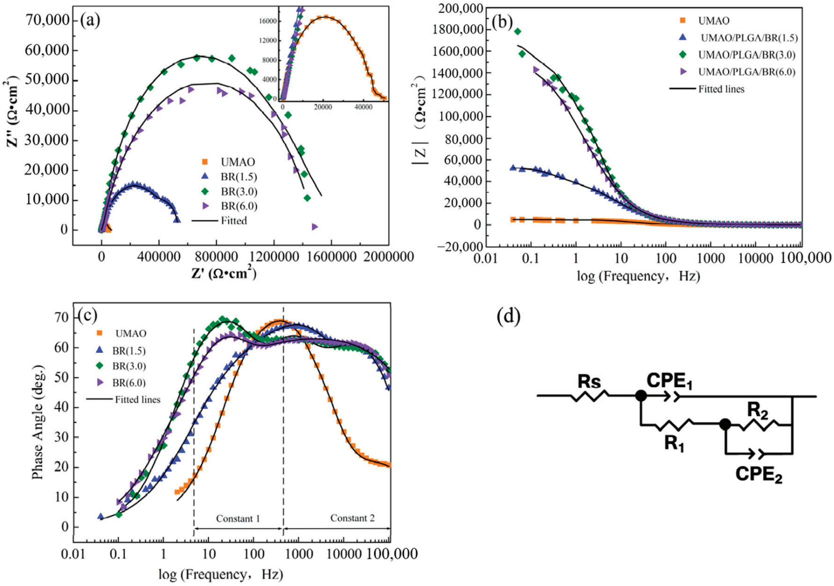

Figure 8. Nyquist, Bode diagrams and equivalent circuits of different coatings: (**a**) Nyquist; (**b**) and (**c**) Bode plots; (**d**) equivalent circuit (CPE, capacitance of coating).

Table 5. Values of the equivalent circuit parameters for the various coatings extracted from the electrochemical impedance spectroscopy (EIS) plots. CPE, capacitance of coating.

Sample	Rs (Ω·cm²)	CPE_1 (F·cm²)	R_1(Ω·cm²)	CPE_2 (F·cm²)	R_2(Ω·cm²)
UMAO	269.2	4.35×10^{-7}	4.37×10^{4}	2.59×10^{-5}	1.18×10^{4}
BR1.5	126.9	1.67×10^{-7}	4.31×10^{5}	4.16×10^{-6}	1.17×10^{5}
BR3.0	152.1	1.09×10^{-7}	7.02×10^{5}	1.06×10^{-8}	1.61×10^{6}
BR6.0	117.9	1.46×10^{-7}	1.95×10^{5}	7.49×10^{-9}	1.29×10^{6}

Therefore, a conclusion can be drawn from the polarization curve and the EIS impedance; that is, the corrosion resistance of the coating was improved by doping BR in the PLGA solution to form a drug-loaded coating. The main reason was that the addition of BR to the PLGA solution was equivalent to a filler, which can fully block the defects, such as pores, of the ceramic layer in the drug-loaded coating and prevent the body fluid from penetrating the Mg matrix too quickly, thereby improving the corrosion resistance.

3.7. Surface Morphology and Phase Composition Analysis in SBF

SEM images of UMAO and UMAO/PLGA/BR (3.0) coatings soaked in SBF solution for 0, 3, 7, and 14 days are shown in Figure 9. Figure 9a_1,b_1 shows the surface morphology of UMAO coating and UMAO/PLGA/BR coating without soaking. Compared with the UMAO coating, after 3 days of soaking, the surface of the coating was gray, and insect-like substances were deposited on the surface of the UMAO film around the pores (Figure 9a_2,b_2). After being immersed for 7 days, cracks appeared on the surface of the coating, and white deposits in the shape of flower clusters were attached to the cracks. This deposit can effectively fill the cracks and form a new composite surface to prevent the corrosive medium from passing through the pores or cracks (Figure 9a$_3$,b$_3$), which was also reported in other studies [51,52]. After 14 days of soaking, the cracks deepened, the number increased, and the white deposits increased. The surface of the coating material became rough, and its surface area increased to provide an interface for ion adsorption (Figure 9a$_4$,b$_4$). Because of the extension in the immersion time, Ca and P elements were enriched and nucleated on the surface, and the mass increased with time. At the same time, Mg ions gradually degraded from the surface and were replaced by Ca ions, which'adsorb more CO_3^{2-} and PO_4^{3-} on the surface of the coating material; when the solubility product of forming bone-like apatite was reached, a new phase was formed on the surface [53,54], so the BR coating had excellent biological activity.

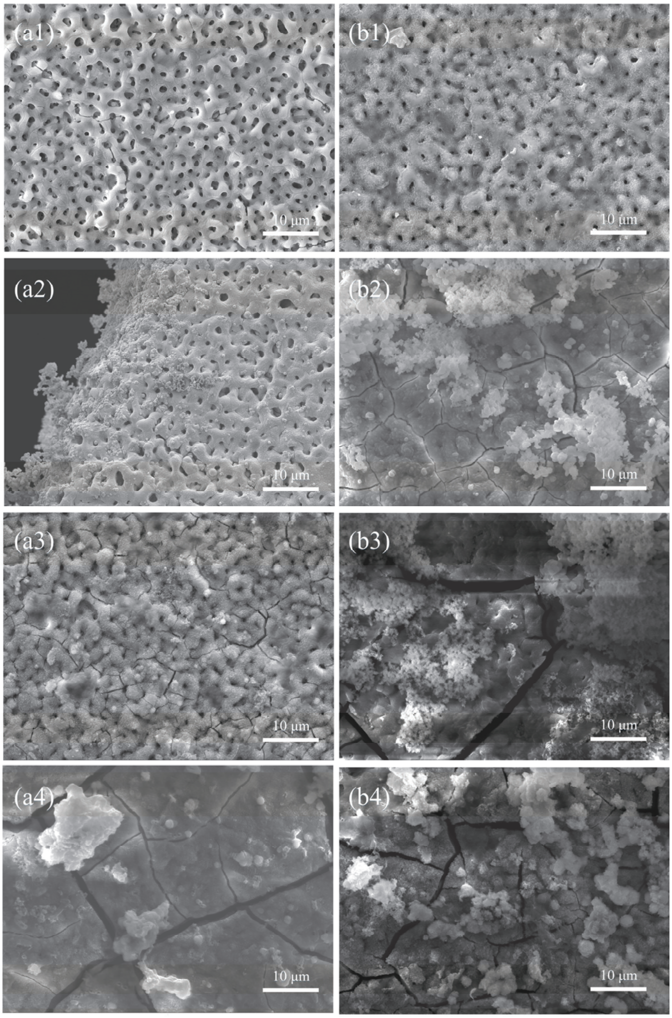

Figure 9. SEM patterns of different coatings after immersion in SBF. 0 days: (**a$_1$**) UMAO; (**b$_1$**) UMAO/PLGA/BR. 3 days: (**a$_2$**) UMAO; (**b$_2$**) UMAO/PLGA/BR. 7 days: (**a$_3$**) UMAO; (**b$_3$**) UMAO/PLGA/BR. 14 days: (**a$_4$**) UMAO; (**b$_4$**) UMAO/PLGA/BR.

3.8. Slow-Release Drug Measurements

The drug-loaded coating on the metal surface gave it functional requirements [55,56]. According to the conditions and methods under Section 2.6, the UMAO/PLGA/BR (3.0) sample was subjected to an in vitro release test. The peak area at 345 nm was measured and used to calculate the cumulative release of BR. The results are shown in Figure 10. The cumulative release of BR from the UMAO/PLGA/BR coating reached 92.13% after soaking in the SBF solution for 28 days. Peng [18] and Wang [19] studied the drugs released for 2–3 days. This prolonged the action time of the drug, increased the concentration of the drug in the local lesion, and avoided the physical and mental harm to the patient caused by long-term oral administration or external topical administration.

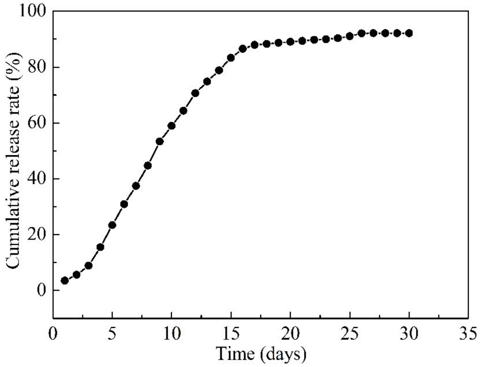

Figure 10. Cumulative release curve of the UMAO/PLGA/BR coating in vitro.

4. Conclusions

The UMAO coating has through-pores and these were sealed by the capillarity of the PLGA/BR coatings to inhibit permeation of body fluid. The corrosion resistance of the UMAO coating was significantly improved by the coverage of PLGA/BR coatings with higher impedance and lower current density. This is because the PLGA/BR coating with high cross-link density and networks has a better capacity to inhibit the permeation of ions. In addition, after the BR-loaded coating was immersed in SBF for 14 days, a large amount of substance adhered to the surface, and the prepared composite coating had excellent in vitro biological activity. After 28 days, the cumulative amount of released BR was 98.12%. Thus, the inclusion of PLGA/BR on the UMAO coatings induces an antimicrobial effect.

Author Contributions: Data analysis, L.M. and Z.M.; manuscript writing, L.M. and S.Y.; literature search, chart making, Z.M. and S.Y.; research design, J.W. and Z.M.; data collection, J.W. and L.M.; writing—original draft preparation, L.M. and S.Y.; software, L.M. and Z.M.; revise the manuscript and finalize the version to be published, L.M. and M.L. All authors have read and agreed to the published version of the manuscript.

Funding: The research was financially supported by the National Natural Science Foundation of China (No. 31370979). Fundamental Research Funds from the Provincial Education Department Fundamental Research Project, China (2019-KYYWF-1370). Jiamusi University PhD Special Scientific Research Fund Launch Project (JMSUBZ2019-10).

Conflicts of Interest: The authors declare no conflict of interest.

References

1. Raphel, J.; Holodniy, M.; Goodman, S.B.; Heilshorn, S.C. Multifunctional coatings to simultaneously promote osseointegration and prevent infection of orthopaedic implants. *Biomaterials* **2016**, *84*, 301–314. [CrossRef] [PubMed]
2. Goodman, S.B.; Yao, Z.; Keeney, M.; Yang, F. The future of biologic coatings for orthopaedic implants. *Biomaterials* **2013**, *34*, 3174–3183. [CrossRef] [PubMed]

3. Surmenev, R.A.; Surmeneva, M.A.; Ivanova, A.A. Significance of calcium phosphate coatings for the enhancement of new bone osteogenesis-A review. *Acta Biomater* **2014**, *10*, 557–579. [CrossRef] [PubMed]
4. Chen, Y.; Xu, Z.; Smith, C.; Sankar, J. Recent advances on the development of magnesium alloys for biodegradable implants. *Acta Biomater.* **2014**, *10*, 4561–4573. [CrossRef] [PubMed]
5. Li, H.; Pang, S.; Liu, Y.; Sun, L.; Liaw, P.K.; Zhang, T. Biodegradable Mg-Zn-Ca-Sr bulk metallic glasses with enhanced corrosion performance for biomedical application. *Mater. Des.* **2015**, *67*, 9–19. [CrossRef]
6. Sezer, N.; Evis, Z.; Kayhan, S.M.; Tahmasebifar, A.; Koç, M. Review of magnesium-based biomaterials and their applications. *J. Magnes. Alloy.* **2018**, *6*, 23–43. [CrossRef]
7. Bakhsheshi-Rad, H.R.; Hamzah, E.; Ismail, A.F.; Aziz, M.; Daroonparvar, M.; Saebnoori, E.; Chami, A. In vitro degradation behavior, antibacterial activity and cyto-toxicity of TiO_2-MAO/ZnHA composite coating on Mg alloy for orthopedic implants. *Surf. Coat. Technol.* **2018**, *334*, 450–460. [CrossRef]
8. Razavi, M.; Fathi, M.; Savabi, O.; Vashaee, D.; Tayebi, L. Regenerative influence of nanostructured bredigite ($Ca_7MgSi_4O_{16}$)/anodic spark coating on biodegradable AZ91 magnesium alloy implants for bone healing. *Mater. Lett.* **2015**, *155*, 97–111. [CrossRef]
9. Fierascu, I.; Fierascu, I.C.; Dinu-Pirvu, C.E.; Fierascu, R.C.; Anuta, V.; Velescu, B.S.; Jinga, M.; Jinga, V. A Short overview of recent developments on antimicrobial coatings based on phytosynthesized metal nanoparticles. *Coatings* **2019**, *9*, 787. [CrossRef]
10. Sun, J.; Zhu, Y.; Meng, L.; Chen, P.; Shi, T.; Liu, X.; Zheng, Y. Electrophoretic deposition of colloidal particles on Mg with cytocompatibility, antibacterial performance, and corrosion resistance. *Acta Biomater.* **2016**, *45*, 387–398. [CrossRef]
11. Wang, L.; Zhou, J.; Liang, J.; Chen, J. Thermal control coatings on magnesium alloys prepared by plasma electrolytic oxidation. *Appl. Surf. Sci.* **2013**, *280*, 151–155. [CrossRef]
12. Ma, C.X.; Lu, Y.; Sun, P.P.; Yuan, Y.; Jing, X.Y.; Zhang, M.L. Characterization of plasma electrolytic oxidation coatings formed on Mg-Li alloy in an alkaline polyphosphate electrolyte. *Surf. Coat. Technol.* **2011**, *206*, 287–294. [CrossRef]
13. Imwinkelried, T.; Beck, S.; Iizuka, T.; Schaller, B. Effect of a plasma electrolytic coating on the strength retention of in vivo and in vitro degraded magnesium implants. *Acta Biomater.* **2013**, *9*, 8643–8649. [CrossRef] [PubMed]
14. Cui, L.Y.; Liu, H.P.; Zhang, W.L.; Han, Z.Z.; Deng, M.X.; Zeng, R.C.; Li, S.Q.; Wang, Z.L. Corrosion resistance of a super hydrophobic micro-arc oxidation coating on mg-4li-1ca alloy. *J. Mater. Sci. Technol.* **2017**, *33*, 1263–1271. [CrossRef]
15. Zeng, R.; Zhang, F.; Song, L. Corrosion resistance of a super-hydrophobic surface on micro-arc oxidation coated mg-li-ca alloy. *J. Alloy. Compd.* **2017**, *728*, 815–826. [CrossRef]
16. Kong, K.; Hiraishi, N.; Nassar, M. Effect of phytic acidetchant on resin-dentin bonding: Monomer penetration and stability of dentin collagen. *J. Prosthodont Res.* **2016**, *61*, 251–258. [CrossRef]
17. Li, M.Q.; Liu, J.; Li, J.G. The enhanced corrosion resistance of UMAO coatings on Mg by silane treatment. *Mater. Int.* **2014**, *5*, 486–491. [CrossRef]
18. Peng, S.h.; Li, M.Q.; Wang, J.Y. Corrosion behavior and biological activity of micro-arc oxidation coating with puerarin on pure magnesium surface. *Results Phys.* **2019**, *12*, 1481–1489. [CrossRef]
19. Wang, J.Y.; Li, M.Q.; Zhang, D.Q. Corrosion resistance and cell compatibility in vitro of Chinese herbal extract coating on magnesium. *Results Phys.* **2019**, *12*, 1465–1474. [CrossRef]
20. Zhu, M.; Wang, H.; Liu, J. A mesoporous silica nanoparticu-late/β-TCP/BG composite drug delivery system for osteoarticular tuberculosis therap. *Biomaterials* **2011**, *32*, 1986–1995. [CrossRef]
21. Martínez-Vázquez, F.J.; Perera, F.H.; Miranda, P. Improving the compressive strength of bioceramic robocast scaffolds by poly-mer infiltration. *Acta Biomater.* **2010**, *6*, 4361–4368. [CrossRef] [PubMed]
22. Karacan, I.; Ben-Nissan, B.; Wang, H.A.; Juritza, A.; Swain, M.; Mueller, W.; Chu, J.; Stamboulis, A.; Macha, I.; Taraschi, V. Mechanical testing of antimicrobial biocomposite coating on metallic medical implants as drugdelivery system. *Mater. Sci. Eng. C* **2019**, *104*, 749–757. [CrossRef]
23. Colceriu, B.L.; Prejmerean, C.; Prodan, D.; Baldea, I.; Vlassa, M.; Filip, M.; Moldovan, M.; Moldovan, M.-A.; Antoniac, A.; Prejmerean, V.; et al. New pre-reacted glass containing dental composites (giomers) with improved fluoride release and biocompatibility. *Materials* **2019**, *12*, 4021. [CrossRef]

24. Borcherding, K.; Marx, D.; Gätjen, L.; Bormann, N.; Wildemann, B.; Specht, U.; Salz, D.; Thiel, K.; Grunwald, I. Burst release of antibiotics combined with long-term release of silver targeting implant-associated infections: Design, characterization and in vitro evaluation of novel implant hybrid surface. *Materials* **2019**, *12*, 3838. [CrossRef]
25. Trujillo-Nolasco, R.M.; Morales-Avila, E.; Ocampo-García, B.E.; Ferro-Flores, G.; Gibbens-Bandala, B.V.; Escudero-Castellanos, A.; Isaac-Olive, K. Preparation and in vitro evaluation of radiolabeled HA-PLGA nanoparticles as novel MTX delivery system for local treatment of rheumatoid arthritis. *Mater. Sci. Eng. C* **2019**, *103*, 109766. [CrossRef]
26. Sevostyanov, M.A.; Baikin, A.S.; Sergienko, K.V. Biodegradable stent coatings on the basis of PLGA polymers of different molecular mass, sustaining a steady release of the thrombolityc enzyme streptokinase. *React. Funct. Polym.* **2020**, *10*, 1–9. [CrossRef]
27. Qian, J.M.; Xu, W.J.; Yong, X.Q.; Jin, X.X.; Zhang, W. Fabrication and in vitro biocompatibility of biomorphic PLGA/nHA composite scaffolds for bone tissue engineering. *Mater. Sci. Eng. C* **2014**, *36*, 95–101. [CrossRef] [PubMed]
28. Wu, H.; Li, N.; Cheng, Y. In vitro Study on Biodegradable AZ31 Magnesium Alloy Fibers Reinforced PLGA Composite. *J. Mater. Sci. Technol.* **2013**, *6*, 545–550. [CrossRef]
29. Pang, W.Y.; Wang, X.L.; Mok, S.K.; Lai, W.P.; Chow, H.K.; Leung, P.C.; Yao, X.S.; Wong, W.S. Naringin improves bone properties in ovariectomized mice and exerts oestrogenlike activities in rat osteoblast-like (UMR106) cells. *Br. J. Pharmacol.* **2010**, *159*, 1693–1703. [CrossRef]
30. Wu, J.-B.; Fong, Y.-C.; Tsai, H.-Y.; Chen, Y.-F.; Tsuzuki, M.; Tang, C. Naringin-induced bone morphogenetic protein-2 expression via PI3K, Akt, c-Fos/c-Jun and AP-1 pathway in osteoblasts. *Eur. J. Pharmacol.* **2008**, *588*, 333–341. [CrossRef]
31. Afewerki, S.; Bassous, N.; Harb, S.; Palo-Nieto, C.; Ruiz-Esparza, G.U.; Marciano, F.R.; Webster, T.J.; Furtado, A.S.A.; Lobo, A.O. Advances in dual functional antimicrobial and osteoinductive biomaterials for orthopaedic applications. *Nanomed. Nanotechnol. Biol. Med.* **2020**, *24*, 102–113. [CrossRef] [PubMed]
32. Waterman, J.; Pietak, A.; Birbilis, N.; Woodfield, T.; Dias, G.; Staiger, M.P. Corrosion resistance of biomimetic calcium phosphate coatings on magnesium due to varying pretreatment time. *Mater. Sci. Eng. B* **2011**, *20*, 1756–1760. [CrossRef]
33. Cui, L.Y.; Gao, S.D.; Li, P.P.; Zeng, R.C.; Zhang, F.; Li, S.Q. Corrosion resistance of a self-healing micro-arc oxidation/poly methyltrimeth oxysilane composite coating on magnesium alloy az31. *Corros. Sci.* **2017**, *118*, 84–95. [CrossRef]
34. Wang, Y.M.; Guo, J.W.; Wu, Y.F. Biocorrosion resistance of coated magnesium alloy by microarc oxidation in electrolyte containing zirconium and calcium salts. *Front. Mater. Sci.* **2014**, *20*, 256–366. [CrossRef]
35. Li, J.N.; Cao, P.; Zhang, X.N.; Zhang, S.X.; He, Y.H. In vitro degradation and cell attachment of a PLGA coated biodegradable Mg–6Zn based alloy. *J. Mater. Sci.* **2010**, *45*, 6038–6045. [CrossRef]
36. Batra, U.; Kapoor, S.; Sharma, S. Influence of Magnesium Ion Substitution on Structura land Thermal Behavior of Nanodimensional Hydroxyapatite. *J. Mater. Eng. Perform.* **2013**, *22*, 1798–1806. [CrossRef]
37. Diana, M.V.; Ionut, C.I.; Elena, U. Magnesium Doped Hydroxyapatite-Based Coatings Obtained by Pulsed Galvanostatic Electrochemical Deposition with Adjustable Electrochemical Behavior. *Coatings* **2020**, *10*, 2–17.
38. Zhang, F.; Zhang, C.; Song, L.; Zeng, R.-C.; Li, S.; Cui, H. Fabrication of the Superhydrophobic Surface on Magnesium Alloy and Its Corrosion Resistance. *J. Mater. Sci. Technol.* **2015**, *31*, 1139–1143. [CrossRef]
39. Taheri, M.; Kish, J.; Birbilis, N.; Danaie, M.; McNally, E.; McDermid, J. Towards a Physical Description for the Origin of Enhanced Catalytic Activity of Corroding Magnesium Surfaces. *Electrochim. Acta* **2014**, *116*, 396–403. [CrossRef]
40. Mousa, H.M.; Lee, D.H.; Kim, C.S.; Kim, C.S. A novel simple strategy for in situ deposition of apatite layer on AZ31B magnesium alloy for bone tissue regeneration. *Appl. Surf. Sci.* **2015**, *351*, 55–65. [CrossRef]
41. Vaz, J.M.; Taketa, T.B.; Hernã¡ndez-Montelongo, J.; Chevallier, P.; Cotta, M.A.; Mantovani, D.; Beppu, M.M. Antibacterial properties of chitosan-based coatings are affected by spacer-length and molecular weight. *Appl. Surf. Sci.* **2018**, *445*, 478–487. [CrossRef]
42. Pozzo, L.D.Y.; Conceição, T.; Spinelli, A.; Scharnagl, N.; Pires, A.T. Chitosan coatings crosslinked with genipin for corrosion protection of AZ31 magnesium alloy sheets. *Carbohydr. Polym.* **2018**, *181*, 71–77. [CrossRef] [PubMed]

43. Toorani, M.; Aliofkhazraei, M. Review of electrochemical properties of hybrid coating systems on Mg withplasma electrolytic oxidation process as pretreatment. *Surf. Interfaces* **2019**, *14*, 262–295. [CrossRef]
44. Zhang, X.P.; Zhao, Z.P.; Wu, F.M.; Wang, Y.L.; Wu, J. Corrosion and wear resistance of AZ91D magnesium alloy with and without microarc oxidation coating in Hank's solution. *J. Mater. Sci.* **2007**, *42*, 8523–8528. [CrossRef]
45. Razavi, M.; Fathi, M.; Savabi, O.; Beni, B.H.; Vashaee, D.; Tayebi, L. Surface microstructure and in vitro analysis of nanostructured akermanite ($Ca_2MgSi_2O_7$) coating on biodegradable magnesium alloy for biomedical applications. *Colloids Surfaces B: Biointerfaces* **2014**, *117*, 432–440. [CrossRef]
46. Chen, J.; Wang, J.; Han, E.; Dong, J.; Ke, W. AC impedance spectroscopy study of the corrosion behavior of an AZ91 magnesium alloy in 0.1M sodium sulfate solution. *Electrochim. Acta* **2007**, *52*, 3299–3309. [CrossRef]
47. Liu, M.; Schmutz, P.; Uggowitzer, P.J.; Song, G.-L.; Atrens, A. The influence of yttrium (Y) on the corrosion of Mg–Y binary alloys. *Corros. Sci.* **2010**, *52*, 3687–3701. [CrossRef]
48. Niu, B.; Shi, P.; Shanshan, E.; Wei, D.; Li, Q.; Chen, Y. Preparation and characterization of HA sol–gel coating on MAO coated AZ31 alloy. *Surf. Coat. Technol.* **2016**, *286*, 42–48. [CrossRef]
49. Zhang, M.; Cai, S.; Zhang, F.; Xu, G.; Wang, F.; Yu, N.; Wu, X. Preparation and corrosion resistance of magnesium phytic acid/hydroxyapatite composite coatings on biodegradable AZ31 magnesium alloy. *J. Mater. Sci. Mater. Electron.* **2017**, *28*, 82. [CrossRef]
50. Jamesh, M.; Kumar, S.; Narayanan, T.S. Electrode position of Hydroxyapatite Coating on Magnesium for Biomedical Applications. *J. Coat. Technol. Res.* **2012**, *9*, 495–502. [CrossRef]
51. Bhattacharjee, A.; Gupta, A.; Verma, M.; Anand, M.P.; Sengupta, P.; Saravanan, M.; Manna, I.; Balani, K. Antibacterial and magnetic response of site-specific cobalt incorporated hydroxyapatite. *Ceram. Int.* **2020**, *46*, 513–522. [CrossRef]
52. Wang, H.; Eliaz, N.; Xiang, Z.; Hsu, H.P.; Spector, M.; Hobbs, L.W. Early bone apposition in vivo on plasma-sprayed and electrochemically deposited hydroxyapatite coatings on titanium alloy. *Biomaterials* **2006**, *27*, 4192–4203. [CrossRef] [PubMed]
53. Cheon, K.H.; Gao, C.; Kang, M.H.; Jung, H.D.; Jang, T.S.; Kim, H.E. A crack-free anti-corrosive coating strategy for magnesium implants under deformation. *Corros. Sci.* **2017**, *11*, 6–24. [CrossRef]
54. Müller, L.; Müller, F.A. Preparation of SBF with different HCO3- content and its influence on the composition of biomimetic apatites. *Acta Biomater.* **2006**, *2*, 181–189. [CrossRef] [PubMed]
55. Maczynska, B.; Secewicz, A.; Smutnicka, D.; Szymczyk, P.; Dudek-Wicher, R.; Junka, A.; Bartoszewicz, M. In vitro efficacy of gentamicin released from collagen sponge in eradication of bacterial biofilm preformed on hydroxyapatite surface. *PLoS ONE* **2019**, *14*, 217–229. [CrossRef]
56. Llorens, E.; Calderon, S.; Del Valle, L.J.; Puiggalí, J. Polybiguanide (PHMB) loaded in PLA scaffolds displaying high hydrophobic, biocompatibility and antibacterial properties. *Mater. Sci. Eng. C* **2015**, *50*, 74–84. [CrossRef]

coatings

Article

Mangrove Inspired Anti-Corrosion Coatings

Miaomiao Cui [1,2], Peng-Yuan Wang [1], Zuankai Wang [2,*] and Bin Wang [1,*]

[1] Shenzhen Institutes of Advanced Technology, Chinese Academy of Sciences, Shenzhen 518055, China; miaomicui2-c@my.cityu.edu.hk (M.C.); py.wang@siat.ac.cn (P.-Y.W.)
[2] Department of Mechanical Engineering, City University of Hong Kong, Hong Kong, China
* Correspondence: zuanwang@cityu.edu.hk (Z.W.); bin.wang@siat.ac.cn (B.W.)

Received: 8 October 2019; Accepted: 28 October 2019; Published: 1 November 2019

Abstract: Marine corrosion accounts for one-third of the total corrosion cost and has been one of the greatest challenges for modern society. Organic coatings are known as the most widely used protective means. An effective control of the transport of corrosive substances is the key to the anti-corrosion performance. In nature, the mangrove survives and thrives in marine tidal zones despite high salinity and humidity. We first showed that the mangrove leaves have salt glands that can secrete excessive ions to control the ion transport in and out. Inspired by this, we proposed a design of bio-inspired, anti-corrosion coating that mimics this functional feature, and fabricated the bipolar, hydrophobic coatings by doping ion-selective resins and constructing surface structures, which restrict the transport of corrosive substances and the electrochemical corrosion at the coating/metal interface. Our results show that the bio-inspired coatings effectively block and control the transport of both the Na^+ and Cl^-, and, together with the hydrophobic surface, the coating system exhibits significantly improved anti-corrosion properties, more than a three orders of magnitude decrease in corrosion current density when compared with the control group (epoxy varnish). Therefore, the mangrove-inspired coatings show a promising protective strategy for the ever-demanding corrosion issues plaguing modern industries.

Keywords: bio-inspiration; anti-corrosion coating; salt gland; mangrove

1. Introduction

Corrosion, often metal corrosion, is the material destruction that leads to failure in function. It has been a major problem plaguing mankind dating back to ancient times. The first written description of corrosion appeared in the works of Plato (427–347 B.C.) [1] and the first patent of a protective paint appeared in 1625 [2]. Since a large number of metallic materials are developed and utilized in various fields such as marine oil and gas exploitation and transportation industries, the accompanying problem of corrosion becomes greater, which brings enormous economic loss and poses great threats to personal safety and the natural environment. According to the National Association of Corrosion Engineers International study 2016, the direct global corrosion cost was estimated to be \$2.5 trillion, which is equivalent to roughly 3.4% of the global Gross Domestic Product [3]. This study also reported that implementing corrosion control/prevention practices could result in savings of 15%–35% of the cost of damage. Among a variety of anti-corrosion techniques including the passive coatings and active methods [4], organic anti-corrosion coatings, which isolate and protect the substrate metal kinetically, are the most cost-effective and environmentally-friendly approach for the ever-pressing corrosion issue [5].

The fundamental principles of corrosion reveal that material corrosion is thermodynamically spontaneous and kinetically mediated by corrosive substances such as H_2O, Na^+, and Cl^-. These substances invade and transport through the coating to the coating/substrate interface, which leads to an accelerated corrosion reaction [6] that consists of chemical corrosion and electrochemical corrosion.

Coatings **2019**, *9*, 725; doi:10.3390/coatings9110725

Moreover, the electrochemical corrosion processes at a high rate and it is a complex process that includes anodic and cathodic reactions. The anodic reaction transfers metal atoms into metal cations. This process can be accelerated by Cl^-, especially the pitting corrosion process [7,8]. On the other hand, the cathodic reaction generates OH^- followed by the aggregation of Na^+, and this process could accelerate the accumulation of corrosion products, which leads to peeling-off of the coating [9,10]. These reactions, supplied by the penetrated corrosive substances, not only consume the metal substrate but also lead to the failure of the protective coatings. Therefore, the key to high-performance anti-corrosion coatings requires effective blocking of corrosive substances at the external surface and control of ion transportation within the coating [11–13].

Among the rapid research progress in protective coatings, learning from nature to design novel anti-corrosion materials is one of the best ways for creating these materials. Over the course of evolution, nature develops ingenious strategies that can be implemented to address the issues of surface blocking and ion control in anti-corrosion coatings. One representative dealing with the blocking is the superhydrophobic coating bio-inspired from self-cleaning lotus leaves, which protects metals from corrosion and has been studied extensively. The mechanism involves an isolative air layer formed between the external corrosive solution and the substrate, usually fulfilled by the hierarchical structure and the chemical constituents of the coating. Once the corrosive medium penetrates into the coating as time goes by, controlling the transportation of corrosive ions becomes significant to delay and, thus, prevent a corrosive reaction. Research efforts in controlling the transmission of corrosive agents can be passive, e.g., by adding fillers, such as zinc particles [14]. The mechanism involves the blocking and prolonging of the path of corrosive agents, and the preferred corrosion of zinc rather than steel due to a higher electrochemical activity. The other is an active approach that includes combining with conductive/reactive components to identify and interact with the ions selectively. A variety of ion-selective organic coatings doped with different ion exchange resins, first studied by Wang et al. [15–17], show effective control of the moving direction of ions such as Cl^- and Na^+. The ion-selective coating that interacts with one type of ions is called single polar coating. An anionic coating (cation-selective film) blocks the invasion of anions (e.g., Cl^-) and allows the passage of cations (e.g., Na^+), while a cationic coating blocks the transmission of cations. A bipolar coating composed of cationic and anionic layers, which can restrict both types of ions, shows promising application in metal protection. Besides, conductive polymers, such as polyaniline (PANI) and modified PANI [18], have also been used for ion selective anti-corrosion coatings [8]. However, the ion selective coatings can only adjust the transport of ions and cannot deal with the water infiltration, which deteriorate the protective function of the coatings greatly. Therefore, preventing the invasion of H_2O into the coating layer is another important consideration of developing advanced anti-corrosion coatings.

Effective control of ion-containing fluids can also be observed in nature, e.g., the mangrove plants which survive and thrive in the marine intertidal environments featuring high humidity and high salinity through salt secretion [19]. The harsh habitat is close to the anti-corrosion coatings that protect the substrate metals in marine surroundings [20], and the strategies utilized by the mangrove through salt glands are vivid inspirations for developing ion-control coatings, formulated first in this work. In an aim to develop high-performance anti-corrosion coatings addressing the control of ion transport and external blocking, we explore the salt secretion of the mangrove, and, for the first time, fabricate mangrove-inspired anti-corrosion coatings employing ion-selective resins and hydrophobic surface construction. The structural and functional features of the salt glands on the mangrove (*Ceriops tagal (perr.) C. B. Rob*) are presented, and the bio-inspired, bipolar hydrophobic coatings were fabricated to exclude external H_2O and corrosive ions (Cl^- and Na^+). Our results show that the bio-inspired anti-corrosion coatings exhibit excellent properties in restraining the corrosive ion intrusion and transport within the coating, which leads to significantly improved anti-corrosion performance.

2. Materials and Methods

2.1. Observation of the Mangrove Leaves

The optical images of living mangrove were taken by a digital camera. Mature mangrove (*Ceriops tagal (perr.) C. B. Rob)* leaves and some branches of the mangrove were collected from Shenzhen Bay. The mangrove branches were cultured in nutrition solutions that were diluted by 100 mL tap water and 100 mL 3.5 wt % NaCl solution, respectively, for eight days.

For scanning electron microscopy, mangrove leaf samples were sputter-coated using a Leica EM ACE200 Automatic low vacuum coating apparatus (platinum, 30 s) (Leica, Wetzlar, Germany), and then observed by a ZEISS SUPRA55 Field emission sweep electron microscope (Carl Zeiss, Jena, Germany). The elemental mappings through energy-dispersive X-ray spectroscopy (EDS) of the samples were scanned by an Oxford X-Max 20 Electrically cooled X-ray spectrometer (Oxford, England).

2.2. Fabrication of the Mangrove-Inspired Coatings

Epoxy varnish (E-44 bisphenol A epoxy resin) was used as the film forming material. Single-polar coatings (two types) were obtained by doping different ion-selective resins, the 719 (202) strong base styrene anion exchange resin, and the 732 strong acid styrene cation exchange resin, respectively, into the epoxy varnish as paints. The ion exchange resins and epoxy varnish were diluted by xylene, and the doping concentrations were 0, 2.5 wt %, 5 wt %, 10 wt %, and 20 wt % for both groups. After the paints were evenly distributed in the epoxy varnish, TY-650 polyamide was mixed to cure the epoxy varnish. Then they were brush-coated on silica gel plate and also metal substrates (Q235) to obtain the single-polar coatings and the coated metal samples, respectively.

Q235 steel with the size of 10 mm × 10 mm × 5 mm was the metal substrate and the main elements are (wt %), C 0.127, Si 0.15, Mn 0.41, P 0.018, S 0.019, Fe balance. All metal substrates were polished with water on graded sandpapers (150#, 400#, 600#, 800#, and 1000#) step-by-step and were linked with copper wire by soldering. Metal samples were sealed by epoxy resin with a working surface of 10 mm × 10 mm exposed. Sealed samples were polished with water phase sandpapers (150#, 400#, 600#, 800#, and 1000#,) step-by-step, washed by anhydrous ethanol, dried, and kept in a dryer until utilization.

For the bipolar, hydrophobic coatings, a hydrophobic surface layer was fabricated using a template method. A superhydrophobic silicon plate was fabricated following the method in previous work [21,22]. The silicon nanowires and grooves were fabricated based on a 425-mm thick silicon wafer. A standard Micro-Electro-Mechanical System process technology was employed to fabricate rough structures on a silicon surface, which consists of two essential structural features, silicon micropillars, and silicon grooves. A photolithography process was first used to selectively cover a photoresist on a silicon wafer, which was followed by reactive ion etching (RIE) to etch the wafer areas that are not protected by the photoresist, and deep RIE was used to further etch the silicon substrate. This process formed silicon micropillars. The deep RIE process included cyclic passivation and etching modes in which C4F8 and SF6 were used. In the etching cycle, the SF6 flow rate was 130 sc·cm and platen power was set at 12 W. In the passivation cycle, the C4F8 flow rate was 85 sc·cm. Lastly, the photoresist was removed and deep RIE was used to further etch the silicon substrate covered by photoresist, which formed a silicon groove. Then, the surface fabrication process was completed. The prepared silicon wafer was taken as an original template, and PDMS was applied to copy the structure on the coating surface. The thicknesses of all fabricated coatings were measured by a micrometer. The thicknesses of bare metal substrates were monitored at three different points, and the average of all the measurements was taken as the thickness of metals (TM). The total thickness of coatings and metal substrate (TT) were measured by the same processes. Then the thickness of the coating is the difference of the TT and the TM. For the first type of single polar coatings, the coating thicknesses of the fabricated coatings and control groups were kept the same (45 ± 5 µm). For the second type of bipolar coatings, the total coating thicknesses of the fabricated bipolar coatings and control groups were kept the same (90 ± 5 µm), since those were fabricated layer-by-layer.

2.3. Electrochemical Measurements

Electrochemical tests including open circuit potential (OCP), electrochemical impedance spectroscopy (EIS), and polarization curves were performed on CHI760E. The electrochemical experiments were carried out in 3.5 wt % NaCl aqueous solution and a three-electrode configuration was applied, including the as-prepared samples (Q235 steel coated with the epoxy varnish, the bioinspired single-polar coatings, and the bioinspired bipolar, hydrophobic coatings), platinum plate, and saturated calomel electrode (SCE) as working, counter, and reference electrodes, respectively. If there is no other specific indication, all potentials reported in this paper are taking SCE as the reference. EIS tests were performed in a frequency range of 10^5 through 0.01 Hz at the open circuit potential with an amplitude of 10 mV. Potentiodynamic polarization curves were obtained by setting the sweeping range of ±300 mV versus the rest potential value, and a rate of 1 mV/s was employed for scanning. The measured results were further analyzed by using software Cview.

2.4. Wettability and Ion-Resistant Property

The surface wettability was measured using a contact angle meter (DSA-100, KRüSS Instruments, Hamburg, Germany) recording the contacting scenario of a water droplet to the surface. For the ion-selectivity analysis, the fabricated single-polar coatings were fixed in a custom-designed equipment, as shown in Figure 5a, between the 3.5 wt % NaCl solution (30 mL) on the left side and the ultrapure water (100 mL) on the right side. With increasing time at fixed intervals, 100 μL solution on the left side was taken out and the concentrations of Cl^- and Na^+ were measured by ion chromatography (ICS-900, DIONEX, Sunnyvale, CA, USA) and inductively coupled the plasma mass spectrometer (iCAP Q, Thermo Scientific, Bremen, Germany).

3. Results and Discussion

3.1. Salt Particles Deposited on Mangrove Leaves and Salt Gland

Mangrove plants live along the marine coast sustaining the high salinity of seawater (living mangrove forest shown in Figure 1a). On the mangrove leaves, there are plenty of deposited particles (Figure 1b). To analyze the elements of the deposited particles, EDS was used and the results show that the main elements are Cl and Na with an atom ratio of approximately 1 (Figure 1c–e). Thus, the deposited particles are mainly NaCl particles. As reported in references [23–26], salt glands on the mangrove leaves can secrete salt solution to adapt to the harsh environment. However, the salt contained in the marine atmosphere can also be deposited on leaves. To further explore the source of the salt particles, we washed the fresh leaves (growing on branches) with distilled water to remove the deposited particles and cultured the collected branches in nutrition solutions diluted by tap water (NTW) and 3.5 wt % NaCl (NSW), respectively. After eight days, the cultured leaves were collected. The optical images of mangrove leaves cultured in NTW and NSW are shown in Figure 2a,b respectively. There are plenty of particles on leaves cultured in NSW, while no clear deposited particles on leaves cultured in NTW were observed. The same results can be seen in SEM images, as shown in Figure 2c,d with more particles observed in the sites of salt glands. EDS was applied and the results (Figure 2e,f) show that the deposited particles are NaCl. Thus, we conclude that, even though there may be two sources for the deposited salt particles on the fresh mangrove leaves, the salt glands of the mangrove leaves within the salted environment perform salt secretion well, which results in salt particles deposited on the leaf surfaces.

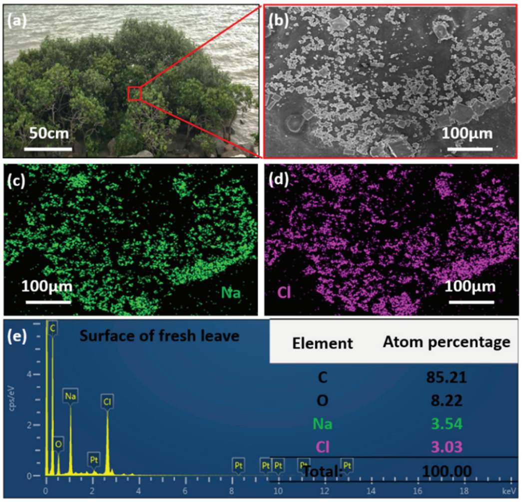

Figure 1. The mangrove and the deposited salt on the surface of fresh mangrove leaves. (**a**) The natural mangrove plants along the Shenzhen Bay. (**b**) SEM of the deposited salt on mangrove leaves, (**c**), (**d**) and (**e**) EDS of the deposited salt particles.

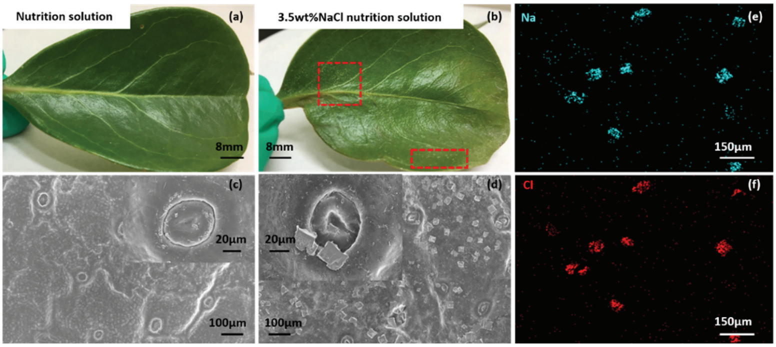

Figure 2. The deposited salt on the surface of cultured mangrove leaves. (**a**) and (**b**) are mangrove leaves cultured by nutrition solution and 3.5 wt. % NaCl nutrition solution, respectively. (**c**) and (**d**) are SEM images of mangrove leaves deposited with salt particles and the inserted images are the salt glands of mangrove leaves. (**e**) and (**f**) are EDS of the deposited salt particles.

Salt glands on mangrove leaves are multi-cellular tissues typically including cell types differentiated into basal collecting cells and distal secretory cells. The collecting cells are presumed to create a salt efflux gradient to collect salt from neighboring mesophyll cells and transport it to the secretory cells. The secretory cells are completely surrounded by a cuticle, with the exception of where they contact the subtending basal collecting cells, which is a feature that appears to channel the flow of salt through the secretory cells and prevent leakage back into the neighboring tissue via the apoplast [27]. We observe salt glands on both the top and lower surfaces of the mangrove leaves, as shown in Figure 3a,b. The magnified image (Figure 3d) of the salt gland shows that it is different from the stoma (breathing tissue). Based on the results we observed, we made a schematic illustration of salt gland distribution on the mangrove leaves. Salt glands function as a safety guard to control the ion transport into and out of the leaf to maintain healthy. From the perspective of bio-inspiration, this function is also necessary for an effective anti-corrosion coating, as well as needed to control the transport of corrosive ions and water within the coating system. For this aim, we design and fabricate mangrove-inspired protective coatings that inhibit and control the transport of corrosive ions.

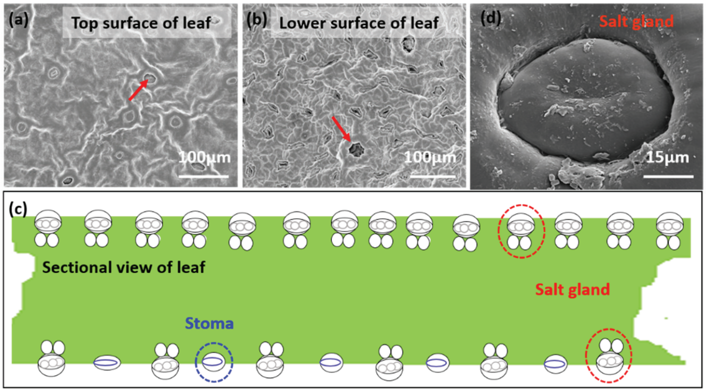

Figure 3. Salt glands distributed on the top and lower surfaces of mangrove leaves. (**a**) and (**b**) are morphologies of mangrove leaves on both surfaces. (**c**) Schematic illustration of the distribution of the salt glands on mangrove leaves. (**d**) SEM image of the salt gland on mangrove leaves.

3.2. Design and Properties of Mangrove-Inspired, Single-Polar and Bipolar Coatings

As ions diffuse/transport from a high concentration to a low concentration without external energy input/interference, we employed doping pigment materials that react with ions to resist or reduce this tendency. Ion exchangeable pigments have been applied in organic coatings to improve the anti-corrosion performance by preventing the transport of corrosive ions. In this case, we chose two types of commercial ion-exchange resins (719 (202) strong-base styrene anion exchange resin and 732 strong acid styrene cation exchange resin) as pigments to modify the epoxy varnish, which can function as inhibiting corrosive ions.

Anion exchange resin has positive charges that exclude cationic ions. Thus, doping anion exchange resin into epoxy can obtain a coating that blocks cations and we call this coating as cationic coatings, as illustrated in Figure 4a. Similarly, doping cation exchange resin can obtain anionic coatings (Figure 4b). These bio-inspired, single-polar coatings, with different doping concentrations, were tested by performing potentiodynamic polarization curves to find the optimized percentage, as shown in Figure 4c,d and Tables 1 and 2. It is clear that Q235 covered with epoxy varnish has decreased corrosion current density compared with the bare substrate, while the anti-corrosion property was further improved by the single-polar, cationic coatings. The lowest current density of Q235 protected with the cationic coating was 1.0091×10^{-7} A/cm^2, which corresponds to a doping concentration of 10 wt % of anion exchange resin. Similarly, the single-polar, anionic coatings also showed enhanced anti-corrosion properties compared with the epoxy varnish on the Q235 substrate, and the optimal doping amount was 5 wt % of cation exchange resin.

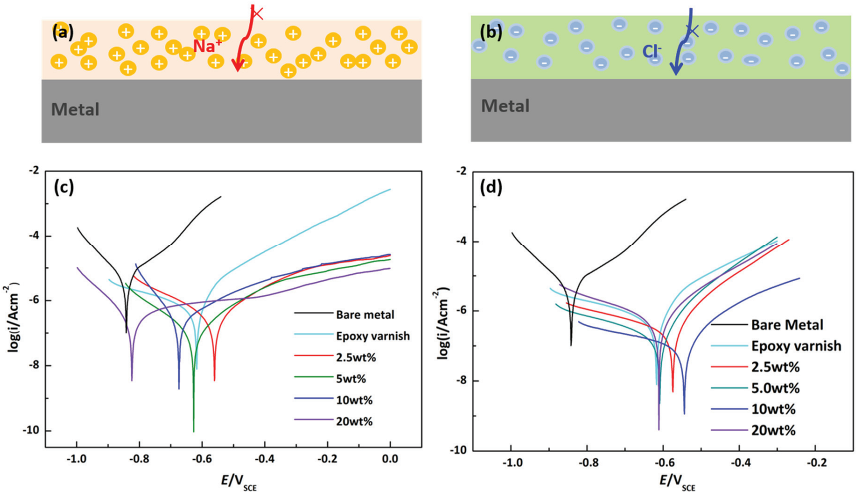

Figure 4. The single-polar, ion-selective coatings and the protective performance. (**a**) and (**b**) are the schematic illustrations of the repulsion function of the cationic coating and anionic coatings. (**c**) and (**d**) are potentiodynamic polarization curves of the cationic and anionic coatings with different doping concentrations of anion and cation exchange resins.

Table 1. Fitting results of Q235 steel coated with cationic coatings with different concentrations of anion exchange resin.

Parameters	Bare Metal	Epoxy Varnish	2.50 wt %	5.00 wt %	10.00 wt %	20.00 wt %
E_{corr}/V	−0.84156	−0.6171	−0.56056	−0.6270	−0.674	−0.82369
I_{corr}/Acm^{-2}	3.1212×10^{-6}	6.1134×10^{-7}	4.2421×10^{-7}	1.2796×10^{-7}	3.0586×10^{-7}	4.6885×10^{-7}
R_p/Ωcm^2	2.6962×10^5	8.9052×10^5	1.3214×10^6	4.9000×10^6	2.2036×10^6	1.7568×10^6

Table 2. Fitting results of Q235 steel coated with anionic coatings with different concentrations of cation exchange resin.

Parameters	Bare Metal	Epoxy Varnish	2.50 wt %	5.00 wt %	10.00 wt %	20.00 wt %
E_{corr}/V	−0.84156	−0.6171	−0.5724	−0.5740	−0.5450	−0.59219
I_{corr}/Acm^{-2}	3.1213×10^{-6}	6.1134×10^{-7}	3.0475×10^{-7}	2.9602×10^{-7}	1.0091×10^{-7}	8.1367×10^{-7}
R_p/Ωcm^2	2.6962×10^5	8.9052×10^5	1.88×10^6	1.89×10^6	1.9357×10^6	1.9203×10^6

The different single-polar coatings (cationic and anionic) exhibit clear superior protective performance than the epoxy varnish coatings (e.g., the much lower corrosion current densities and higher corrosion resistance). This is due to the resisting/blocking ability of the coatings to corrosive ions (Na^+ and Cl^-) resulting from electrostatic repulsion, which is investigated by the ion-selectivity measurements, as shown in Figure 5a. The single-polar, cationic/anionic coatings were placed and fixed between the 3.5 wt % NaCl aqueous solution and the ultrapure water. Measuring the concentration changes of Na^+ and Cl^- of the ultrapure water with increasing time provides information about the ion-selectivity/ion-blocking properties of the single-polar coatings. For cationic coatings (Figure 5b), the concentration of Na^+ is much lower than that of Cl^- throughout the testing time range, which illustrates a good blocking ability of Na^+. This accounts for the lower corrosion current density of the cationic coatings covering Q235 than that of epoxy varnish. The anionic coatings clearly block Cl^-, as the concentration of Cl^- is much lower than Na^+ during the entire time range (Figure 5c), and this explains the improved anti-corrosion properties of Q235 steel coated with anionic coatings.

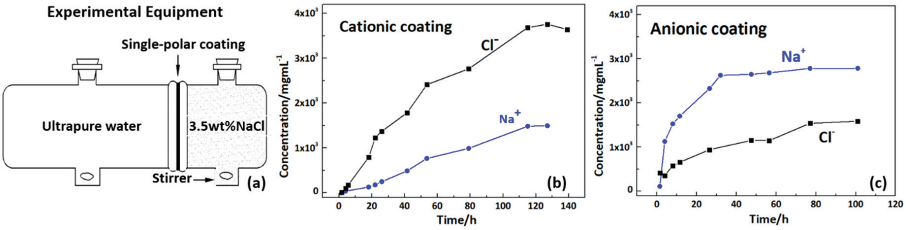

Figure 5. The ion-selectivity of the single-polar coatings. (**a**) Illustration of the custom-designed experimental equipment. (**b**) and (**c**) are the plots of the concentrations of Na^+ and Cl^- in ultrapure water versus increasing time for the cationic and anionic coatings.

Another consideration of the anti-corrosion coatings is the water transmission. The ion-exchange resins could easily absorb water from surroundings, which is not favorable for corrosion inhibition. Our results of the single-polar, cationic, and anionic coatings immersed in 100 mL 3.5 wt % NaCl aqueous solution show significant water uptake (calculated via Equation (1)), which is much higher than the epoxy varnish (Figure 6a). For this, we include an external hydrophobic layer on the single-polar cationic/anionic coating systems in the design. In addition, a high-performance protective coating should control the transport of both the Na^+ and Cl^- ions at the same time. Therefore, we present a design of bipolar, hydrophobic coating system (Figure 6b), which shows our top-down, bio-inspired approach that can block corrosive substances such as water and control transport of corrosive ions within the coating to enhance corrosion protection. The top hydrophobic surface, fabricated by copying the hierarchical structure of microgrooves and micropillars, is shown in Figure 6c, and the contact angle of the water droplet is about 139.1°, which indicates the hydrophobicity.

$$\eta = (w - w_0)/w_0 \qquad (1)$$

w- weight of coating at certain immersion times, w_0- weight of the coating before immersion

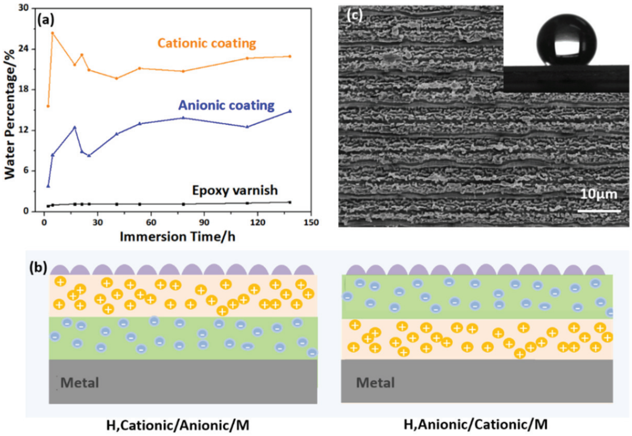

Figure 6. Water absorption property of the coatings, design of bipolar, hydrophobic coatings, and the surface structure of the hydrophobic layer. (**a**) The water uptake with increasing immersing time of the single-polar and epoxy coatings. (**b**) The constructed bipolar, hydrophobic coating systems: hydrophobic, cationic/anionic/metal (H, Cationic/Anionic/M) and hydrophobic, anionic/cationic/metal (H, Anionic/Cationic/M). (**c**) The morphology of the hydrophobic surface with an insert showing the contact angle of a droplet about 139.1°.

3.3. Anti-Corrosion Performance of the Bipolar, Hydrophobic Coating

The representative polarization curves of Q235 with different bipolar, hydrophobic coatings and epoxy varnish after being immersed in 3.5 wt % NaCl solution for 10 days are shown in Figure 7 and the corresponding fitting results are listed in Table 3. For Q235 coated with epoxy varnish, the corrosion current density is 6.1134×10^{-7} A/cm^2 (Table 3). For Q235 protected by bipolar coatings, the corrosion current density decreased significantly, which indicates a significant increase in anti-corrosion performance. The corrosion current density is only 8.3562×10^{-11} A/cm^2 for the hydrophobic,anionic/cationic/metal system, and that for the hydrophobic,cationic/anionic/metal system is 1.6966×10^{-11} A/cm^2, which is more than three orders of magnitude of decrease in the corrosion current density when compared to the epoxy varnish. This demonstrates a substantial enhancement in corrosion protection. The change of polarization resistance is in accordance with the change of the corrosion current density, as shown in Table 3.

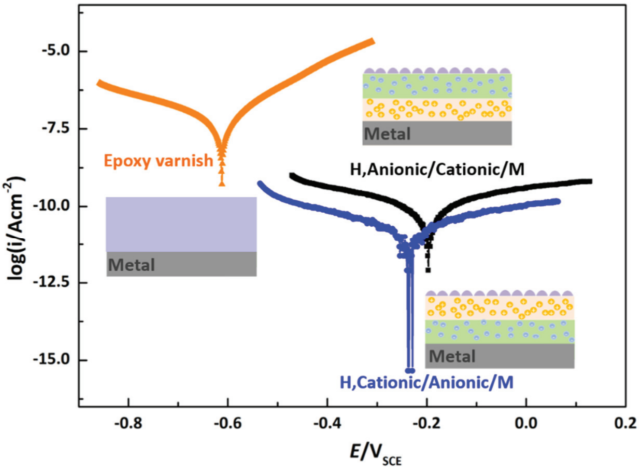

Figure 7. The potentiodynamic polarization curves of different coating systems after being immersed in 3.5 wt. % NaCl aqueous solution for 10 days.

Table 3. Fitting results of Q235 steel coated with the bipolar, hydrophobic coatings and the epoxy varnish after 10 days of immersion.

Parameters	Epoxy Varnish	H, Anionic/Cationic/M	H, Cationic/Anionic/M
E_{corr}/V	−0.6117	−0.1941	−0.2308
I_{corr}/Acm^{-2}	6.1134×10^{-7}	8.3562×10^{-11}	1.6966×10^{-11}
R_p/Ωcm^2	8.9052×10^{5}	2.3228×10^{9}	1.3604×10^{10}

Electrochemical impedance spectroscopy was employed to investigate the protective performance of the bipolar, hydrophobic coatings. The impedance modulus |Z| decreased with the increase of immersion time, which indicates that the coating was gradually broken and, thus, the corrosion protection decreased (Figure 8a,b). The corrosion protection of the hydrophobic, cationic coating/anionic coating/metal (H, Cationic/Anionic/M) system was much better than that of the hydrophobic, anionic coating/cationic coating/metal (H, Anionic/Cationic/M) system. This could be attributed to the different degrees in changes of water absorption after applying the hydrophobic surface. The single-polar cationic coatings absorb much more water than the anionic coatings (Figure 6a), and an external hydrophobic surface could lead to a more significant decrease in water uptake, and, thus, a higher increase in corrosion inhibition and anti-corrosion performance enhancement for the H, Cationic/Anionic/M system. Additionally, the impedance modulus |Z| of the H, Cationic/Anionic/M system still remained a high value after immersion for 10 days (the low frequency range in Figure 8a). For the H, Anionic/Cationic/M system, the impedance modulus |Z| clearly decreased after 1-day immersion, and this decrease was substantial after 10 days, which suggests that the surface was broken. These results indicate that the H, Cationic/Anionic/M system has better anti-corrosion performance than the H, Anionic /Cationic/M system.

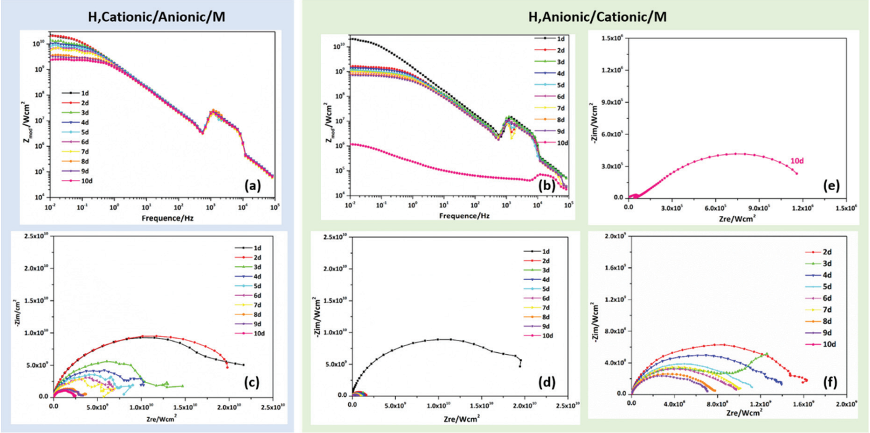

Figure 8. The anti-corrosion capability of the bipolar, hydrophobic coatings during immersion from one to ten days. (**a**) and (**b**) are Bode plots of the H, Cationic/Anionic/M system and H, Anionic/Cationic/M system, respectively. (**c**) is the Nyquist plot of the H, Cationic/Anionic/M system, and (**d**), (**e**), and (**f**) are those of the H, Anionic/Cationic/M system.

The same results can be observed through the Nyquist plots. The results include the impedance change of the different bipolar, hydrophobic coating systems during immersion in 3.5 wt % NaCl solution for 10 days (Figure 8c–f). A large radius of the impedance represents a higher corrosion resistance, and, thus, better anti-corrosion property. Since the radius of the impedance becomes smaller, the anti-corrosion performance of the coatings decreases. Moreover, it is observed that the H, Anionic/Cationic/M system loses protective ability at a faster rate than the H, Cationic/Anionic/M system when comparing the changes of the radius of the impedances. Therefore, the mangrove-inspired, bipolar hydrophobic coatings (H, Cationic/Anionic) can protect the substrate Q235 steel more significantly and for a much longer time.

4. Conclusions

To control the corrosive substances, e.g., water, Na^+, and Cl^-, is the key for a high-performance anti-corrosion coating to inhibit the corrosion reaction. Strategies developed by nature could provide numerous ingenious designs for dealing with that issue. In this study, we investigated the mangrove salt glands, which are distributed on both surfaces of the leaves (*Ceriops tagal (perr.) C. B. Rob*), and the salt secretion of the salt glands. Inspired by the function of controlling transport of ions into and out of the plant, we designed single-polar and bipolar coatings that have different ion-selective abilities and, thus, control of transport of Na^+ and Cl^-. We further fabricated mangrove-inspired, bipolar hydrophobic coatings that have a top-down protective ability. Our electrochemical evaluations show that, among the manufactured mangrove-inspired protective coatings, the bipolar, hydrophobic coatings (H, Cationic/Anionic) possess significant outstanding and long-term anti-corrosion performance.

Author Contributions: Conceptualization, M.C., Z.W., and B.W. Data curation, M.C., Z.W., and B.W. Investigation and methodology, M.C., Z.W., and B.W. Writing-original draft, M.C. Writing-review and editing, M.C., B.W., Z.W., and P.-Y.W.

Funding: This research received no external funding.

Acknowledgments: B.W. appreciated the financial supports from the Natural Science Foundation of China (No. 51703240) and the Shenzhen Peacock Technology Innovation Fund (No. KQJSCX20180330170430100). Z.W. is grateful for financial support from Shenzhen Science and Technology Innovation Council (JCYJ20170413141208098), Innovation Technology Fund (9440175), Research Grants Council of Hong Kong (No. C1018-17G, No. 11275216), and the City University of Hong Kong (No. 9360140, No. 9667139). P.-Y.W. thanks the supports from the National Key Research and Development Program of China (2018YFC1105201), the general program of National Natural and Science Foundation of China (31870988), the CAS-ITRI cooperation program (CAS-ITRI201902), and the International cooperative research project of the Shenzhen collaborative innovation program (20180921173048123).

Conflicts of Interest: The authors declare no conflict of interest.

References

1. Baeckmann, W.V.; Schwenk, W.; Prinz, W. Handbook of Cathodic Corrosion Protection. *Biochem. Biophys. Res. Commun.* **1997**, *307*, 810–813.
2. Baeckmann, W.V.; Schwenk, W.; Prinz, W. The Invention of Protective Devices. In *Handbook of Cathodic Corrosion Protection*, 3rd ed.; Baeckmann, W.V., Schwenk, W., Eds.; Elsevier: Houston, TX, USA, 1997; pp. 224–229.
3. International Measures of Prevention, Application, and Economics of Corrosion Technologies Study. Available online: http://impact.nace.org/economic-impact.aspx (accessed on 1 March 2016).
4. Cui, M.M.; Wang, B.; Wang, Z.K. Nature-Inspired strategy for anti-corrosion. *Adv. Eng. Mater.* **2019**, *21*. [CrossRef]
5. Wang, B.B.; Wang, Z.Y.; Cao, G.W.; Liu, Y.J.; Ke, W. Local corrosion behavior of 2024 aluminum alloy in salt lake atmosphere of western China. *Acta Metall. Sin.* **2014**, *50*, 49–56.
6. Petrov, N.N.; Falina, I.V.; Koval', T.V.; Gorokhov, R.V.; Shel'deshov, N.V.; Bukov, N.N. Electrical-percolation effects in epoxy resin/ion-exchange resin/polyaniline anti-corrosion composite materials. *Prot. Met. Phys. Chem.* **2017**, *53*, 725–732. [CrossRef]
7. Dong, Y.H.; Liu, Y.N.; Zhou, Q. Comparative studies on the corrosion protection effect of different ions selective polyaniline coatings. *Adv. Mater. Res.* **2011**, *287*, 2464–2469. [CrossRef]
8. Dong, Y.H.; Zhang, Q.Y.; Su, X.M.; Zhou, Q. Preparation and investigation of the protective properties of bipolar coatings. *Prog. Org. Coat.* **2013**, *76*, 662–669. [CrossRef]
9. Wang, J.G.; Torardi, C.C.; Duch, M.W. Polyaniline-related ion-barrier anti-corrosion coatings. *Synth. Met.* **2007**, *157*, 846–850. [CrossRef]
10. Couture, G.; Alaaeddine, A.; Boschet, F.; Ameduri, B. Polymeric materials as anion-exchange membranes for alkaline fuel cells. *Prog. Polym. Sci.* **2011**, *36*, 1521–1557. [CrossRef]
11. Lyon, S.B.; Bingham, R.; Mills, D.J. Advances in corrosion protection by organic coatings: What we know and what we would like to know. *Prog. Org. Coat.* **2017**, *102*, 2–7. [CrossRef]
12. Sørensen, P.A.; Dam-Johansen, K.; Weinell, C.E.; Kiil, S. Cathodic delamination of seawater-immersed anticorrosive coatings: Mapping of parameters affecting the rate. *Prog. Org. Coat.* **2010**, *68*, 283–292. [CrossRef]
13. Montoya, R.; García-Galván, F.R.; Jiménez-Morales, A.; Galván, J.C. A cathodic delamination study of coatings with and without mechanical defects. *Corros. Sci.* **2014**, *84*, 432–436. [CrossRef]
14. Kalendová, A. Effects of particle sizes and shapes of zinc metal on the properties of anticorrosive coatings. *Prog. Org. Coat.* **2003**, *46*, 324–332.
15. Wang, Z.C.; Zhang, Y.Z.; Gu, Z.J. A study on anti-corrosion performance of ion-selective phenolic coatings for carbon steel by EIS. *Mater. Prot.* **1998**, *31*, 1–4.
16. Wang, Z.C.; Gu, Z.J. Corrosion behaviour of copper covered with ion-selective phenolic coatings by EIS. *ElectroChemistry* **1997**, *3*, 271–276.
17. Wang, Z.C.; Gu, Z.J. Electrochemical and corrosion behaviour of A3 steel covered with ion-selective organic coating. *J. Xiamen Univ.* **1997**, *36*, 387–393. (In Chinese)
18. Pereira da Silva, J.E.; Córdoba de Torresi, S.I.; Torresi, R.M. Polyaniline acrylic coatings for corrosion inhibition: The role played by counter-ions. *Corros. Sci.* **2005**, *47*, 811–822. [CrossRef]
19. Wang, H.L.; Liao, S.Y. Salt glands and epidermal non-glandular hair structures in mangrove and coastal plants in DaYa bay. *J. Oceanogr. Taiwan Strait* **2000**, *19*, 372–378.

20. Fu, X.M.; Su, L.R.; Wang, X.Y. A study on the framework of blance sheet of marine biological resources. *Pac. J.* **2017**, *25*, 104.
21. Hao, C.L.; Li, J.; Liu, Y.; Zhou, X.F.; Liu, Y.H.; Liu, R.; Che, L.F.; Zhou, W.Z.; Sun, D.; Li, L.; et al. Superhydrophobic-Like tunable droplet bouncing on slippery liquid interfaces. *Nat. Commun.* **2015**, *6*, 7986. [CrossRef]
22. Liu, C.R.; Sun, J.; Xiang, C.H.; Che, L.F.; Wang, Z.K.; Zhou, X.F. Long-Range spontaneous droplet self-propulsion on wettability gradient surfaces. *Sci. Rep.* **2017**, *7*, 7552. [CrossRef]
23. Liang, W.L.; Ma, X.L.; Wan, P.; Liu, L.Y. Plant salt-tolerance mechanism: A review. *Biochem. Biophys. Res. Commun.* **2018**, *495*, 286–291. [CrossRef] [PubMed]
24. Tan, W.K.; Lin, Q.S.; Lim, T.M.; Kumar, P.; Loh, C.S. Dynamic secretion changes in the salt glands of the mangrove tree species avicennia officinalis in response to a changing saline environment. *Plant Cell Environ.* **2013**, *36*, 1410–1422. [CrossRef] [PubMed]
25. Tyerman, S.D. The devil in the detail of secretions. *Plant Cell Environ.* **2013**, *36*, 1407–1409. [CrossRef] [PubMed]
26. Deinlein, U.; Stephan, A.B.; Horie, T.; Luo, W.; Xu, G.; Schroeder, J.I. Plant salt-tolerance mechanisms. *Trends Plant Sci.* **2014**, *19*, 371–379. [CrossRef]
27. Dassanayake, M.; Larkin, J.C. Making plants break a sweat: The structure, function, and evolution of plant salt glands. *Front. Plant Sci.* **2017**, *8*, 406. [CrossRef]

coatings

Article

Guiding Stem Cell Differentiation and Proliferation Activities Based on Nanometer-Thick Functionalized Poly-*p*-Xylylene Coatings

Chih-Yu Wu [1,2,3,†], Yu-Chih Chiang [3,4,†], Jane Christy [1], Abel Po-Hao Huang [4,5], Nai-Yun Chang [1], Wenny [1], Yu-Chih Chiu [6], Yen-Ching Yang [1], Po-Chun Chen [6,*], Peng-Yuan Wang [7,8,*] and Hsien-Yeh Chen [1,2,3,*]

[1] Department of Chemical Engineering, National Taiwan University, Taipei 10617, Taiwan; picorna.tw@yahoo.com.tw (C.-Y.W.); b07504085@ntu.edu.tw (J.C.); Changnaiyun@ntu.edu.tw (N.-Y.C.); r06524094@ntu.edu.tw (W.); youngeddie@cgmh.org.tw (Y.-C.Y.)
[2] Advanced Research Center for Green Materials Science and Technology, National Taiwan University, Taipei 10617, Taiwan
[3] Molecular Imaging Center, National Taiwan University, Taipei 10617, Taiwan; munichiang@ntu.edu.tw
[4] School of Dentistry, Graduate Institute of Clinical Dentistry, National Taiwan University, Taipei 10048, Taiwan; howhuang6138@ntu.edu.tw
[5] Division of Neurosurgery, Department of Surgery, National Taiwan University Hospital, Taipei 10048, Taiwan
[6] Department of Materials and Mineral Resources Engineering, National Taipei University of Technology, Taipei 10608, Taiwan; t107788007@ntut.edu.tw
[7] Center for Human Tissues and Organs Degeneration, Institute of Biomedicine and Biotechnology, Shenzhen Institutes of Advanced Technology, Chinese Academy of Sciences, Shenzhen 518055, China
[8] Department of Chemistry and Biotechnology, Swinburne University of Technology, Melbourne, VIC 3122, Australia
[*] Correspondence: cpc@mail.ntut.edu.tw (P.-C.C.); py.wang@siat.ac.cn (P.-Y.W.); hsychen@ntu.edu.tw (H.-Y.C.); Tel.: +886-2-33669476 (H.-Y.C.); Fax: +886-2-23623040 (H.-Y.C.)
[†] Chih-Yu Wu and Yu-Chih Chiang contributed equally to this work.

Citation: Wu, C.-Y.; Chiang, Y.-C.; Christy, J.; Huang, A.P.-H.; Chang, N.-Y.; Wenny; Chiu, Y.-C.; Yang, Y.-C.; Chen, P.-C.; Wang, P.-Y.; et al. Guiding Stem Cell Differentiation and Proliferation Activities Based on Nanometer-Thick Functionalized Poly-*p*-Xylylene Coatings. *Coatings* **2021**, *11*, 582. https://doi.org/10.3390/coatings11050582

Academic Editor: Alenka Vesel

Received: 23 March 2021
Accepted: 12 May 2021
Published: 17 May 2021

Abstract: Modifications of biomaterials based on the combination of physical, chemical, and biological cues for manipulating stem cell growth are needed for modern regenerative medicine. The exploitation of these sophisticated modifications remains a challenge, including substrate limitation, biocompatibility, and versatile and general cues for stem cell activities. In this report, a vapor-phase coating technique based on the functionalization of poly-*p*-xylylene (PPX) was used to generate a surface modification for use with stem cells in culture. The coating provided the ability for covalent conjugation that immobilized bone morphogenetic protein 2 (BMP-2) and fibroblast growth factor 2 (FGF-2), and the modified coating surfaces enabled direct stem cell differentiation and controlled proliferation because of the specific activities. The ligations were realized between the growth factors and the maleimide-modified surface, and the conjugation reactions proceeded with high specificity and rapid kinetics under mild conditions. The conjugation densities were approximately 140 $\mathrm{ng \cdot cm^{-2}}$ for BMP-2 and 155 $\mathrm{ng \cdot cm^{-2}}$ for FGF-2. Guiding the activities of the human adipose-derived stem cells (hADSCs) was achieved by modifying surfaces to promote the hADSC differentiation capacity and proliferation rate. The reported coating system demonstrated biocompatibility, substrate-independent conformity, and stability, and it could provide an effective and versatile interface platform for further use in biomedical applications.

Keywords: growth factor; surface modification; CVD polymerization; biointerface; stem cells

1. Introduction

Surface properties are fundamental to advanced biomaterials that are designed to induce biological functions, and they include tuning surface wettability; the ability to enhance or to resist protein adsorption, cell adhesion or resistance; antibacterial action; and engineered niches for stem cell proliferation, migration, and differentiation [1–5]. In particular, sophisticated applications of these modification techniques that make stem cells renew themselves and retain their potency (i.e., the capability to differentiate into specialized cell types) [6,7] are under development. Promising results of unlimited cell expansion or lineage-specific differentiation in a reproducible and controlled manner and efficient and controlled differentiation commitment of specific cells and tissues were achieved in vitro and in vivo with combinations of mimicked physical, chemical, and/or biological cues [8–10]. Emerging therapeutic uses, encouraged by the advances in modern regenerative medicine, have also benefited from these promising results from research on stem cells used for tissue transplantation and repair. The current obstacles to achieving sophisticated material modifications include the potential harm from substances used during the process, the need for multiple steps to achieve the required sophistication, and techniques that are based on previous performance in a case-by-case manner and with a limited selection of materials.

The study herein aims to demonstrate an effective and general interface modification method for use in defining stem cell fate and enhancing the functions related to proliferation rate and multilineage differentiation capacity. The proposed modification technique was realized by the functionalization of poly-*p*-xylylene that includes a maleimide side group. The functional polymer was synthesized as an interface layer generated in one vapor-phase coating process and applied to the material surface through the exploitation of a chemical vapor deposition (CVD) polymerization process used to prepare maleimide-functionalized poly-*p*-xylylene (hereafter referred to as maleimide-PPX) coatings. Compared to other similar poly-*p*-xylylene systems, this technology, free of solvents, initiators, and catalysts, produced a coating that exhibited good conformability with the topology and geometry of substrates [11–13] with excellent cohesive properties and thermal stability on various substrates, including metals, oxides, polymers, nonvolatile liquids, silicon, and glass [12]. Most importantly, in the current study, conjugation-immobilized (i) bone morphogenetic protein 2 (BMP-2) and (ii) fibroblast growth factor 2 (FGF-2) enabled the modified coating surfaces to direct stem cell differentiation and controlled proliferation driven by the functions specified by (i) and (ii), respectively. The resulting BMP-2- and FGF-2-modified substrates were expected to be sustainable and multifunctional, so that they could provide an effective and flexible interface platform for biomedical applications.

2. Materials and Methods

2.1. CVD Surface Modifications

The synthesis of the coating, poly[(4-N-maleimidomethyl-*p*-xylylene)-co(*p*-xylylene)] (maleimide-PPX), was conducted by a custom-built CVD system (Kao Duen Technology Co., Ltd., Taipei, Taiwan) consisting of a sublimation zone, pyrolysis furnace, and deposition chamber. During the CVD process, the starting material (dimer) of 4-N-maleimidomethyl-[2.2]paracyclophane, which was prepared following procedures reported elsewhere [14], was first sublimated at approximately 120 °C in the sublimation zone. The sublimated species were then transferred to the pyrolysis furnace (560 °C) with a constant flow (30–50 sccm) of argon carrier gas. Following pyrolysis, the resulting highly reactive monomers were transferred into the deposition chamber and polymerized onto a rotating holder at 20 °C to form a uniformly deposited film of maleimide-PPX. To optimize the deposition, a pressure of 75 mTorr was maintained throughout the CVD process, and deposition rates were controlled at approximately 0.5 $\text{Å}\cdot\text{s}^{-1}$, which was monitored via an in-situ quartz crystal microbalance (STM-100/MF, Sycon Instruments, Syracuse, NY, USA). The thickness of the polymer layer was measured as approximately 100–150 nm by using spectroscopic ellipsometry (M2000, Woollam Co., Inc., Lincoln, NE, USA) after retrieving the coated samples from the CVD system. The resultant polymer coating was also characterized by using Fourier transform infrared (FT-IR, PerkinElmer, Waltham, MA, USA) and X-ray photoelectron spectroscopy (XPS, Thermo Scientific, Leicestershire, UK) to verify the anticipated chemical compositions.

2.2. Growth Factor Immobilization

Selected human recombinant growth factors, including BMP-2 and FGF-2, were obtained commercially from R&D Systems Inc. (Minneapolis, MN, USA) and reconstituted into a 100 $\mu g \cdot mL^{-1}$ solution following the manufacturer's instructions. These two growth factors were then conjugated to the maleimide-PPX coated substrates via a coupling reaction between the maleimide and the thiol (sulfhydryl) groups under conditions of 4 °C and pH 6.5–7.5 for 6 h. Dithiothreitol (DTT, Sigma Aldrich, St. Louis, MO, USA) (5 mM) was used as a reducing agent for the BMP-2 and FGF-2 immobilization. A rinsing process was performed three times with PBS to remove any unbound molecules.

2.3. Characterizations

FT-IR spectra were recorded using a spectrum 100 FT-IR spectrometer (PerkinElmer, Waltham, MA, USA) equipped with an advanced grazing angle specular reflectance accessory (AGA, PIKE Technologies, Fitchburg, WI, USA) and a liquid nitrogen-cooled MCT detector. The samples were mounted in a nitrogen-purged chamber to eliminate noise from the CO_2 and H_2O, and the recorded spectra were corrected for any residual baseline drift. The XPS data were recorded using a Theta Probe X-ray photoelectron spectrometer (Thermal Scientific, Leicestershire, UK) with a monochromatized AlKα X-ray source at an X-ray power of 150 kW. The pass energies were 200.0 eV and 20.0 eV for the survey scan and the high-resolution C_{1s} elemental scan, respectively. The XPS spectrum atomic analysis was reported based on atomic concentrations (%), and the results were compared to theoretical values calculated based on the structure. The binding capacities of the modified surfaces for the growth factor protein were measured using a standard QCM instrument (ANT Technologies, Taipei, Taiwan) with a quiescent mode under sealed conditions, and the measuring of the deposited protein mass was based on the fundamental frequency shift as compared with unbinding or unmodified surfaces. For the antibody affinity experiments performed by flow mode, the QCM instrument was further equipped with a flow injection analysis (FIA) device (MasterFlex, Cole-Parmer Instrument Co., Chicago, IL, USA), and a continuous frequency variation recording device was used for the characterization. The flow rate was controlled using a peristaltic pump connected to the FIA device, and the pumping process was temporarily stopped for 25 min (10 min after injection) to allow anti-BMP-2 or anti-FGF-2 antibodies to bind to the proteins. All experiments were carried out at 25 °C, and each sample was measured in triplicate. The frequency shift ΔF resulting of a deposited mass Δm is described by the Sauerbrey equation [15]:

$$\Delta \mathrm{F} = \frac{-2\Delta m f^2}{A\sqrt{\mu\rho_q}} = -C_f \Delta m$$

where f is the intrinsic crystal frequency (9 MHz), A is the piezo-electrically active area (0.091 cm^2), ρ_q is the quartz crystal density (2.648 g/cm^3), μ is the shear modulus of the quartz crystals (2.947 × 1011 dyn/cm^2), C_f is the mass sensitivity (2.013 Hz/ng for a 9 MHz crystal), and Δm is the adding mass on the crystal surface due to specific binding, respectively.

2.4. μCP and Immunofluorescence

Confinement of the reactions using μCP was performed using two different poly-(dimethylsiloxane) (PDMS) stamps consisting of squares with 30 μm × 30 μm sides (for BMP-2) and 50 μm × 50 μm sides (for FGF-2) and arrays with 100 μm center–center spacing. Solutions with the growth factor proteins (BMP-2 or FGF-2) were used as the inking solutions and allowed to react on top of the maleimide-PPX-modified substrates for 6 h. The μCP process was performed at 4 °C and 55% humidity. The resulting sample was washed twice with PBS to remove any unbound molecules. For the self-assembled binding of the primary and secondary antibodies, the BMP-2- and FGF-2-modified samples were incubated in the corresponding antibody solution, anti-BMP-2 antibody (50 $\mu g \cdot mL^{-1}$ in PBS, R&D Systems, Minneapolis, MN, USA) or anti-FGF-2 antibody (50 $\mu g \cdot mL^{-1}$ in PBS, R&D Systems, Minneapolis, MN, USA), for 2 h, and the samples were washed twice with PBS to remove any unbound antibodies. Subsequently, fluorescently labeled secondary antibodies were incubated with the samples for 1 h and washed twice with PBS to remove any unbound antibodies. The samples with fluorescence signals were analyzed under a LEICA fluorescence microscope (DMI3000B, Leica Microsystems, Wetzlar, Germany).

2.5. Induced Cellular Activities

Tissue culture polystyrene (TCPS) plate substrates (24 well, Corning) were modified with a CVD copolymer coating and conjugated with BMP-2 or FGF-2 growth factor proteins following the procedures described above, and the modified TCPS plates were used for cell culture experiments. The pure maleimide-PPX coating surface and the untreated TCPS plate surface served as controls for the comparison. Normal human adipose-derived stem cells (hADSCs) were isolated from subcutaneous adipose tissue following the reported procedures [13], and the protocols were approved by the Internal Ethical Committee of National Taiwan University Hospital. To evaluate differentiation and proliferation activities, the hADSC cultures were initially seeded at a density of 1×10^5 cells·cm^{-2} and 2×10^4 cells·cm^{-2}, respectively, for the following characterization. Each experiment was conducted in triplicate.

2.6. Osteogenesis

Osteogenic differentiation-induced activity was examined by culturing hADSCs in osteogenic differentiation medium [16]. The osteogenic activity of early stage alkaline phosphatase (ALP) expression was analyzed using a 5-Bromo-4-Chloro-3-Indolyl Phosphate / Nitroblue Tetrazolium (BCIP/NBT) liquid substrate system (Sigma-Aldrich, St. Louis, MO, USA) at day 10, whereas the late stage osteogenic activity, as indicated by calcium deposition, was confirmed by staining with a 2% alizarin red S solution (ARS, Sigma Aldrich, St. Louis, MO, USA) at day 21. The resulting ALP and ARS signals were quantitatively measured using a microplate spectrophotometer (BioTek Instruments, Winooski, VT, USA) with an absorbance wavelength of 405 nm following the manufacturer's instructions.

2.7. Chondrogenesis

Chondrogenic differentiation-induced activity was examined in chondrogenic differentiation medium [16] for 14 days. The cultured cells were fixed in 10% formalin (Macron Fine Chemicals, Center Valley, PA, USA), and the proteoglycan present in the cartilage matrix was detected by staining with 0.4% (w/v) toluidine blue O (Sigma-Aldrich) in 0.1 M sodium acetate buffer (pH 4.0). The sulfated glycosaminoglycan (sGAG) content was further analyzed by using a 1,9-dimethylmethylene blue (DMMB, Sigma-Aldrich) dye-binding spectrophotometric assay, and quantification was based on the absorbance difference between 525 and 595 nm [17]. The expression profiles of the chondrogenesis-related gene encoding collagen type II were also analyzed.

2.8. Adipogenesis

For the analysis of adipogenic differentiation induced activity, hADSCs were cultured in adipogenic differentiation medium [16]. On day 10, the cells were fixed with 10% formalin and then stained with 0.25% (w/v) oil red O (Sigma-Aldrich) to observe lipid droplets. The resulting oil red O signals were further quantified using a microplate spectrophotometer (BioTek Instruments, Winooski, VT, USA) with an absorbance wavelength of 510 nm following the protocol reported [18]. The expression profiles of the adipogenic gene Fatty Acid-Binding Protein 4 (FABP-4) were also analyzed.

2.9. Proliferation Activities

To judge proliferation activities, a cell growth medium recipe and culture conditions were used as previously described [19]. After culturing with cells for 1 day and 5 days, the resulting cultured sample surfaces were observed and photographed using an optical microscope to determine cell proliferation levels. The cell numbers for the studied surfaces were further measured quantitatively using a 3-(4,5-Dimethylthiazol-2-yl)-2,5-diphenyltetrazolium Bromide (MTT) assay (Sigma-Aldrich) according to the manufacturer's instructions. The normalized ratio of cells on day 5 to cells on day 1 was used to evaluate the cell proliferation-induced capacities of the modified surfaces.

2.10. Gene Expression Profiles

The gene expression levels were determined by quantitative real-time polymerase chain reaction (qPCR) analysis following the manufacturer's protocols. Briefly, total RNA from the hADSCs and differentiated cells was extracted with TRIzol reagent (Thermo Fisher Scientific, Waltham, MA, USA), and then the RNA concentration was determined using a NanoDrop ND-1000 spectrophotometer (Thermo Fisher Scientific). Complementary DNA (cDNA) was synthesized subsequently from the RNA template using a high-capacity cDNA reverse transcription kit (Thermo Fisher Scientific). Gene expression level was analyzed using a StepOnePlus™ Real-Time PCR System (Thermo Fisher Scientific) with gene-specific primers (as indicated in Table 1), and the β-actin was used as a loading control to normalize the expression of the target gene(s) between different samples. The thermal program for PCR was as follows: 35 cycles of 94 °C for 30 s; 60 °C for 30 s; and 72 °C for 1 min followed by incubation at 72 °C for 5 min. The fold changes in gene expression were calculated with the delta-delta Ct method [20].

Table 1. PCR primer sets used in this study.

Gene Name	Primer Sequence (5′-3′)	Product Length (bp)
Collagen type II	Forward- ACG GCG AGA AGG GAG AAG TTG Reverse- GGG GGT CCA GGG TTG CCA TTG	352
FABP-4	Forward- TGG GCC AGG AAT TTG ACG AA Reverse- GAC GCA TTC CAC CAC CAG TT	158
β-Actin	Forward- CAG GAG ATG GCC ACT GCC GCA Reverse- TCC TTC TGC ATC CTG TCA GCA	275

2.11. Statistical Analysis

All data are reported as the mean ± standard deviation (S.D.) and are representative of three or more independent experiments. According to the unpaired *t*-test, GraphPad Prism 7 software (GraphPad Software, Inc., San Diego, CA, USA) was used to test the statistical differences between the experimental group and the control group, and a two-tailed *p*-value less than 0.05 was considered significant.

3. Results

The synthesis of the maleimide-PPX coating was conducted similarly to that of other poly-*p*-xylylene (PPX) systems; that is, a precursor of a maleimide-substituted [2.2]paracyclophane (prepared in-house) [21] was sublimated at approximately 120 °C and pyrolyzed at approximately 560 °C to generate reactive monomers of quinodimethane. The entire process involved vapor-phase deposition and polymerization (chemical vapor deposition, CVD) under a reduced pressure of 75 mTorr, and a deposition rate of approximately 0.5–1.0 $\text{Å}\cdot\text{s}^{-1}$ was regulated during the CVD process with a linear-dependent time theoretical parameter [22,23] that was controlled to ensure that the final coating thickness was in the range of 100–150 nm. As shown in Figure 1a, the rational maleimide functionality enabled the resultant coating to readily undergo a maleimide-thiol coupling reaction to the target molecules that contain thiols through a Michael-type nucleophilic addition at pH 6.5–7.5 [14], and successful conjugation created through this reaction to attach protein molecules without compromising protein structures and functions has been shown [24]. The important application of using maleimide-PPX to conjugate FGF-2 and BMP-2 growth factor proteins was therefore exploited under mild reaction conditions. The successful conjugation was confirmed by comparing the Fourier transform infrared (FT-IR) spectra with those of a pure maleimide-PPX coating, and the characteristic absorption values of N–H peaks in the range from 3200 to 3600 cm^{-1}, which represent the immobilized FGF-2 and BMP-2 proteins, were detected (Figure 1b). The additional FT-IR spectra that comparing maleimide-PPX surface with parylene-C surface combined with the X-ray photoelectron spectroscopy (XPS) survey to verify the anticipated chemical compositions of the maleimide-PPX coating are included in Supplementary Figure S1. Most importantly, the FT-IR spectra showing the thiol groups of BMP-2 and FGF-2 proteins (i.e., the S-H band at 2634 cm^{-1}) were highlighted in Supplementary Figure S2. After conjugating BMP-2 and FGF-2 to the coating surface, the S-H peak disappeared (see Figure 1). This result proved that the two adhesion cues BMP-2 and FGF-2 are covalently bonded to the coating surface.

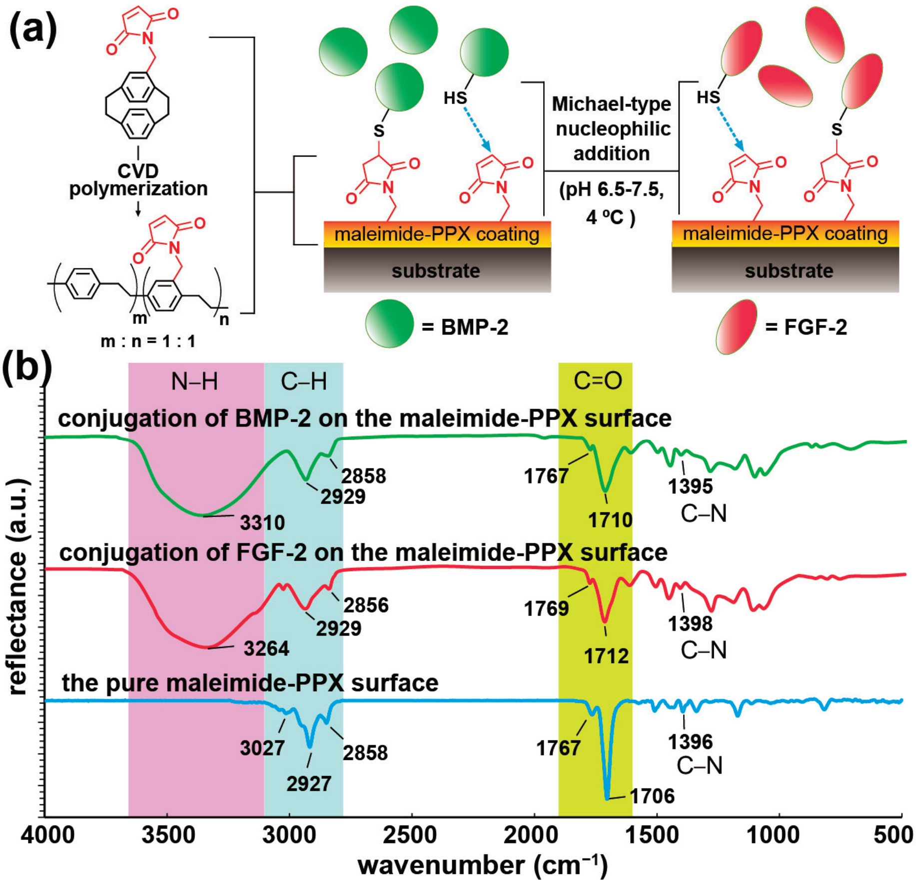

Figure 1. (**a**) Schematic illustration of the created cell differentiation-induced surfaces using the maleimide-PPX coating to immobilize the BMP-2 and FGF-2 growth factor proteins. (**b**) FT-IR spectra show the immobilized BMP-2 and FGF-2 on the maleimide-PPX surface. The peaks in the range from 3200 cm^{-1} to 3600 cm^{-1} indicate the characteristic N–H band absorption of BMP-2 and FGF-2. FT-IR spectra of the pure maleimide-PPX surfaces are also presented for comparison. The peaks located at 1396 cm^{-1} (C–N) and 1706 cm^{-1} (C=O) correspond to the characteristic stretching bands for the maleimide groups.

Furthermore, the generation of the maleimide-PPX coating and the subsequent conjugation of FGF-2 and BMP-2 were seamlessly performed on a quartz crystal microbalance (QCM) sensor chip, and the recorded frequencies before and after conjugation were compared to estimate the density of conjugated FGF-2 and BMP-2, which was thus determined as approximately 140 ng·cm^{-2} for BMP-2 and 155 ng·cm^{-2} for FGF-2 (Figure 2a). These results showed agreement with other similar PPX systems that have been used to attach biomolecules. Theoretically, the conjugation density is tunable, and the effectiveness of the resultant biological activities is predictable [25]. On the other hand, as presented in Figure 2b, a dynamic QCM analysis in which anti-BMP-2 or anti-FGF-2 antibodies could bind to the modified surfaces was performed in the elapsed time, and the results indicated significantly decreasing frequencies due to the binding of anti-BMP-2 antibody and anti-FGF-2 antibody on the BMP-2-modified and the FGF-2-modified coatings, respectively, compared to the nearly unchanged frequencies on the pure coating surfaces. Notably, the small frequency drop in the pure coating study cannot be considered as expected antibody-antigen specific bonding, because this reduction level of frequency may be due to the limitations of the QCM equipment and the measurement errors caused by random fluctuations in the experimental phase [26]. The results not only confirmed the identity and activity of the immobilized FGF-2 and BMP-2 proteins but also indicated a firm attachment of these proteins by covalent conjugation, which was also found by the abovementioned FT-IR data. Other supporting data were used to verify the reactivity and specificity of the immobilized FGF-2 and BMP-2 surfaces. As shown in Figure 2c, they were derived from the use of a microcontact printing (µCP) technique with a PDMS stamp to induce a selective reaction with BMP-2 and FGF-2 at confined locations of the maleimide-PPX coating surfaces. Subsequently, solutions with a primary antibody and a fluorescently labeled secondary antibody (fluorescein for the BMP-2 secondary antibody and Alexa Fluor® 555 for the FGF-2 secondary antibody) were incubated with these selectively modified samples, and the combined self-assembled bindings between the growth factor proteins and these antibodies showed strong, distinguishable fluorescence signals in the green channel with fluorescein on the BMP-2-modified regions and in the red channel by Alexa Fluor® 555 on the FGF-2 regions. These patterns were consistent with those from the µCP stamps. The specific binding affinities of the two growth factor proteins were unambiguously verified.

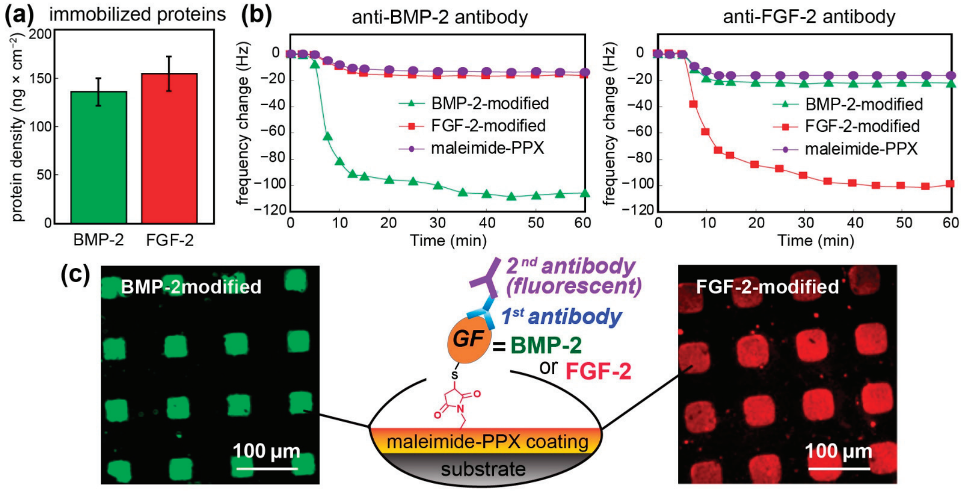

Figure 2. (**a**) Quantification of the conjugation densities of BMP-2 and FGF-2 by using QCM analysis. (**b**) QCM dynamic analysis of the binding affinity of the studied surfaces toward anti-BMP-2 and anti-FGF-2 antibodies. (**c**) The activity and specificity of the immobilized growth factors were verified by exploiting a µCP technique to spatially confine the conjugation of BMP-2 and FGF-2 to defined locations. Combinations of self-assembled binding affinities by first antibodies (anti-BMP-2 and anti-FGF-2) and by secondary antibodies (fluorescently labeled secondary antibodies) show that the fluorescence patterns are consistent with the µCP patterns.

The induction of these hADSCs toward osteogenic differentiation was studied by examining their alkaline phosphatase (ALP) expression in the early stage and alizarin red staining (ARS) in the mature stage of osteogenesis, and the results in Figure 3a indicated the enhanced ALP expression at day 10 on the modified surfaces of BMP-2 compared to the expression levels on the control surfaces consisting of pure maleimide-PPX and unmodified tissue culture polystyrene (TCPS) plates. Similar results from experiments on enriched calcium deposition, as evaluated by ARS signals at day 21, were also observed for the BMP-2 surfaces. Statistical analysis of these ALP and ARS signals, shown in Figure 3b,c, further confirm the enhanced osteogenesis on the growth factor-modified surface (*** $p < 0.001$ relative to the control surfaces). The BMP-2-modified surface had a greater level of osteogenesis activity signal expression, with a 276.9% higher intensity compared to the lowest level, which was for the TCPS control surface. Furthermore, the hADSC activity toward chondrogenic differentiation was investigated on those surfaces by detecting the known mechanism and characteristic indications of chondrogenesis, as determined at day 14 by (i) staining and characterizing the color and intensity changes caused by the metachromatic binding between toluidine blue and cartilage polysaccharides, (ii) sulfate glycosaminoglycan (sGAG) deposition, and (iii) collagen type II expression. The results presented in Figure 4a–c reveal that the intensities and signals for (i), (ii), and (iii) were all consistently greater on the BMP-2-modified surface than they were on the other surfaces (*** $p < 0.001$), indicating that chondrogenesis was best enhanced on this modified surface among those studied.

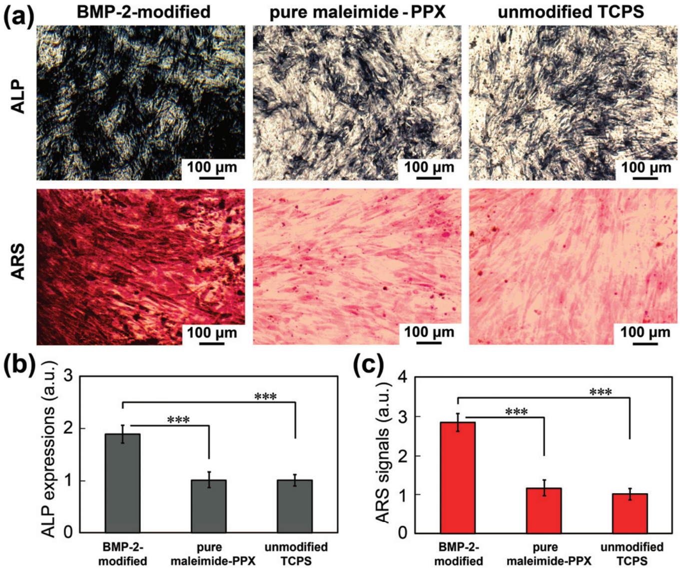

Figure 3. The osteogenesis activities of hADSCs were examined on the modified surfaces with immobilized BMP-2 growth factor protein. Pure maleimide-PPX coating surfaces and unmodified tissue culture polystyrene (TCPS) surfaces were used for the comparison. (**a**) The early stage osteogenesis marker, ALP expression, was analyzed at day 10, and the mature stage marker, calcium deposition, was observed at day 21 using alizarin red staining (ARS). The results of statistical analyses of the quantified (**b**) ALP signals and (**c**) ARS signals were also compared for the studied surfaces. The data bars represent the mean value (n = 3) and the standard deviation (±SD) based on three independent experiments. The significance level *** stands for *** $p < 0.001$, and is shown by the results of the unpaired *t*-test.

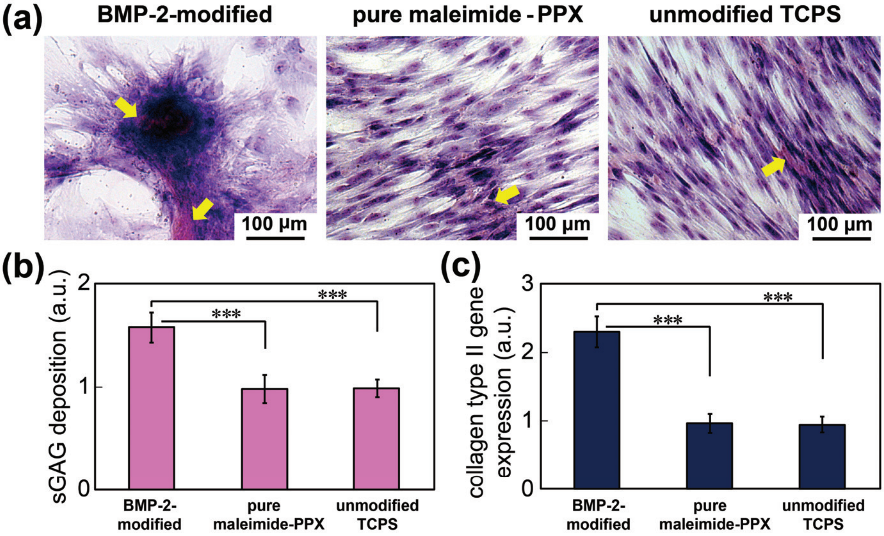

Figure 4. Chondrogenic activities of hADSCs were examined on the studied surfaces. (**a**) Toluidine blue staining was performed on day 14 to trigger the metachromatic color change (yellow arrows). The detected intensities from (**b**) sulfated glycosaminoglycan (sGAG) by using a spectrophotometric 1,9-dimethylmethylene blue (DMMB) dye binding assay and (**c**) the chondrogenic marker collagen type II gene expression by quantitative PCR analysis were statistically analyzed and compared for the studied surfaces. The data bars represent the mean value (n = 3) and the standard deviation (±SD) based on three independent experiments. The significance level *** stands for *** $p < 0.001$, and is shown by the results of the unpaired *t*-test.

Furthermore, the adipogenic induction of hADSCs on the modified coating surfaces was analyzed by observing the light-refraction of lipid droplets, which accumulate during adipogenesis, within the differentiated cells at day 10. A characteristic staining technique in which oil red O dye binds to lipids was used to visualize the lipid droplets (Figure 5a). In addition, 172.3% increases in adipogenesis activity based on quantitative oil red O staining were confirmed for the FGF-2-modified surfaces, significant difference (*** $p < 0.001$) compared to that for other surfaces (Figure 5b), and the expression of the FABP-4 gene was detected (Figure 5c), further supporting the quantitative results. Finally, in another demonstration, the functions that determine stem cell action, as based on the use of the growth factor-modified coating, were examined by culturing normal human adipose-derived stem cells (hADSCs) on the modified surfaces. As displayed in Figure 6, the analysis by using phase-contrast microscopy and MTT assay revealed high biocompatibility for cell growth (data are included in Supplementary Figure S3) and reflected a consistent level of cell adhesion for all the studied surfaces on day 1 (Figure 6a,b). Notably, significant variation was discovered between these surfaces over an extended culture time frame such that, at day 5, the FGF-2-modified surfaces specifically exhibited profound proliferation of hADSCs compared to that of the pure maleimide-PPX coating surface and unmodified TCPS surface (Figure 6a,b). Statistically, the proliferation ratio of cell number that was normalized by day 5 to day 1 unambiguously revealed the anticipated results by showing an approximate 377.8% higher ratio for the FGF-2-modified surfaces, a significant difference (*** $p < 0.001$) compared to that for other surfaces, and the enhanced hADSC proliferation activity from using the growth factor-modified coating technique was also evident (Figure 6c).

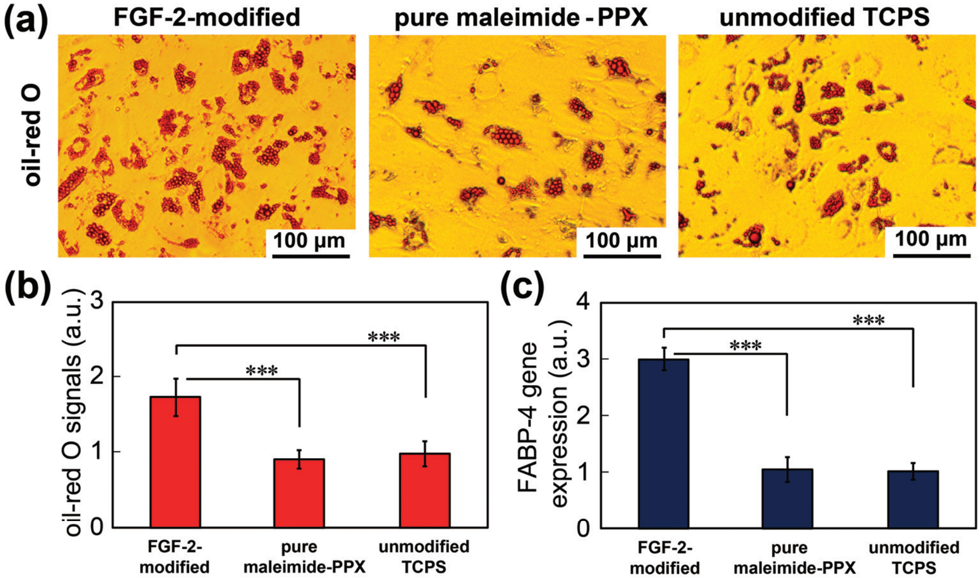

Figure 5. The adipogenic activities of the hADSCs were examined on the studied surfaces. (**a**) Recorded oil-red O staining images of differentiated cells on these surfaces at day 10. Statistical analyses of the (**b**) oil red O signal intensities obtained by spectrophotometry and the (**c**) FABP-4 marker gene expression obtained by quantitative PCR was performed and compared for these sample surfaces. The data bars represent the mean value (n = 3) and the standard deviation (±SD) based on three independent experiments. The significance level *** stands for *** $p < 0.001$, and is shown by the results of the unpaired *t*-test.

The conjugation was attributed to the maleimide-equipped functionality, which was readily accessible to site-specific and covalent binding to thiol moieties through Michael-type nucleophilic addition with high specificity and rapid kinetics under mild conditions at room temperature in aqueous solutions of pH 7.4. Such conjugation reactions have been shown to be successful without perturbing the protein structures or functions [13,24,27]. In addition, the covalent immobilization of the growth factors to biomaterial interfaces addresses challenges associated with delivering freely diffusible growth factors and has thus emerged as a promising method of achieving localized and sustained growth factor delivery based on a phenomenon called juxtracrine signaling (or contact-dependent signaling) [3,28,29]. Immobilized growth factors (i.e., BMP-2 and FGF-2) provide chemical cues for the guidance of stem cell behaviors and are therefore applicable to the material surface, where they demonstrate the concept. More importantly, both BMP-2 and FGF-2-functionalized surfaces can promote multilineage differentiation. However, only the FGF-2-functionalized surface had an enhanced effect on the normal growth of cultures, and this result is consistent with other publications. BMP-2, which belongs to the transforming growth factor beta (TGF-β) family, is now recognized as a multipurpose cytokine. When the chemical composition of the modified coatings and the conjugation reactions were confirmed, the current coating technique was also demonstrated to direct cellular activities for mesenchymal stem cells (MSCs) and induce BMP-2 function via activation of the SMAD signaling mechanism [30,31], which leads to MSC multilineage differentiation that includes not only osteogenesis and chondrogenesis [32] but also adipogenesis [33–35]. On the other hand, FGF-2 has been shown to be part of a signaling pathway distinct from that of BMP-2 that enhances the self-renewal of MSCs such that they maintain their multilineage differentiation potential [36–38]. The coating material, poly-*p*-xylylene, is a highly biocompatible polymer of Class VI in the United States Pharmacopeia (USP), and the biocompatibility (or cell viability) examinations associated with the polymer system (thin films) or the same produced devices were well-reported during the past including biocompatibility against various types of cells (including hADSCs). The convincing results of stem cell differentiation in this report also clearly support the argument that the cells are alive, especially in the final stage of cell differentiation. Compared with committed or differentiated cells, the most fascinating feature of undifferentiated stem cells is their strong plasticity [39,40], and the coating technology based on the proposed growth factor modifications by using vapor-phase maleimide-PPX can give full play to these characteristics of stem cells. The statistical quantification of these guided cellular activities and, for comparison, that of the pure maleimide-PPX coating surfaces and the unmodified TCPS control surfaces, is further analyzed and summarized in Table 2. These results clearly support that the surface-modified products can promote the differentiation and proliferation of stem cells under various induction conditions, so as to achieve the expected effects for potential regenerative medicine applications.

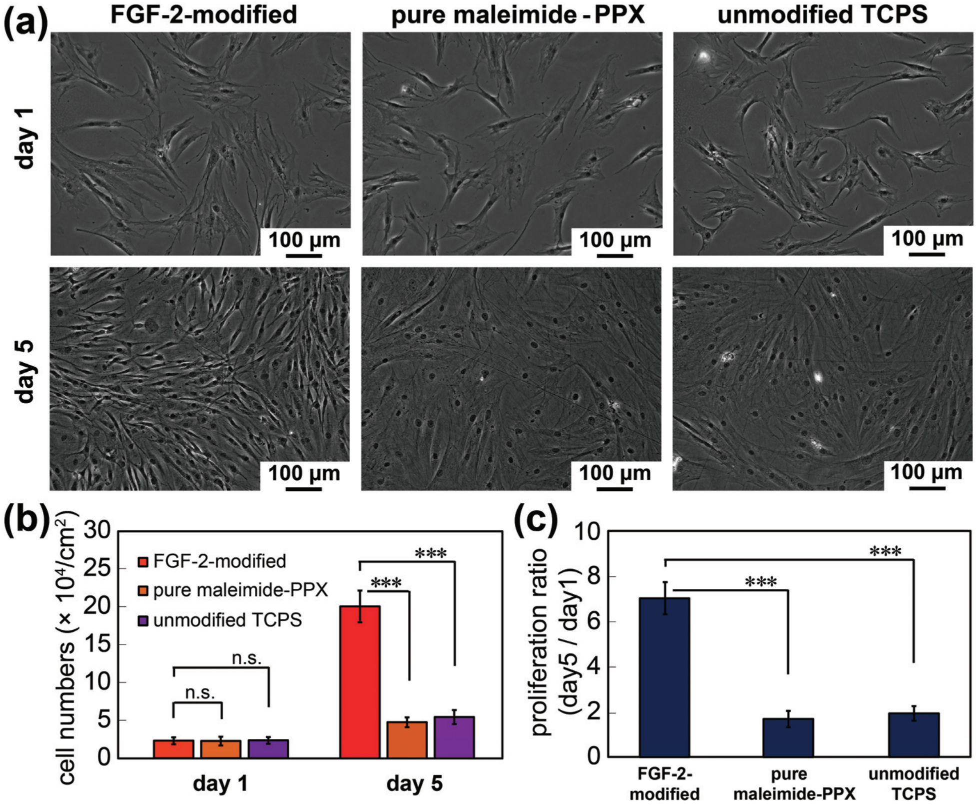

Figure 6. The proliferation activities of hADSCs were examined on the studied surfaces. (**a**) Phase-contrast micrographs of cell growth patterns recorded on day 1 and day 5. (**b**) Estimated cell numbers on day 1 and day 5 were compared for these surfaces. (**c**) The proliferation ratio that statistically normalized the cell numbers on day 5 to day 1 was compared for these studied surfaces. The data bars represent the mean value (n = 3) and the standard deviation (±SD) based on three independent experiments. The significance levels n.s. and *** stand for nonsignificant difference and *** $p < 0.001$, respectively, and are shown by the results of the unpaired *t*-test.

Table 2. Enhanced induction properties of growth factor-modified surfaces based on the maleimide-functionalized poly-*p*-xylylene (maleimide-PPX) coating [a].

Induction [b]	**BMP-2 Modified**	**FGF-2 Modified**	**Maleimide-PPX Coating**	**Unmodified TCPS**	**Potential Applications**
osteogenesis	277%	-	108%	100%	bone regeneration [41,42]
chondrogenesis	156%	-	100%	100%	cartilage regeneration [43]
adipogenesis	-	172%	94%	100%	soft tissue reconstruction [44–46]
proliferation	-	378%	94%	100%	repair damage from wound or cuts [47]

[a] Data were normalized and compared against data from a control surface of commercially available tissue culture polystyrene (TCPS) plates. [b] Data were compared and shown based on results from alizarin red staining, 1,9-dimethylmethylene blue staining, oil-red O staining, and cellular expansion rates.

4. Conclusions

In this study, an effective and general interface modification method for use in defining stem cell fate and enhancing the functions related to proliferation rate and multilineage differentiation capacity was demonstrated. The introduced surface modification was synthesized based on a clean and dry vapor deposition process that rendered a functional polymer coating. Most importantly, the facile integration of the maleimide functionality into the coating enabled the covalent conjugation of BMP-2 and FGF-2 growth factor proteins in mild conditions, which enabled guided differentiation and proliferation of the MSCs. With the proven concept that coating technology can be used not only on a variety of substrate materials, but also for conformity and stability on devices with sophisticated topology and geometry, we foresee that these findings have significant potential for further use in biomedical applications because of the various controllable parameters in favorable conditions offered by this coating technology.

Supplementary Materials: The following are available online at https://www.mdpi.com/article/10.3390/coatings11050582/s1, Figure S1: Maleimide-functionalized poly-p-xylylene (maleimide-PPX) coating. (a) Infrared reflec-tion-absorption spectroscopy (IRRAS) spectra for the maleimide-PPX coating. The peaks located at 1396 cm^{-1} (C–N), 1706 and 1767 cm^{-1} (C=O) correspond to the characteristic band stretches for the maleimide groups. Infrared reflection absorption spectroscopy (IRRAS) spectra for the Parylene-C coating which has no maleimide was also shown for the better comparison. (b) X-ray photoelectron spectroscopy (XPS) characterization of the maleimide-PPX coating. The table com-pares the experimental values of the XPS survey high-resolution C1 s spectra with the theoretical predictions. The signal at 285.0 eV is attributed to the aliphatic and aromatic carbons (C–C, C–H), and the intensity at 84.5 at% compares well with the theoretical concentration of 84.2 at%. The C–N bond was detected with 5.6 at%, which compares well with the theoretical value of 5.3 at%. The peak at 288.6 eV was assigned to the O=C–N group of the maleimide (7.1 at%) and agrees with the theoretical value of 10.5 at%. The signal at 291.4 eV (2.8 at%) indicates $\pi \rightarrow \pi^*$ transitions, Figure S2: FT-IR spectra of BMP-2 (bone morphogenetic protein 2) and FGF-2 (fibroblast growth factor 2) alone. The thiol groups of the BMP-2 and FGF-2 proteins (i.e., S-H band at 2634 cm^{-1}) in the spec-tra were highlighted, Figure S3: Biocompatibility analysis of the maleimide-PPX coatings. The human adipose-derived stem cells (hADSCs) were cultured on each surface for 1 day and the cell viabilities were then quantified by using a 3-(4,5-dimethylthiazol-2-yl)-2,5-diphenyltetrazolium bromide (MTT) assay. The data bars represent the mean value and the standard deviation (±SD) based on three inde-pendent samples. The p-value large than 0.05 indicates the studied surface has a good biocom-patibility with no significant difference (n.s.) as compared to the unmodified TCPS surfaces.

Author Contributions: Conceptualization, C.-Y.W., Y.-C.C. (Yu-Chih Chiang), Y.-C.Y., P.-C.C., P.-Y.W., and H.-Y.C.; methodology, C.-Y.W., Y.-C.C. (Yu-Chih Chiang), Y.-C.Y., P.-C.C., P.-Y.W. and H.-Y.C.; software, C.-Y.W., Y.-C.C. (Yu-Chih Chiang), Y.-C.C. (Yu-Chih Chiu), and Y.-C.Y.; validation, C.-Y.W., A.P.-H.H., and W.; formal analysis, C.-Y.W., J.C. and Y.-C.C. (Yu-Chih Chiu); investigation, Y.-C.C. (Yu-Chih Chiu), N.-Y.C. and Y.-C.Y., ; resources, P.-C.C., P.-Y.W., and H.-Y.C.; data curation, Y.-C.C. (Yu-Chih Chiang), A.P.-H.H. and W.; writing—original draft preparation, C.-Y.W., Y.-C.C. (Yu-Chih Chiang), P.-C.C., P.-Y.W. and H.-Y.C.; writing—review and editing, C.-Y.W., Y.-C.C. (Yu-Chih Chiang), P.-C.C., P.-Y.W. and H.-Y.C.; visualization, C.-Y.W., N.-Y.C. and J.C.; supervision, P.-C.C., P.-Y.W. and H.-Y.C.; project administration, P.-C.C., P.-Y.W. and H.-Y.C.; funding acquisition, P.-C.C., P.-Y.W. and H.-Y.C. All authors have read and agreed to the published version of the manuscript.

Funding: H.-Y.C. gratefully acknowledges support from the Ministry of Science and Technology of Taiwan (MOST 108-2221-E-002-169-MY3). P.-C.C. gratefully acknowledges support from the Ministry of Science and Technology of Taiwan (MOST 107-2221-E-027-009-MY2; 108-2321-B-010-008-MY2). P.-Y.W. acknowledges the support from the National Key Research and Development Program of China (2018YFC1105201), the National Natural Science Foundation of China. This work was further supported by the "Advanced Research Center For Green Materials Science and Technology" from The Featured Area Research Center Program within the framework of the Higher Education Sprout Project by the Ministry of Education (107L9006) and the Ministry of Science and Technology in Taiwan (MOST 107-3017-F-002-001).

Institutional Review Board Statement: Not applicable.

Informed Consent Statement: Not applicable.

Data Availability Statement: All data generated or analyzed during this study are included in this published article and its supplementary information files.

Conflicts of Interest: The authors declare no competing financial interests. The funders had no role in the design of the study; in the collection, analyses, or interpretation of data; in the writing of the manuscript, or in the decision to publish the results.

Abbreviations

PPX	Poly-*p*-xylylene
BMP-2	Bone Morphogenetic Protein 2
FGF-2	Fibroblast Growth Factor 2
hADSCs	Human Adipose-Derived Stem Cells
CVD	Chemical Vapor Deposition
Maleimide-PPX	Poly[(4-N-maleimidomethyl-*p*-xylylene)-co(*p*-xylylene)]
TGF-β	Transforming Growth Factor Beta
MSCs	Mesenchymal Stem Cells
FT-IR	Fourier Transform Infrared
XPS	X-ray Photoelectron Spectroscopy
DTT	Dithiothreitol
QCM	Quartz Crystal Microbalance
μCP	Microcontact Printing
PDMS	Poly(dimethylsiloxane)
TCPS	Tissue Culture Polystyrene
ALP	Alkaline Phosphatase
ARS	Alizarin Red S
sGAG	Sulfated Glycosaminoglycan
DMMB	1,9-Dimethylmethylene Blue
FABP-4	Fatty Acid-Binding Protein 4
MTT	3-(4,5-Dimethylthiazol-2-yl)-2,5-diphenyltetrazolium Bromide
qPCR	Quantitative Real-Time Polymerase Chain Reaction

References

1. Ito, Y.; Tada, S. Bio-orthogonal and combinatorial approaches for the design of binding growth factors. *Biomaterials* **2013**, *34*, 7565–7574. [CrossRef]
2. Fu, R.H.; Wang, Y.C.; Liu, S.P.; Huang, C.M.; Kang, Y.H.; Tsai, C.H.; Shyu, W.C.; Lin, S.Z. Differentiation of stem cells: Strategies for modifying surface biomaterials. *Cell Transplant.* **2011**, *20*, 37–47. [CrossRef]
3. Masters, K.S. Covalent growth factor immobilization strategies for tissue repair and regeneration. *Macromol. Biosci.* **2011**, *11*, 1149–1163. [CrossRef]
4. Kusamori, K.; Takayama, Y.; Nishikawa, M. Stable Surface Modification of Mesenchymal Stem Cells Using the Avidin-Biotin Complex Technique. *Curr. Protoc. Stem Cell Biol.* **2018**, *47*, e66. [CrossRef] [PubMed]
5. Sengupta, P.; Prasad, B.L.V. Surface Modification of Polymers for Tissue Engineering Applications: Arginine Acts as a Sticky Protein Equivalent for Viable Cell Accommodation. *ACS Omega* **2018**, *3*, 4242–4251. [CrossRef] [PubMed]
6. Mahla, R.S. Stem Cells Applications in Regenerative Medicine and Disease Therapeutics. *Int. J. Cell Biol.* **2016**, *2016*, 6940283. [CrossRef] [PubMed]
7. Gimble, J.M.; Katz, A.J.; Bunnell, B.A. Adipose-derived stem cells for regenerative medicine. *Circ. Res.* **2007**, *100*, 1249–1260. [CrossRef] [PubMed]
8. Dellatore, S.M.; Garcia, A.S.; Miller, W.M. Mimicking Stem Cell Niches to Increase Stem Cell Expansion. *Curr. Opin. Biotechnol.* **2008**, *19*, 534–540. [CrossRef]
9. Lu, Z.; Roohani-Esfahani, S.I.; Wang, G.; Zreiqat, H. Bone Biomimetic Microenvironment Induces Osteogenic Differentiation of Adipose Tissue-derived Mesenchymal Stem Cells. *Nanomedicine* **2012**, *8*, 507–515. [CrossRef]
10. Donnelly, H.; Salmeron-Sanchez, M.; Dalby, M.J. Designing Stem Cell Niches for Differentiation and Self-renewal. *J. R. Soc. Interface* **2018**, *15*, 20180388. [CrossRef] [PubMed]
11. Chen, H.-Y.; Lahann, J. Designable Biointerfaces Using Vapor-Based Reactive Polymers. *Langmuir* **2010**, *27*, 34–48. [CrossRef]
12. Sun, H.-Y.; Fang, C.-Y.; Lin, T.-J.; Chen, Y.-C.; Lin, C.-Y.; Ho, H.-Y.; Chen, M.H.C.; Yu, J.; Lee, D.-J.; Chang, C.-H.; et al. Thiol-Reactive Parylenes as a Robust Coating for Biomedical Materials. *Adv. Mater. Interfaces* **2014**, *1*. [CrossRef]
13. Tsai, Y.-T.; Wu, C.-Y.; Guan, Z.-Y.; Sun, H.-Y.; Cheng, N.-C.; Yeh, S.-Y.; Chen, H.-Y. Topologically Controlled Cell Differentiation Based on Vapor-Deposited Polymer Coatings. *Langmuir* **2017**, *33*, 8943–8949. [CrossRef] [PubMed]
14. Lahann, J.; Langer, R. Novel Poly(p-xylylenes): Thin Films with Tailored Chemical and Optical Properties. *Macromolecules* **2002**, *35*, 4380–4386. [CrossRef]
15. Sauerbrey, G. Verwendung von Schwingquarzen zur Wägung dünner Schichten und zur Mikrowägung. *Z. Phys.* **1959**, *155*, 206–222. [CrossRef]
16. Wu, C.-Y.; Liu, H.-Y.; Huang, C.-W.; Yeh, S.-Y.; Cheng, N.-C.; Ding, S.-T.; Chen, H.-Y. Synergistically Controlled Stemness and Multilineage Differentiation Capacity of Stem Cells on Multifunctional Biointerfaces. *Adv. Mater. Interfaces* **2017**, *4*, 1700243. [CrossRef]
17. Zheng, C.H.; Levenston, M.E. Fact versus artifact: Avoiding erroneous estimates of sulfated glycosaminoglycan content using the dimethylmethylene blue colorimetric assay for tissue-engineered constructs. *Eur. Cells Mater.* **2015**, *29*, 224–236. [CrossRef]
18. Kraus, N.A.; Ehebauer, F.; Zapp, B.; Rudolphi, B.; Kraus, B.J.; Kraus, D. Quantitative assessment of adipocyte differentiation in cell culture. *Adipocyte* **2016**, *5*, 351–358. [CrossRef]
19. Zuk, P.A.; Zhu, M.; Ashjian, P.; De Ugarte, D.A.; Huang, J.I.; Mizuno, H.; Alfonso, Z.C.; Fraser, J.K.; Benhaim, P.; Hendrick, M.H. Human Adipose Tissue is a Source of Multipotent Stem Cells. *Mol. Biol. Cell* **2002**, *13*, 4279–4295. [CrossRef]
20. Livak, K.J.; Schmittgen, T.D. Analysis of relative gene expression data using real-time quantitative PCR and the 2(-Delta Delta C(T)) Method. *Methods* **2001**, *25*, 402–408. [CrossRef]
21. Tsai, M.-Y.; Lin, C.-Y.; Huang, C.-H.; Gu, J.-A.; Huang, S.-T.; Yu, J.; Chen, H.-Y. Vapor-based synthesis of maleimide-functionalized coating for biointerface engineering. *Chem. Commun.* **2012**, *48*, 10969–10971. [CrossRef]
22. Hoyle, C.E.; Bowman, C.N. Thiol-ene click chemistry. *Angew. Chem. Int. Ed. Engl.* **2010**, *49*, 1540–1573. [CrossRef] [PubMed]
23. Brewer, C.F.; Riehm, J.P. Evidence for possible nonspecific reactions between N-ethylmaleimide and proteins. *Anal. Biochem.* **1967**, *18*, 248–255. [CrossRef]
24. Chen, Y.C.; Sun, T.P.; Su, C.T.; Wu, J.T.; Lin, C.Y.; Yu, J.; Huang, C.W.; Chen, C.J.; Chen, H.Y. Sustained immobilization of growth factor proteins based on functionalized parylenes. *ACS Appl. Mater. Interfaces* **2014**, *6*, 21906–21910. [CrossRef] [PubMed]
25. Wu, J.-T.; Sun, T.-P.; Huang, C.-W.; Su, C.-T.; Wu, C.-Y.; Yeh, S.-Y.; Yang, D.-K.; Chen, L.-C.; Ding, S.-T.; Chen, H.-Y. Tunable coverage of immobilized biomolecules for biofunctional interface design. *Biomater. Sci.* **2015**, *3*, 1266–1269. [CrossRef]
26. Della Ventura, B.; Sakac, N.; Funari, R.; Velotta, R. Flexible immunosensor for the detection of salivary alpha-amylase in body fluids. *Talanta* **2017**, *174*, 52–58. [CrossRef] [PubMed]
27. Sun, T.P.; Tai, C.H.; Wu, J.T.; Wu, C.Y.; Liang, W.C.; Chen, H.Y. Multifaceted and route-controlled click reactions based on vapor-deposited coatings. *Biomater. Sci.* **2016**, *4*, 265–271. [CrossRef]
28. Pagán, M.; Suazo, D.; Del Toro, N.; Griebenow, K. A Comparative Study of Different Protein Immobilization Methods for the Construction of an Efficient Nano-structured Lactate Oxidase-SWCNT-biosensor. *Biosens. Bioelectron.* **2015**, *64*, 138–146. [CrossRef] [PubMed]
29. Chou, C.H.; Modo, M. Human neural stem cell-induced endothelial morphogenesis requires autocrine/paracrine and juxtacrine signaling. *Sci. Rep.* **2016**, *6*, 29029. [CrossRef]

30. Shi, Y.; Massagué, J. Mechanisms of TGF-β Signaling from Cell Membrane to the Nucleus. *Cell* **2003**, *113*, 685–700. [CrossRef]
31. Mueller, T.D. Chapter One—Mechanisms of BMP–Receptor Interaction and Activation. In *Vitamins & Hormones*; Litwack, G., Ed.; Academic Press: Los Angeles, CA, USA, 2015; Volume 99, pp. 1–61.
32. Shea, C.M.; Edgar, C.M.; Einhorn, T.A.; Gerstenfeld, L.C. BMP Treatment of C3H10T1/2 Mesenchymal Stem Cells Induces Both Chondrogenesis and Osteogenesis. *J. Cell. Biochem.* **2003**, *90*, 1112–1127. [CrossRef]
33. Lee, S.Y.; Lee, J.H.; Kim, J.Y.; Bae, Y.C.; Suh, K.T.; Jung, J.S. BMP2 increases adipogenic differentiation in the presence of dexamethasone, which is inhibited by the treatment of TNF-alpha in human adipose tissue-derived stromal cells. *Cell. Physiol. Biochem.* **2014**, *34*, 1339–1350. [CrossRef] [PubMed]
34. Sottile, V.; Seuwen, S. Bone morphogenetic protein-2 stimulates adipogenic di¡erentiation of mesenchymal precursor cells in synergy with BRL 49653 (rosiglitazone). *FEBS Lett.* **2000**, *475*, 201–204. [CrossRef]
35. Vanhatupa, S.; Ojansivu, M.; Autio, R.; Juntunen, M.; Miettinen, S. Bone Morphogenetic Protein-2 Induces Donor-Dependent Osteogenic and Adipogenic Differentiation in Human Adipose Stem Cells. *Stem Cells Transl. Med.* **2015**, *4*, 1391–1402. [CrossRef] [PubMed]
36. Chiou, M.; Xu, Y.; Longaker, M.T. Mitogenic and Chondrogenic Effects of Fibroblast Growth Factor-2 in Adipose Derived Mesenchymal Cells. *Biochem. Biophys. Res. Commun.* **2006**, *343*, 644–652. [CrossRef]
37. Hankemeier, S.; Keus, M.; Zeichen, J.; Jagodzinski, M.; Barkhausen, T.; Bosch, U.; Krettek, C.; Van Griensven, M. Modulation of Proliferation and Differentiation of Human Bone Marrow Stromal Cells by Fibroblast Growth Factor 2: Potential Implication for Tissue Engineering of Tendons and Ligaments. *Tissue Eng.* **2005**, *11*, 41–49. [CrossRef] [PubMed]
38. Kakudo, N.; Shimotsuma, A.; Kusumoto, K. Fibroblast Growth Factor-2 Stimulates Adipogenic Differentiation of Human Adipose-derived Stem Cell. *Biochem. Biophys. Res. Commun.* **2007**, *395*, 239–244. [CrossRef]
39. Merrell, A.J.; Stanger, B.Z. Adult cell plasticity in vivo: De-differentiation and transdifferentiation are back in style. *Nat. Rev. Mol. Cell Biol.* **2016**, *17*, 413–425. [CrossRef]
40. Chiacchiera, F.; Morey, L.; Mozzetta, C. Editorial: Epigenetic Regulation of Stem Cell Plasticity in Tissue Regeneration and Disease. *Front. Cell Dev. Biol.* **2020**, *8*, 82. [CrossRef]
41. Hernigou, P.; Poignard, A.; Beaujean, F.; Rouard, H. Percutaneous Autologous Bone-Marrow Grafting for Nonunions: Influence of the Number and Concentration of Progenitor Cells. *JBJS* **2005**, *87*, 1430–1437. [CrossRef]
42. Giuliani, N.; Lisignoli, G.; Magnani, M.; Racano, C.; Bolzoni, M.; Dalla Palma, B.; Spolzino, A.; Manferdini, C.; Abati, C.; Toscani, D.; et al. New Insights into Osteogenic and Chondrogenic Differentiation of Human Bone Marrow Mesenchymal Stem Cells and Their Potential Clinical Applications for Bone Regeneration in Pediatric Orthopaedics. *Stem Cells Int.* **2013**, *2013*, 312501. [CrossRef]
43. Chen, H.; Wang, H.; Li, B.; Feng, B.; He, X.; Fu, W.; Yuan, H.; Xu, Z. Enhanced chondrogenic differentiation of human mesenchymal stems cells on citric acid-modified chitosan hydrogel for tracheal cartilage regeneration applications. *RSC Adv.* **2018**, *8*, 16910–16917. [CrossRef]
44. Tan, S.S.; Ng, Z.Y.; Zhan, W.; Rozen, W. Role of Adipose-derived Stem Cells in Fat Grafting and Reconstructive Surgery. *J. Cutan. Aesthet. Surg.* **2016**, *9*, 152–156. [CrossRef] [PubMed]
45. Yoshimura, K.; Sato, K.; Aoi, N.; Kurita, M.; Inoue, K.; Suga, H.; Eto, H.; Kato, H.; Hirohi, T.; Harii, K. Cell-assisted lipotransfer for facial lipoatrophy: Efficacy of clinical use of adipose-derived stem cells. *Dermatol. Surg.* **2008**, *34*, 1178–1185. [CrossRef]
46. Yoshimura, K.; Sato, K.; Aoi, N.; Kurita, M.; Hirohi, T.; Harii, K. Cell-assisted lipotransfer for cosmetic breast augmentation: Supportive use of adipose-derived stem/stromal cells. *Aesthetic Plast. Surg.* **2008**, *32*, 48–57. [CrossRef] [PubMed]
47. Cooper, G.M. *The Cell: A Molecular Approach*, 2nd ed.; Sinauer Associates: Sunderland, MA, USA, 2000.

coatings

MDPI

Article

Vapor-Phase Fabrication of a Maleimide-Functionalized Poly-*p*-xylylene with a Three-Dimensional Structure

Shu-Man Hu [1,†], Chin-Yun Lee [1,†], Yu-Ming Chang [1], Jia-Qi Xiao [1], Tatsuya Kusanagi [1], Ting-Ying Wu [1], Nai-Yun Chang [1], Jane Christy [1], Ya-Ru Chiu [1], Chao-Wei Huang [2], Yen-Ching Yang [1,*], Yu-Chih Chiang [3,4,*] and Hsien-Yeh Chen [1,4,5,*]

[1] Department of Chemical Engineering, National Taiwan University, Taipei 10617, Taiwan; r09524083@ntu.edu.tw (S.-M.H.); r09524048@ntu.edu.tw (C.-Y.L.); r09524079@ntu.edu.tw (Y.-M.C.); r09524013@ntu.edu.tw (J.-Q.X.); r09524111@ntu.edu.tw (T.K.); tilee824@gmail.com (T.-Y.W.); Changnaiyun@ntu.edu.tw (N.-Y.C.); b07504085@ntu.edu.tw (J.C.); iwbs24921@gmail.com (Y.-R.C.)
[2] Department of Tropical Agriculture and International Cooperation, National Pingtung University of Science and Technology, Pingtung 912301, Taiwan; cwhuang@mail.npust.edu.tw
[3] School of Dentistry, Graduate Institute of Clinical Dentistry, National Taiwan University and National Taiwan University Hospital, Taipei 10048, Taiwan
[4] Molecular Imaging Center, National Taiwan University, Taipei 10617, Taiwan
[5] Advanced Research Center for Green Materials Science and Technology, National Taiwan University, Taipei 10617, Taiwan
* Correspondence: youngeddie.tw@googlemail.com (Y.-C.Y.); munichiang@ntu.edu.tw (Y.-C.C.); hsychen@ntu.edu.tw (H.-Y.C.); Tel.: +886-2-33669476 (H.-Y.C.)
† Authors contributed equally to this work.

Abstract: A vapor-phase process, involving the sublimation of an ice substrate/template and the vapor deposition of a maleimide-functionalized poly-*p*-xylylene, has been reported to synthesize an advanced porous material, with readily clickable chemical interface properties, to perform a Michael-type addition of a maleimide functionality for conjugation with a thiol group. In contrast to the conventional chemical vapor deposition of poly-*p*-xylylenes on a solid surface that forms thin film coatings, the process reported herein additionally results in deposition on a dynamic and sublimating ice surface (template), rendering the construction of a three-dimensional, porous, maleimide-functionalized poly-*p*-xylylene. The process seamlessly exploits the refined chemical vapor deposition polymerization from maleimide-substituted [2,2]paracyclophane and ensures the preservation and transformation of the maleimide functionality to the final porous poly-*p*-xylylene products. The functionalization and production of a porous maleimide-functionalized poly-*p*-xylylene were completed in a single step, thus avoiding complicated steps or post-functionalization procedures that are commonly seen in conventional approaches to produce functional materials. More importantly, the equipped maleimide functionality provides a rapid and efficient route for click conjugation toward thiol-terminated molecules, and the reaction can be performed under mild conditions at room temperature in a water solution without the need for a catalyst, an initiator, or other energy sources. The introduced vapor-based process enables a straightforward synthesis approach to produce not only a pore-forming structure of a three-dimensional material, but also an in situ-derived maleimide functional group, to conduct a covalent click reaction with thiol-terminal molecules, which are abundant in biological environments. These advanced materials are expected to have a wide variety of new applications.

Keywords: vapor sublimation and deposition; functional poly-*p*-xylylene; maleimide; porous material; orthogonal conjugation

Citation: Hu, S.-M.; Lee, C.-Y.; Chang, Y.-M.; Xiao, J.-Q.; Kusanagi, T.; Wu, T.-Y.; Chang, N.-Y.; Christy, J.; Chiu, Y.-R.; Huang, C.-W.; et al. Vapor-Phase Fabrication of a Maleimide-Functionalized Poly-*p*-xylylene with a Three-Dimensional Structure. *Coatings* **2021**, *11*, 466. https://doi.org/10.3390/coatings11040466

Academic Editor: Alessandro Patelli

Received: 12 March 2021
Accepted: 13 April 2021
Published: 16 April 2021

1. Introduction

Porous materials, owing to their remarkable interface properties, have been widely applied in sensing, catalysis, biomedical, drug delivery, adsorption/desorption applications, etc. [1–4]. These applications can especially be highlighted in their drug delivery and emerging biomedical applications due to the multiple premium interface properties that are required [5,6]. The benefits of porous structures are attributed to their large surface area, the adjustable number of pores, and a functionalized surface, which can provide multifunctional active sites [7]. In addition to porous properties, bioconjugation functionalities that provide selectivity and orthogonal reactivity, while avoiding any side reactions in the vast and diverse conditions of biological microenvironments, are key to achieving successful biointerface construction. For example, thiol–maleimide "click" chemistry and maleimide functional polymers selectively target thiol-containing cysteine residues in proteins and enzymes, with excellent levels of selective conjugation being achieved. Cysteine-reactive polymers can be applied to prevent the degradation of sensitive poly(ester) backbones [8]. In addition, the prototypical click chemistry reaction, Cu(I)-catalyzed azide–alkyne cycloaddition (CuAAC), involves a modification to the triazole-forming 1,3-dipolar cycloaddition. The application of CuAAC to produce fluorogenic compounds would be a powerful way to track biomolecules in the cell [9]. Specific reactions can also be applied for protein modification. The ligation between trans-cyclooctene and 3,6-di-(2-pyridyl)-s-tetrazine enables protein modification at low concentrations. This reaction can tolerate multiple functional groups and proceed in high-yield organic solvents, water, or cell media [10]. Recently, many bio-orthogonal reactions have been developed that enable the efficient formation of a specific product in complex environments, which is particularly beneficial for biological research [11].

These fascinating chemistries, however, have seldom been exploited during the fabrication of porous materials and are sporadically seen using complicated synthetic approaches [12] or by post-modification attempts, which involve using harsh solvents or potentially harmful chemicals during the modification process [13,14].

In the current study, we introduced a simple and versatile approach, based on a vapor-phase fabrication process, to produce a functionalized porous polymer material. Fabrication occurred by the vapor deposition of a poly-*p*-xylylene polymer on an iced substrate (vapor sublimation), which was discovered in our previous reports, and was compared to the conventional vapor deposition of poly-*p*-xylylene on a still and nonsublimated substrate to produce a thin, dense coating [15]. This sublimation mechanism resulted in the formation of a porous poly-*p*-xylylene monolith [16,17]. Such a unique fabrication process, with the use of doped ice templates, has also been exploited to fabricate tissue repair membranes [18] and scaffolds for stem cell cultures [19]; however, only composites combined with other functional materials have been used for these works in the past. On the other hand, the functionalization of the poly-*p*-xylylene polymers can be prepared by modifying the substituents of [2,2]paracyclophane precursors, and a variety of such substitutions have been produced for functionalized poly-*p*-xylylene polymer and copolymer coatings and applications [20–32]. Therefore, in the current work, we hypothesized that maleimide-substituted [2,2]paracyclophane could be used during vapor sublimation on an iced substrate, and that vapor deposition by such a precursor can produce a maleimide-functionalized poly-*p*-xylylene in porous and monolith forms (Figure 1). Compared to the maleimide-functionalized coating prepared previously [33], the current monolith poly-*p*-xylylene comprised (i) porous and structural information in three dimensions and (ii) a maleimide functionality that exhibits specific reactivity toward thiol-terminated biomolecules. This unique fabrication process, and the resultant polymer product, combines interface properties from its surface porosity, topology, and specific chemical reactivity and provides a robust tool with enhanced synergistic ability for biointerface engineering.

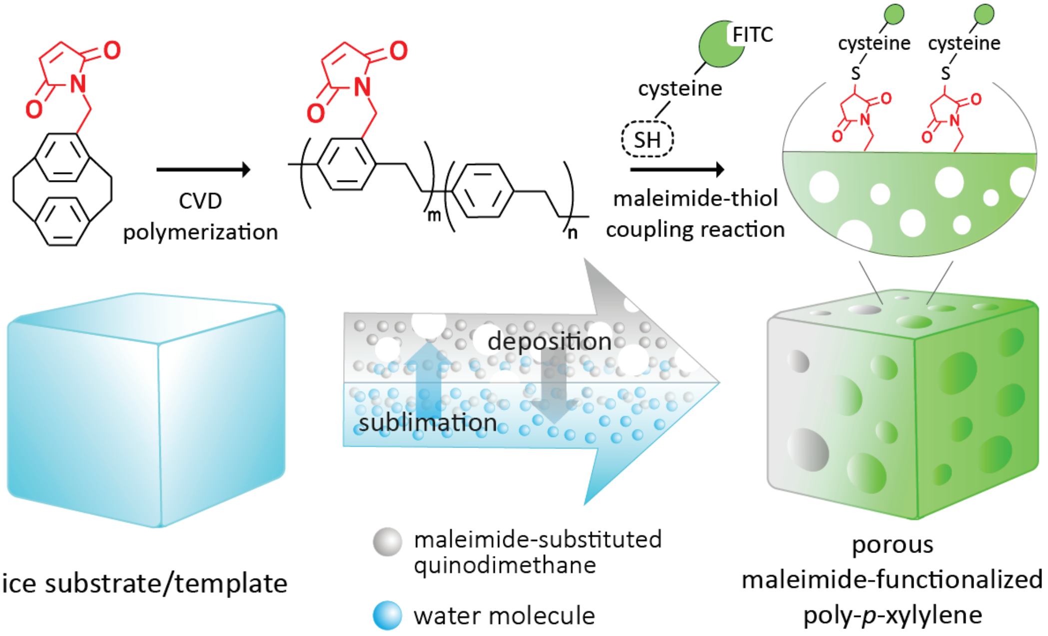

Figure 1. A schematic illustration of vapor-phase fabrication by chemical vapor deposition polymerization of 4-N-maleimidomethyl-[2,2]paracyclophane on a sublimating ice substrate/template to construct a porous and maleimide-functionalized poly-*p*-xylylene material. The resultant functional material exhibits interface chemical properties and is readily able to perform the maleimide-thiol click reaction under mild conditions.

2. Materials and Methods

2.1. Fabrication Process

For the production of poly-*p*-xylylene three-dimensional porous materials, cube-shaped ice templates, with the dimensions of 300 µm × 300 µm × 300 µm, were prepared in order to prove the concept of the reported fabrication process. Using a negative mold of polydimethylsiloxane (PDMS) with the same dimensions to prepare this ice template, it was created as previously reported for the PDMS mold [34]. For the preparation of the ice templates, deionized water was held in the PDMS mold, and then the solution underwent a solidification process using a liquid nitrogen bath to transform the water into ice, which was then retrieved from the PDMS mold after a few minutes to obtain the ice templates. The obtained ice templates were then used for further vapor sublimation and deposition processes. During the vapor deposition, 4-N-maleimidomethyl-[2,2]paracyclophane was used as the starting material, and the monomer was polymerized and deposited to form poly[(4-N-maleimidomethyl-*p*-xylylene)-co-(p-xylylene)] via chemical vapor deposition (CVD) polymerization. The starting materials were vaporized under reduced pressure at 100 mTorr and approximately 90 °C, followed by pyrolysis at approximately 670 °C, for conversion to highly reactive monomers. During the vapor sublimation, the prepared ice templates were placed in the chamber with an operating environment of approximately 4 °C and 100 mTorr, which is below the triple point for ice. From a thermodynamic point of view, ice naturally undergoes a sublimation process from the solid phase to the vapor phase. Under the same conditions, the vapor-phase monomer of the maleimide-functionalized poly-*p*-xylylene underwent polymerization and was then simultaneously deposited onto the ice surface. During the above fabrication process, argon gas, with a mass flow rate of 20 sccm (standard cubic centimeter per minute), was used as a carrier gas for transporting the starting material for the sublimation of the maleimide-substituted [2,2]paracyclophane.

Depending on the feed amount of the starting material, the deposition rate was adjusted to approximately 0.5 to 1.0 Å/s and monitored by a real-time quartz crystal microbalance (QCM) sensor (STM-100/MF, East Syracuse, NY, USA) mounted in the deposition chamber.

2.2. Characterizations

Ice substrate/template images were recorded by using a cryo-SEM (scanning electron microscope) instrument (Tabletop TM-3000, Hitachi, Tokyo, Japan), and the samples were examined at the sample stage by cooling with a continuous supply of liquid nitrogen. SEM was performed with an electron energy of 15 keV and a pressure of 100 mTorr. The detection of poly-*p*-xylylene bulks was performed with a Nova NanoSEM 230 scanning electron microscope (FEI, Hillsboro, OR, USA) that was operated at room temperature under a reduced pressure of 4×10^{-6} Torr. A micro-CT (micro computed tomography) X-ray imaging system (SkyScan 1176, Bruker, Billerica, MA, USA) was used to examine the three-dimensional images of the porous structures that scanned the sample at 40 kV. The scanning resolution was 9 µm voxels with an integration time of 2000 ms per projection. The acquired projection images were converted into three dimensional (3D) images using CTvox software (Bruker, Billerica, MA, USA). The FTIR spectra were recorded with a Spectrum 100 FTIR spectrometer (PerkinElmer, Waltham, MA, USA). During spectral acquisition, a liquid nitrogen-cooled mercury–cadmium–telluride (MCT) detector and an advanced grazing angle specular reflectance accessory (PIKE Technologies, Fitchburg, WI, USA) were applied. The scanning range was from 500 cm^{-1} to 4000 cm^{-1} with 64 acquisitions each time. The X-ray photoelectron spectroscopy (XPS) was completed using monochromatic Al K-alpha radiation as the X-ray source with 150 kW of power. The process was performed with a Theta Probe X-ray photoelectron spectrometer (Thermo Scientific, Leicestershire, UK). Elemental analysis of high-resolution C1s was performed at a flux energy level of 20 eV, and the experimental results were compared with the theoretical (calculated) values based on the proposed chemical structures. Analysis of the real-time mass spectra was carried out with a residual gas analyzer (RGA, Hiden Analytical, Warrington, UK) mounted on the deposition chamber. The RGA was operated at 10^{-9} Torr in an ultrahigh vacuum with an ionizing emission current of 20 µA and ionizing electron energy of 70 eV. The fluorescence images were obtained with a TCS SP5 CLSM confocal laser-scanning microscope (Leica Microsystems, Wetzlar, Germany) with an Ar/ArKr laser light source (wavelength: 488 nm) to detect the fluorescein (FITC)-labeled cysteine (emission wavelength: 505–525 nm).

2.3. Conjugations

The conjugation of FITC-labeled cysteine (Thermo Fisher Scientific, Waltham, MA, USA) was carried out by the reaction of a 5 mM molecular solution of FITC-labeled cysteine with the thiol groups of a manufactured sample of porous material for 4 h at 20 °C. To remove excess and unreacted reagents from the conjugated samples, a washing process was performed using the following procedure: wash three times with phosphate buffered saline (PBS, pH = 7.4, containing Tween 20, Sigma-Aldrich, St. Louis, MO, USA), once with PBS (without Tween 20) and finally rinse with deionized water.

3. Results and Discussion

To fabricate the proposed maleimide-functionalized poly-*p*-xylylene materials, ice templates were first constructed, and a reported mechanism showed that the vapor deposition of polychloro-*p*-xylylene on a dynamic substrate of the sublimating ice can result in a final porous and three-dimensional polychloro-*p*-xylylene material [17]. Theoretically, other poly-*p*-xylylene systems, such as its functionalized derivatives [15] and the maleimide-functionalized poly-*p*-xylylene proposed herein, which have been deposited using the same conventional chemical vapor deposition (CVD) polymerization, should be extendable and applied on an ice substrate. Thus, in this experiment, the preparation of the ice substrates/templates was enabled by using a polydimethylsiloxane (PDMS) mold, with the dimensions of 300 µm × 300 µm × 300 µm, and resulted in ice cubes with the same dimensions, analogous to how ice cubes are made. For vapor deposition, a maleimide-substituted [2,2]paracyclophane starting material was synthesized via the reported routes [33]; theoretically, in the conventional CVD polymerization, these starting materials were sublimated at approximately 90 °C under a reduced pressure of 100 mTorr and pyrolyzed at 540 °C, forming highly reactive monomer quinodimethanes species. Finally, these monomers underwent radical polymerization upon condensation at a low temperature (40 °C or below) and solid substrate formation of thin-film coatings [27,33,35]. However, in the experiments herein, the vapor deposition and polymerization occurred on the prepared ice substrates/templates and under the devised thermodynamic conditions (10 °C and under 100 mTorr). The ice substrate transformed from its solid phase to a vapor phase by sublimation, and the deposition and polymerization of quinodimethane occurred on the dynamic ice substrate instead of a conventional solid substrate. The vapor composition during the process was measured by a mass spectrometric residual gas analyzer (RGA). The recorded mass spectra in Figure 2 indicated the presence of sublimating H_2O molecules at 18 amu, the Ar carrier gas at 40 amu, and pyrolyzed quinodimethane monomers and derivatives, including N-ethylmaleimide and maleimide-substituted quinodimethane, at 104 amu, 125 amu, and 213 amu, respectively. These data support the hypothesis that the proposed vapor-phase species existed and underwent the sublimation and deposition processes at the substrate interface. The two processes finally resulted in a construction mechanism [16,17] to build a porous, three-dimensional, maleimide-functionalized poly-*p*-xylylene material. As shown in Figure 3a, the scanning electron microscopy (SEM) images revealed that the resultant porous materials represented replica structures as ice substrates/templates with the same measured dimensions (300 µm × 300 µm × 300 µm). Moreover, the formed porous structures were measured to be in the range of 3 µm to 45 µm, which was confirmed with an average of 20 µm based on micro-computed tomography (micro-CT) analysis (Figure 3b). In addition, the expected interconnection of the pores due to the voids of vapor sublimation and the nucleated polymerization of the poly-*p*-xylylene was confirmed by the reconstructed micro-CT scanning images in Figure 3b, and a video is also included in the Supplementary Materials. From the pore distribution data, the total porosity was 53.8%, of which open porosity accounts for the majority (99.8%). There is an advantage to this structure when combining cell therapy or drug delivery. This structure is beneficial for cell growth, as open pores will not stop drugs from moving, and the drug can also be released smoothly to work in the open pore. Moreover, with closed pores, the materials will be blocked from the outside. However, closed pores only account for 0.2% of the total pores. Various types of porosity and pore sizes were computed during the micro-CT analysis (Figure 3c). Hence, in this study, we demonstrate that micro-CT is versatile in evaluating scaffolds and is able to characterize them from multiple aspects.

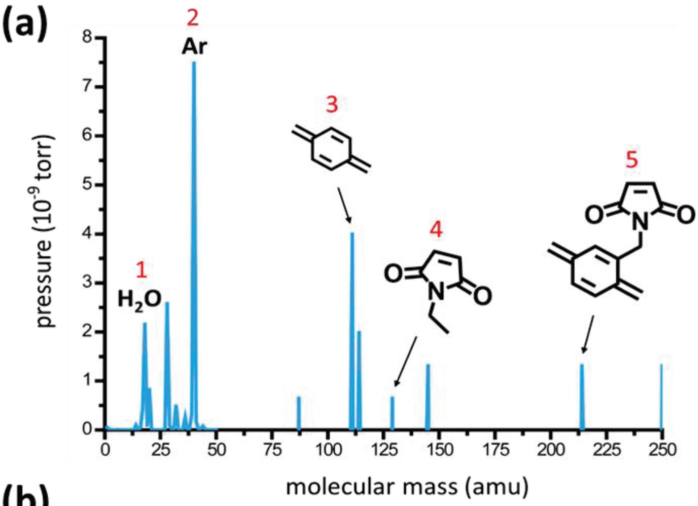

(b)

No.	Composition	Molecular Mass (amu)	Pressure (10^{-9} torr)
1	H_2O	18	2.2
2	Ar	40	7.5
3	quinodimethane	104	4
4	N-ethylmaleimide	125	0.6
5	maleimide-substituted quinodimethane	213	1.4

Figure 2. The characterizations of the vapor compositions, based on mass spectrometric analysis using a (residual gas analyzer) RGA during the fabrication process. The recorded mass spectra in (**a**) show the presence of 5 expected molecules: (1) the sublimating water molecules at 18 amu, (2) the carrier gas of argon at 40 amu, (3) the depositing quinodimethane at 104 amu, (4) a fraction of N-ethylmaleimide at 125 amu, and (5) the maleimide-substituted quinodimethane at 213 amu. (**b**) A table summarizing the details of the detected molecules in the vapor compositions.

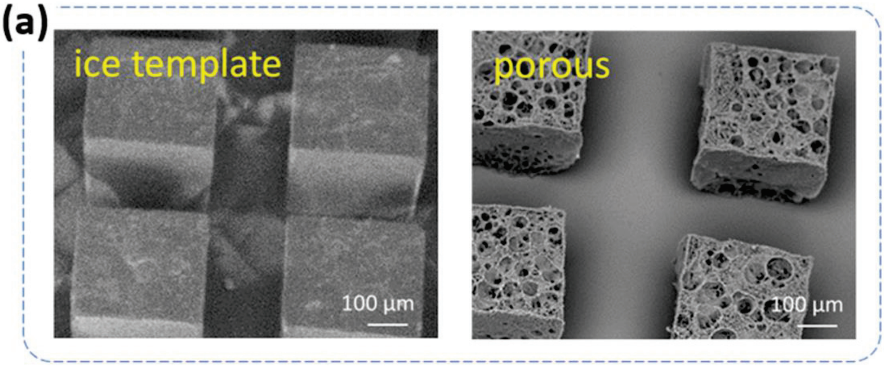

Figure 3. *Cont.*

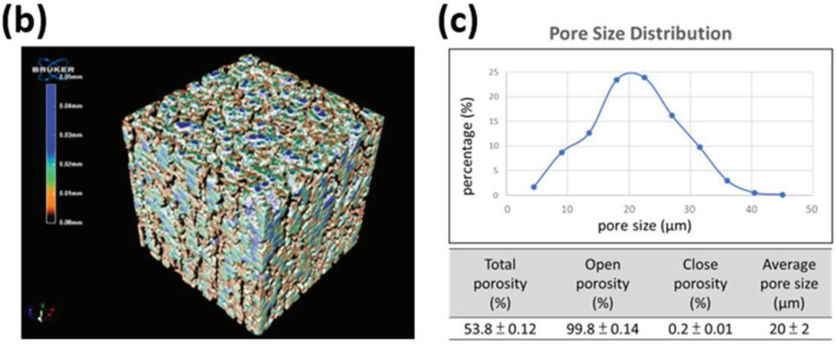

Total porosity (%)	Open porosity (%)	Close porosity (%)	Average pore size (µm)
53.8 ± 0.12	99.8 ± 0.14	0.2 ± 0.01	20 ± 2

Figure 3. The characterization of the porous structures and porosity. (**a**) Scanning electron microscopy (SEM) images showed that cube-shaped ice templates, with the dimensions of 300 µm × 300 µm × 300 µm, were used to form porous maleimide-functionalized poly-*p*-xylylene materials by the proposed fabrication method. (**b**) A reconstructed micro-CT image shows the three-dimensional structure and the pore structures. (**c**) The calculated pore size distribution based on a micro-CT analysis suggests an interconnected pore structure (high open porosity) with an average porosity of 53.8 ± 0.12% and an average pore size of 20 ± 2 µm.

Furthermore, the chemical structures of the resulting porous materials were verified by using Fourier transform infrared (FT-IR) spectroscopy, X-ray photoelectron spectroscopy (XPS), and mass spectrometry analysis. As shown in Figure 4, the FT-IR spectra compared the characteristic peaks of the porous materials of the maleimide-functionalized poly-*p*-xylylene with the thin-film form of this polymer that was deposited on a conventional, gold-coated silicon wafer solid substrate. The verification of the maleimide functionality was found from the peaks between 1704 to 1775 cm^{-1} that were attributed to C=O bands, while the peak at 1345 cm^{-1} was from the C-N bond of maleimide. Additionally, the characteristic peaks widely seen for poly-*p*-xylylenes and their derivatives were also observed from 2920 to 2854 cm^{-1} [26,27,30,32,33,36]. Compared to the pure poly-*p*-xylylene, the spectra of the maleimide-functionalized poly-*p*-xylylene were found to be significantly higher with the peaks of C=O and C-N bonds. In addition, the comparison with pure (non-functionalized) poly-*p*-xylylene spectra showed an absence of C=O and C-N bonds for the pure poly-*p*-xylylene, and strong aromatic C=C bands (1530 to 1480 cm^{-1}) were discovered for the pure poly-*p*-xylylene but weak bands were discovered for the maleimide-functionalized poly-*p*-xylylene groups. The variations in the aromatic C=C bands, and in other fingerprint regions for different poly-p-xylylene derivatives, were also previously reported [30,33,37,38]. On the other hand, XPS analyses confirmed the molecular compositions and chemical structures. As shown in the XPS high-resolution C_{1s} spectrum (Figure 5), the signal at 285.0 eV belonged to the aliphatic and aromatic carbons (C–C, C–H). In addition, the 76.7 atom% intensity was consistent with the theoretical concentration of 76.2 atom%, and the anticipated binding states, including C-C=O, C-N, O=C-N, and $\pi \rightarrow \pi^*$ transition bonds (indicated in the enlarged image), were also analyzed. The characteristic signals at 286.0 eV and 286.7 eV, whose calculated values were 9.6 atom% and 4.6 atom%, respectively, corresponded to the C–C=O and C–N bonds matching the theoretical values of 9.5 atom% and 4.8 atom%, respectively. The signal at 289.2 eV had a comparably low value from O=C–N bonds (6.7 atom% compared to the theoretical value of 9.5 atom%), and the signal at 291.5 eV (2.4 atom%) indicated $\pi \rightarrow \pi^*$ transitions that are characteristic of aromatic polymers and have been reported for other functionalized poly-*p*-xylylenes [38]. Collectively, the combined FT-IR and XPS data confirm the chemical structures and support the assumption of the synthesized porous maleimide-functionalized poly-*p*-xylylene materials.

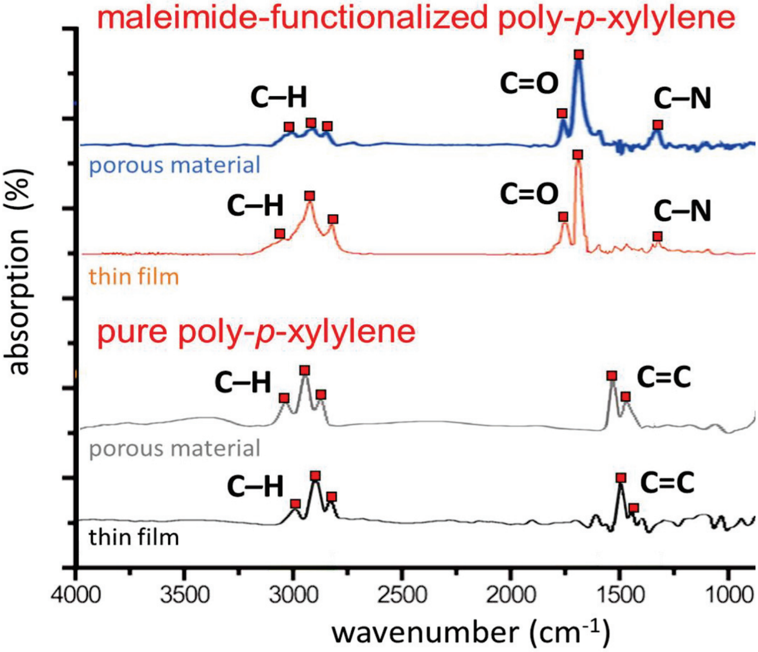

Figure 4. Fourier transform infrared (FT-IR) analysis showed consistent spectra. Characteristic peaks of the maleimide-functionalized poly-*p*-xylylene were detected for C-H, C=O, and C-N on the fabricated porous materials. The results were compared to a thin-film maleimide-functionalized poly-*p*-xylylene and pure (non-functionalized) poly-*p*-xylylenes.

To further verify the maleimide functionality of the fabricated 3D porous materials that would be available to perform bio-orthogonal reactions toward thiol-terminated molecules, we devised a series of conjugation experiments for the fabricated samples. The maleimide functionality enabled a Michael-type addition that crossed the unsaturated carbon–carbon bonds of the maleimide moiety and specifically reacted with a thiol group. The reaction represented a class of mild, but specific, reactions that were able to conjugate thiol-terminated molecules (widely available in biological systems) at room temperature and in water solvents without the need for metal catalysts, a high temperature, or UV irradiation. Analogous to a series of click reactions, including thiol-ene or thiol-yne reactions and azide–alkyne 1,3-dipolar cycloaddition, the maleimide-thiol coupling reaction has also been described due to its click characteristics and benign reaction conditions [39]. In these experiments, fluorescein (FITC)-labeled cysteines were selected as a model molecule for demonstration, and via the aforementioned reaction mechanism, maleimide specifically clicked to the thiol terminus of a cysteine residue (i.e., the distributed maleimide functionality at the material interface readily reacted with cysteine-FITC, and green-channeled FITC fluorescence signals were therefore detected in the expected and registered areas). As indicated in Figure 6, the FITC signals detected by the confocal laser scanning microscopy (CLSM) showed the same 300 μm × 300 μm × 300 μm array patterns that were consistent in both the ice substrates/templates and the fabricated maleimide-functionalized poly-*p*-xylylene porous materials. The coupling reaction ensured firm covalent bonding between the maleimide and thiol, and precise interface chemistry could be realized compared to approaches using physical adsorption and desorption, which comprise loosely bound interactions that are usually uncontrollable [40]. Therefore, in control experiments, a nonfunctionalized poly-*p*-xylylene porous material was fabricated from unsubstituted [2,2]paracyclophane, and the same ice substrates/templates were used to attempt the same conjugation reaction by applying cysteine-FITC molecules to the fabricated samples. However, due to the lack of the required maleimide functionality, only the physically and loosely bound cysteine-FITC molecules were attached to the sample surfaces; a regular wash process with detergent removed these physically adsorbed molecules from the samples, and only suppressed fluorescence signals were detected [25,30]. In addition, the CLSM images were collected along the z-axis with a devised distance interval (Z= 10 µm, 50 µm, 90 µm, 130 µm, 170 µm, 210 µm, 250 µm, and 290 µm). These images, in the specific positions shown in Figure 6, indicated distinct patterns of the attached fluorescence signals and are believed to be due to conjugation occurring on the anisotropic porous structure of a maleimide-functionalized poly-*p*-xylylene within the material's 3D architecture. The sustained intensity of the fluorescence signals after the wash process also confirmed the firm attachment of cysteine-FITC via the conjugation reaction. The fabricated maleimide-functionalized poly-*p*-xylylene materials provided a porous structure and additionally exhibited clickable functional conduct from the maleimide available on the material interface for specific targeting of thiol-terminated molecules, which are widely seen in biological systems. Such porous and functional products are expected to have unlimited applicability.

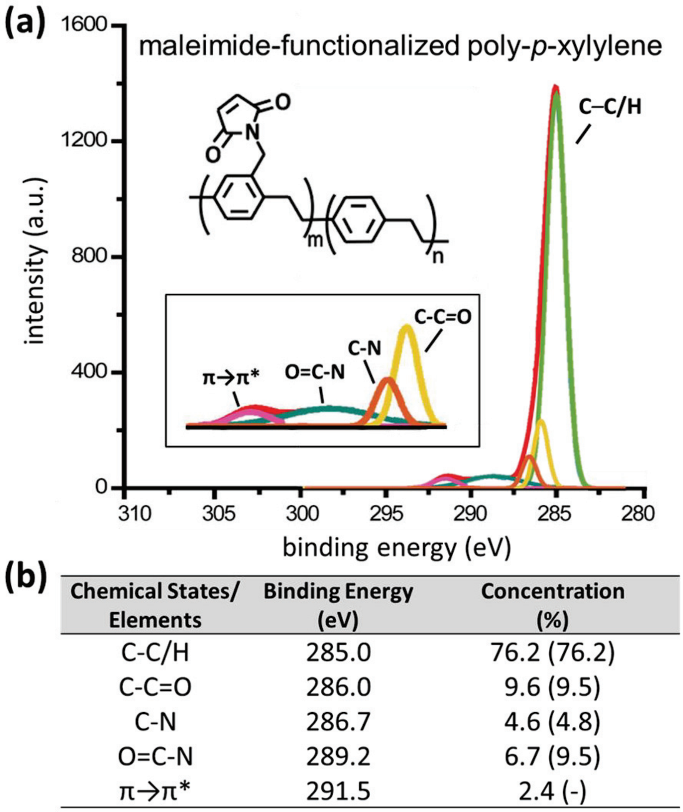

Chemical States/ Elements	Binding Energy (eV)	Concentration (%)
C-C/H	285.0	76.2 (76.2)
C-C=O	286.0	9.6 (9.5)
C-N	286.7	4.6 (4.8)
O=C-N	289.2	6.7 (9.5)
π→π*	291.5	2.4 (-)

Figure 5. (**a**) X-ray photoelectron spectroscopy (XPS) high-resolution analysis shows the recorded spectra of the fabricated porous maleimide-functionalized poly-*p*-xylylene. Details of the deconvolution spectra showing components with respect to a specific binding energy, including C-C=O, C-N, O=C-N, and π→π* transition bonds, are indicated in the enlarged image. (**b**) Detailed chemical compositions were confirmed by comparing the binding energies of the expected chemical states for the experimental values with the theoretical values (in brackets).

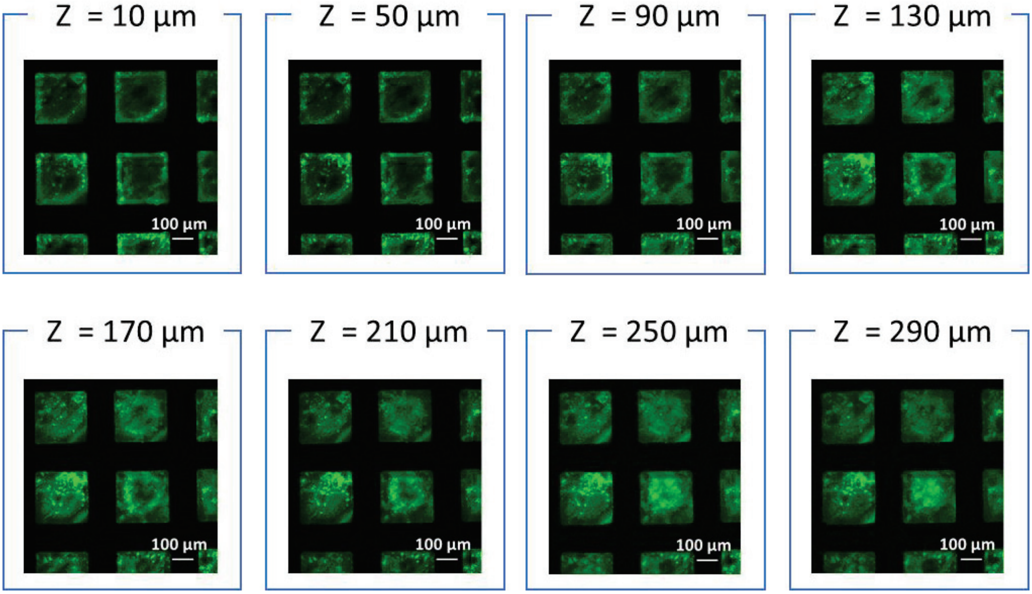

Figure 6. An analysis of the reactivity of the fabricated porous maleimide-functionalized poly-*p*-xylylenes. The fluorescence images recorded by confocal laser scanning microscopy (CLSM) showed consistent 300 µm × 300 µm arrayed patterns that confirmed the conjugation between the fluorescein (FITC)-labeled cysteine and the maleimide group on the porous materials, and the images at various Z-axes (with a 40 µm spacing interval from 10 µm to 290 µm) further verified the reactivity on the interface of the porous materials in three dimensions.

4. Conclusions

A unique fabrication process by vapor sublimation and vapor deposition to produce a porous and functionalized poly-*p*-xylylene monolith material was introduced in the current work. The monolith comprised structural information in terms of porosity and topology and, more importantly, a maleimide functional moiety for specific conjugation reactivity via a maleimide–thiol coupling reaction. The vapor-phase fabrication process was simple, clean, and free of harsh chemical agents, and the poly-*p*-xylylene used is a USP (United States Pharmacopoeia) Class VI biocompatible material, which is favorable for sensitive applications. The enhanced and synergistic interface properties, combining the porosity and chemical functionality of the fabricated porous monolith, represent robust bioengineering materials and will be useful for unlimited applications in scaffolding for tissue engineering, biosensors, bioimaging, targeted drug-eluting devices, and regenerative materials.

Supplementary Materials: The following are available online at https://www.mdpi.com/article/10.3390/coatings11040466/s1, Video S1: Reconstruction images of the three-dimensional pore structure by micro-CT.

Author Contributions: Conceptualization, S.-M.H., C.-Y.L., Y.-C.Y., Y.-C.C. and H.-Y.C.; methodology, S.-M.H., C.-Y.L., Y.-C.Y. and H.-Y.C.; precursor synthesis, T.K., T.-Y.W., N.-Y.C., J.C., Y.-R.C.; CVD polymerization and characterizations, S.-M.H., C.-Y.L., T.-Y.W., Y.-R.C.; micro-CT software analysis, J.-Q.X., and Y.-M.C.; validation, S.-M.H., C.-Y.L., T.K. and T.-Y.W.; fluorescence visualization and analysis, C.-Y.L. and C.-W.H.; XPS analysis, S.-M.H., J.C., and Y.-R.C.; FT-IR analysis S.-M.H., C.-Y.L., and Y.-R.C.; data curation, S.-M.H., C.-Y.L., Y.-M.C. and Y.-R.C.; writing—original draft preparation, S.-M.H., C.-Y.L., Y.-C.Y. and H.-Y.C.; writing—review and editing, S.-M.H., C.-Y.L., Y.-C.C. and H.-Y.C.; supervision, Y.-C.Y., Y.-C.C. and H.-Y.C.; project administration, Y.-C.Y., Y.-C.C. and H.-Y.C.; funding acquisition, Y.-C.C. and H.-Y.C. All authors have read and agreed to the published version of the manuscript.

Funding: This research was funded by the Ministry of Science and Technology of Taiwan (MOST 108-2221-E-002-169-MY3; 108-2218-E-007-045; 109-2314-B-002-041-MY3; 109-2634-F-002-042). In addition, this work was further supported by the "Advanced Research Center for Green Materials Science and Technology" from The Featured Area Research Center Program within the framework of the Higher Education Sprout Project by the Ministry of Education (109L9006).

Institutional Review Board Statement: Not applicable.

Informed Consent Statement: Not applicable.

Data Availability Statement: All data generated or analyzed during this study are included in this published article and its supplementary information files.

Conflicts of Interest: The authors declare no conflict of interest. The funders had no role in the design of the study; in the collection, analyses, or interpretation of data; in the writing of the manuscript, or in the decision to publish the results.

References

1. Chai, G.S.; Yoon, S.B.; Yu, J.-S.; Choi, J.-H.; Sung, Y.-E. Ordered Porous Carbons with Tunable Pore Sizes as Catalyst Supports in Direct Methanol Fuel Cell. *J. Phys. Chem. B* **2004**, *108*, 7074–7079. [CrossRef]
2. Kosuge, K.; Kubo, S.; Kikukawa, N.; Takemori, M. Effect of Pore Structure in Mesoporous Silicas on VOC Dynamic Adsorption/Desorption Performance. *Langmuir* **2007**, *23*, 3095–3102. [CrossRef]
3. Li, Y.Y.; Cunin, F.; Link, J.R.; Gao, T.; Betts, R.E.; Reiver, S.H.; Chin, V.; Bhatia, S.N.; Sailor, M.J. Polymer Replicas of Photonic Porous Silicon for Sensing and Drug Delivery Applications. *Science* **2003**, *299*, 2045–2047. [CrossRef] [PubMed]
4. Wales, D.J.; Grand, J.; Ting, V.P.; Burke, R.D.; Edler, K.J.; Bowen, C.R.; Mintova, S.; Burrows, A.D. Gas Sensing Using Porous Materials for Automotive Applications. *Chem. Soc. Rev.* **2015**, *44*, 4290–4321. [CrossRef]
5. Horcajada, P.; Chalati, T.; Serre, C.; Gillet, B.; Sebrie, C.; Baati, T.; Eubank, J.F.; Heurtaux, D.; Clayette, P.; Kreuz, C. Porous Metal–Organic-Framework Nanoscale Carriers as a Potential Platform for Drug Delivery and Imaging. *Nat. Mater.* **2010**, *9*, 172–178. [CrossRef]
6. Santos, H.A.; Mäkilä, E.; Airaksinen, A.J.; Bimbo, L.M.; Hirvonen, J. Porous Silicon Nanoparticles for Nanomedicine: Preparation and Biomedical Applications. *Nanomedicine* **2014**, *9*, 535–554. [CrossRef] [PubMed]
7. Zhang, Y.; Yang, L.; Yan, L.; Wang, G.; Liu, A. Recent Advances in the Synthesis of Spherical and Nanomof-Derived Multifunctional Porous Carbon for Nanomedicine Applications. *Coord. Chem. Rev.* **2019**, *391*, 69–89. [CrossRef]
8. Pounder, R.J.; Stanford, M.J.; Brooks, P.; Richards, S.P.; Dove, A.P. Metal Free Thiol–Maleimide 'Click' Reaction as a Mild Functionalisation Strategy for Degradable Polymers. *Chem. Commun.* **2008**, 5158–5160. [CrossRef] [PubMed]
9. Tron, G.C.; Pirali, T.; Billington, R.A.; Canonico, P.L.; Sorba, G.; Genazzani, A.A. Click Chemistry Reactions in Medicinal Chemistry: Applications of the 1, 3-dipolar Cycloaddition Between Azides and Alkynes. *Med. Res. Rev.* **2008**, *28*, 278–308. [CrossRef]
10. Blackman, M.L.; Royzen, M.; Fox, J.M. Tetrazine Ligation: Fast Bioconjugation Based on Inverse-Electron-Demand Diels−Alder Reactivity. *J. Am. Chem. Soc.* **2008**, *130*, 13518–13519. [CrossRef]
11. Best, M.D. Click Chemistry and Bioorthogonal Reactions: Unprecedented Selectivity in the Labeling of Biological Molecules. *Biochemistry* **2009**, *48*, 6571–6584. [CrossRef]
12. Ciampi, S.; Böcking, T.; Kilian, K.A.; Harper, J.B.; Gooding, J.J. Click Chemistry in Mesoporous Materials: Functionalization of Porous Silicon Rugate Filters. *Langmuir* **2008**, *24*, 5888–5892. [CrossRef] [PubMed]
13. Xi, W.; Scott, T.F.; Kloxin, C.J.; Bowman, C.N. Click Chemistry in Materials Science. *Adv. Funct. Mater.* **2014**, *24*, 2572–2590. [CrossRef]
14. L'abbé, G. Decomposition and Addition Reactions of Organic Azides. *Chem. Rev.* **1969**, *69*, 345–363. [CrossRef]
15. Chen, H.-Y.; Lahann, J. Designable Biointerfaces Using Vapor-Based Reactive Polymers. *Langmuir* **2010**, *27*, 34–48. [CrossRef]
16. Tung, H.-Y.; Guan, Z.-Y.; Liu, T.-Y.; Chen, H.-Y. Vapor Sublimation and Deposition to Build Porous Particles and Composites. *Nat. Commun.* **2018**, *9*, 2564. [CrossRef]
17. Tung, H.-Y.; Sun, T.-P.; Sun, H.-Y.; Guan, Z.-Y.; Hu, S.-K.; Chao, L.; Chen, H.-Y. Construction and Control of 3D Porous Structure Based on Vapor Deposition on Sublimation Solids. *Appl. Mater. Today* **2017**, *7*, 77–81. [CrossRef]
18. Lin, C.-W.; Guan, Z.-Y.; Lu, M.; Wu, T.-Y.; Cheng, N.-C.; Chen, H.-Y.; Yu, J. Synergistically Enhanced Wound Healing of a Vapor-Constructed Porous Scaffold. *ACS Appl. Bio Mater.* **2020**, *3*, 5678–5686. [CrossRef]
19. Wu, C.-Y.; Guo, C.-L.; Yang, Y.-C.; Huang, C.-W.; Zeng, J.-Y.; Guan, Z.-Y.; Chiang, Y.-C.; Wang, P.-Y.; Chen, H.-Y. Parylene-Based Porous Scaffold with Functionalized Encapsulation of Platelet-Rich Plasma and Living Stem Cells for Tissue Engineering Applications. *ACS Appl. Bio Mater.* **2020**, *3*, 7193–7201. [CrossRef]
20. Wu, C.-Y.; Liu, H.-Y.; Huang, C.-W.; Yeh, S.-Y.; Cheng, N.-C.; Ding, S.-T.; Chen, H.-Y. Synergistically Controlled Stemness and Multilineage Differentiation Capacity of Stem Cells on Multifunctional Biointerfaces. *Adv. Mater. Interfaces* **2017**. [CrossRef]
21. Wu, C.-Y.; Chang, C.-W.; Yuan, R.-H.; Chiang, Y.-C.; Chen, J.-T.; Kang, D.-Y.; Chen, H.-Y. Multifunctional Nanoparticles with Controllable Dimensions and Tripled Orthogonal Reactivity. *Nanoscale* **2017**, *9*, 14787–14791. [CrossRef]
22. Guan, Z.-Y.; Wu, C.-Y.; Chen, H.-Y. Stepwise and Programmable Cell Differentiation Pathways of Controlled Functional Biointerfaces. *Acs Biomater. Sci. Eng.* **2017**, *3*, 1815–1821. [CrossRef]

23. Chen, H.-Y. Micro- and Nano-Surface Structures Based on Vapor-Deposited Polymers. *Beilstein J. Nanotechnol.* **2017**, *8*, 1366–1374. [CrossRef] [PubMed]
24. Wu, C.-Y.; Huang, C.-W.; Guan, Z.-Y.; Wu, J.-T.; Yeh, S.-Y.; Su, C.-T.; Chang, C.-H.; Ding, S.-T.; Chen, H.-Y. Vapor-based Coatings for Antibacterial and Osteogenic Functionalization and the Immunological Compatibility. *Mater. Sci. Eng. C* **2016**, *69*, 283–291. [CrossRef] [PubMed]
25. Sun, T.-P.; Tai, C.-H.; Wu, J.-T.; Wu, C.-Y.; Liang, W.-C.; Chen, H.-Y. Multifaceted and Route-Controlled "Click" Reactions based on Vapor-Deposited Coatings. *Biomater. Sci.* **2016**, *4*, 265–271. [CrossRef]
26. Guan, Z.-Y.; Wu, C.-Y.; Wu, J.-T.; Tai, C.-H.; Yu, J.; Chen, H.-Y. Multifunctional and Continuous Gradients of Biointerfaces Based on Dual Reverse Click Reactions. *ACS Appl. Mater. Interfaces* **2016**, *8*, 13812–13818. [CrossRef]
27. Tsai, M.-Y.; Chen, Y.-C.; Lin, T.-J.; Hsu, Y.-C.; Lin, C.-Y.; Yuan, R.-H.; Yu, J.; Teng, M.-S.; Hirtz, M.; Chen, M.H.-C.; et al. Vapor-Based Multicomponent Coatings for Antifouling and Biofunctional Synergic Modifications. *Adv. Funct. Mater.* **2014**, *24*, 2281–2287. [CrossRef]
28. Sun, H.-Y.; Fang, C.-Y.; Lin, T.-J.; Chen, Y.-C.; Lin, C.-Y.; Ho, H.-Y.; Chen, M.H.C.; Yu, J.; Lee, D.-J.; Chang, C.-H.; et al. Thiol-Reactive Parylenes as a Robust Coating for Biomedical Materials. *Adv. Mater. Interfaces* **2014**, *1*, 1400093. [CrossRef]
29. Su, C.-T.; Yuan, R.-H.; Chen, Y.-C.; Lin, T.-J.; Chien, H.-W.; Hsieh, C.-C.; Tsai, W.-B.; Chang, C.-H.; Chen, H.-Y. A Facile Approach Toward Protein-Resistant Biointerfaces Based on Photodefinable Poly-P-Xylylene Coating. *Colloids Surf. B Biointerfaces* **2014**, *116*, 727–733. [CrossRef]
30. Chen, H.-Y.; Lin, T.-J.; Tsai, M.-Y.; Su, C.-T.; Yuan, R.-H.; Hsieh, C.-C.; Yang, Y.-J.; Hsu, C.-C.; Hsiao, H.-M.; Hsu, Y.-C. Vapor-Based Tri-Functional Coatings. *Chem. Commun.* **2013**, *49*, 4531–4533. [CrossRef]
31. Wu, M.-G.; Hsu, H.-L.; Hsiao, K.-W.; Hsieh, C.-C.; Chen, H.-Y. Vapor-Deposited Parylene Photoresist: A Multipotent Approach toward Chemically and Topographically Defined Biointerfaces. *Langmuir* **2012**, *28*, 14313–14322. [CrossRef] [PubMed]
32. Wu, J.-T.; Huang, C.-H.; Liang, W.-C.; Wu, Y.-L.; Yu, J.; Chen, H.-Y. Reactive Polymer Coatings: A General Route to Thiol-ene and Thiol-yne Click Reactions. *Macromol. Rapid Commun.* **2012**, *33*, 922–927. [CrossRef] [PubMed]
33. Tsai, M.-Y.; Lin, C.-Y.; Huang, C.-H.; Gu, J.-A.; Huang, S.-T.; Yu, J.; Chen, H.-Y. Vapor-based Synthesis of Maleimide-Functionalized Coating for Biointerface Engineering. *Chem. Commun.* **2012**, *48*, 10969–10971. [CrossRef]
34. Chen, H.Y.; Lahann, J. Vapor-Assisted Micropatterning in Replica Structures: A Solventless Approach towards Topologically and Chemically Designable Surfaces. *Adv. Mater.* **2007**, *19*, 3801–3808. [CrossRef]
35. Tsai, Y.-T.; Wu, C.-Y.; Guan, Z.-Y.; Sun, H.-Y.; Cheng, N.-C.; Yeh, S.-Y.; Chen, H.-Y. Topologically Controlled Cell Differentiation Based on Vapor-Deposited Polymer Coatings. *Langmuir* **2017**. [CrossRef] [PubMed]
36. Guan, Z.-Y.; Wu, C.-Y.; Chen, T.-Y.; Huang, S.-T.; Chiang, Y.-C.; Chen, H.-Y. Clickable and Photo-Erasable Surface Functionalities by Using Vapor-Deposited Polymer Coatings. *ACS Biomater. Sci. Eng.* **2019**, *5*, 1753–1761. [CrossRef]
37. Chen, Y.-C.; Sun, T.-P.; Su, C.-T.; Wu, J.-T.; Lin, C.-Y.; Yu, J.; Huang, C.-W.; Chen, C.-J.; Chen, H.-Y. Sustained Immobilization of Growth Factor Proteins Based on Functionalized Parylenes. *ACS Appl. Mater. Interfaces* **2014**, *6*, 21906–21910. [CrossRef] [PubMed]
38. Lahann, J.; Langer, R. Novel Poly(p-xylylenes): Thin Films with Tailored Chemical and Optical Properties. *Macromolecules* **2002**, *35*, 4380–4386. [CrossRef]
39. Deng, X.; Friedmann, C.; Lahann, J. Bio-orthogonal “Double-Click” Chemistry Based on Multifunctional Coatings. *Angew. Chem. Int. Ed.* **2011**, *50*, 6522–6526. [CrossRef] [PubMed]
40. Guan, Z.-Y.; Huang, C.-W.; Huang, M.-C.; Wu, C.-Y.; Liu, H.-Y.; Ding, S.-T.; Chen, H.-Y. Controlling Multi-Function of Biomaterials Interfaces Based on Multiple and Competing Adsorption of Functional Proteins. *Colloids Surf. B Biointerfaces* **2017**, *149*, 130–137. [CrossRef]

MDPI
St. Alban-Anlage 66
4052 Basel
Switzerland
Tel. +41 61 683 77 34
Fax +41 61 302 89 18
www.mdpi.com

Coatings Editorial Office
E-mail: coatings@mdpi.com
www.mdpi.com/journal/coatings

MDPI
St. Alban-Anlage 66
4052 Basel
Switzerland

Tel: +41 61 683 77 34
Fax: +41 61 302 89 18

www.mdpi.com

ISBN 978-3-0365-2244-9